Magnetosphere

Thesis submitted for the degree of
Doctor of Philosophy
at the University of Leicester

Lisa Baddeley

Radio and Space Plasma Physics Group
Department of Physics and Astronomy
University of Leicester

October 2003

Abstract

Wave-Particle Interactions in the Terrestrial Magnetosphere

Lisa Baddeley

This thesis examines small scale poloidal mode magnetohydrodynamic waves which have an energy generation mechanism internal to the magnetosphere in the form of unstable particle populations. The energy from these particles is fed into a resonant wave mode and, ultimately, dissipated in the terrestrial ionosphere.

By analysing Ion Distribution Functions (IDFs) the statistical occurrence of the driving magnetospheric particle populations is presented. Results indicate that the dominant driving particle populations are those of ~ 10 - 40 keV protons. The free energy of the particles has been quantified, revealing the dominance of the lower energy particle populations. The majority of unstable low energy protons contain > 10^{10} J of free energy in comparison to the higher energy protons which contain < 10^9 J.

Using this method, one event, using conjugate ionospheric – magnetospheric data is examined and compared to a similar conjugate event of a rare subset of small scale waves called Giant Pulsations (Pgs). The available free energy is compared to the energy dissipated into the conjugate ionospheres. Estimates of the energy at the source and sink reveal that ~ 10^{10} J is transferred for the first event. Pgs are shown to transfer ten times this energy. The statistical study reveals that 10^{10} J is frequently available from unstable IDFs but 10^{11} J is not, thus providing an explanation for both the rarity of Pgs and the ubiquity of other small scale waves.

Observations also suggest that dawn sector waves are driven by the drift-bounce resonance mechanism, while in the dusk sector waves are driven by both drift and drift-bounce resonance mechanisms.

Additionally, ionospheric observations indicate that the occurrence of small scale pulsations could be more abundant than previously thought. This implies that the quantity of energy being transported round the magnetospheric cavity and into the ionosphere via wave-particle interactions has previously been underestimated.

To my Mum and Dad

Declarations

The research detailed in Chapter 6 of this thesis also appears in the following publications:

Baddeley, L. J., T. K. Yeoman, D. M. Wright, J. A. Davies, K. J. Trattner, and J. L. Roeder, Morning sector drift-bounce resonance driven ULF waves observed in artificially induced HF radar backscatter, *Ann. Geophys.*, 20, 1487, 2002.

Acknowledgements

I would like to thank everyone who has helped me through the three years of my PhD. As well as undertaking all the research detailed in this thesis I have had immense fun these past few years, from cage dancing in Dundee to singing 'My Way' in a karaoke bar in Tokyo. There are so many people to whom I'm immensely grateful, but here are a few who I would like to personally thank.

Firstly, Professor Stan Cowley for giving me the opportunity to undertake my research in the Radio and Space Plasma Physics group here at Leicester University and also the Particle Physics and Astronomy Research Council (PPARC) for funding my studentship.

A huge thank you to my supervisor Dr. Tim Yeoman. I would like to take this opportunity to show my appreciation not only for the guidance and help you've provided but also the vast quantities of gin and anecdotal conversation. I would also like to apologise for still being a shandy drinker..sorry!!

I would like to thank everyone in the research group who has helped me over the years, a few in particular. Emma; my partner in shoe shopping, gin drinking and many other escapades, thank you for your friendship and support and I'm sure we will continue our mission to make physics a more fashionable environment. Darren; thank you for taking me under your wing as a ULF bod, your guidance and friendship has been invaluable, and I really didn't mean to poison you with that chilli soup!! Steve; the man who taught me IDL and also imparted the knowledge that it's never too early to drink, as somewhere in the world there is a bar open! Jim; the words 'I'm from Holland..isn't that weird?' and 'Maximum Usable Frequency' will always stay with me. Jonny (Butthead); whenever I hear 'Trouble' by Coldplay, or see the word 'pants' it'll remind me of my mad office mate! Ade; the big brother I never had, thank you so much for everything you've done for me (and I'm not a fussy eater!!). Mark; thank you also for your words of wisdom and also the trips to see the Foxes!!

I would also like to thank Dr. Graham Wynn for being a fantastic friend and for always being there for me. Thanks also to David Hunt, for making me laugh more than anyone else in the world (whale oil beef hooked)! Thank you to Mike for being my rock and companion during this time, I will never forget you. A quick mention to Leicester volleyball club, Andy Collins and Tim Shaw for providing me with a violent release for pent up aggression!

Finally, thank you to my mum and dad for always believing in me and providing me with that invaluable 'Bank of Baddeley'!

Contents

Chapter 1

Solar Terrestrial Relations

1. Introduction

The subject of space plasma physics encompasses a vast array of systems from planetary magnetic fields to those of neutron stars and it is thought that ~ 95 % of the known universe exists in a plasma state. This thesis presents the results of investigations into solar-terrestrial interactions. In particular, it focuses on the relationship between the Earth's magnetic field and the particle populations within it which have origins in both the solar wind and the Earth's ionosphere. The energy contained in the particle populations is fed into the terrestrial magnetic field where it manifests itself as Ultra Low Frequency (ULF) magnetohydrodynamic (MHD) waves. The term Ultra Low Frequency covers geomagnetic pulsations with a frequency range of ~1 mHz to 1 Hz. The 'ultra' is included to signify that the pulsation frequency is lower than the natural frequencies of the ambient plasma such as the gyrofrequencies of the particles. The ULF waves then dissipate this energy into the ionosphere at an altitude of ~ 100 km, warming up the atmosphere. This process is a major route through which solar energy can enter into and effect the Earth's atmosphere. Whilst current theory is broadly successful in explaining many of the details, the energy of the particle populations involved in the interactions and also the nature of the wave modes themselves are little understood. This thesis expands and improves upon previous work by quantifying, for the first time, the amount of energy that is transferred. This technique is then applied in a statistical and case study manner to new data revealing for the first time the prevalence of these ULF waves and also the dominant particle energies which drive them. This thesis also employs new conjugate observational techniques using satellite and radar data to determine the nature of the standing wave mode and the resonance mechanism.

Chapter 1 of this thesis gives a brief overview of solar terrestrial interactions, allowing the scope of the research to be understood in context. Chapter 2 will introduce a more detailed theory, in particular that of MHD waves and wave–particle interactions and how these manifest themselves in the terrestrial magnetosphere. Chapter 3 gives an overview of previous work undertaken in this subject and discusses some of the unanswered questions that this thesis addresses in more detail. Chapter 4 details the instrumentation and experimental techniques used to obtain the data. Chapter 5 details a statistical study which analyses the nature and prevalence of the magnetospheric particle populations responsible for driving the small scale ULF waves. The study focuses on analysing the amount of 'free energy' available to drive the waves and also the energy of the interacting particles. Chapter 6 details a case study of conjugate ionospheric ULF wave observations and magnetospheric observations of the driving particle population. The chapter also describes energy calculations undertaken at both the magnetospheric source and ionospheric sink of the observed wave and compares this with results for a larger amplitude wave, a Giant Pulsation. Chapter 7 describes another statistical study which focuses on small scale ULF wave observations in the ionosphere. Two case studies of waves which display a signature in ground magnetometers are also discussed. The final chapter, Chapter 8 summarizes the work undertaken here and also outlines possible future directions for the research.

1.1. The Sun

The sun is a typical G class star, with its main constituents being Hydrogen (~90%) and Helium (~9%); although there are trace (~1%) amounts of heavier elements. Held together under its own gravitational attraction, solar material is compressed to such high densities and pressures that nuclear fusion can take place in its core. The sun's atmosphere is composed of three separate layers: the photosphere, chromosphere and corona, as illustrated in figure 1.1. The photosphere forms a thin shell of only 500 km in thickness, yet the densities here are of the order of 10^{23} m^{-3} and thus this layer is responsible for the majority of the sun's light. Above the photosphere is the chromosphere, which has a density of the order of 10^{17} m^{-3} and then the corona where densities have decreased to 10^{14} m^{-3}. The temperature in the corona is large enough (~2×10^{6} K) for the hydrogen and helium to become completely ionised, thus resulting in the formation of a fully ionised plasma. The gas pressure at the base of the corona dwarfs the effect of the solar gravitational pull on the plasma and thus the plasma streams away from the sun, forming the solar wind. This plasma is accelerated away from the sun to a supersonic speed of ~ 450 km s^{-1} within ~ 10 solar radii. Not only is the plasma emitted from the sun, but due to the phenomenon of 'frozen-in-flux', by which magnetic fields and plasma are 'frozen' together, the sun's magnetic field is carried along with it, forming the Interplanetary Magnetic Field (IMF). As a magnetic flux tube is dragged out from the sun, the foot of the tube still remains anchored to the sun. When multiple flux tubes are then viewed above the ecliptic plane they form a spiral, the so-called garden hose pattern, which is illustrated in figure 1.2. This phenomenon was first

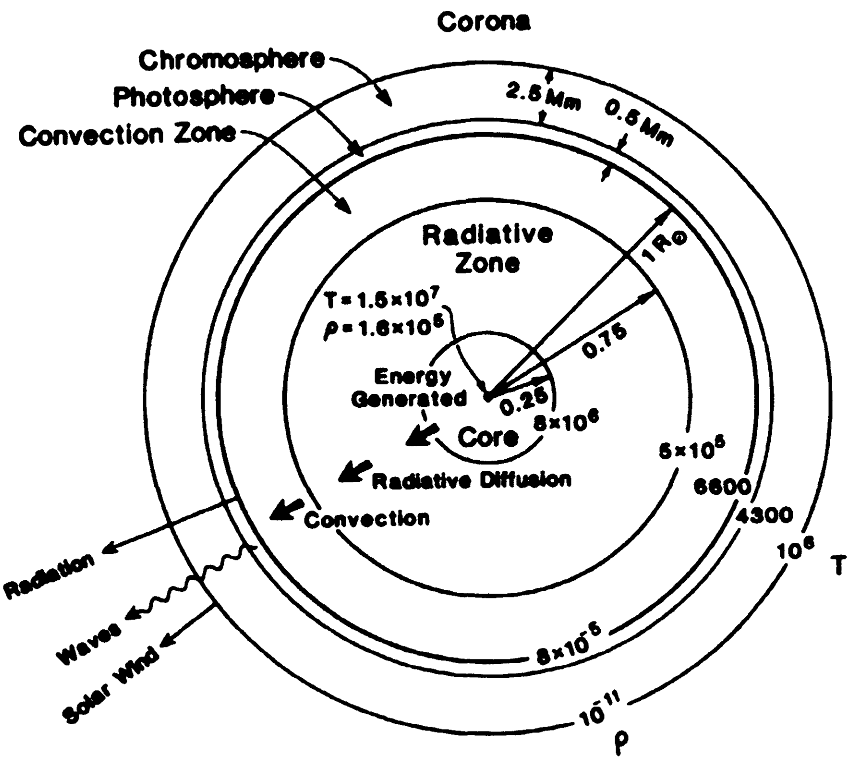

Figure 1.1. A cross sectional schematic of the solar interior (from *Kivelson and Russell* 1995). The sun can be divided into zones which depend on relative temperature and densities.

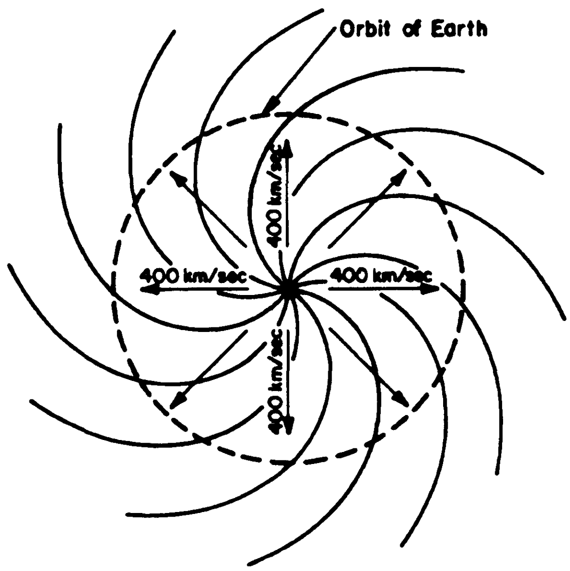

Figure 1.2. The 'garden hose' configuration of the interplanetary magnetic field (IMF) (from *Kivelson and Russell,* 1995). The foot of the field line remians attached to the sun but due to the phenomenon of 'frozen in flow' the magnetic field lines are carried away from the sun with the solar plasma. The flow is accelerated away from the sun to velocities of ~ 400 km s^{-1}.

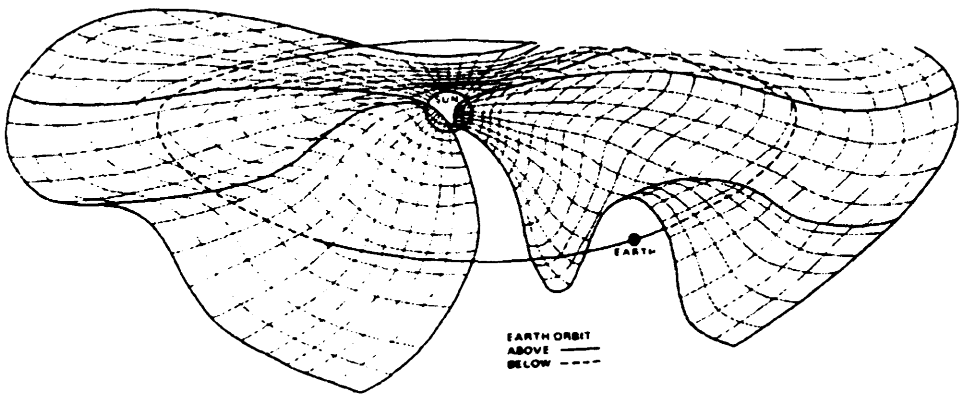

Figure 1.3. The effect of the tilt of the solar magnetic axis with respect to the rotation axis produces the 'ballerina skirt' effect. This changes the location of the Earth with respect to the solar wind current sheet from (*Kivelson and Russell* 1995).

documented by *Parker* (1963) and is called the Parker Spiral. When viewed in the ecliptic plane, this results in the IMF in the northern hemisphere pointing away from the sun and towards it in the southern hemisphere, with a thin current sheet separating the two. This situation is further complicated by the fact that the sun's magnetic field also reverses polarity every 11 years and its rotation axis is tilted with respect to its dipole axis. The latter forces this current sheet out of the ecliptic into a 'ballerina skirt' configuration, shown in figure 1.3. Coupled with highly variable flow speeds and phenomena such as coronal mass ejections this results in a highly variable interplanetary medium at the Earth.

1.2. The Earth's Magnetosphere

The Earth possesses its own magnetic field, generated by a rotating metallic core at the centre of the planet. The field generated is approximately dipolar with an equatorial surface field strength of ~ 30,000 nT and is offset by ~ 11.5° from the planetary rotation axis. The Earth's magnetosphere is defined as the cavity in which the terrestrial magnetic field is confined by the impinging IMF. This concept was first considered by Sydney Chapman and Vincenzo Ferraro (*Chapman and Ferraro,* 1931), when they applied the concept of 'frozen-in-flux' to the Earth's magnetosphere. They reasoned that the solar wind plasma would remain frozen to the IMF and plasma of terrestrial origin would remain frozen to the geomagnetic field. When the two plasma populations meet each other they would not interact, but would remain in two distinct regions, separated by a thin current sheet boundary called the magnetopause. Across the magnetopause, the magnetic field usually undergoes a sharp change of strength and direction and as a consequence of this a sheet of electrical current must flow in the plasma in this interface, called the Chapman-Ferraro current. The magnetosphere is illustrated schematically in the noon midnight meridian in figure 1.4. The magnetopause is located between 9 and 11 R_E (where R_E represents one Earth radius; ~ 6400 km) upstream on the dayside. However, on the nightside the magnetosphere extends into a magnetotail hundreds of R_E long in an antisunward direction. Upstream of the dayside magnetopause lies the bow shock. This forms as a consequence of the supersonic solar wind flow. Across the shock the flow is slowed, compressed and heated, forming a layer of turbulent plasma outside the magnetopause called the magnetosheath.

1.2.1. The Dungey Cycle

In 1961, James Dungey (*Dungey,* 1961) realised that this frozen in flux approximation would break down in some regions, one such region being the dayside current sheet boundary layer.

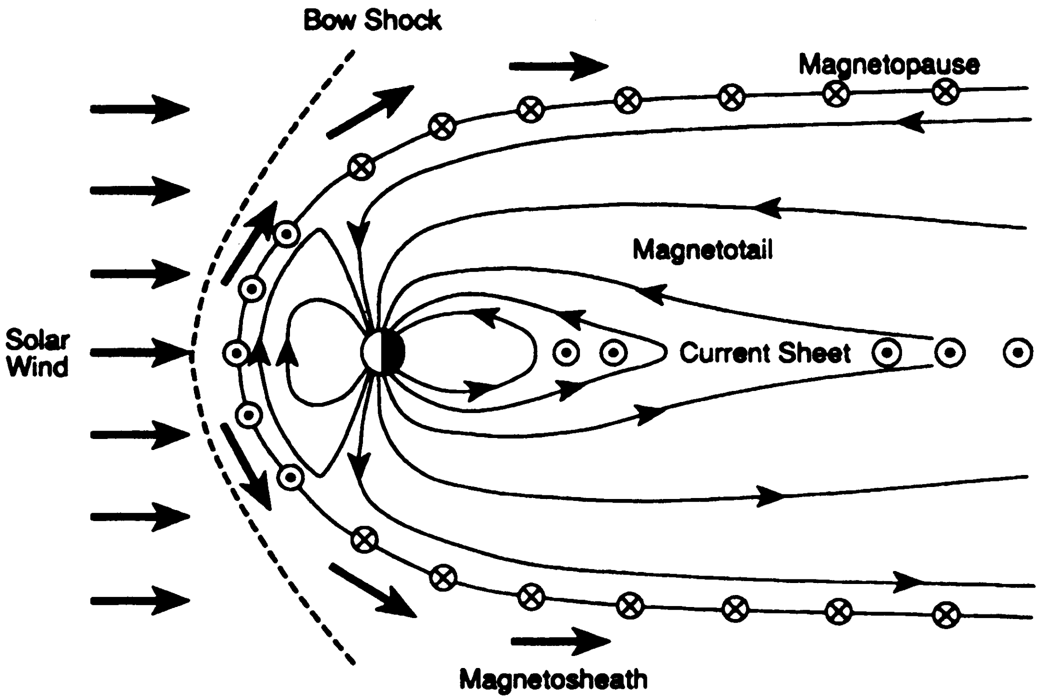

Figure 1.4. Cross section of the Chapman Ferraro model of the magnetosphere in the noon-midnight meridian. The arrowed solid lines show the terrestrial magnetic field lines. The current systems are represented by the circles. The circled dots indicate currents out of the plane of the diagram and the circled crosses represent currents into the plane (from *Kivelson and Russell,* 1995).

Here, it is possible to have anti-parallel magnetic fields. This, coupled with the small scale size of the plasma means the plasma regime becomes diffusion dominated allowing field lines from both regimes to break and reconnect with different flux tubes. This process produces geomagnetic field lines that are 'open' to the IMF, thus allowing mass, momentum and energy transfer from the solar wind into the Earth's magnetosphere. This process was termed magnetic reconnection. These newly reconnected field lines (1 and 1' in figure 1.5), connected at one end to the sun and at the other to the Earth, are dragged anti-sunward through magnetic tension forces and solar wind flow, across the polar cap and into the magnetotail, where the energy and flux is stored (flux tubes 2 to 5 in figure 1.5). This energy is released in the centre of the tail when the scale size of the plasma is again small and the fields are anti-parallel, thus allowing the flux tubes to reconnect once more (flux tubes 6 and 6'). This energy release is one of the primary mechanisms by which plasma of solar origin can enter the Earth's inner magnetosphere. If the flux is allowed to build up in the tail, the sudden energy release forms part of what is called a substorm (*Lester*, 2000). This newly injected plasma forms what is termed the magnetospheric ring current. Once injected into the dipolar magnetosphere electrons will drift eastwards while ions will drift westward, thus causing a westward current to flow. The motion of these ions will be discussed in more detail in chapter 2. In the region tailward of this reconnection region the disconnected flux tubes flow back into the solar wind (flux tube 7'), while Earthward of the reconnection region the newly closed field lines flow back towards the Earth where they convect around the flanks of the inner magnetosphere towards the dayside magnetopause (flux tubes 7 to 9). The cycle then repeats itself. This entire process is known as the Dungey cycle and is communicated to the ionosphere where it drives a twin cell convection pattern in the high latitude ionospheres. One such cell is shown below the schematic of the magnetosphere in figure 1.5. The numbers equate to the positions of the feet of the field lines indicated in the main figure.

1.2.2. Regions of the Magnetosphere

The magnetosphere can be divided up into specific regions, each characterized by a different plasma environment as shown in figure 1.6. On the dayside particles can enter into the magnetosphere through magnetic reconnection between the terrestrial magnetic field and the IMF. Particles are accelerated down the field lines at the cusp and into the high latitude ionosphere. The majority of particles enter into the inner magnetosphere through processes in the tail. The tail lobes map down to the high latitude nightside ionosphere. The environment is that of very low density (< 0.1 cm $^{-3}$) plasma of both

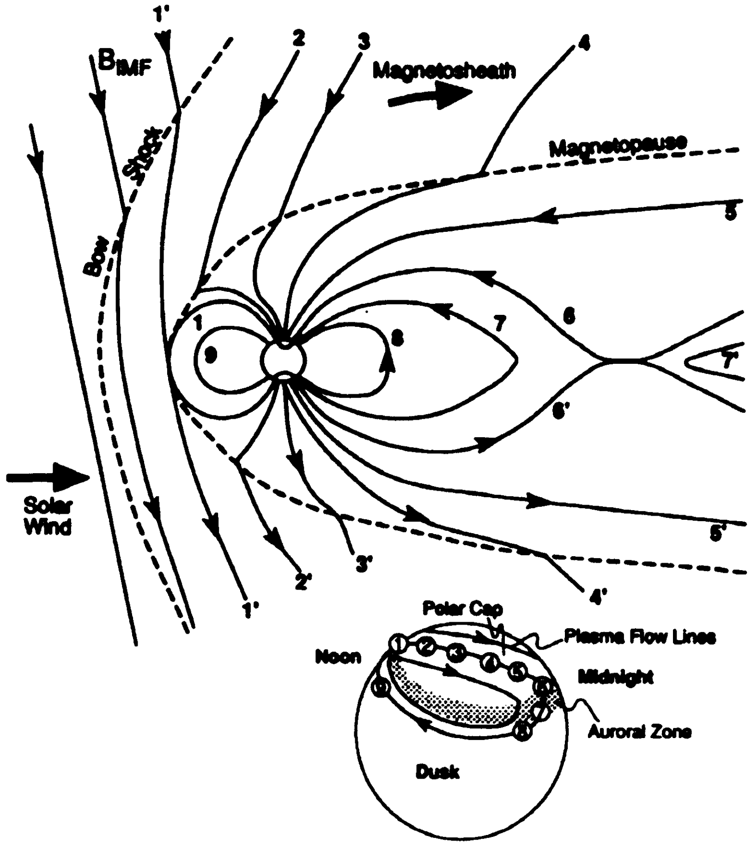

Figure 1.5. Cross section of Dungeys 'open' magnetosphere in the noon midnight meridian. The numbered magnetic field lines indicate the different phases of magnetic reconnection between the terrestrial magnetosphere and the IMF. The smaller schematic indicates the position of the foot of the field line in the ionosphere as it moves through the Dungey cycle (from *Kivelson and Russell*, 1995).

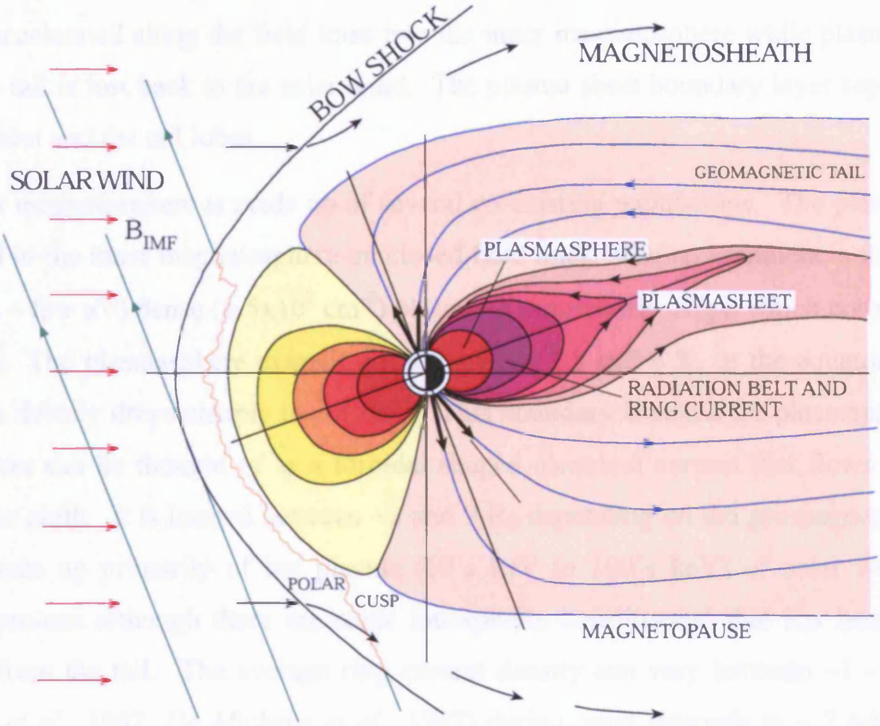

Figure 1.6. Schematic of the magnetosphere, indicating the various plasma enivronments (adapted from *Kivelson and Russell*, 1995).

magnetospheric and solar wind origin, with particle energies of a few eV. In between the tail lobes is the plasmasheet. Here, the plasma is hotter (energies ~ few keV) and denser (~1 cm^{-3}) than that of the tail lobes but is again made up a mixture of solar wind and ionospheric particles. Upon reconnection in the tail, plasma earthward of the reconnection point is accelerated along the field lines into the inner magnetosphere while plasma further down the tail is lost back to the solar wind. The plasma sheet boundary layer separates the plasma sheet and the tail lobes.

The inner magnetosphere is made up of several co-existing populations. The plasmasphere is located in the inner magnetosphere on closed field lines. The environment is that of cool (energies ~ few eV) dense ($\geq 5 \times 10^2$ cm^{-3}) plasma of ionospheric origin which corotates with the Earth. The plasmasphere extends out to between 2.5 and 6 R_E in the equatorial plane, where the density drops sharply to ~ 1 cm^{-3}. This boundary is called the plasmapause. The ring current can be thought of as a toroidal shaped electrical current that flows westward around the earth. It is located between ~2 and 9 R_E depending on the geomagnetic activity and is made up primarily of hot plasma (10's keV to 100's keV) of solar wind origin (mainly protons although there are some ionospheric constituents) that has been injected inwards from the tail. The average ring current density can very between ~1 - 4 nA m^{-2} (e.g. *Lui et al.,* 1992; *De Michelis et al.,* 1997) during quiet intervals to ~ 7 nA m^{-2} (e.g. *Lui et al.,* 1987) during stormtime conditions. This corresponds to energy densities of between ~ 10 keV cm^{-3} and ~ 100 keV cm^{-3}. The ring current is the primary energy source region for ULF waves driven through wave-particle interactions.

1.3. The Ionosphere

Beneath the magnetosphere lies the Earth's upper atmosphere, extending upwards from an altitude of ~85 km. Solar radiation in the ultraviolet (UV) and extreme ultraviolet (EUV) is incident on the upper atmosphere and causes partial ionisation of the chemical compounds found here, thus forming an ionosphere. It is this ionisation that allows coupling to take place between the magnetosphere, the ionosphere and ultimately the Earth's upper atmosphere. This partial ionisation means that electric currents are able to flow in the ionosphere. The ionosphere is divided into three regions (D, E and F) which are classified in terms of ionic species. Figure 1.7 shows an altitude profile of the three regions and accompanying conductivity profiles and particle drifts associated with the system. The D-region lies below a height of ~90 km and is only weakly ionised due to the high collision

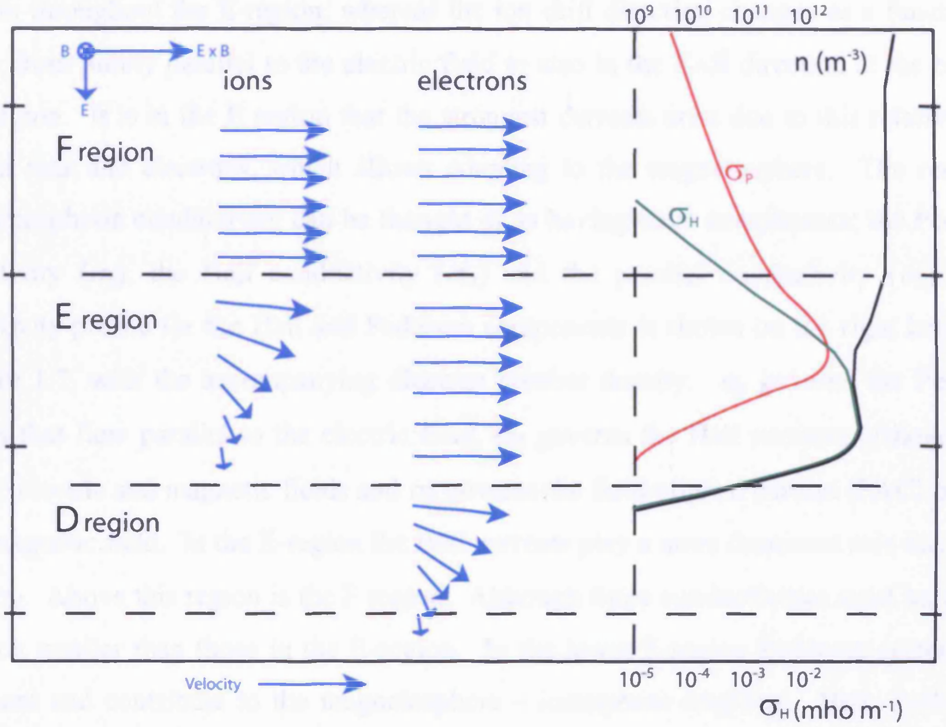

Figure 1.7. An altitude profile of the ionosphere showing the relative drifts of ions and electrons (left-hand side) and the corresponding Hall and Pedersen conductivities (σ_H and σ_P, respectively) and electron number density, n, (right-hand side). The blue arrows show the net horizontal particle drift with respect to **E** and **E**$\wedge$**B** assuming a vertical field (from *Grocott*, 2002).

frequencies. As such there are only electron drifts to consider. At the bottom of the D region the electrons drift in the direction of the electric field, however as the altitude increases and thus the ionization of the medium increases, the electrons drift in a direction perpendicular to both the electric and magnetic field, so called $\mathbf{E}\wedge\mathbf{B}$ drift. Above that is the E region, which stretches from 90 to 150 km in altitude. This region is dominated by singly-charged molecular ion species such as O_2^+ and NO^+. The electrons drift in the $\mathbf{E}\wedge\mathbf{B}$ direction throughout the E-region, whereas the ion drift direction changes as a function of altitude from purely parallel to the electric field to also in the $\mathbf{E}\wedge\mathbf{B}$ direction at the base of the F-region. It is in the E region that the strongest currents arise due to this relative drift between ions and electrons, which allows coupling to the magnetosphere. The resultant finite ionospheric conductivity can be thought of as having three components; the Pedersen conductivity (σ_p), the Hall conductivity (σ_H) and the parallel conductivity ($\sigma_{||}$). The conductivity profile for the Hall and Pedersen components is shown on the right hand side of figure 1.7, with the accompanying electron number density. σ_p governs the Pedersen currents that flow parallel to the electric field, σ_H governs the Hall currents orthogonal to both the electric and magnetic fields and $\sigma_{||}$ governs the field-aligned current (FAC) parallel to the magnetic field. In the E-region the Hall currents play a more dominant role due to the larger σ_H. Above this region is the F region. Although finite conductivities exist here, they are much smaller than those in the E-region. In the lower F-region Pedersen currents are significant and contribute to the magnetosphere – ionosphere coupling. Here, collisional effects between electrons and ions are smaller and both drift in the $\mathbf{E}\wedge\mathbf{B}$ direction.

1.4. Summary

This chapter has provided a background as to the nature of the terrestrial magnetosphere and its interaction with the IMF. It has also introduced the main regions of the magnetosphere, in particular the ring current region, which will play a pivotal role in this thesis. Chapter 2 will go onto discuss how the phenomena of ULF waves manifest themselves in the magnetospheric system.

Chapter 2

Magnetohydrodynamic (MHD) Wave Theory

2. Introduction

The first sinusoidal oscillations in the Earth's magnetic field were recorded ~ 150 years ago by *Balfor Stewart* (1861) and given the term 'geomagnetic pulsations'. It wasn't until nearly 100 years later that *J. W. Dungey* (1954) first suggested that these pulsations were due to hydromagnetic waves. The Earth's magnetosphere is an extremely complex system of plasma populations and magnetic fields, the motion of each interdependent on the other. Given the complexity of the system this chapter will first introduce the fundamental equations that govern any magnetized fluid environment. The equations will then be manipulated to demonstrate how different wave modes can propagate through the system. Constraints will be placed on the system using in the first instance a simple box model of the magnetosphere and later a more realistic dipole model to illustrate the specific wave modes observed in the terrestrial magnetosphere. The wave modes of interest in this thesis derive their energy through interactions with energetic particle populations that make up the plasma environment of the magnetosphere. Equations which govern individual particle motion in the presence of a magnetic field will first be examined before embarking on a method of describing the particle population motion as a whole using particle distribution functions. The latter method is more congenial to describing the plasma environment of the magnetosphere when examining the concept of wave particle interactions. Circumstances under which interactions and energy exchange occurs between the particle populations and wave modes will be discussed in detail with reference to the 'Battenberg cake' (see appendix) model. The ionospheric manifestation of these waves is the primary tool through which information is obtained. The energy dissipation process wherein energy which has been transferred from the particle populations to the wave modes and is then dissipated into the ionosphere through Joule heating is also discussed.

2.1. General Equations for a Magnetized Fluid

To describe any magnetized fluid requires Maxwell's equations, Ohms law and also the equations of mass and momentum conservation.

Faraday's law of induction states that a time varying magnetic field, **B** will be accompanied by an electric field **E**,

$$\nabla \wedge \mathbf{E} = -\frac{\partial \mathbf{B}}{\partial t}. \tag{2.1}$$

The resulting current system, **J** and its associated magnetic field are related by Ampère's Law,

$$\nabla \wedge \mathbf{B} = \mu_0 \mathbf{J} + \mu_0 \varepsilon_0 \frac{\partial \mathbf{E}}{\partial t}, \tag{2.2}$$

where μ_0 and ε_0 are the permeability and permittivity of free space. In equation (2.2), the first term on the right hand side represents the conduction current and the second term represents the displacement current. The relative importance of these two terms depends on the timescales of interest. Due to the low frequency phenomena and hence long timescales dealt with in this thesis the displacement current can be ignored. Equation (2.2) can now be re-written as

$$\nabla \wedge \mathbf{B} = \mu_0 \mathbf{J}. \tag{2.3}$$

The hydromagnetic form of Ohms law relates the velocity of the plasma flow, **v** to both the electric and magnetic fields. In a magnetized fluid of conductivity σ forces on the charged particle due to both magnetic and electric fields must be considered when evaluating any current systems,

$$\mathbf{J} = \sigma(\mathbf{E} + \mathbf{v} \wedge \mathbf{B}). \tag{2.4}$$

Using these equations it can be determined if the plasma will remain frozen to the magnetic field lines or if there will be diffusion of the plasma through the field. Combining equations (2.1) and (2.4) gives

$$\frac{\partial \mathbf{B}}{\partial t} = \nabla \wedge \left(\mathbf{v} \wedge \mathbf{B} - \frac{\mathbf{J}}{\sigma} \right). \tag{2.5}$$

Incorporating Ampère's law, given the fact that $\nabla.\mathbf{B} = 0$ and using the standard vector identity $\nabla^2 \mathbf{A} = \nabla(\nabla.\mathbf{A}) - \nabla \wedge \nabla \wedge \mathbf{A}$, then

$$\frac{\partial \mathbf{B}}{\partial t} = \nabla \wedge (\mathbf{v} \wedge \mathbf{B}) + \eta \nabla^2 \mathbf{B}, \tag{2.6}$$

where, $\eta = \dfrac{1}{\mu_0 \sigma}$.

The first term on the right hand side of equation (2.6) is the convective term while the second is the diffusion term. Dimensionally, equation (2.6) takes the form $\dfrac{\partial \mathbf{B}}{\partial t} = \dfrac{\mathbf{vB}}{L_o} + \dfrac{\eta \mathbf{B}}{L_o^{\ 2}}$.

The frozen-in-flux approximation, by which the magnetic field is frozen to the plasma, arises as a consequence of the extremely high electrical conductivities, σ and also the large scale size of the system, L_o. This results in a dominance of the convective term in equation (2.6). The dominance of either term is characterised by the Magnetic Reynolds number, R_m which is defined as the ratio of the convective and diffusive terms of the medium

$$R_m = \mu_0 \sigma v L_0. \tag{2.7}$$

In the solar wind, $R_m \sim 10^{11}$, implying that the system is dominated by convection and thus the plasma and magnetic fields appear frozen together. In the Earth's magnetosphere there are regions where this frozen in approximation breaks down such as at the magnetopause where reconnection occurs and also where there are large gradients across the magnetic field which occur in a magnetic dipole. Generally however, in the global MHD regime of the magnetosphere $\sigma \rightarrow \infty$ therefore, from equation (2.4)

$$\mathbf{E} = -\mathbf{v} \wedge \mathbf{B}. \tag{2.8}$$

This can also be interpreted as the fact that there will be an immediate response which will counter any attempts to produce an electric field in the rest frame of a perfectly conducting plasma. The particle motion in a system governed by the convective term in equation (2.6) and will be in a motion perpendicular to both the electric field and magnetic field. However since the particles are also gyrating around the field line the field lines must be dragged along with the particle motion. This motion of the field and the particles moving as one, the $\mathbf{E} \wedge \mathbf{B}$ drift, is another way of considering the frozen in flow and is described in more detail in section 2.7 of this chapter.

The general motion of the plasma is governed by conservation equations. The mass conservation or continuity equation deals with the inflow and outflow of ions and electrons in a unit of volume,

$$\frac{\partial \rho}{\partial t} + \nabla.(\rho \mathbf{v}) = 0, \tag{2.9}$$

where ρ is the total mass density. An application of Newton's second law gives the general form of momentum conservation or equation of motion,

$$\rho \frac{\mathrm{d}\mathbf{v}}{\mathrm{d}t} = \rho \mathbf{g} - \nabla P + \rho_{\mathrm{q}} \mathbf{E} + \mathbf{J} \wedge \mathbf{B}. \tag{2.10}$$

In the plasma environment considered in this thesis, the contributions due to the electric force, $\rho_q\mathbf{E}$ and also due to gravity, $\rho\mathbf{g}$ are negligible, in comparison to the magnetic force, $\mathbf{J}\wedge\mathbf{B}$ and the pressure force, ∇P thus the equation can be reduced to

$$\rho \frac{\mathrm{d}\mathbf{v}}{\mathrm{d}t} = -\nabla P + \mathbf{J} \wedge \mathbf{B}. \tag{2.11}$$

This set of basic equations can provide a solid base with which to evaluate the dynamics of the magnetosphere.

2.2. Wave Motion in a Magnetised Fluid

The magnetosphere is not a static system. Therefore it is more pertinent to analyse the system using a two component method composed of a larger background stable component, x_0 and a smaller perturbation component, x_1 where $x_0 >> x_1$. This can be applied to the parameters which describe the system,

$$\mathbf{B} = \mathbf{B}_0 + \mathbf{b}, \tag{2.12}$$

$$\mathbf{v} = \mathbf{v}_0 + \mathbf{v}_1, \tag{2.13}$$

$$\rho = \rho_0 + \rho_1. \tag{2.14}$$

By manipulating Maxwell's equations using this method any perturbations can be characterised. This allows a more detailed understanding of mechanisms such as energy transfer and propagation direction of any disturbance. The equations can be reduced further as the temporal and spatial derivatives of the steady state background components, x_0 can be eliminated, (i.e. $\mathrm{d}\mathbf{v}_0/\mathrm{d}t = 0$). Using the polytropic equation of state, the plasma pressure and density can be related using the sound speed, $C_S = (\gamma P/\rho)^{1/2}$, where γ is the ratio of specific heats. By substituting into equation (2.11) for **J** (using Ampère's law) and C_S^2,

$$\rho_0 \frac{d\mathbf{v_1}}{dt} + C_s^2 \nabla \rho + \mathbf{B_0} \wedge \frac{\nabla \wedge \mathbf{b}}{\mu_0} = 0. \tag{2.15}$$

Substitute for **E** from equation (2.8) into Faradays law,

$$\frac{\partial \mathbf{b}}{\partial t} = \nabla \wedge (\mathbf{v_1} \wedge \mathbf{B_0}). \tag{2.16}$$

Equation (2.9) will also take the form

$$\frac{\partial \rho_1}{\partial t} + \rho_0 (\nabla . \mathbf{v_1}) = 0. \tag{2.17}$$

First consider a general wave field which varies as $\exp i(\mathbf{k}.\mathbf{r}-\omega t)$, where $\mathbf{k}=(2\pi/\lambda)\hat{\mathbf{k}}$ with λ defining the wavelength, $\hat{\mathbf{k}}$ indicating the wave propagation direction unit vector and ω is the wave angular frequency. Allowing the wave field to take this form allows the temporal and spatial derivatives in equations (2.15) to (2.17) to be replaced with $-i\omega$ and $i\mathbf{k}$ respectively. Combining equations (2.16) and (2.17) and using the vector identity $\mathbf{A} \wedge (\mathbf{B} \wedge \mathbf{C}) = (\mathbf{A}.\mathbf{C})\mathbf{B} - (\mathbf{A}.\mathbf{B})\mathbf{C}$ an equation defining the magnetic perturbation **b** as a function of the wave field parameters can be obtained,

$$\mathbf{b} = \mathbf{B_0} \frac{(\mathbf{k}.\mathbf{v_1})}{\omega} - \mathbf{v_1} \frac{(\mathbf{k}.\mathbf{B_0})}{\omega}. \tag{2.18}$$

Combining equations (2.15) and (2.18) (integrating the notation change described above for the spatial and temporal derivatives in equation (2.15)) reveals a linearized fluid equation, which can be analysed in directions both along and perpendicular to the background magnetic field.

$$-\omega^2 \mathbf{v_1} + (C_s^2 + \mathbf{V_A}^2)(\mathbf{k}.\mathbf{v_1})\mathbf{k} + (\mathbf{k}.\mathbf{V_A})[(\mathbf{k}.\mathbf{V_A})\mathbf{v_1} - (\mathbf{V_A}.\mathbf{v_1})\mathbf{k} - (\mathbf{k}.\mathbf{v_1})\mathbf{V_A}] = 0 \tag{2.19}$$

where $\mathbf{V_A}$ is a vector in the direction of the background magnetic field with the magnitude of the Alfvén speed, $\mathbf{V_A} = \mathrm{V_a}\hat{\mathbf{B}}$, where

$$V_a = \left(\frac{\mathbf{B_0}^2}{\mu_0 \rho_0} \right)^{\frac{1}{2}}. \tag{2.20}$$

2.3. Magnetoacoustic Waves

By taking the dot product of equation (2.19) with firstly **k** and then $\mathbf{V_A}$ the variation of the wave field can be determined both along the direction of the propagation vector, **k** and also along the direction of the magnetic field, $\mathbf{B_0}$. Combine the two resulting equations together and let $\mathbf{k}.\mathbf{V_A}=kV_A\cos\theta$, where θ is defined as the angle between the background magnetic field, $\mathbf{B_0}$ and the wave propagation vector, **k**. The resulting equation is in the form of a quadratic in $\omega^2/\mathbf{k}^2$,

$$\frac{\omega^4}{\mathbf{k}^4} - (C_S^2 + V_A^2)\frac{\omega^2}{\mathbf{k}^2} + C_S^2 V_A^2 \cos^2\theta = 0. \tag{2.21}$$

The solution of which takes the form

$$\frac{\omega^2}{\mathbf{k}^2} = \frac{(C_s^2 + V_A^2)}{2} \pm \frac{1}{2}\left[(C_S^2 + V_A^2)^2 - 4C_S^2 V_A^2 \cos^2\theta\right]^{\frac{1}{2}}. \tag{2.22}$$

Equation (2.22) is called the dispersion relation, the solutions of which can now be examined at two extremes depending upon the angle θ; propagation parallel ($\theta = 0$) and perpendicular ($\theta = \pi/2$) to the background magnetic field. For these two propagation directions there exist two solutions; the positive root and the negative root. The positive root solution is called the fast mode while the negative root solution is called the slow mode. The solutions are listed in table 2.1 for each mode and the propagation velocities both along and perpendicular to the field.

The parameter u in table 2.1 is called the phase velocity and is defined as $u = \omega/k$. Both modes are referred to more generally as magnetoacoustic waves. If the phase velocity of each mode is examined graphically (figure 2.1) it can be seen that although the fast mode propagates in all directions in the plane of the oscillations, it does so fastest across the field, ($\theta = \pi/2$). In comparison, the slow mode propagates fastest along the field, with no phase velocity component perpendicular to the field. The propagation velocity of the slow mode depends only on the plasma pressure and as such is only important in a 'warm' plasma environment. In regions such as the magnetotail where energetic particle

Fast Mode	Slow Mode	
$u=\pm V_a$	$u=\pm C_S$	Parallel propagation ($\theta = 0$)
$u=\pm(V_a^2+C_S^2)^{1/2}$	$u=0$	Perpendicular propagation ($\theta = 90$)

Table 2.1. Phase velocity parallel and prependicular to the background magnetic field for the fast and slow magnetoacoustic waves.

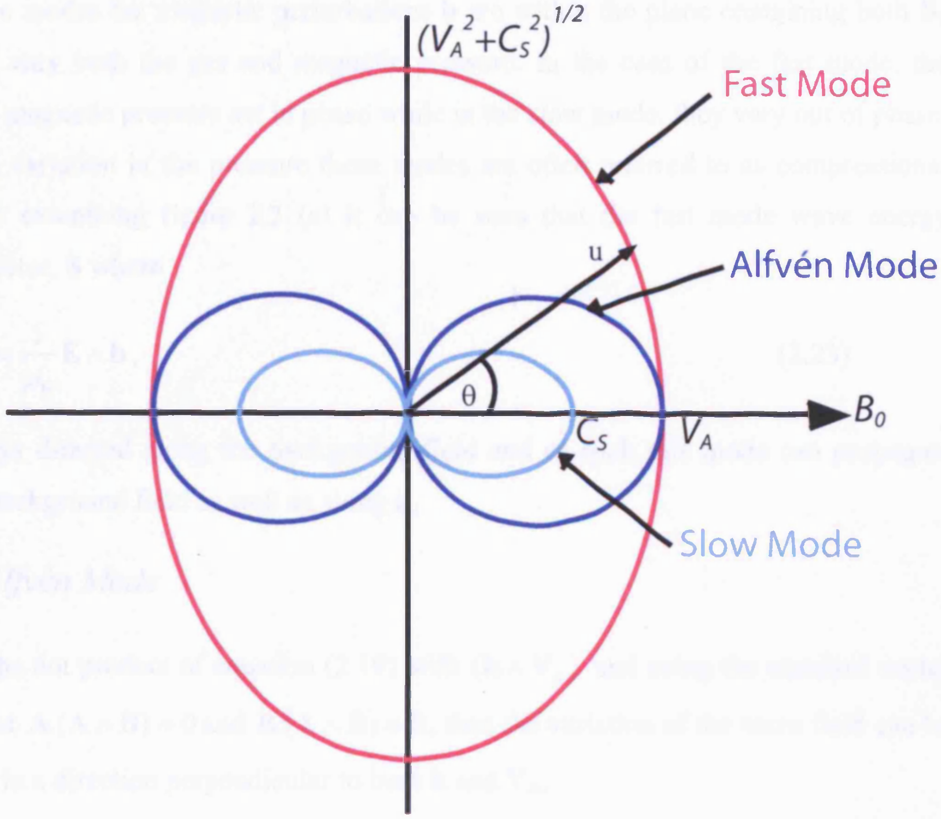

Figure 2.1. Phase velociy u as a function of angle, θ to the background magnetic field, $\mathbf{B_0}$ for the three propagation modes; Fast, slow and Alfvén. The Alfvén mode and the fast mode propagate at the Alfvén velocity, $\mathbf{V_A}$ parallel to the background field, while the slow mode propagates at the sound speed, C_S.

injections occur this mode must be considered however it is not thought to be important in the context of the work undertaken in this thesis and will not be discussed further.

For both the modes the magnetic perturbations **b** are within the plane containing both $\mathbf{B_0}$ and **k**, and vary both the gas and magnetic pressure. In the case of the fast mode, the plasma and magnetic pressure act in phase while in the slow mode, they vary out of phase. Due to this variation in the pressure these modes are often referred to as compressional waves. By examining figure 2.2 (a) it can be seen that the fast mode wave energy Poynting vector, **S** where

$$\mathbf{S} = \frac{1}{\mu_0}\mathbf{E} \wedge \mathbf{b}, \tag{2.23}$$

is not always directed along the background field and as such this mode can propagate across the background field as well as along it.

2.4. *The Alfvén Mode*

By taking the dot product of equation (2.19) with $(\mathbf{k} \wedge \mathbf{V_A})$ and using the standard vector relations that $\mathbf{A}.(\mathbf{A} \wedge \mathbf{B}) = 0$ and $\mathbf{B}.(\mathbf{A} \wedge \mathbf{B}) = 0$, then the variation of the wave field can be determined in a direction perpendicular to both **k** and $\mathbf{V_A}$,

$$\frac{\omega^2}{\mathbf{k}^2} = V_A^{\,2} \cos^2\theta. \tag{2.24}$$

This is the Alfvén wave dispersion relation. The mode is supported by tension associated with the magnetic field line and the perturbations, **b** are in a direction transverse to the plane containing both the wave propagation direction, **k** and the background field, $\mathbf{B_0}$. It is analogous to the vibrations of a guitar string. In comparison to the fast and slow modes, there are no density or pressure variations and the Poynting vector, **S** is always directed along the direction of the background field, thus the Alfvén mode is field-guided and cannot propagate across the magnetic field, but will remain confined to a particular field line as shown in 2.2 (b). This mode is the main focus of study for this thesis.

2.5. *Waves in a Simple Box Model Magnetosphere*

The basic wave modes which a magnetised fluid will support (fast, slow and Alfvén) have been introduced and described in a simple manner. In reality these modes are generally coupled together. The following sections will now detail how this coupling can occur.

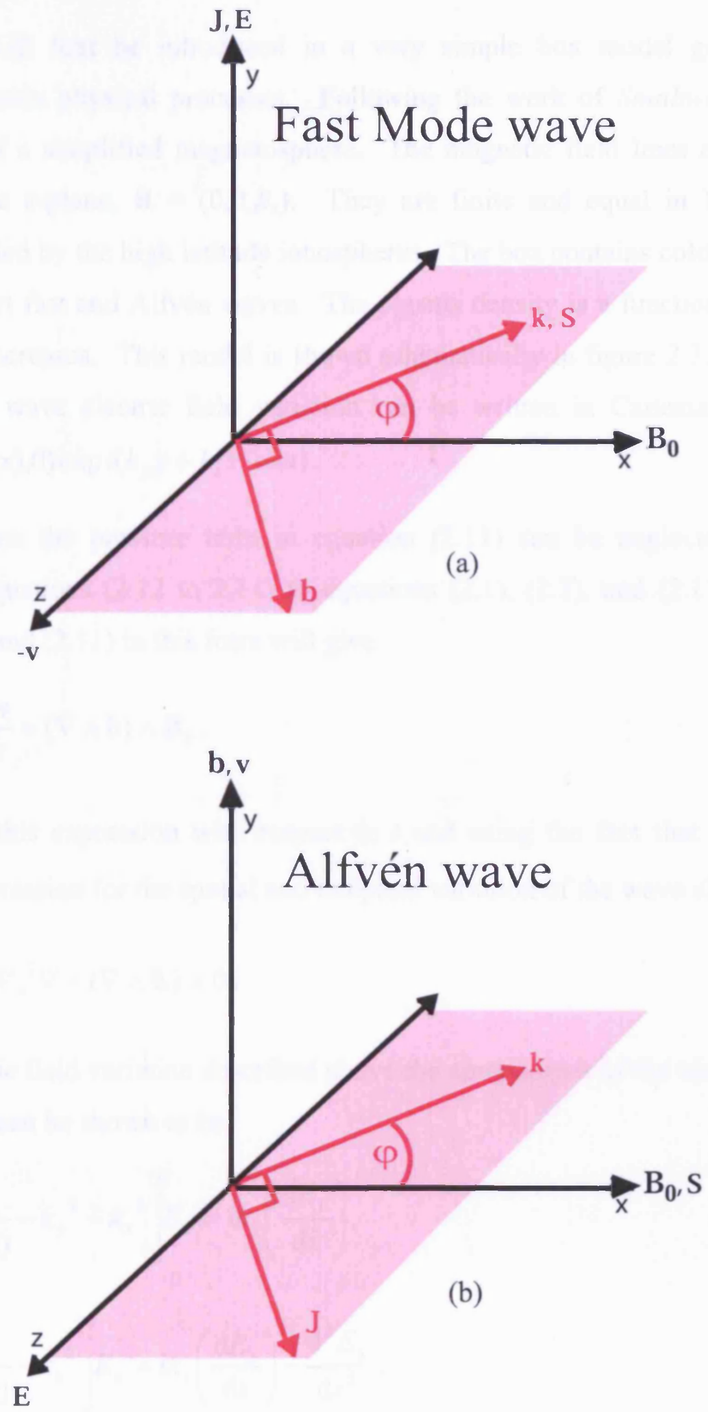

Figure 2.2. The propagation direction for a (a) fast mode wave and (b) an Alfvén mode wave with respect to the background magnetic field, $\mathbf{B_0}$. The field pertubation **b**, direction of the wave velocity **v**, current **J**, wave vector **k** and Poynting flux direction **S** are all marked for each mode.

This concept will first be introduced in a very simple box model geometry which illustrates the main physical processes. Following the work of *Southwood* (1974) the model is that of a simplified magnetosphere. The magnetic field lines are straight and contained in the z-plane, $\mathbf{B} = (0,0,B_z)$. They are finite and equal in length in the z direction, bounded by the high latitude ionospheres. The box contains cold plasma, thus it will only support fast and Alfvén waves. The plasma density is a function of x only and increases as x increases. This model is shown schematically in figure 2.3. In this closed box model the wave electric field variation can be written in Cartesian co-ordinates; $\mathbf{E} = (E_x(x), E_y(x), 0)\exp i(k_y y + k_z z - \omega t)$.

In a cold plasma the pressure term in equation (2.11) can be neglected. Apply the conditions in equations (2.12 to 2.14) to equations (2.1), (2.3), and (2.11). Combining equations (2.3) and (2.11) in this form will give

$$\mu_0 \rho_0 \frac{\partial \mathbf{v}}{\partial t} = (\nabla \wedge \mathbf{b}) \wedge \mathbf{B_0}. \qquad (2.25)$$

Differentiating this expression with respect to t and using the fact that $\mathbf{v} = (\mathbf{E} \wedge \mathbf{B})/\mathbf{B}^2$ results in an expression for the spatial and temporal variation of the wave electric field,

$$\frac{\partial^2 \mathbf{E}}{\partial t^2} + V_A{}^2 \nabla \wedge (\nabla \wedge \mathbf{E}) = 0. \qquad (2.26)$$

Using the electric field variation described above the components of the electric field from equation (2.26) can be shown to be

$$\left[\frac{\omega^2}{V_A{}^2(x)} - k_y{}^2 - k_z{}^2\right] E_x = \mathrm{i}k_y \left(\frac{\mathrm{d}E_y}{\mathrm{d}x}\right), \qquad (2.27)$$

$$\left[\frac{\omega^2}{V_A{}^2(x)} - k_z{}^2\right] E_y = \mathrm{i}k_y \left(\frac{\mathrm{d}E_x}{\mathrm{d}x}\right) - \frac{\mathrm{d}^2 E_y}{\mathrm{d}x^2}, \qquad (2.28)$$

$$\mathrm{i}k_z \frac{\mathrm{d}E_x}{\mathrm{d}x} = -k_y k_z E_y. \qquad (2.29)$$

Equations (2.27) and (2.28) represent the x and y components, with (2.29) forming the complete set of coupled MHD equations.

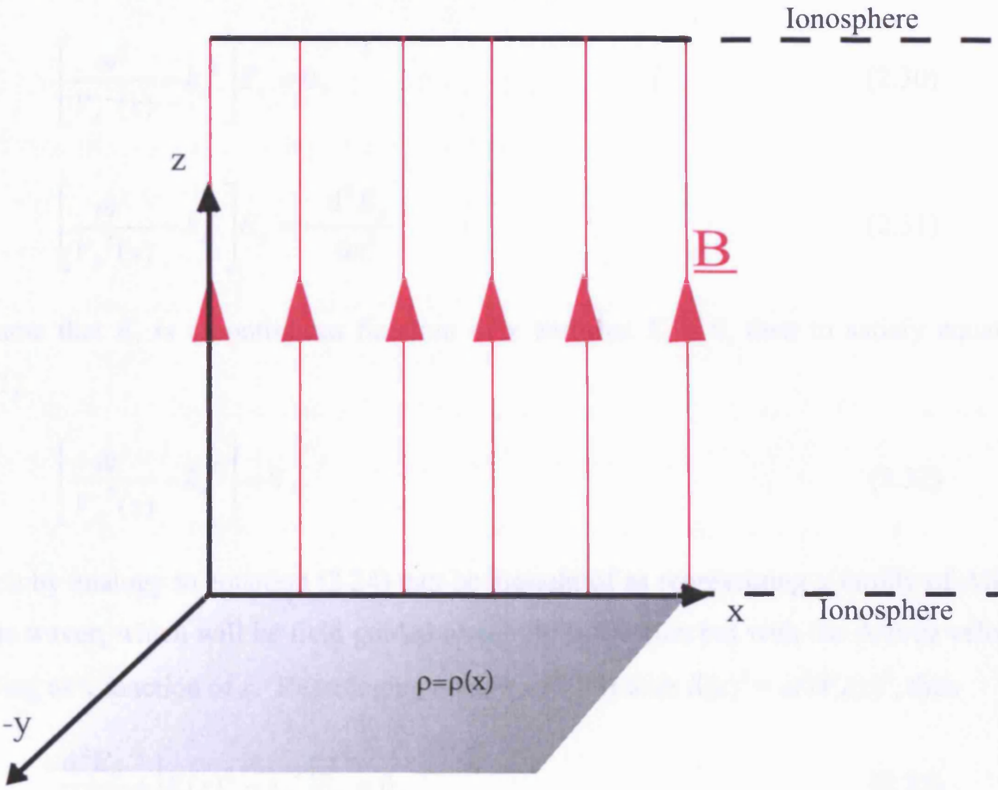

Figure 2.3. A simple box model of the magnetosphere. The magnetic field lines are straight and contained in the z-plane, **B**=(0,0,B_Z). They are finite and equal in length in the z direction, bounded by the high latitude ionospheres. The box contains cold plasma, thus it will only support fast and Alfvén waves. The plasma density is a function of x only and increases as x increases.

Consider the wave electric field variation first in two dimensions only, i.e. $k_y = 0$. Here, equations (2.27) and (2.28) become decoupled to give

$$\left[\frac{\omega^2}{V_A^{\,2}(x)} - k_z^{\,2}\right]E_x = 0, \tag{2.30}$$

$$\left[\frac{\omega^2}{V_A^{\,2}(x)} - k_z^{\,2}\right]E_y = -\frac{\mathrm{d}^2 E_y}{\mathrm{d}x^2}. \tag{2.31}$$

Assume that E_x is a continuous function of x and that $E_x \neq 0$, then to satisfy equation (2.31),

$$\left[\frac{\omega^2}{V_A^{\,2}(x)} - k_z^{\,2}\right] = 0, \tag{2.32}$$

which by analogy to equation (2.24) can be thought of as representing a family of Alfvén mode waves, which will be field guided along the z direction but with the Alfvén velocity varying as a function of x. Rearranging equation (2.30) with $K(x)^2 = \omega^2/V_A(x)^2$, then

$$\frac{\mathrm{d}^2 E_y}{\mathrm{d}x^2} + \left[K(x)^2 - k_z^{\,2}\right]E_y = 0. \tag{2.33}$$

Equation (2.33) represents a mode propagating across the field (i.e. a fast mode). From equation (2.32) at a point along the x-axis, the medium will allow a field guided Alfvén mode to propagate, i.e., $\left[K(x)^2 - k_z^{\,2}\right] = 0$ this will result in a reflection point x_c in equation (2.33) (i.e. $\mathrm{d}^2E_y/\mathrm{d}x^2 = 0$). As the fast mode wave moves away from this reflection point in the increasing (decreasing) x direction the sign of the E_y component will become positive (negative) due to K being a function of x. This will manifest itself as a phase change across this point in the E_y and associated b_x components of the wave field. It also implies that the solution to equation (2.32) must change in nature across this region from an oscillatory one to an evanescent one. To understand what this x_c point represents combine the coupled equations (2.27) and (2.28) into a single equation,

$$\frac{\mathrm{d}^2 E_y}{\mathrm{d}x^2} - \mathrm{C}\left(\frac{\mathrm{d}E_y}{\mathrm{d}x}\right) + \left[K(x)^2 - k_y^{\,2} - k_z^{\,2}\right]E_y = 0, \tag{2.34}$$

where, $C = \dfrac{k_y^2\left(\dfrac{dK^2}{dx}\right)}{(K(x)^2 - k_z^2)(K(x)^2 - k_y^2 - k_z^2)}$.

In this more general case there is another reflection point where $\lfloor K(x)^2 - k_y^2 - k_z^2 \rfloor = 0$, x_r. If this situation is considered physically, any incoming fast wave (from a large x) will encounter the reflection point x_r before encountering x_c. This places x_c in the evanescent region of the fast mode wave. An incoming fast mode wave of a given ω and k_z will be partly reflected at x_r but an evanescent fast mode wave will continue through the medium. At x_c, the component of the fast mode phase velocity along the field line matches the local Alfvén mode for that field line and resonance occurs. Energy is transferred from the fast mode to the field line in what is termed a Field Line Resonance (FLR).

Since the resonant Alfvén waves are field guided and, to a first approximation, the field lines are fixed in the ionospheres then the FLRs will be standing waves which can only support certain frequencies. For a field line of length l the parallel wavelength is limited by the condition

$$\lambda_{//} = \frac{2l}{n}, \tag{2.35}$$

where n is an integer. This gives rise to harmonics of standing waves. Figure 2.4 illustrates these standing modes using the simple box model on the right hand side of the figures and then how this would look in a dipole field geometry. Figure 2.4 (a) indicates a fundamental electric field standing mode structure, also referred to as on odd mode. The corresponding magnetic field structure is also shown. The electric field structure is symmetric about the equator with nodes in the ionospheres with an antinode in the equatorial plane. As a result of Faradays law this corresponds to anti nodes in the ionospheres and a node in the equatorial plane in the magnetic field structure. Figure 2.4 (b) indicates a second harmonic standing mode (or even mode), with the corresponding electric and magnetic field structures. This mode is by comparison anti-symmetric about the equator with a node at the equator and antinodes in the ionosphere. As these standing waves are field guided Alfvén waves, their Poynting vectors will be directed along the field, into the ionospheres. The wave energy will then be dissipated into the collisional medium of the ionosphere through joule heating effects.

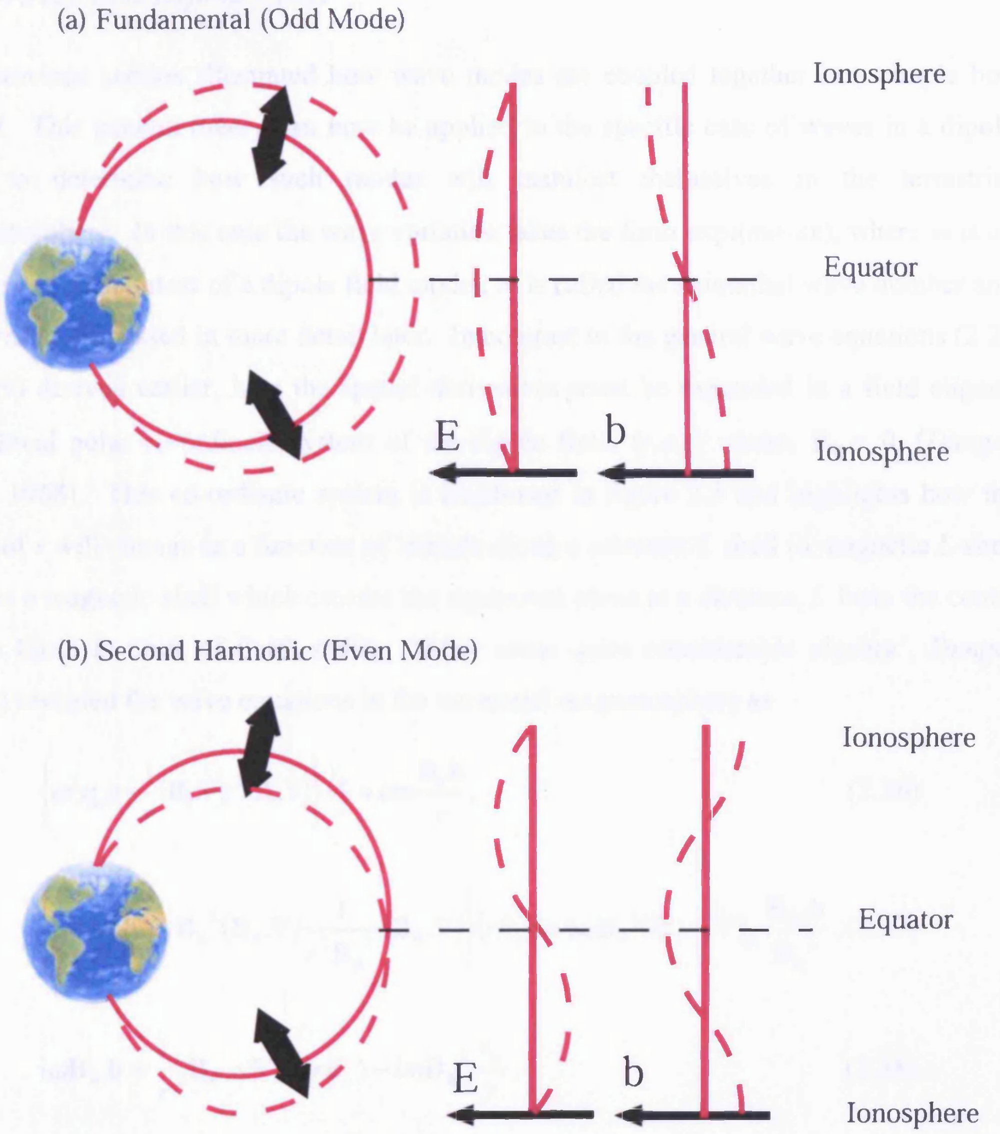

Figure 2.4. The standing mode structure of a field line for a fundamental (a) and second harmonic (b) osscilation. Both the electric and magnetic pertubations are shown along the field lines.

2.6. Waves in a Dipole Field

The previous section illustrated how wave modes are coupled together in a simple box model. This general theory can now be applied to the specific case of waves in a dipole field to determine how such modes will manifest themselves in the terrestrial magnetosphere. In this case the wave variation takes the form $\exp i(m\phi-\omega t)$, where m is an integer. In the context of a dipole field model, m is called the azimuthal wave number and this will be discussed in more detail later. In contrast to the general wave equations (2.27 to 2.29) derived earlier, here the spatial derivatives must be expanded in a field aligned cylindrical polar co-ordinate system of the dipole field, (r,ϕ,z) where, $\mathbf{B}_\varphi = 0$, (*Dungey* 1963, 1968). This co-ordiante system is illustrated in figure 2.5 and highlights how the value of r will change as a function of latitude along a constant L shell (a magnetic L-shell defines a magnetic shell which crosses the equatorial plane at a distance, L from the centre of the Earth in units of Earth radii). 'After some quite considerable algebra', *Dungey* (1963) revealed the wave equations in the terrestrial magnetosphere as

$$\left\{\omega^2\mu_0\rho-\frac{1}{r}(\mathbf{B}_0.\nabla)r^2(\mathbf{B}_0.\nabla)\right\}\frac{v_\varphi}{r}=\omega m\frac{\mathbf{B}_0.\mathbf{b}}{r}, \tag{2.36}$$

$$\left\{\omega^2\mu_0\rho-r\mathbf{B}_0^{\ 2}(\mathbf{B}_0.\nabla)\frac{1}{r^2\mathbf{B}_0^{\ 2}}(\mathbf{B}_0.\nabla)\right\}(rE_\varphi)=\mathrm{i}\omega\mathbf{B}_0^{\ 2}(\mathbf{B}_0\wedge\nabla)_\varphi\frac{\mathbf{B}_0.\mathbf{b}}{\mathbf{B}_0^{\ 2}}, \tag{2.37}$$

$$\mathrm{i}\omega\mathbf{B}_0.\mathbf{b}=\frac{1}{r}(\mathbf{B}_0\wedge\nabla)_\varphi(rE_\varphi)-\mathrm{i}m\mathbf{B}_0^{\ 2}\frac{v_\varphi}{r}, \tag{2.38}$$

where m is the azimuthal wave number. The parameter m quantifies the phase change of the wave per degree of magnetic longitude and hence determines the complete number of wave cycles that would fit around the Earth,

$$m=\frac{2\pi L R_E}{\lambda}, \tag{2.39}$$

where λ is the azimuthal wavelength (in m) at a specific L – shell location, L, in the magnetosphere. Equations (2.36) to (2.38) are analogous to equations (2.27) to (2.29). Equations (2.36) and (2.37) only contain one spatial operator $\mathbf{B_0}.\nabla$, the derivative along the background magnetic field and are coupled by the $\mathbf{B_0}.\mathbf{b}$ terms which represent the compressional terms of the magnetic perturbation. Equation (2.38) indicates how the

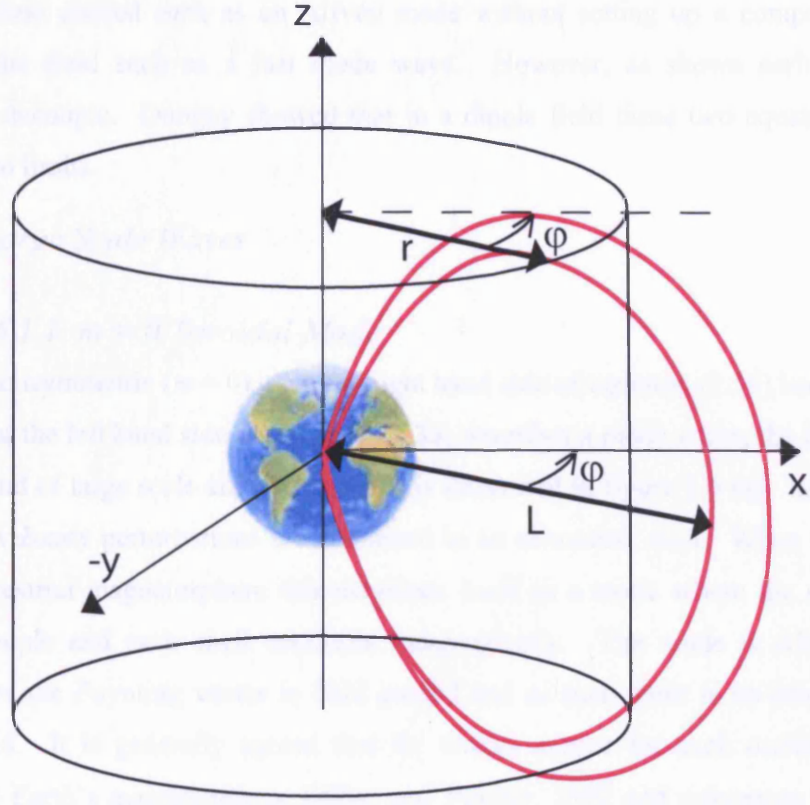

Figure 2.5. Schematic of the co-ordinate system used by Dungey (1963, 1968) to describe ULF wave modes in a dipole field. The system is in cylindrical polar co-ordinates (r, ϕ, z). The parameter L denotes a particular field line which crosses the equatorial plane at a distance L Earth radii.

azimuthal electric field E_θ is related to both v_ϕ and any compressional terms. Generally equations (2.36) and (2.37) are coupled, implying that it would not be possible to have a mode purely field guided such as an Alfvén mode without setting up a compressional wave across the field such as a fast mode wave. However, as shown earlier these equations can decouple. Dungey showed that in a dipole field these two equations can decouple in two limits.

2.6.1. Large Scale Waves

2.6.1.1. m = 0 Toroidal Mode

If the wave is axisymmetric ($m = 0$), then the right hand side of equation (2.36) becomes 0. This means that the left hand side of equation (2.36) describes a mode where the E-field is purely radial and of large scale size. This mode is illustrated in figure 2.6 (a). In turn the magnetic and velocity perturbations are contained in an azimuthal shell. When applying this to the terrestrial magnetosphere this manifests itself as a mode where the magnetic L - shells decouple and each shell oscillates independently. The mode is Alfvénic in nature therefore the Poynting vector is field guided and as such there is no propagation across the field. It is generally agreed that the energy source for such oscillations is external to the Earth's magnetosphere (*Allan and Poulter,* 1992 and references therein). Mechanisms such as an increase in solar wind pressure (solar wind buffeting) or the Kelvin Helmholtz instability (similar in effect to instabilities generated by wind over water), generated by the solar wind flow over the magnetospheric flanks are the two major sources of energy and are shown schematically in figures 2.7 and 2.8 respectively. Section 2.5 described in detail the coupling between the two wave modes in these scenarios, an externally driven fast mode wave and a field guided Alfvén wave.

2.6.1.2. m = 0 Poloidal Mode

By applying this condition to equation (2.37) another large scale mode is possible. In this case the E-field is also purely azimuthal, with velocity and magnetic perturbations in a plane perpendicular to this. In this mode the $\mathbf{B_0}.\mathbf{b} \neq 0$ and as such the wave can propagate across the field as a fast mode wave. Due to the axisymmetric nature of the system all motion in the meridian plane will must be the same. This mode is referred to as a global cavity mode (*Allan and Poulter,* 1992 and references therein) in which the whole magnetospheric cavity inflates and deflates in a 'breathing' mode. This again has an external source, most notably increases in solar wind pressure.

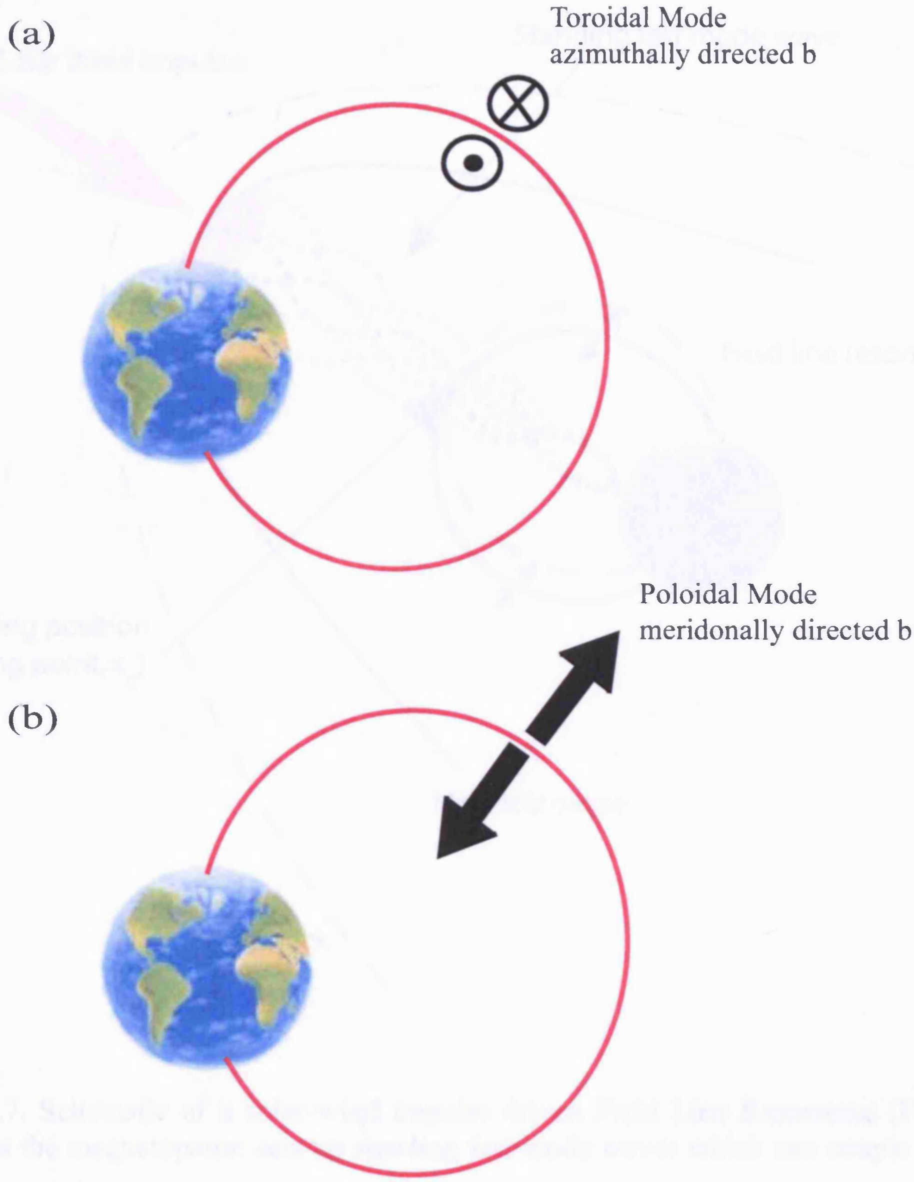

Figure 2.6. Schematic of poloidal and toroidal mode osscilations. The toroidal mode is shown in figure 2.6 (a) and is a mode where the E-field is purely radial and of large scale size. In turn the magnetic and velocity perturbations are contained in an azimuthal shell. The polidal mode is shown in figure 2.6 (b) and is a mode where the E-field is azimuthally directed and of small azimuthal scale with both the magnetic and velocity perturbations contained in a meridian plane.

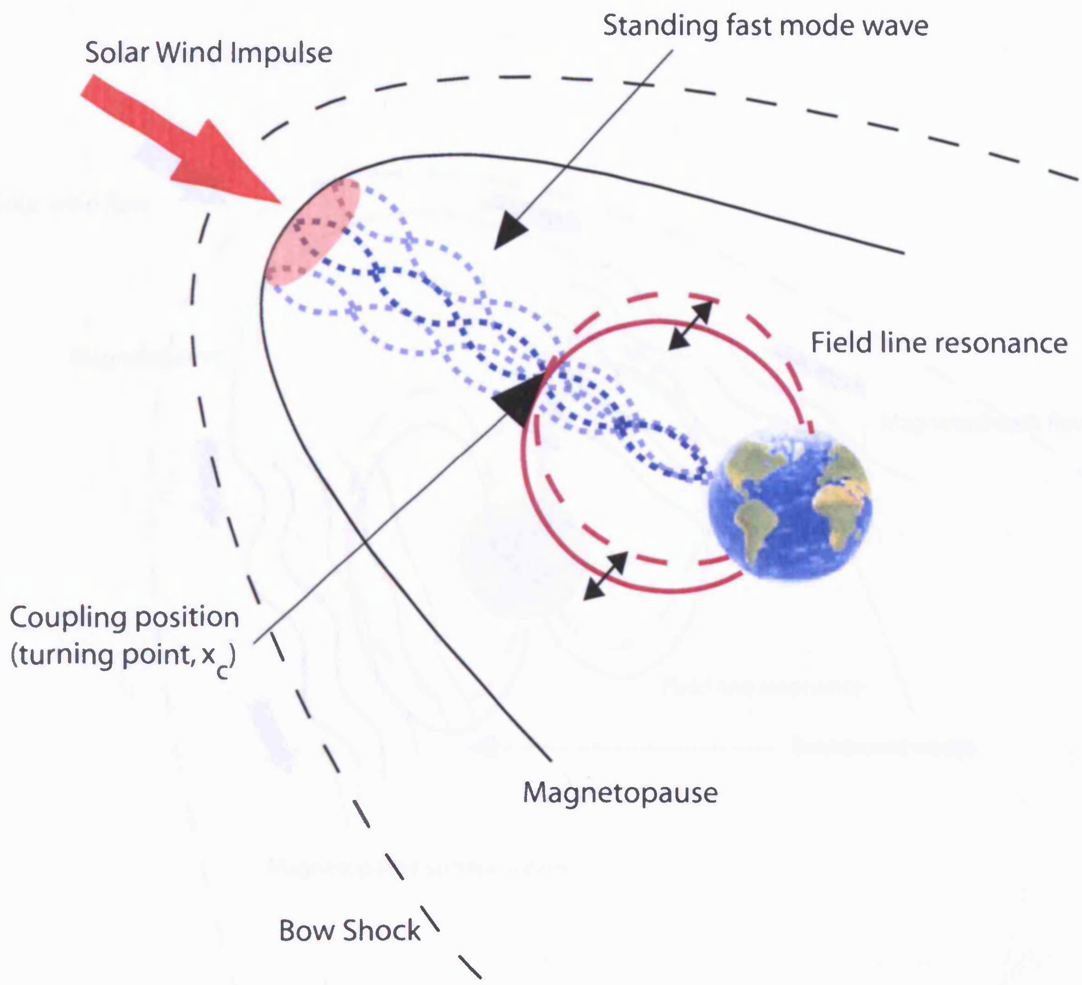

Figure 2.7. Schematic of a solar wind impulse driven Field Line Resonance (FLR). An impulse at the magnetopause sets up standing fast mode waves which can couple to a field line.

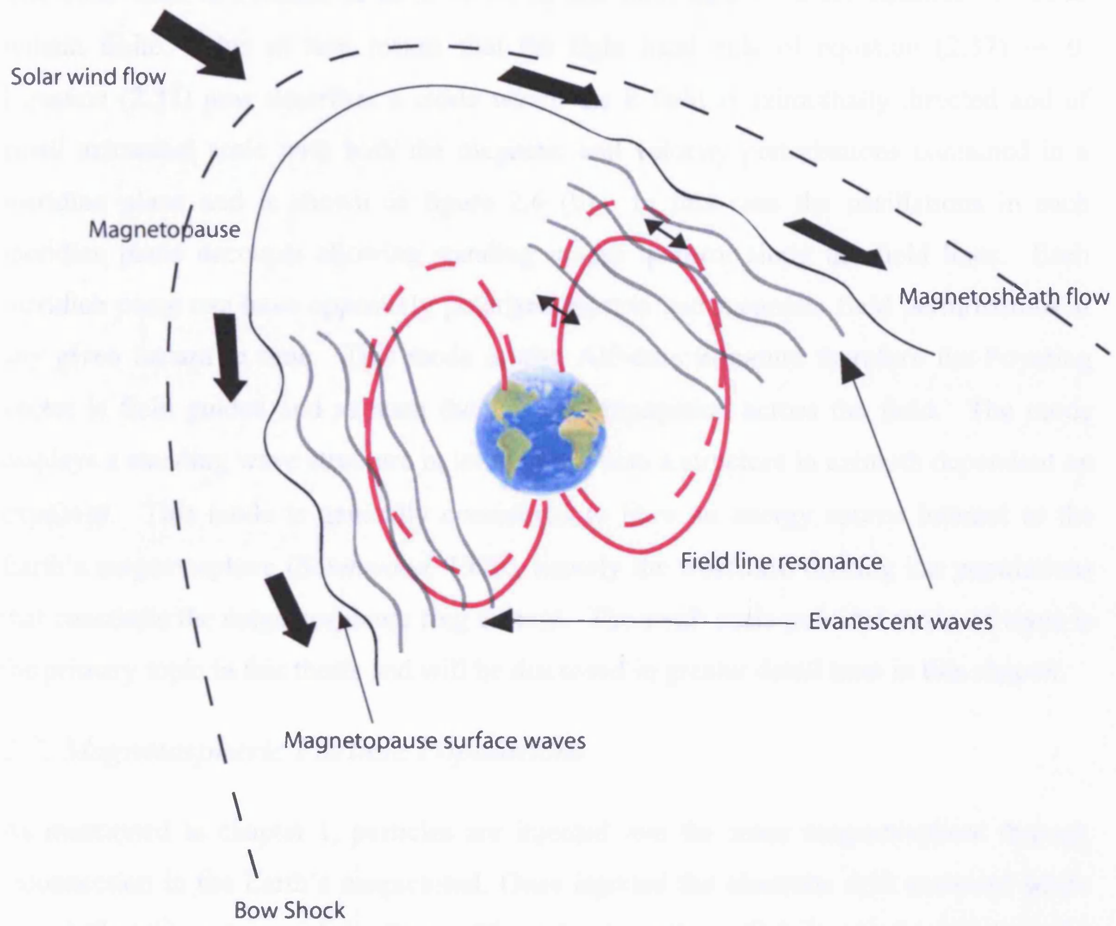

Figure 2.8. Schematic of waves driven by the Kelvin Helmholtz instability mechanism at the magnetopause flanks. The 'wind over water' effect at the magnetopause gives rise to evanescent waves which propgate into the magnetosphere driving large scale Field Line Resonances (FLRs).

2.6.2. Small Scale Waves

2.6.2.1. $m \rightarrow \infty$ Poloidal Mode

The other limit to consider is as $m \rightarrow \infty$. In this limit $\mathbf{B_0.b} \rightarrow 0$ for equation (2.36) to remain finite. This in turn means that the right hand side of equation (2.37) $\rightarrow 0$. Equation (2.37) now describes a mode where the E-field is azimuthally directed and of small azimuthal scale with both the magnetic and velocity perturbations contained in a meridian plane and is shown in figure 2.6 (b). In this case the oscillations in each meridian plane decouple allowing standing modes to form along the field lines. Each meridian plane can have oppositely polarised electric and magnetic field perturbations at any given instant in time. This mode is also Alfvénic in nature therefore the Poynting vector is field guided and as such there is no propagation across the field. The mode displays a standing wave structure in latitude and also a structure in azimuth dependent on $\exp i(m\varphi)$. This mode is generally considered to have an energy source internal to the Earth's magnetosphere (*Southwood,* 1976), namely the westward drifting ion populations that constitute the magnetospheric ring current. The small scale poloidal mode of wave is the primary topic in this thesis and will be discussed in greater detail later in this chapter.

2.7. Magnetospheric Particle Populations

As mentioned in chapter 1, particles are injected into the inner magnetosphere through reconnection in the Earth's magnetotail. Once injected the electrons drift eastward while ions drift westward around the Earth. The primary region of interest in this thesis is the magnetospheric ring current, which generally lies at between ~ 2 and 9 R_E and is centred on the equatorial plane. Additionally, only ion populations are considered as these have the same azimuthal drift direction as the interacting wave populations examined in this thesis. Once injected into the magnetosphere the ions follow trajectories determined by their energy and also the relative magnetic field strength of the terrestrial field. Generally, there are three forms of motion to consider; gyration around the field, bounce motion along the field and drift motion across the field.

Particles will gyrate around a magnetic field line in a circle at a velocity, $v_\perp$ or angular frequency, $\Omega = qB/m$ rad s^{-1}, where q is the charge of the particle and m is the particle mass. The factor of q implies that electrons and ions will gyrate in an opposite direction. A particle will also move along the field line at velocity, $v_{//}$. This motion is a direct consequence of applying Newton's 2nd law to the system. In the terrestrial magnetosphere, the magnetic field strength varies which in turn affects the particle motion. At the polar regions, the field lines converge which equates to a change in field strength along the magnetic field. As the particles gyrate around the field line they have a magnetic moment, $\mu \propto v_\perp^2/B$. This is called the first adiabatic invariant. As the field lines converge, B increases therefore so must $v_\perp$ due to the first adiabatic invariant. Since the velocity of the particle is made up of both a parallel and perpendicular component, as $v_\perp$ increases, $v_{//}$ must decrease. At a certain field strength the particle velocity along the field will become 0. At this point the particle is 'mirrored' and its parallel velocity is directed in the opposite direction, back up the field line. In the Earth's magnetosphere this occurs at both the polar regions and a 'magnetic bottle' is formed, where the particles bounce back and forth between hemispheres. To determine at what point along the field line the particle mirrors, the particle pitch angle α; the angle the particle velocity vector makes with the magnetic field line, must be examined. Using the particle magnetic moment,

$$\frac{v_\perp^2}{B} = \frac{v^2 \sin^2 \alpha}{B} = \text{const}. \tag{2.40}$$

The field strength at which the particle mirrors can be defined as

$$B_m = \frac{B_{eq}}{\sin^2 \alpha_{\text{eq}}}. \tag{2.41}$$

Notice that the mirror point depends only on the pitch angle at the equator and the equatorial magnetic field. This means that particles of larger pitch angles will be confined closer to the equatorial plane while those with smaller pitch angles (i.e. those which are more field aligned) will travel further down the field lines. As the particles move further down the field lines towards the ionosphere, some are lost through collisional and scattering processes as the particle densities increase. The particle angular bounce frequency, ω_{bounce} is given by

$$\omega_{\text{bounce}} = \frac{\pi\sqrt{W}}{\sqrt{2m_p L \mathbf{R}_\mathbf{E} \mathrm{T(y)}}}, \tag{2.42}$$

where W is the proton energy in eV, L is the proton's L-shell location and the function T(y) is a function of particle pitch angle α, where T(y) ~ (1.3 – 0.56 sin α), (*Glassmeier et al.,* 1999; *Schulz and Lanzerotti*, 1974).

The particles will also convect around the Earth. Where the 'frozen in flow' condition holds the field lines will drift with the plasma. In the terrestrial magnetosphere this flow is observed earthward of the tail reconnection site and forms part of the Dungey cycle, where the newly reconnected field lines convect from the tail towards the front of the magnetosphere. The motion is determined by a combination of forces acting on the particle from both the electric and magnetic fields and its velocity vector will be perpendicular to both **E** and **B** and is called the **E**∧**B** drift velocity,

$$\mathbf{V}_{\mathrm{E\wedge B}} = \frac{\mathbf{E} \wedge \mathbf{B}}{\mathbf{B}^2}. \tag{2.43}$$

Additionally, there is also a drift motion perpendicular to **B**. This represents a breakdown of frozen in flow which is a consequence of changes in the magnetic field, across the field, i.e. ∇B. This increase in the magnetic field causes the particle gyroradius to decrease, which leads to a drift in a direction, **B**∧∇B, (i.e. across the field and also in a direction perpendicular to the increasing field) in the case of ions,

$$\mathbf{V}_{\nabla \mathrm{B}} = \frac{W_{\perp}}{qB^3} \mathbf{B} \wedge \nabla B, \tag{2.44}$$

where, $W_{\perp}$ is the energy due to the perpendicular velocity component. The **E**∧**B** and ∇B motions are shown in figure 2.9. Another form of motion exists due to the fact that the field line which the particles are gyrating around is curved. This curvature introduces a centripetal force which, coupled with the particle motion along the field, results in a motion across the field. This final motion is called curvature drift. The two motions , gradient drift and curvature drift are normally considered together under the term gradient – curvature drift. *Chisham* (1996) quantified the angular drift frequency of the particles in terms of these motions

$$\omega_{\mathrm{drift}} = -\frac{6WLP(\alpha)}{B_s \mathrm{R_E^2}} + \frac{2\Psi_0(0)L^3 \sin\varphi}{B_s \mathrm{R_E^2}} + \Omega_{\mathrm{E}} \tag{2.45}$$

$$\omega_{\mathrm{drift}} = -\frac{6WL(0.35 + 0.15 \sin\alpha)}{B_s \mathrm{R_E^2}} + \frac{EL^2}{B_s \mathrm{R_E}}, \tag{2.46}$$

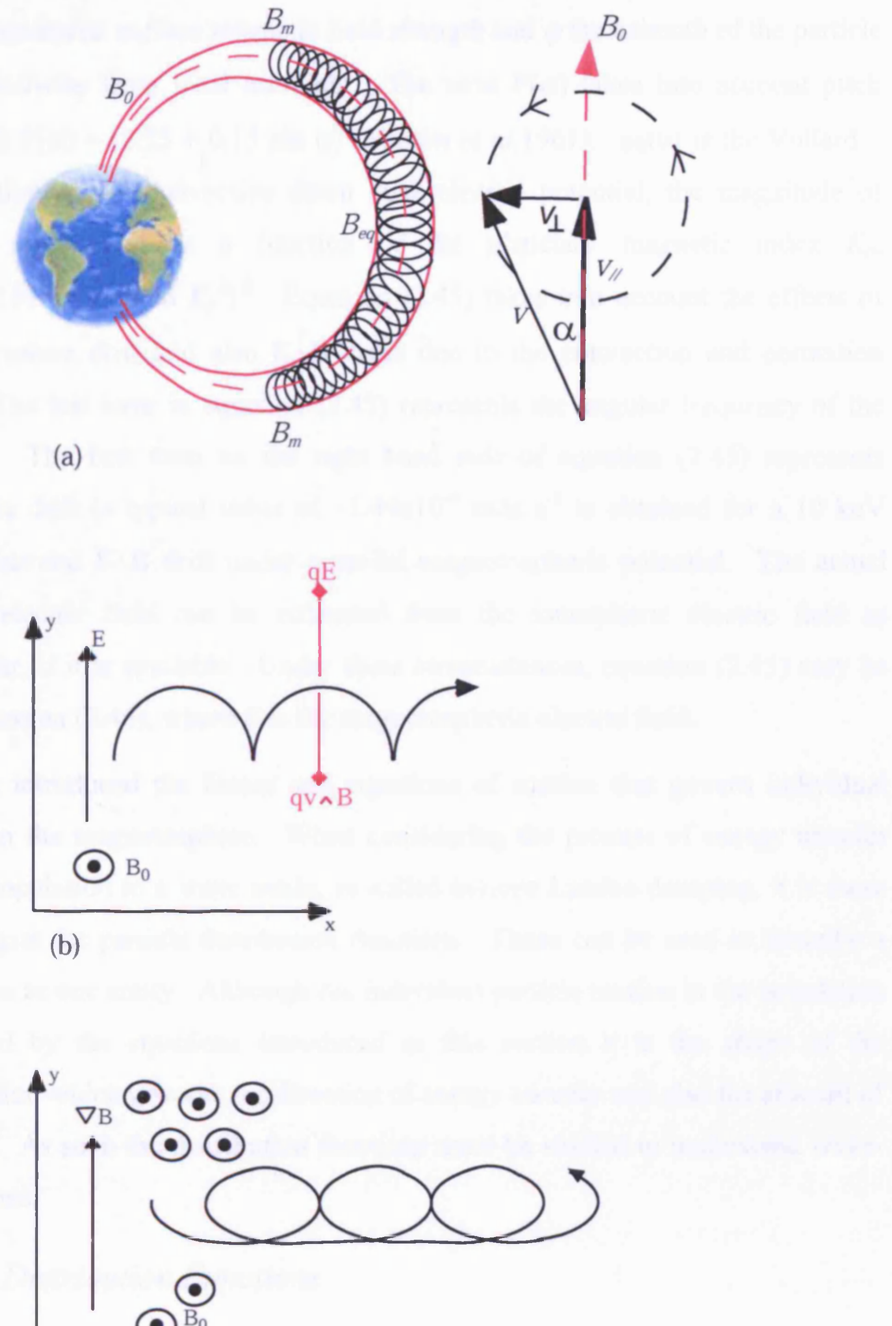

Figure 2.9. Particle motion in the presence of a magnetic field. (a) The particles will gyrate around the field lines and bounce between hemispheres due to gradients along the field. (b) the **E**∧**B** drift motion perpendicular to both the magnetic and electric fields. (c) the gradient **B** drift as a consequence of increasing field strength across the field.

where, B_s is the equatorial surface magnetic field strength and φ the azimuth of the particle measured anticlockwise from local midnight. The term $P(\alpha)$ takes into account pitch angle effects with $P(\alpha) \sim (0.35 + 0.15 \sin \alpha)$ (*Hamlin et al.*1961). $\psi_0(0)$ is the Vollard – Stern representation of the convective dawn dusk electric potential, the magnitude of which can be represented as a function of the planetary magnetic index K_p, $\psi_0(0) \sim 45(1 - 0.159K + 0.0093\ K_p^2)^{-3}$. Equation (2.45) takes into account the effects of gradient and curvature drift and also $\mathbf{E}\wedge\mathbf{B}$ drifts due to the convection and corotation electric fields. The last term in equation (2.45) represents the angular frequency of the Earth's rotation. The first term on the right hand side of equation (2.45) represents gradient-curvature drift (a typical value of -1.44×10^{-4} rads s^{-1} is obtained for a 10 keV proton) and the second $\mathbf{E}\wedge\mathbf{B}$ drift under a model magnetospheric potential. The actual magnetospheric electric field can be estimated from the ionospheric electric field as measured by radar, if it is available. Under these circumstances, equation (2.45) may be replaced with equation (2.46), where E is the magnetospheric electric field.

This section has introduced the forces and equations of motion that govern individual particle motion in the magnetosphere. When considering the process of energy transfer from a particle population to a wave mode, so called inverse Landau damping, it is more useful to investigate the particle distribution functions. These can be used to describe a plasma population as one entity. Although the individual particle motion in the population will be governed by the equations introduced in this section it is the shape of the distribution function which governs the direction of energy transfer and also the amount of energy available. As such the distribution functions must be studied to understand wave-particle interactions.

2.7.1. Particle Distribution Functions

Particle distribution functions are mathematically described as a 7-D quantity which considers the number of particles in a unit of spatial volume, which are also in a unit volume of velocity space, at a particular time t, $f(\mathbf{r},\mathrm{v},t)$. This method allows an easier visualization of the plasma which contains particles of different velocities moving in different directions. Generally, an ideal thermalized plasma will follow a Maxwellian type particle distribution; that is, one which is monotonically decreasing as the particle energy W, increases. The particular distribution function that is applied here is a Kappa distribution, which is very similar to a Maxwellian distribution, but is modified slightly to allow a better description of higher energy particles. A Kappa distribution is a more accurate description of typical magnetospheric particle populations, though in all literature they are often referred to, incorrectly, as Maxwellian. In keeping with the literature this thesis will also describe the particle populations as Maxwellian although it will first discuss the subtle differences between the two. A Maxwellian distribution takes the form

$$f(\mathbf{r},\mathbf{v}) = A_s \exp\left[-\frac{\frac{1}{2}m_p(\mathbf{v}-\mathbf{u_s})^2}{kT_s}\right], \tag{2.47}$$

where $\mathbf{v}$ is the velocity of an individual particle, m_p is the particle mass and $\mathbf{u_s}$ is the background velocity flow of the population as a whole. k is the Boltzman constant, T_s is the temperature and A_s is related to the particle number density, n_s such that

$$A_s = n_s\left(\frac{m_p}{2\pi kT}\right)^{\frac{3}{2}}. \tag{2.48}$$

The Kappa distribution has a very similar form,

$$f(\mathbf{r},\mathbf{v}) = A_{\kappa s}\left[1+\frac{\frac{1}{2}m_p(\mathbf{v}-\mathbf{u_s})^2}{\kappa E_{TS}}\right]^{(1-\kappa)}, \tag{2.49}$$

with the term κ characterizing the departure from the Maxwellian form. At higher energies, i.e. where $E >> \kappa E_{TS}$, the Kappa distribution falls off more slowly than a Maxwellian distribution and also in the limit where $\kappa \to \infty$ the Kappa distribution becomes that of a Maxwellian with $kT = E_{TS}$. The particle populations in question are energetic ions which have been injected into the inner magnetosphere on the nightside in a naturally occurring process, such as substorm-associated particle injections. Subsequent to an injection the ions will drift westwards round the Earth forming part of the global ring current.

2.8. Wave-Particle Interactions

Section 2.6 introduced and discussed the various types of waves that occur in the terrestrial magnetosphere and briefly discussed their possible energy sources, i.e. external or internal to the magnetosphere. Section 2.6.2 introduced the primary wave mode of discussion in this thesis; small scale poloidal modes whose energy source is internal to the Earth's magnetosphere in the form of energetic ion populations that make up the global ring current. Section 2.7 then discussed the particle populations, first as individual particle motions before introducing particle distribution functions. This section will discuss under how, and what circumstances, energy is transferred from a particle population to a small scale poloidal wave.

2.8.1. Energy Exchange Through Wave-Particle Interactions

Southwood (1976) and *Hughes et al.* (1978), first suggested that small scale standing poloidal mode waves in the geomagnetic field could interact with particle populations in the terrestrial ring current, more specifically ion populations. Energy transfer can occur between the ion populations and the wave modes in either direction, inducing either wave growth or damping. Figure 2.10 (a) indicates an ion with velocity $V_{particle}$ which encounters a wave travelling at velocity V_{wave}. If $V_{particle} \neq V_{wave}$ then the ion will observe an average electric field, $\overline{\mathbf{E}} = 0$, as it will spend equal amounts of time in both $+Ep$ and $-Ep$ as the wave travels by. If a particle is moving at a velocity $V_{particle}$ where $V_{particle}$ = V_{wave} then energy exchange can occur between the particle and the wave as the particle will remain in a finite region of electric field, $\overline{\mathbf{E}} \neq 0$. This theory can be expanded to consider a population of particles. The ion populations in the magnetosphere have finite energies and thus velocities which are characterised using a distribution function. To determine if an ion population induces wave growth or damping its ion distribution function (IDF), f, must be analysed as a function of particle energy, W. The IDFs are in a standard log - log plot format of particle energy vs. distribution function. Generally in a Maxwellian particle distribution function more particles will exist at an energy W - dW than at W + dW, (df/dW <0) as shown in figure 2.10 (b). This means that if the populations encounters a wave there will be more particles travelling at $V < V_{wave}$ than at $V > V_{wave}$ and energy will be transferred from the wave to the particles through the process of Landau damping (*Landau and Lifshitz 1958*). This is illustrated in figure 2.10 (c) where the population IDF is shown in figure 2.10 (d). However in the magnetosphere, due to the low plasma densities involved (and hence small collision frequencies) any injected plasma populations thermalize only on very long timescales. This can give rise to the possibility the plasma distribution becoming inverted at some point. These 'bump-on-tail' or non-Maxwellian distribution functions exhibit limited energy ranges of positive gradient

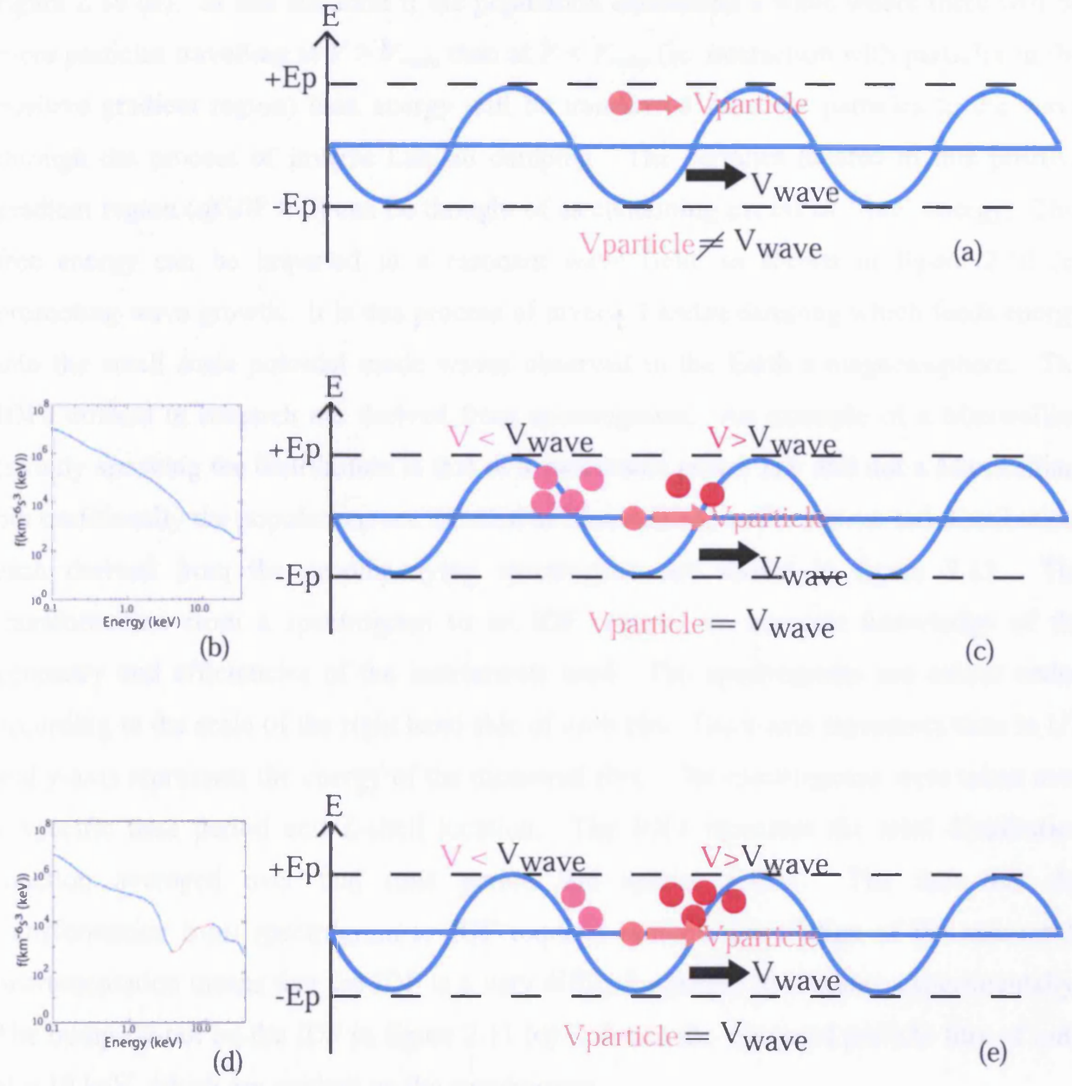

Figure 2.10. The wave electric field varying between *+Ep* and *-Ep* is shown in blue travelling at a velocity V_{wave}. The proton in figure (a) travelling at velocity $V_{particle}$ where $V_{particle} \neq V_{wave}$ will feel no net force from the electric field. Figure (c) indicates a proton population from a monatonic power law particle distribution where the interacting part of the distribution (shown in figure (b))is centered on a particle travelling at $V_{particle} = V_{wave}$. In this situation there are less particles travelling at $V > V_{wave}$ and more travelling at $V < V_{wave}$ thus energy is transferred from the wave to the particles. Figure (e) indicates the situation when a bump-on-tail distribution is considered (indicated in figure (d)) which has excess energy to impart to the wave field though inverse Landau damping.. Here there are more particles travewlling at $V > V_{wave}$ than at $V < V_{wave}$ thus the wave gains energy from the particle population.

regions where more particles will exist at an energy $W + \mathrm{d}W$ than at $W - \mathrm{d}W$ as shown in figure 2.10 (d). In this situation if the population encounters a wave where there will be more particles travelling at $V > V_{wave}$ than at $V < V_{wave}$ (ie. interaction with particles in the positive gradient region) then energy will be transferred from the particles to the wave through the process of inverse Landau damping. The particles located in this positive gradient region ($df/dW > 0$) can be thought of as containing excess or 'free' energy. This free energy can be imparted to a resonant wave field, as shown in figure 2.10 (e) promoting wave growth. It is this process of inverse Landau damping which feeds energy into the small scale poloidal mode waves observed in the Earth's magnetosphere. The IDFs utilised in research are derived from spectrograms. An example of a Maxwellian (strictly speaking the distribution is that of a monotonic power law and not a Maxwellian, but traditionally the populations are labelled as Maxwellian) and bump-on-tail distribution, each derived from the accompanying spectrogram are shown in figure 2.11. The transformation from a spectrogram to an IDF requires an accurate knowledge of the geometry and efficiencies of the instruments used. The spectrograms are colour coded according to the scale of the right hand side of each plot. The x-axis represents time in UT and y-axis represents the energy of the measured flux. The spectrograms were taken over a specific time period and L-shell location. The IDFs represent the total distribution function averaged over that time period and spatial extent. The fact that the transformation from spectrogram to IDF requires intricate knowledge of the spacecraft instrumentation means that the IDF is a very difficult quantity to measure experimentally. The bump-on-tail on the IDF in figure 2.11 (d) is due to the increased particle flux of ions at ~ 10 keV, which are evident on the spectrogram.

The change in particle distribution function ∂f can be due to either a spatial variation in the population across an L shell, ∂L or an actual energy variation at a point in space, ∂W. Theoretically the two can be defined separately using Lioville's theorem although given instrument limitations they cannot be directly measured separately as indicated from the spectrograms,

$$\delta f = -\delta W \left.\frac{\partial f}{\partial W}\right|_{\mu,\mathrm{L}} - \delta L \left.\frac{\partial f}{\partial L}\right|_{\mu,\mathrm{W}} . \tag{2.50}$$

When considering particles moving in the magnetosphere their diffusion can now be considered in both (W,L) space where L is the spatial L-shell location of the particles and

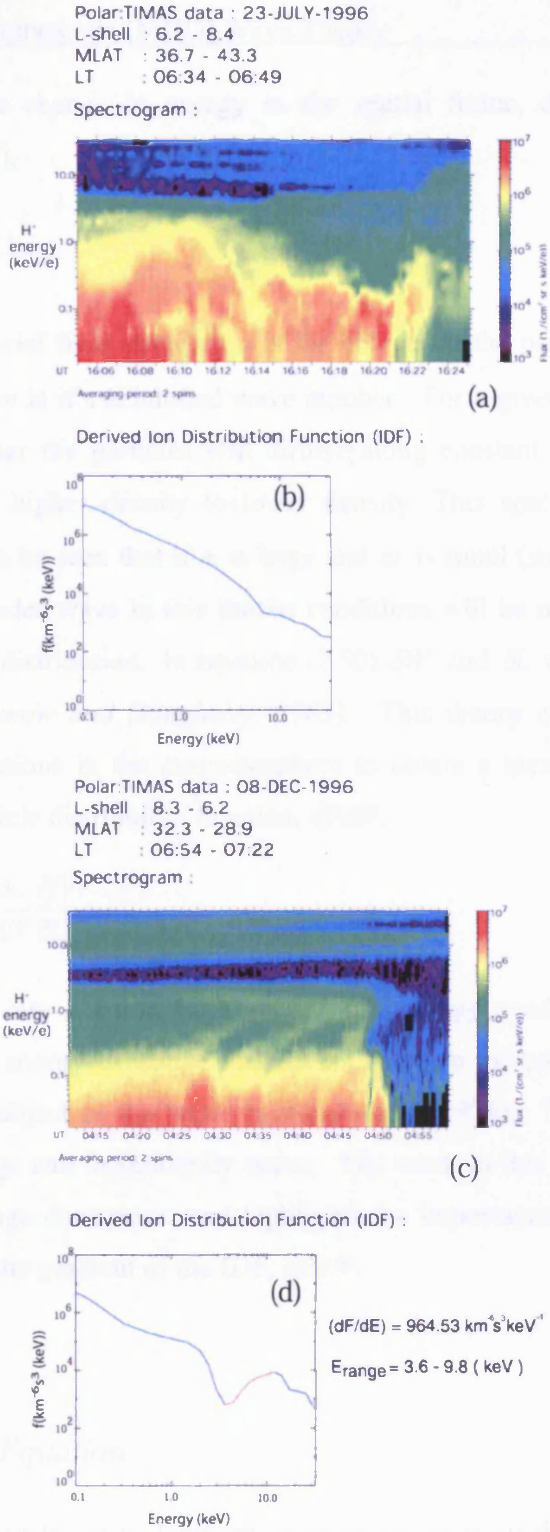

Figure 2.11. Spectrograms of proton flux and the derived Ion Distribution Function (IDF) for a monatonic power law distribution (a,b) and non - Maxwellian (c,d) particle population.

also (f,W) space. The change in energy in the spatial frame, $\mathrm{d}W/\mathrm{d}L$ is defined as (*Southwood et al.,* 1969),

$$\frac{\mathrm{d}W}{\mathrm{d}L}=\frac{q\omega B_{eq}\mathrm{R_E}^2}{mL^2},\qquad(2.51)$$

where B_{eq} is the equatorial field strength, q is the charge on the particle, ω is the wave angular frequency and m is it's azimuthal wave number. For a given wave frequency, ω and azimuthal m number the particles will diffuse along constant contours, f in (W,L) space from regions of higher density to lower density. This spatial gradient quantity $\mathrm{d}L/\mathrm{d}W \propto m/\omega$ and it can be seen that if m is large and ω is small (such is the case for the small scale poloidal modes wave in this thesis) conditions will be more favourable for a larger positive gradient distribution. In equation (2.50) δW and δL can be obtained using adiabatic theory (*Clemmow and Dougherty,* 1969). This theory can be applied to the injected particle populations in the magnetosphere to obtain a measurable quantity, the true gradient of the particle distribution function, df/dW,

$$\frac{\partial f}{\mathrm{d}W}=\left.\frac{\partial f}{\partial W}\right|_{\mu,\mathrm{L}}+\frac{\mathrm{d}L}{\mathrm{d}W}\left.\frac{\partial f}{\partial L}\right|_{\mu,\mathrm{W}}.\qquad(2.52)$$

Equation (2.52) takes into account both spatial and energy gradients in the particle population. The exact energy exchange that occurs between the particle population and the wave field is the subject of the paper by *Southwood* (1976). The paper outlines in detail how this exchange can theoretically occur. The work in this thesis deals with the fact that energy exchange does occur and highlights the importance of the only directly measurable parameter, the gradient of the IDF, df/dW.

2.9. The Resonance Equation

So far it has been demonstrated that for any interactions to occur there needs to be free energy from a particle population available to the wave. A requirement also exists for a suitable resonant wave mode to interact with the particles. By analogy with figure 2.10 (c) the wave velocity must be close to the particle velocity, i.e. they must be phase locked. This allows the particle to view a constant wave electric field. In the dipole field of the magnetosphere this can occur in a region where the particle azimuthal drift velocity is close to that of the wave azimuthal phase velocity. Under these circumstances the 'free energy' of the ion population is available to the wave and thus wave growth occurs. Consider the ion drift frequency in the wave's frame of reference,

$$\Omega_{\mathrm{d}} = \omega_{\mathrm{drift}} - \frac{\omega_{\mathrm{wave}}}{m}, \qquad (2.53)$$

where ω_{wave}/m is the angular phase velocity of the wave and ω_{drift} is the ion drift angular frequency in a stationary frame of reference. Consider a particle which drifts through 2π azimuthally in the wave's frame of reference during one inter-hemispheric bounce along the field line,

$$1 \times \frac{2\pi}{m\Omega_{\mathrm{d}}} = \frac{2\pi}{\omega_{\mathrm{bounce}}}. \qquad (2.54)$$

The term on the left hand side of equation (2.54) represents the drift time for the particle to traverse a wavelength in the azimuth direction in the wave's frame of reference and ω_{bounce} is the ion bounce angular frequency. By substituting in for Ω_d an equation can be obtained which will indicate under what circumstances resonance will occur,

$$\omega_{wave} - m_{wave}\omega_{drift} = N\omega_{bounce}, \qquad (2.55)$$

where N is an integer (usually 0, ±1). This is called the resonance condition (Southwood *et al.*, 1969). The interaction between the particles and the wave electric field is represented graphically in the 'Battenberg cake' diagram first introduced by Southwood and Kivelson (*Southwood and Kivelson*, 1982), in Figure 2.12. The cake represents the electric field perturbation of standing poloidal mode waves in the wave azimuthal drift frame of reference. The Earth's magnetic field lines are then vertically orientated with the northern (southern) ionosphere in the marzipan region at the top (bottom) of the figure. The equator is the central horizontal line traditionally made of jam. The pink (yellow) sponge represents eastward (westward) electric field direction. The magnetic perturbation, **b**, is also shown next to the cake, as well as the azimuthal dependence of the wave, under the cake. The solid and dashed lines across the cake represent different particle trajectories. If the $N = 0$ (solid line) trajectory is considered, this is called *drift resonance* as the particle has a gradient curvature drift which is identical to that of the wave. In this instance the bounce frequency of the particle becomes unimportant as can be seen from inserting $N = 0$ into equation (2.55),

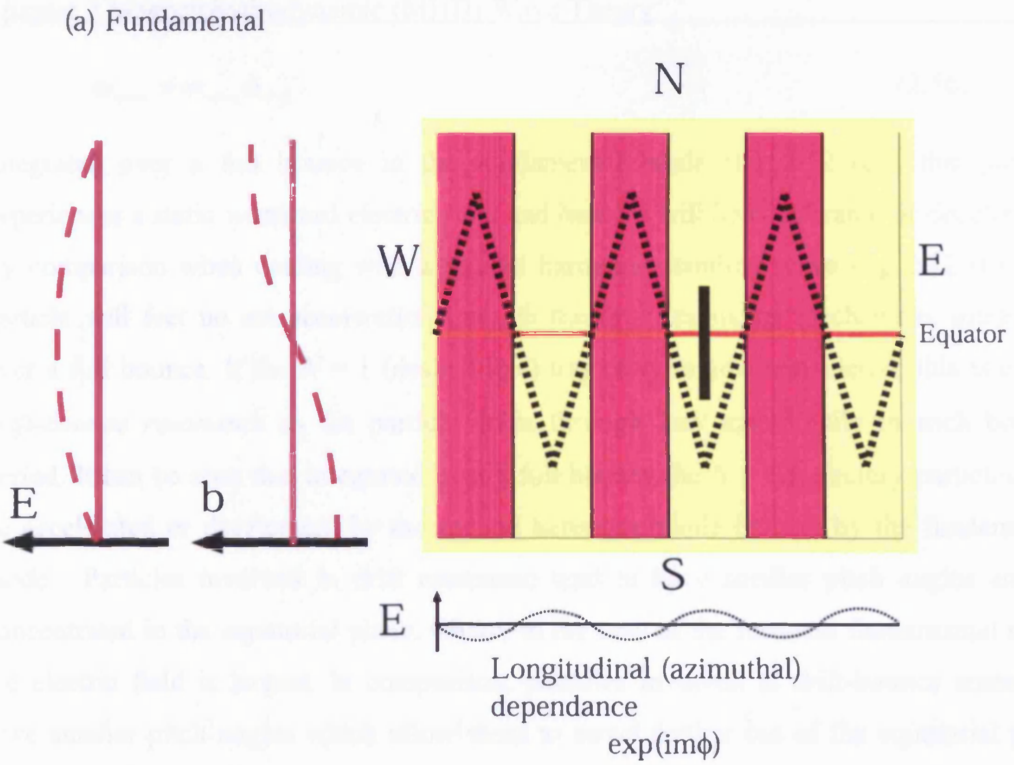

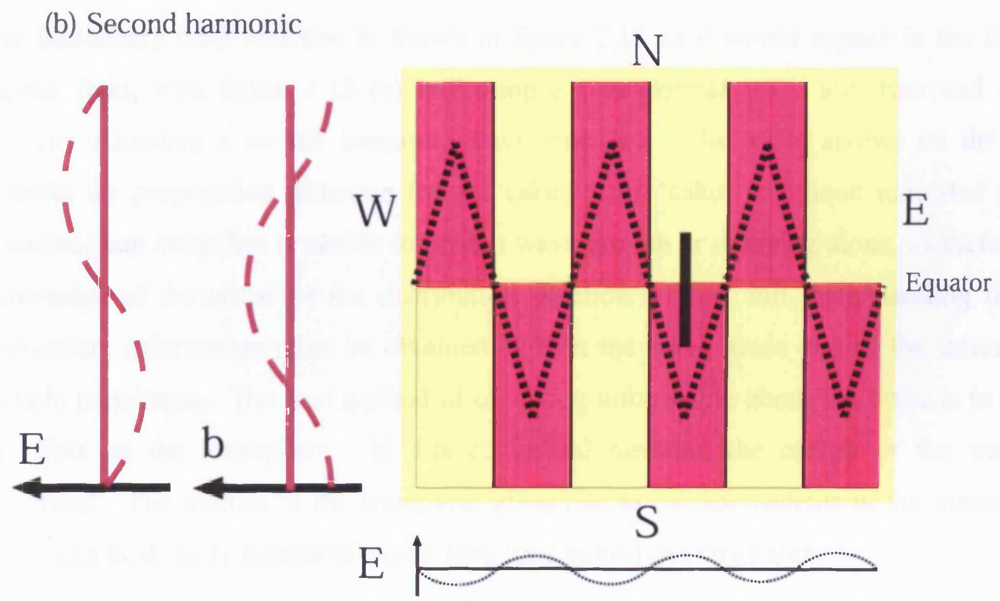

Figure 2.12. The interaction between the particles and the wave electric field as represented graphically in the 'Battenberg cake' diagram (adapted from Southwood and Kivelson, 1982) The cake represents the electric field perturbation of standing poloidal mode waves in the wave azimuthal drift frame of reference. Figure 2.12 (a) indicates a fundamental mode structure while figure 2.12 (b) represents a second harmonic structure. The Earth's magnetic field lines are then vertically orientated with the northern (southern) ionosphere in the marzipan region at the top (bottom) of the figure. The equator is the central horizontal line traditionally made of jam. The pink (yellow) cake represents eastward (westward) electric field direction. Interacting particle trajectories are also shown.

$$\omega_{wave} = m_{wave}\omega_{drift} \,. \tag{2.56}$$

Integrated over a full bounce in the fundamental mode (fig 2.12 (a)), this particle experiences a static westward electric field and hence a will be accelerated or decelerated. By comparison when dealing with a second harmonic standing wave (fig 2.12 (b)), the particle will feel no net acceleration through the drift resonance mechanism, integrated over a full bounce. If the $N = 1$ (dashed line) trajectory is now considered; this is called *drift-bounce resonance* as the particle drifts through $2\pi N$ azimuthally in each bounce period. It can be seen that integrated over a full bounce the $N = 1$ trajectory particles will be accelerated or decelerated by the second harmonic mode but not by the fundamental mode. Particles involved in drift resonance tend to have smaller pitch angles and be concentrated in the equatorial plane, where, in the case of the resonant fundamental mode the electric field is largest. In comparison, particles involved in drift-bounce resonance have smaller pitch angles which allow them to travel further out of the equatorial plane and into the region where the electric field modulations are largest.

The Battenberg cake structure is shown in figure 2.13 as it would appear in the Earth's dipolar field, with figure 2.13 (a) indicating a fundamental wave structure and figure 2.13 (b) indicating a second harmonic wave structure. The white arrows on the plots indicate the propagation direction for the cake. This 'cake' technique indicates where resonance can occur but is unable to predict wave growth or damping alone, as there is no knowledge of the shape of the distribution function. For a full understanding of any interaction, information must be obtained of both the wave mode and of the interacting particle population. The best method of obtaining information about the wave is to study its effect on the ionosphere. In this collisional medium, the energy of the wave is dissipated. The motion of the wave also gives rise to current systems in the ionosphere which can be directly measured over a long time period and large area.

2.10. The Effect of the Ionosphere

It has been shown that the terrestrial magnetic field can support standing mode Alfvén waves. In the magnetosphere the solutions derived earlier remain valid and the wave will have a magnetic perturbation b_y, and an electric field E_x. Upon encountering a collisional medium of finite conductivity such as the ionosphere, these perturbations can give rise to plasma motion and current systems. In the F-region ionosphere (>140km), the plasma will

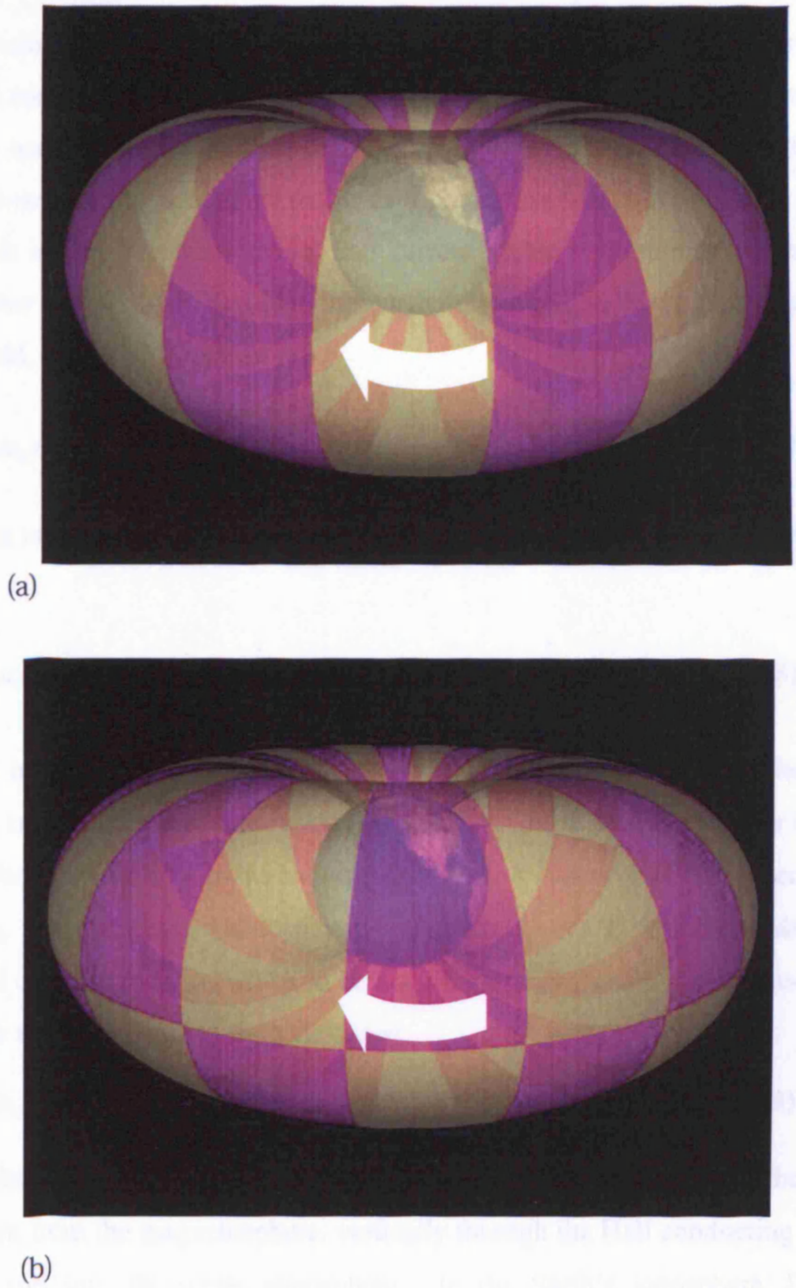

Figure 2.13. The Battenburg cake structure as it would appear in the Earth's dipolar field. Figure 2.13 (a) indicates the fundamental mode structure with figure 2.13 (b) indicating a second harmonic structure. The wave field would propapgate in a westward direction, indicated by the white arrows.

flow in the direction of the bulk drift ($\mathbf{E}\wedge\mathbf{B}$ drift) motion as the particle densities are still small enough to mean that collisions with neutrals are infrequent. As the wave propagates further into the ionosphere the neutral densities will increase. At below ~140 km in altitude in the E-region, the density increases to a point where neutral collisions become important, which can in turn give rise to the current systems mentioned in chapter 1. Following *Hughes* (1983), first consider the currents induced in the x direction by the wave electric field, E_x. Using Ampères law,

$$\frac{\partial b_y}{\partial z} = \mu_0 J_x = \mu_0 \sigma_{\mathrm{p}} E_x . \tag{2.57}$$

If this expression is integrated through the ionosphere with E_x varying slowly with altitude z,

$$\Delta b_y = \mu_0 E_x \int_{z_0}^{z_0+l} \sigma_{\mathrm{p}} \mathrm{d}z = \mu_0 \Sigma_{\mathrm{p}} E_x , \tag{2.58}$$

where Σ_p is the height integrated Pedersen conductivity. The Earth's atmosphere is an insulator and as such cannot support any current systems. If no current systems can flow then there can be no magnetic perturbations, thus $b_y = 0$ below the ionosphere. This implies that $\Delta b_y = b_y$ in the magnetosphere. The wave electric field will also cause ionospheric Hall currents to flow, which in turn gives rise to magnetic perturbations both above and below the ionosphere in the x direction,

$$\Delta b_x = \mu_0 \Sigma_{\mathrm{H}} E_x / 2 , \tag{2.59}$$

where Σ_H is the height integrated Hall conductivity. In this case Δb_x represents the change in b_x as you move from the magnetosphere, vertically through the Hall conducting layer of the ionosphere and into the upper atmosphere. In the Earth's ionosphere $\Sigma_H \sim \Sigma_p$, therefore $\Delta b_x \sim \Delta b_y$, thus the effect of the ionosphere is to cause the magnetic perturbation vector, **b** to rotate through 90°. The Pedersen current forms a current loop with the field aligned currents flowing into and out of the ionosphere and therefore has no associated ground signature. Any ground signature of the wave is actually as a result of a fast mode perturbation, b_x caused entirely by the flow of the Hall currents and not by the initial Alfvén wave directly. This current system is shown in figure 2.14. Above the magnetosphere the magnetic perturbation b_x is associated with a fast mode wave. The dispersion relation for propagation along the background magnetic field (from table 2.1

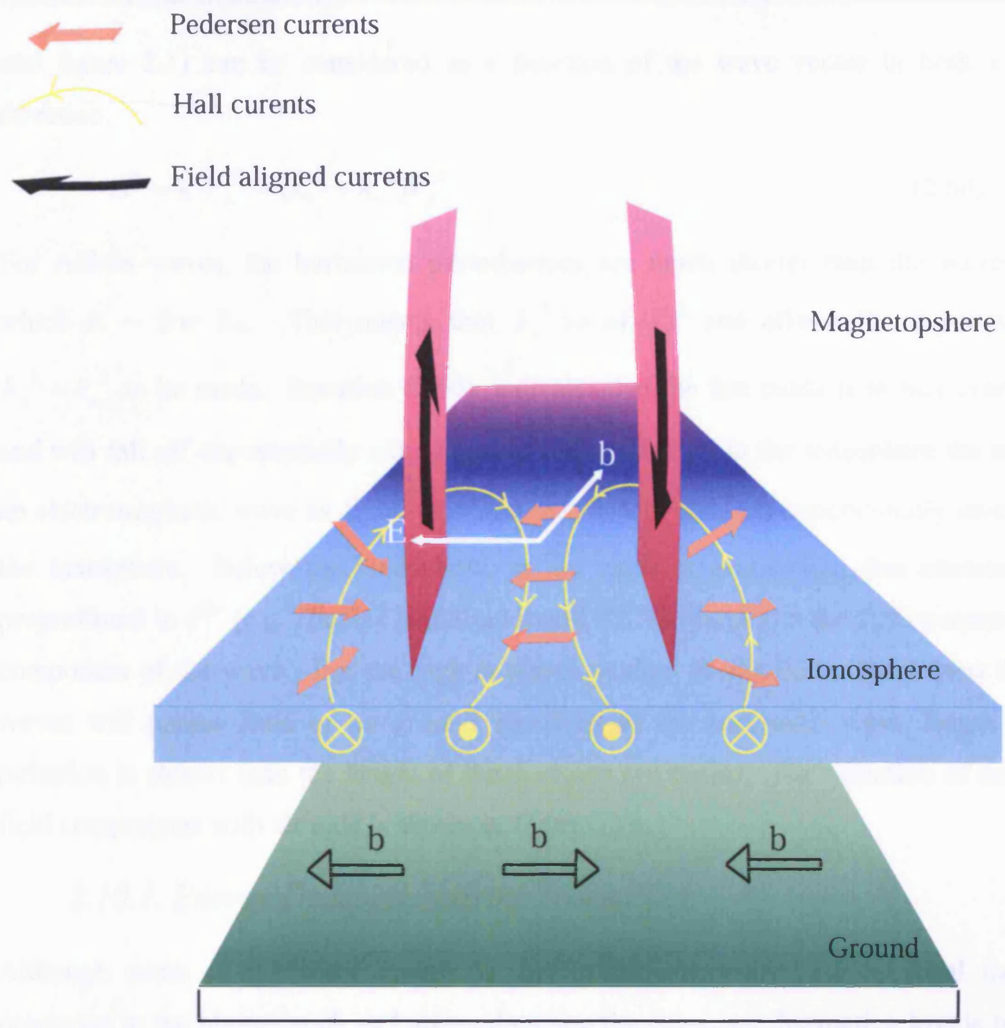

Figure 2.14. The current systems in the ionosphere associated with ULF waves. The electric and magnetic pertubations of the ULF wave are shown in white. The Hall currents (shown in yellow) flow around the field lines in a direction that is dependent upon the field aligned current (shown in black) direction. The Pedersen currents (shown in orange) form a current between the Hall and field aligned current systems. The magnetic pertubation on the ground is also shown. This pertubation is due to the Hall currents and is rotated through 90^{o} from the magnetic pertubation direction in the magnetosphere.

and figure 2.1) can be considered as a function of the wave vector in both x and z direction.

$$\omega^2 = \mathbf{k}^2 V_A{}^2 = (k_x{}^2 + k_z{}^2) V_A{}^2 \tag{2.60}$$

For Alfvén waves, the horizontal perturbations are much shorter than the wavelength, which is ~ few R$_E$. This means that $k_x{}^2 >> \omega^2 / V_A^2$ and allows the approximation $k_x{}^2 = k_z{}^2$ to be made. Equation (2.60), indicates that the fast mode is in fact evanescent and will fall off exponentially with a scale height of $1/k_\perp$. In the ionosphere the mode is an electromagnetic wave as $k_\perp >> \omega/c$ and thus b_x will drop off exponentially away from the ionosphere. Below the ionosphere, as the mode is evanescent, this attenuation is proportional to $e^{-\mathbf{k}z}$ (e.g. *Hughes and Southwood, 1976*) where **k** is the field perpendicular component of the wave. For the high m waves studied in this thesis this means that the waves will posses little or no ground signature as the horizontal wave length of the pulsation is shorter than the height of the E-region (~120km). The variation of magnetic field components with altitude is shown in figure 2.15.

2.10.1. Energy Dissipation in the Ionosphere

Although some of the wave energy is lost in the magnetosphere by local damping processes in the plasma such as Landau damping the dominant dissipative loss is through Joule heating in the ionosphere (*Allan and Poulter*, 1992). In the ionosphere the energy is dumped at ~ 100 km altitude (the altitude corresponding to the ionospheric Pedersen layer), warming up the atmosphere. This process allows energy from the energetic ring current to be dissipated into the ionosphere and represents a significant sink for this system. An ionospheric boundary condition can now be derived,

$$\mathbf{b_m} \wedge \hat{\mathbf{z}} = \mu_0 \Sigma_\mathrm{p} \mathbf{E_m}, \tag{2.61}$$

which arises from the fact that the ionospheric Pedersen currents totally shield the incident magnetic perturbation (the subscript m denotes magnetospheric quantities). By multiplying equation (2.58) by the magnitude of the wave electric field E, the energy dissipation processes in the ionosphere can be understood in terms of an electric field and the Pedersen current,

$$\frac{1}{\mu_0} Eb = \Sigma_\mathrm{p} E^2 = J_p E. \tag{2.62}$$

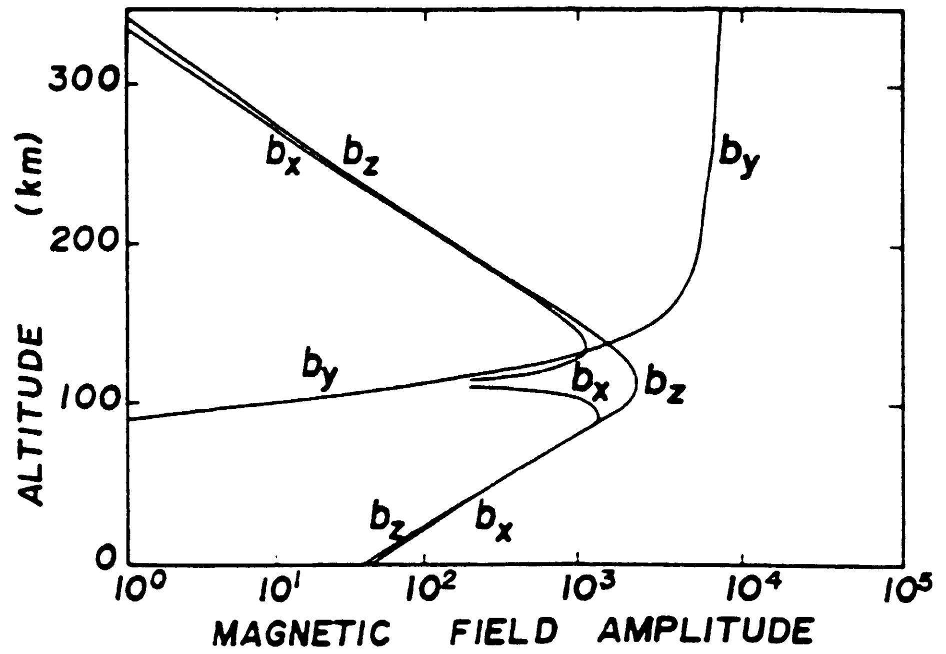

Figure 2.15. The variation with altitude of the wave magnetic field components that occur when an Alfvén wave is incident on the ionosphere. The values were calculated using a realistic model ionosphere. The change in direction of the dominant component occurs in the E-region at around 120 km (taken from *Hughes*, 1983).

This can be interpreted as a balance between the magnitude of the downward Poynting vector, **S** associated with the wave electric and magnetic perturbations and joule heating in the ionosphere. The ionospheric boundary condition will not be satisfied by the incident wave and some partial reflection will occur. If the ionosphere was perfectly conducting, $\Sigma_p = \infty$, the wave is totally reflected and no electric fields are set up in the ionosphere and the field line feet are fixed. In the other extreme if $\Sigma_p = 0$, reflection is again perfect but now $\mathbf{b} = 0$ in the ionosphere and the field lines are free to move. Under normal finite conductivity conditions, the situation is in between these two extremes and as such the wave energy is gradually dissipated into the ionosphere through Joule heating.

2.11. Summary

This chapter has introduced and discussed the physics of MHD ULF pulsations in the magnetosphere. Particular attention has been drawn to small scale high *m* waves which are driven through wave particle interactions internal to the terrestrial magnetosphere between injected ion populations in the ring current and standing modes on the magnetic field lines. The chapter has outlined the resonance conditions required for energy transfer to occur through inverse Landau damping and has shown how the energy from the ring current population is ultimately dissipated into the high latitude ionosphere. In the following chapters, observational evidence in the form of case studies and statistical studies will be presented that both affirm and contradict aspects of this theory. The next chapter will introduce much of the previous work that has been undertaken and highlight many unanswered questions and ambiguities that remain.

Chapter 3

Review and Discussion of Previous Work Undertaken Concerning ULF Waves in the Terrestrial Magnetosphere

3. Introduction

This chapter will review the work undertaken into geomagnetic pulsations in the last 30 years, with particular focus on those waves generated through wave-particle interactions. It will introduce the various ways in which different wave types have been identified using both satellite and ground based datasets. Both statistical studies and case studies in the pre and post-noon sectors will be reviewed, as will two specific well documented categories of high *m* waves; Giant Pulsations (Pgs) and storm time Pc5 pulsations. This chapter will also highlight several remaining questions which this thesis hopes to address and answer in following chapters.

3.1. Wave Classifications

The types of pulsations observed in the magnetosphere fall initially into two main categories, continuous and irregular (sometimes called impulsive). This thesis focuses on the continuous category. The continuous (Pc) and irregular (Pi) pulsation scales shown in table 3.1 were introduced by *Jacobs et al.* (1964) to allow the different types of waves to be categorised according to their frequency. The majority of high *m* particle driven waves are classified as Pc4 (7 – 22 mHz) or Pc5 (2 – 7 mHz) waves. This does not mean that Pc4 and Pc5 waves are exclusively high *m* in nature, the Pc classification only relates to the frequency of the standing mode on the magnetic field lines, not to the azimuthal scale size of the wave.

In chapter 2 the different wave modes and their possible generation mechanisms were introduced. The governing MHD wave equations in a dipolar field revealed three different types of wave, large scale, azimuthally polarized, toroidal mode waves and large and small scale, radially polarized, poloidal mode waves. This thesis is concerned with small scale poloidal mode waves thought to be driven though wave-particle interactions in the magnetosphere. The theory (e.g. *Dungey,* 1963) indicates the wave structure for

	Continuous (Pc)					Irregular (Pi)	
	Pc1	Pc2	Pc3	Pc4	Pc5	Pi1	Pi2
T(s)	0.2-5	5-10	10-45	45-150	150-600	1-40	40-150
Frequency	0.2-5 Hz	0.1-0.2 Hz	22-100 mHz	7-22 mHz	2-7 mHz	0.0025-1 Hz	2-25 mHz

Table 3.1. The continuous (Pc) and irregular (Pi) pulsation scale which allows pulsations to be catagorised in terms of their frequency. The scale was introduced by *Jacobs et al.,* (1964).

the idealised case of when the azimuthal $m \rightarrow \infty$. In reality the waves have a finite m number which implies that the compressional term, $\mathbf{B_0.b}$ in the coupled MHD wave equations (2.36 to 2.38) is also finite. Thus all standing wave modes will have both transverse and compressional components. This introduces complications when finding suitable descriptions for sets of wave modes and also in categorising them. Figure 3.1 indicates the structure of the first two harmonic standing Alfvén modes. Figure 3.1 (a) indicates the structure of an odd (fundamental) mode (symmetric) wave structure and (b) an even (second harmonic) mode (anti-symmetric) wave structure. The N and S in the diagrams indicate the Northern and Southern hemisphere ionospheres. The field line displacement $\boldsymbol{\chi}$, transverse magnetic perturbation $\mathbf{b}_{\perp}$ and compressional (parallel) magnetic perturbation $\mathbf{b}_{//}$ are shown for each. The structure is such that a symmetric mode magnetic perturbation will have a node in the equatorial plane in the transverse component and an antinode in the compressional component. The opposite is true for the anti-symmetric mode structure. The wave polarisation classification deduced from spacecraft data thus depends on the relative magnitude of the two magnetic components. The waves sometimes have a compressional component which is comparable to the radial component (*Hughes et al.*, 1979; *Tonegawa*, 1982) but the wave energy is still considered to the guided along the ambient magnetic field (*Southwood*, 1977) and thus remain Alfvénic in nature.

An example of a radially polarized wave is shown in figure 3.2. The data is from the magnetometer onboard the AMPTE/CCE spacecraft. The magnetic field data are shown in both the radial (b_x) and azimuthal (b_y) direction and also along the background magnetic field direction (b_z). The spacecraft was located at ~ 5 – 7 R_E and at an MLT of ~ 1300. The oscillations are dominant in the radial direction and are also present in the azimuthal direction. There is no evidence of oscillations in the compressional (b_z) component. Given this polarisation configuration and due to the fact that the spacecraft was located near the magnetic equator this event was judged to have a second harmonic standing wave structure (*Takahashi et al.*, 1990).

Figure 3.3 indicates the structure of a wave classed as a compressional mode wave. These wave modes are often observed during active periods and generally associated with the arrival of energetic ion populations that have been injected into the inner magnetosphere (*Takahashi*, 1996). Compressional waves exhibit strong oscillations in both the transverse and compressional magnetic field components. The data is magnetic

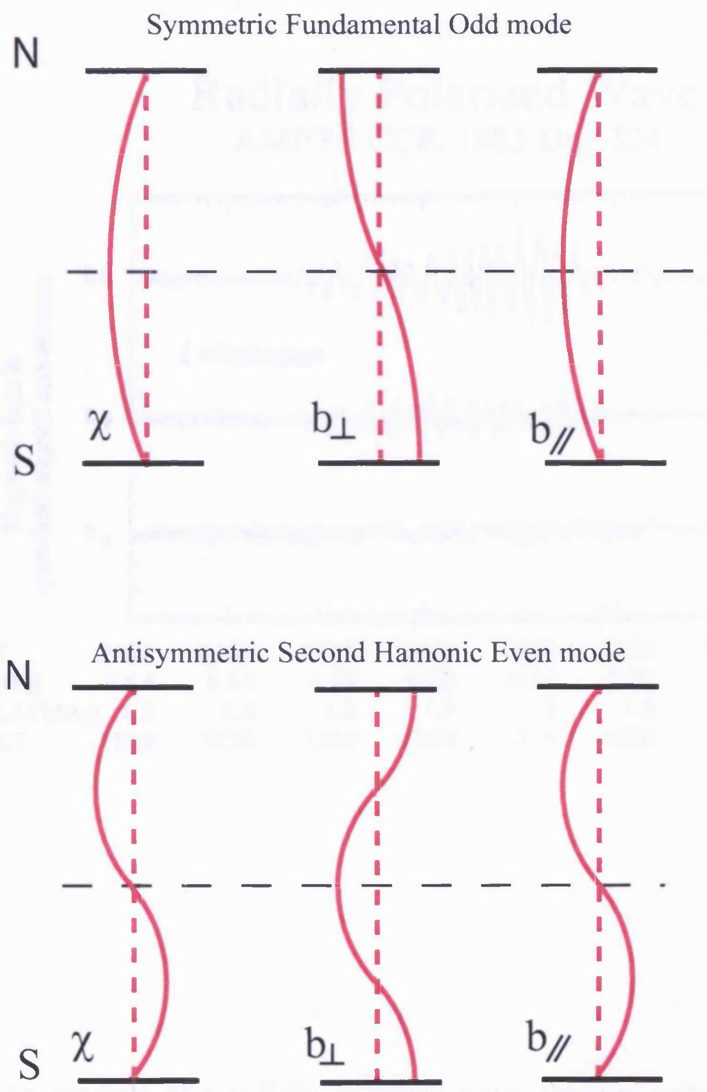

Figure 3.1. Structure of a (a) symmetric odd mode oscillation and (b) antisymmetric even mode. The N and S in the diagrams represent the northern and southern hemipshere ionospheres. The field line displacement χ, transverse $\mathbf{b}_{\perp}$, and compressional $\mathbf{b}_{//}$ magnetic field components are shown (adapted from *Takahashi,* 1996).

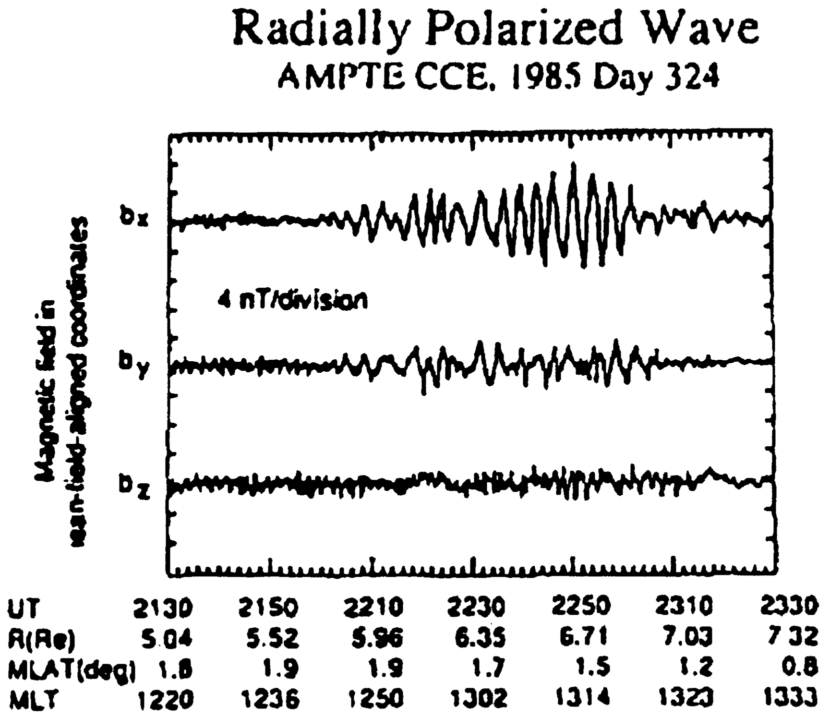

Figure 3.2. An example of a radially polorised wave observed using the magnetometer onboard the AMPTE/CCE spacecraft. The oscillations are present in the radial (b_x) and azimuthal component (b_y) but are virtually absent in the compressional (b_z) component. The satellite was located near the equator, (Taken from *Takahashi et al.*, 1990).

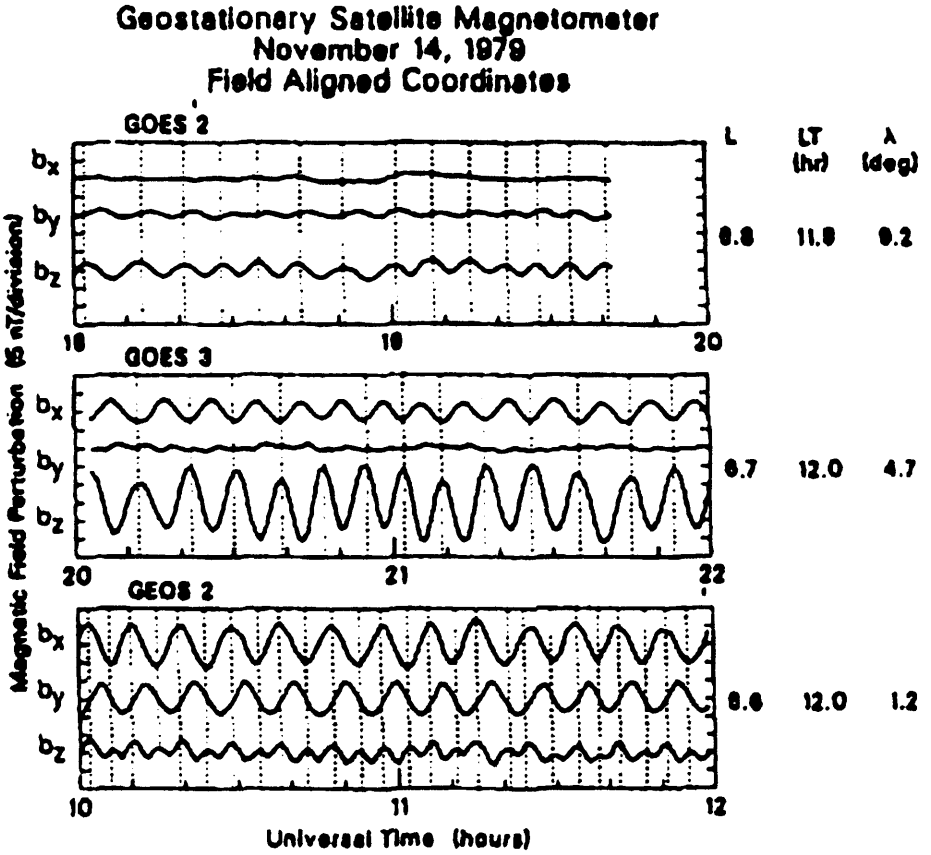

Figure 3.3. Multi-satellite observations of a compressional wave. The λ parameter indicates the number of degrees out of the magnetic equator the spacecraft is located. The co-ordinate system has b_x as the radial component, b_y as the azimuthal component and b_z as the field aligned component. The measurements indicate how the amplitude of the wave variation in the different components varies as a function of magnetic latitude, (taken from *Takahashi et al.*, 1987).

field data from 3 spacecraft, GOES 2, GOES 3 and GEOS 2. The co-ordinate system is the same as that for figure 3.2. The λ parameter indicates the number of degrees out of the magnetic equator each spacecraft was located. The spacecraft were all located at an *L*-shell of ~ 6.6 and a MLT location of ~1200 MLT. The measurements indicate how the amplitude of the wave variation in the compressional (b_z) and transverse (b_x, b_y) components vary as a function of latitude. GEOS 2 (λ = 1.2°) indicates the wave is dominated by the transverse components in both the radial (b_x) and azimuthal (b_y) direction. GOES 3 (λ = 4.7°) indicates the compressional component is now dominant although there is evidence of the wave in the radial component. GOES 2 (λ = 9.2°) indicates the wave only in the compressional component although the amplitude of the wave signal has decreased significantly. Given the fact that this wave has a node in the compressional component near the magnetic equator it was judged to be have an anti-symmetric standing wave structure (*Chen and Hasegawa*, 1991).

These examples highlight many of the problems encountered when trying to classify high *m* ULF waves. Depending on the satellite location, the wave could possibly be classed as a compressional or radially polarized wave. The fact that most early studies into ULF waves were done utilising satellite studies and that the waves display both transverse and compressional components has also lead to a vast array of descriptive terms, such as compressional Alfvén waves, shear Alfvén waves and radially polarized compressional waves. The general understanding that has appeared through studies (e.g. *Kokubun* 1989; *Takahashi et al.*, 1990; *Cramm et al.*, 2000) that utilise this method of looking for nodes and antinodes in the compressional and transverse wave components is that the spacecraft must be located within 5° of the magnetic equator. However, this method has been employed in a less rigorous fashion for spacecraft measurements up to 11° off the magnetic equator. 'Anti-symmetric compressional Pc5 waves show a considerable compressional component even at ~ 2 deg dipole latitude and at the equator they still exhibit a compressional oscillation' *Takahashi et al.* (1987). In their 1990 paper *Takahashi et al.* (1990) noted that the Pc5 waves they observed did not display these similar characteristics (the spacecraft measurements in the 1990 paper were at > 5° off the magnetic equator) and they therefore concluded that the wave was radially polarised. It is at present unclear how reliable this method is at categorising ULF waves or whether it is introducing more terminology than is required.

3.2. Theoretical Models

There are many different theories pertaining to how particle energy is fed into the resonant wave mode, however it is well recognised in all the theories that magnetospheric ion populations are the major energy source for high m pulsations. The different theories are associated with the different states of the ambient plasma in the ring current in the vicinity of the wave. This thesis evaluates the possibility of wave generation through the drift-bounce instability (*Southwood*, 1976; *Southwood and Kivelson*, 1982) which requires a low ($\beta << 1$) plasma state (β is the ratio of the thermal or plasma pressure to the magnetic pressure). I will briefly introduce the other theoretical models here. The drift mirror instability (*Hasegawa*, 1969; *Pokhotelov et al.*, 1986) has been cited as a possible driving mechanism for compressional waves ($\mathbf{b}_{//} > \mathbf{b}_{\perp}$), particularly those observed in the dusk sector during geomagnetically active period, so called storm time Pc5s (*Allan et al.*, 1982). This instability requires a high β plasma and the free energy is thought to manifest itself as a pressure anisotropy in the ambient plasma with $\mathbf{P}_{\perp} > \mathbf{P}_{//}$. The drift mirror instability ignores bounce resonance effects by choosing $N = 0$ in equation (2.55), (*Allan and Poulter*, 1992) and therefore this instability will preferentially excite an odd mode wave. Other theories include the drift Alfvén ballooning mirror instability (DABM), (*Chen and Hasegawa,* 1991) which has been related to radially polarised ($\mathbf{b}_{\perp} > \mathbf{b}_{//}$) waves in the low plasma β regime and also compressionally polarised waves in the high plasma β regime. This instability requires a pressure gradient in the plasma to feed free energy into the wave through wave-particle interactions and is associated with an anti-symmetric standing wave structure. The ballooning mirror instability (*Cheng,* 1982; *Cheng and Qian,* 1994) has also been proposed to drive compressional mode Pc5 waves and also invoke an anti-symmetric mode for such pulsations. Finally there is the drift wave instability (*Hasegawa,* 1971). This instability is excited in a plasma with mixed hot and cold components and has been suggested as the generation mechanism for morning sector waves. It invokes a symmetric standing wave structure.

Although a variety of detailed mechanisms have been proposed, each with varying wave symmetry requirements all require a magnetospheric particle population with free energy available as the energy source and a resonant drift or drift-bounce interaction mechanism.

Thus, knowledge as to the ion distribution function is required to evaluate which interaction a drift or drift-bounce one will dominate in a given region (*Takahashi,* 1996).

3.3. Modelling of Particle Drift Paths

Recent work by *Ozeke and Mann* (2001) has investigated the ring current population which is the energy source for the small scale ULF waves detailed in this chapter. The work illustrates a model in which they reveal the energetically favourable locations in W - L space where the driving bump-on-tail or unstable particle distributions can occur. After an particle injection on the nightside, those protons on open orbits will subsequently be lost as they drift out of the magnetosphere through the dayside magnetopause, leaving only those protons on closed orbits. The model proposes that the boundary between the open and closed particle orbits, following a particle injection, represents a location where unstable particle distributions, $df/dW > 0$, can develop. .The location of these particle populations are determined by ascertaining the position where the open-closed orbit boundary of the azimuthally drifting particle population intersects a drift-bounce resonance curve. During geomagnetically active times, closed orbit paths around the Earth become open and energetic particles can be injected onto them in the inner magnetosphere. If a period of little activity follows these paths become closed once more and the newly injected particles can drift round to the morning sector from their injection point on the nightside, where they will on occasion match the local drift–bounce resonance condition. This is shown in figure 3.4. The panels on the left hand side show the equatorial drift paths of 30 keV protons through 1800 MLT at integer values of L from L = 2 to 10 and pitch angles of 45° at 1800 MLT. The panels on the right hand side show the open-closed orbit boundary for protons with pitch angles of 45° at 1800 MLT. Panels (a) and (b) show the trajectories of protons and the open-closed orbit boundary respectively before a particle injection (where Kp = 2). Panels (c) and (d) show the trajectories during a particle injection when the convection electric field is enhanced (Kp = 3). The dark lines in (c) represent the open trajectories which are populated by the injection. The dotted lines in panels (c) and (e) represent the outermost unpopulated orbit during the injection. Panels (e) and (f) show the trajectories and the open-closed boundary respectively after the injection when the convection electric field has decreased (Kp = 2). The dark lines in (e) represent the closed orbits which have become populated due to the injection. In their model, they used magnetospheric plasma density profiles to

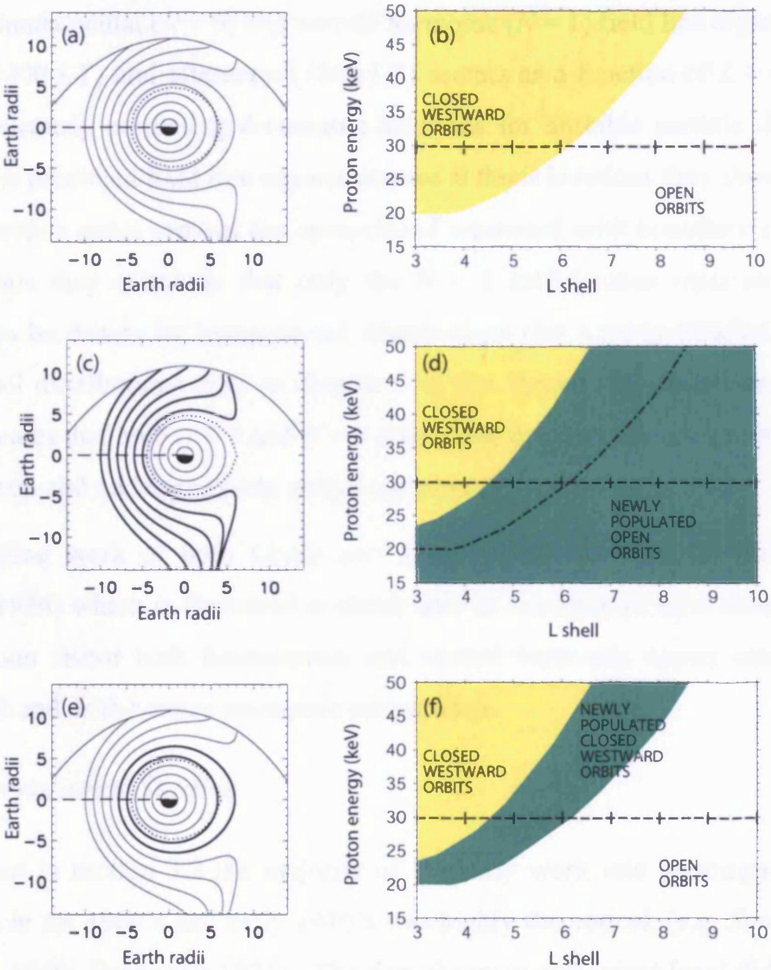

Figure 3.4. The panels on the left hand side show the equatorial drift paths of 30 keV protons through 1800 MLT at integer values of L from L=2 to 10 and pitch angles of 45° at 1800 MLT. The panels on the right hand side show the open-closed orbit boundary for protons with pitch angles of 45° at 1800 MLT. Panels (a) and (b) show the trajectories of protons and the open-closed orbit boundary respectively before a particle injection (where Kp = 2). Panels (c) and (d) show the trajectories during a particle injection when the convection electric field is enhanced (Kp = 3). The dark lines in (c) represent the open trajectories which are populated by the injection. The dotted lines in panels (a) (c) and (e) represent the outermost unpopulated orbit during the injection. Panels (e) and (f) show the trajectories and the open-closed boundary respectively after the injection when the convection electric field has decreased (Kp = 2). The dark lines in (e) represent the closed orbits which have become populated due to the injection (taken from *Ozeke and Mann*, 2001).

obtain the fundamental ($N = 0$) and second harmonic ($N = 1$) field line eigenperiods in the morning (0600 LT) and afternoon (1800 LT) sectors as a function of L – shell location. By simultaneously predicting favourable locations for unstable particle distributions to form and the predicted field line eigenstructures at those locations they show that only the $N = 1$ resonance curve crosses the open-closed westward orbit boundary in the morning sector. Thus they conclude that only the $N = 1$ drift-bounce resonance is a viable candidate to be driven by bump-on-tail distributions (for a more detailed discussion of bump-on-tail distributions refer to chapter 2 of this thesis). In the afternoon sector the model indicates that both $N = 0$ and $N = 1$ interaction mechanisms are possible, indicating that both even and odd eigenmode waves are present.

The modelling work of both *Ozeke and Mann* (2000) and similar earlier model by *Chisham* (1996) which is discussed in detail later in this chapter have thus shown that in the post-noon sector both fundamental and second harmonic waves can be generated though drift and drift-bounce resonance interactions.

3.4. Observational Studies

As discussed in section 3.2 the majority of the early work into geomagnetic pulsations undertaken in the 1960's and early 1970's was highly theoretical, (e.g. *Southwood,* 1976; *Hasegawa*, 1969; *Hasegawa* 1971). The first observational 'giant leap' didn't occur until ~ 1970, when two advances in observational techniques allowed theories to be tested and experimental data to be amassed. For the first time magnetometers that were sensitive enough to detect these pulsations were used on satellites (e.g. ATS 1; *Cummings et al.,* 1969) and also large arrays of closely spaced ground magnetometers were deployed (e.g. *Samson et al.*, 1971). The first experiments used two or more spacecraft separated by some distance to look at phase variation of the wave. This was not easy as most satellites were too far apart to measure the pulsations. The first attempt was made by *Hughes et al.* (1977) using the OGO 5 and ATS 1 satellites. Both spacecraft did detect a Pc4 pulsation around local noon, but as the spacecraft were so far apart, only an upper estimate of ~1R_E was obtained for the resonant region thickness.

Since then the number of satellites used for the studies of ULF waves has grown tremendously. The geostationary satellites used include: ATS 1(*Cummings et al.,* 1969), ATS 6; GOES 2 and 3, (e.g. *Takahashi et al.*, 1987) 4, GOES 5 and 6 (e.g. *Engebretson* et al., 1992); GEOS 2 and SMS 1. Spacecraft with highly elliptical orbits such as HEOS-

1; OGO 3, 5 (e.g. Hughes et al., 1977); ISEE 1 (*Zhu and Kivelson*, 1991), ISEE 2 (e.g. *Hughes and Grard*, 1984) and AMPTE/CCE (e.g. *Takahashi et al.*, 1990, 1992) have also been used. This vast array of satellites have provided ULF wave observations from L = 5, out to the dayside magnetopause and as far as ~ 15 R_E down the magnetotail (*Anderson*, 1993).

Ground instruments utilised in the study of ULF waves are also numerous. Ionospheric observations have been made using UHF (e.g. *Wright et al.*, 1998), HF (e.g. *Yeoman et al.*, 2001) and VHF (e.g. *Allan et al.*, 1982) radar systems and more recently Doppler Sounders (e.g. *Wright et al.*, 1999). Ground magnetometers (e.g. *Chisham and Orr*, 1991) have also been utilised in the study albeit in a more limited fashion due to the fact that for high m waves little or no ground signature is observed as the horizontal wave length of the pulsation is shorter than the height of the E-region (see section 2.9 for a complete discussion).

Various experimental techniques have been employed to ascertain the wave characteristics such as frequency, dominant polarisation, azimuthal m number and also standing mode structure. The results of the majority of studies have identified several families of ULF waves in the region $L = 6 - 9$.

3.4.1. Satellite Based Statistical Studies

Given the nature of high m waves, observations of such phenomena have proved most difficult. Satellites traversing an active region, often at great speed, are not always the optimal instrument to study the phenomena, and as such can often give an incomplete picture of the occurrence of highly localized, small scale waves. Another problem with satellite studies is the nature of the orbit itself. Some of the common wave modes have low magnetic fields in the equatorial plane, and thus these waves are often not detected by spacecraft in this region. Waves have been classified as either compressional waves or radially polarised waves often on the basis of a single satellite measurement near the magnetic equator. However, since the standing wave structure varies along the magnetic field, the dominance of either a compressional component or radial component would be a function of the spacecraft location. Despite these difficulties and given the instrument limitation at the time, there have been several statistical studies which do focus on satellite observations.

Kokubun (1985) used GOES 2 and GOES 3 data to investigate both radially (poloidal; R class) and azimuthally (toroidal; A class) polarized waves. He noted a compressional population of R class ULF waves that did not correlate with ground observations taken at the conjugate point. These waves were most common at dusk. *Kokubun* (1985) also noted a dawn and a dusk population of similarly uncorrelated waves with a transverse, azimuthal polarization. *Kokubun* (1989) extended this study using magnetic field and particle flux measurements from the ATS 6 satellite. The spacecraft was located at 10° magnetic latitude. The A class pulsations were all Pc4 or Pc5 events and were dominant in the morning sector. All had $m < 10$ and displayed a good correlated ground signature in magnetometers located near the ATS 6 foot point which indicated that they were large scale, externally driven pulsations. Approximately 100 R class events were observed occurring at all MLTs. The R class population could be divided further into R class Pc4 pulsations and R class Pc5 compressional pulsations. The compressional Pc5 pulsations were predominantly observed in the dusk sector and the author speculated that they were generated by instabilities in the ring current plasma associated with substorm particle injections. The R class Pc4 pulsations also had a peak occurrence in the afternoon sector although they occurred at all local times and during geomagnetically quiet conditions. The majority of R class Pc4s did not indicate any correlated ground magnetic signature and were judged to be second harmonic even mode pulsations. However, a subsection of this class, called Giant Pulsations or Pgs, did display a ground signature. 12 of these events were observed in the morning sector. Pgs will be discussed later in section 3.6. A summary of the pulsation types; A class pulsations with a clear ground signature, R class pulsations and Pgs, are presented in figure 3.5 as a function of MLT.

Takahashi et al. (1985) were able to make multi-spacecraft measurements of eight compressional Pc5 events observed at geostationary orbit. By utilising data from two satellites in close proximity to one another they were able to directly measure the azimuthal phase velocity and thus the azimuthal wave numbers for the events, finding m = -40 to -120. The distribution of such events is shown in figure 3.6 and is symmetric about noon.

Engebretson et al. (1992) investigated 21 predominantly radial polarized Pc4 wave events with the AMPTE/CCE, GOES 5 and GOES 6 satellites. The waves were observed between 0900 and 1900 MLT and occurred during magnetically quiet times, usually after magnetic storms. The waves were observed mostly near dusk, but with some events seen

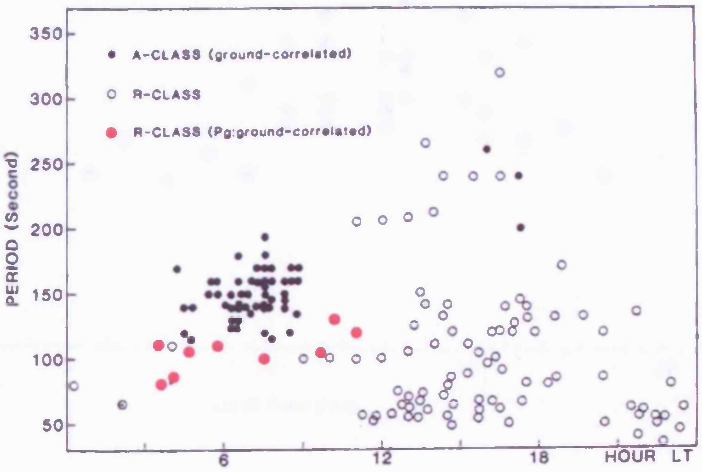

Figure 3.5. Local time dependance of periods of Pc4 and Pc5 pulsations indentified by magnetometer and particle data, (adapted from *Kokubun et al.*, 1989). The Pg pulsations events were identified using ground magnetometer data.

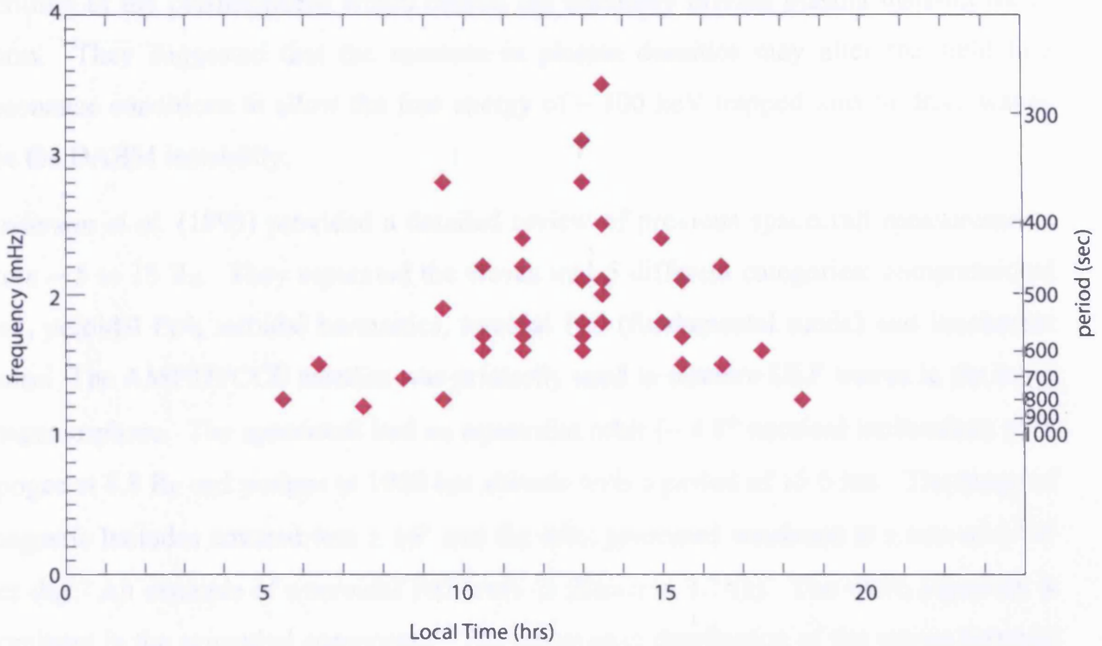

Figure 3.6. The frequency (mHz) and period (secs) of 35 compressional Pc5 events as a function of local time. The events weere measured using a total of 4 satellites, (adapted from *Takahashi et al.,* 1985)

on the morning side. The authors suggested that the pulsations were associated with the refilling of the plasmasphere which caused the necessary driving plasma instabilities to form. They suggested that the increase in plasma densities may alter the field line resonance conditions to allow the free energy of ~ 100 keV trapped ions to drive waves via the DABM instability.

Anderson et al. (1993) provided a detailed review of previous spacecraft measurements from ~ 5 to 15 R_E. They separated the waves into 5 different categories: compressional Pc5, poloidal Pc4, toroidal harmonics, toroidal Pc5 (fundamental mode) and incoherent noise. The AMPTE/CCE satellite was primarily used to observe ULF waves in the inner magnetosphere. The spacecraft had an equatorial orbit (~ 4.8° nominal inclination) with apogee at 8.8 R_E and perigee at 1000 km altitude with a period of 15.6 hrs. The range of magnetic latitudes covered was ± 16° and the orbit precessed westward at a rate of 0.77° per day. An example of a toroidal Pc5 wave is shown in 3.7 (a). The wave signature is dominant in the azimuthal component. The occurrence distribution of the waves between $L = 5 - 9$ and an MLAT of between 0 and 16° for all MLTs is shown in figures 3.7 (b) and (c). Figures 3.8 and 3.9 show examples and distributions for a poloidal Pc4 wave and a compressional Pc5 waves in the same format. The authors suggest that the compressional Pc5 and poloidal Pc4 pulsations derive their energy from an internal energy source such as magnetospheric ion populations. The results of the study indicate that the dawn sector was primarily populated with azimuthally polarized, large scale, waves, although there is also evidence of a smaller population of both poloidal Pc4 waves and compressional Pc5 waves. In the post-noon sector both poloidal Pc4 waves and compressional Pc5 waves dominate, although the compressional waves are concentrated at dusk.

Woch et al. (1990) presented a study of 76 compressional Pc5 events observed by the GEOS 2 satellite. The spacecraft was located at 3.5° magnetic latitude. Two populations of events were identified. The first was termed a "diamagnetic" population, which occurred during an increase in the measured ion intensities and a consequent reduction in the magnetic field due to the diamagnetic effect of the ions. This population was concentrated at the dusk sector and it was noted that the times of the pulsation onset is consistent with $\nabla \mathbf{B}$ drift time of 30 keV ions from the midnight meridian to the spacecraft. The second population was termed a "non-diamagnetic" population, which was not associated with recently injected particles but occurred under steady geomagnetic

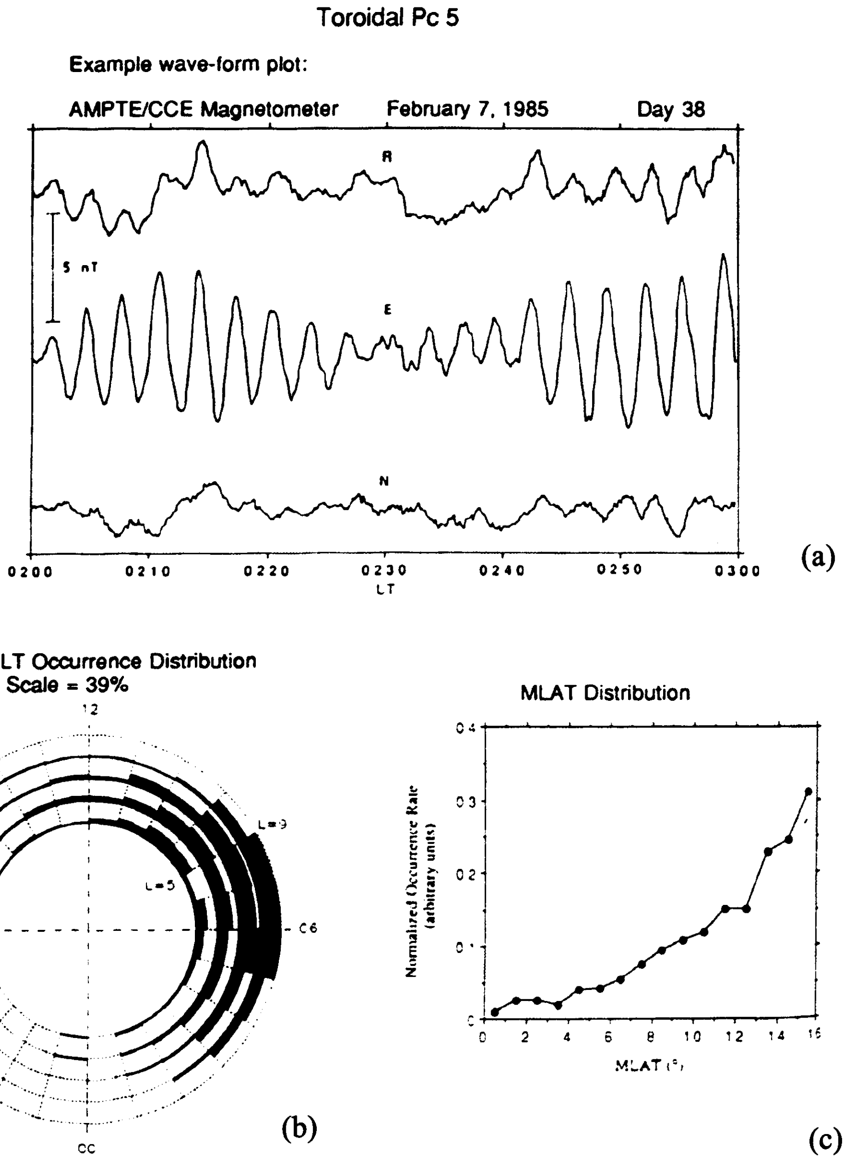

Figure 3.7. Example of toroidal Pc5 wave observed by the AMPTE/CCE satellite. The wave signature is dominant in the azimuthal component, *E*. There is little or no evidence of the wave in either the field aligned or radial component. (b) the occurrence distribution for the toroidal Pc5 waves between L = 5 - 9. (c) the MLAT distribution of the data. (Taken from *Anderson,* 1993)

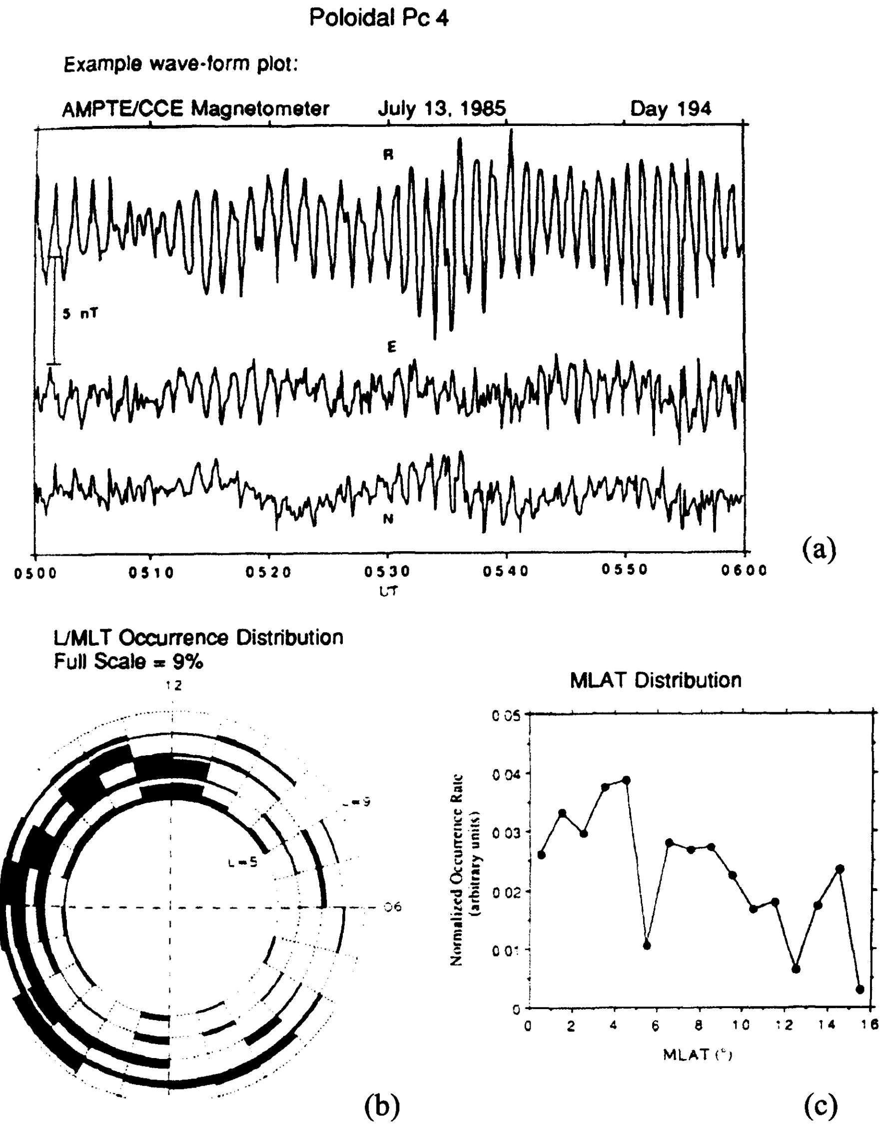

Figure 3.8 (a) Example of a typical wave form for a poloidal Pc4 wave observed by the AMPTE/CCE satellite. The wave signature is largest in the radial component R, although it is also seen in azimuthal component E (postitve eastwards) and to some extent in the compressional component, N (positive northwards). (b) the occurrence distribution for poloidal Pc4 waves between L = 5 - 9 (c) the MLAT distribution of the data. (Taken from *Anderson,* 1993)

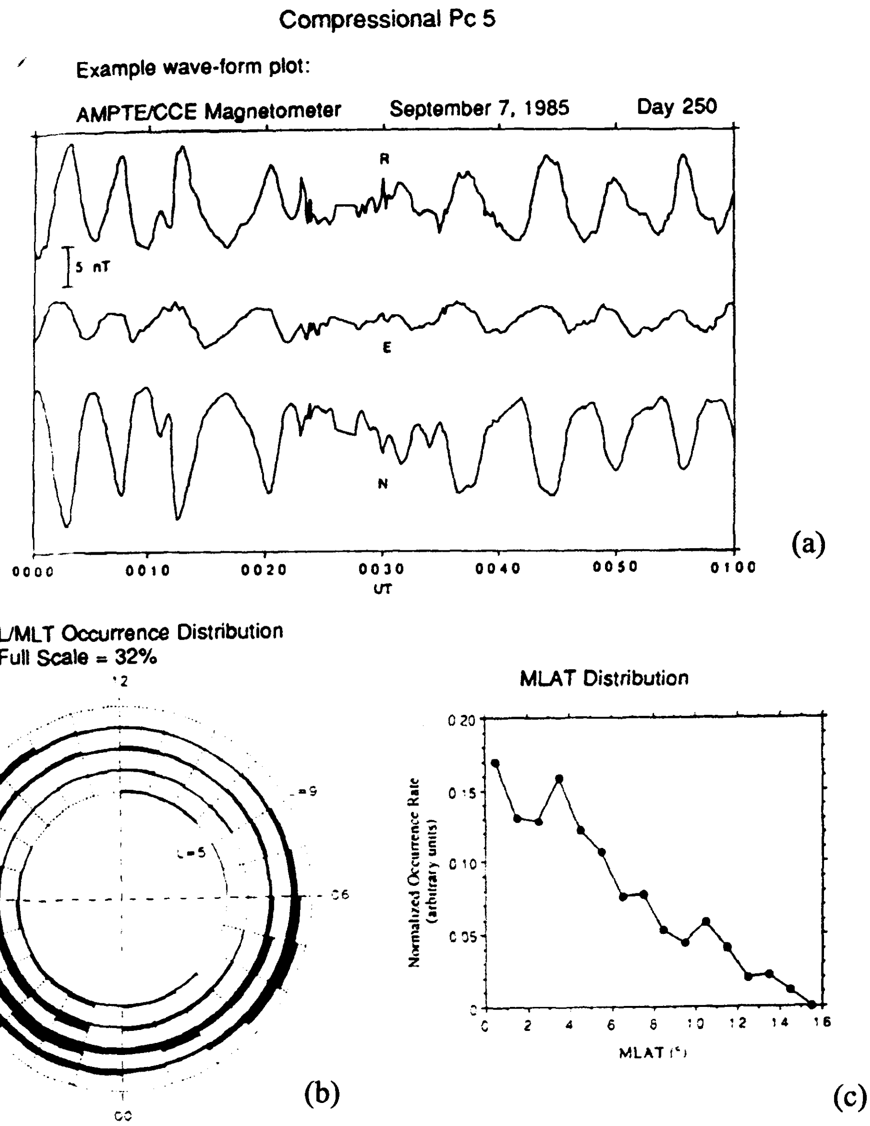

Figure 3.9. Example of compressional Pc5 wave observed by the AMPTE/CCE satellite. The wave signature is largest in both the radial component R and the field aligned component N, although it is also seen in azimuthal component E (postitve eastwards). (b) the occurrence distribution for compressional Pc5 waves between L = 5 - 9. (c) the MLAT distribution of the data, (taken from *Anderson,* 1993).

conditions with an enhanced ring current (i.e. a substorm recovery phase). This population was symmetric about noon. Both populations were westward propagating with the wave propagation characteristics closely connected with the ion magnetic gradient curvature drifts. In the case of the non diamagnetic population the frequency and phase of the wave varied so as to keep the azimuthal *m* number almost constant (~ -70), whereas for the diamagnetic population the wavelength was observed to vary with the frequency so as to keep the phase velocity constant. The authors concluded that the diamagnetic population was associated with substorms and are thus related to the classical storm time Pc5s. Both modes were judged to be even (anti-symmetric) mode oscillations. The authors suggested that the waves could be generated through a drift mirror interaction with either 10 keV or 200 keV protons. The distribution in both frequency and MLT of both the non-diamagnetic and diamagnetic populations are shown in figure 3.10.

Zhu and Kivelson (1991) and *Lessard et al.* (1999) have also identified strong populations of compressional waves on both the dawn and dusk flanks in data sets from the ISEE-1 and ISEE-2 spacecraft and the AMPTE-IRM spacecraft respectively. The spacecraft utilised for these two studies have orbital inclinations of ~ 30°, with apogee at ~ 20 R_E and perigee at ~ 1 R_E for the ISEE spacecraft and ~ 700 km for the AMPTE-IRM spacecraft. Both have similar orbital periods of ~ 50 hours.

Takahashi et al. (1987) used data from 4 satellites, (SCATHA (P78 – 2), GOES2, GOES3 and GEOS 2) to observe a Pc5 pulsation which lasted ~ 50 hours and was observed over the entire dayside. The authors categorise this as a global Pc5 but note that it could have similar field structure to other storm time Pc5 pulsations (see section 3.5) as it was observed during a substorm recovery phase. The wave compressional component had a minimum at the magnetic equator while the transverse components had a maximum at the equator and minimum several degrees off the equator. They deduced that the wave had an anti-symmetric structure but do not suggest a precise generation mechanism.

3.4.2. Ground Based Statistical Studies

With the arrival of several high latitude radar systems such as STARE (the Scandinavian Twin Auroral Radar Experiment; *Greenwald et al.*, 1978), SABRE (the Sweden And Britain auroral Radar Experiment; *Nielsen et al.*, 1983), BARS (Bistatic Auroral Radar System; *McNamara et al.*, 1983) and CUTLASS (Co-Operative UK Twin Located

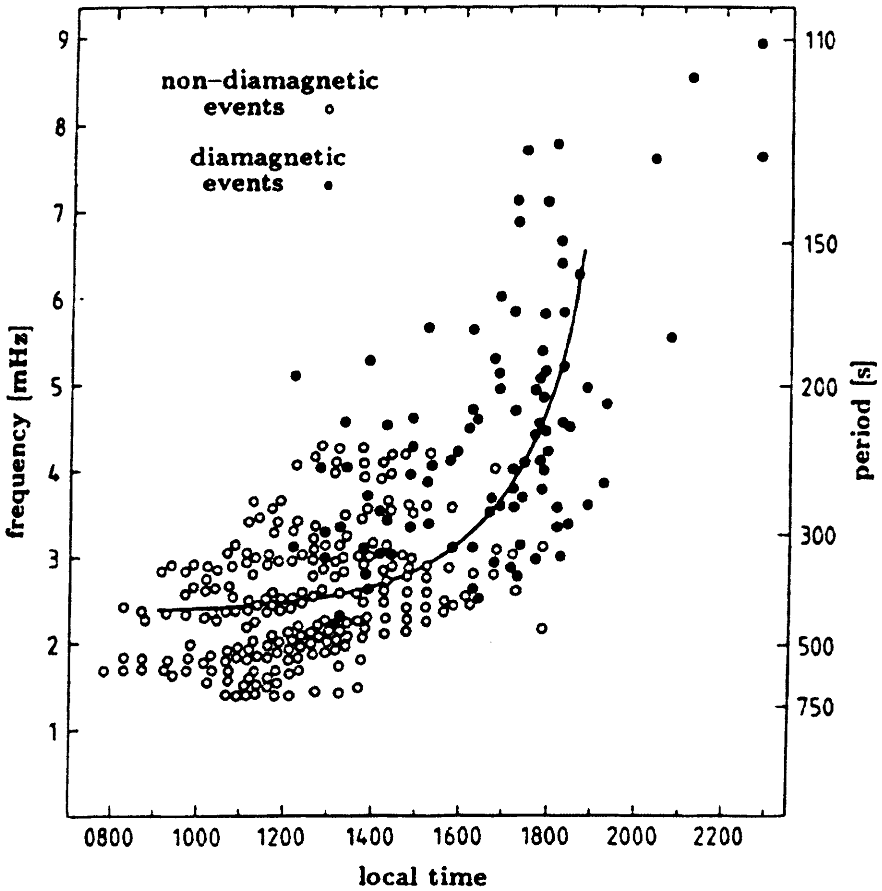

Figure 3.10. The wave frequency variation of diamagnetic and nondiamagnetic events as a function of local time, (taken from *Woch et al.*, 1990).

Auroral Sounding System, *Milan et al.*, 1997) and also the new DOPE (DOppler Pulsation experiment, *Wright et al.*, 1997) HF system, ground based studies of small scale ULF waves have become possible.

Wright et al. (1997) investigated 10 large scale ($m \sim 3 - 8$) Pc4 and Pc5 wave events observed by the DOPE HF sounder which occurred between 6 and 16 MLT with the distribution centred on 12 MLT. *Yeoman et al.* (2000) expanded this study to include data up to October 1998. In total, 79 events which displayed a conjugate ground signature were observed and 52 events, so called uncorrelated waves (UWs) which didn't. The majority (41 events) of the UWs occurred in the pre-noon sector and had a frequency range of 3 – 9 mHz. Using an expression derived by *Yeoman et al.* (1992) typical m numbers for this population of waves was calculated to be ~ -40 to -100. The distribution of these events as a function of MLT is shown in figure 3.11.

These recent ground based studies seem to suggest that there is a whole population of high m waves in the morning sector, which, due to instrument limitations, have been previously undetected. Preliminary studies, such as that of *Yeoman et al.* (2000) and *Wright et al.* (1997, 1999) indicate that these morning sector waves display characteristics resembling those of Pg pulsations, but due to their small amplitude and scale size do not possess any ground signature.

3.4.3. Case Studies of Morning Sector ULF Waves

Early satellite based statistical studies suggested that the post-noon sector was the dominant region of the magnetosphere for internally generated ULF waves however recent studies utilising ground based studies which offer far superior spatial and temporal coverage of the wave field have indicated that the pre-noon sector could be equally as active. The majority of waves identified in the pre-noon sector are toroidal Pc5 waves or poloidal Pc4 waves. The toroidal Pc5 waves are of large scale size and thus are not thought to be driven by a generation mechanism internal to the magnetosphere. As such these waves will not be discussed further. The poloidal Pc4 waves are of small scale sizes and as thus thought to be driven through a resonant interaction mechanism with the magnetospheric ring current. Many of the statistical studies outlined above do not state the exact driving mechanism, partly due to limitations on the amount of available information. A case study of a morning sector wave was presented by *Hughes and Grard* (1984). They utilised magnetic and electric field measurements from 3 spacecraft

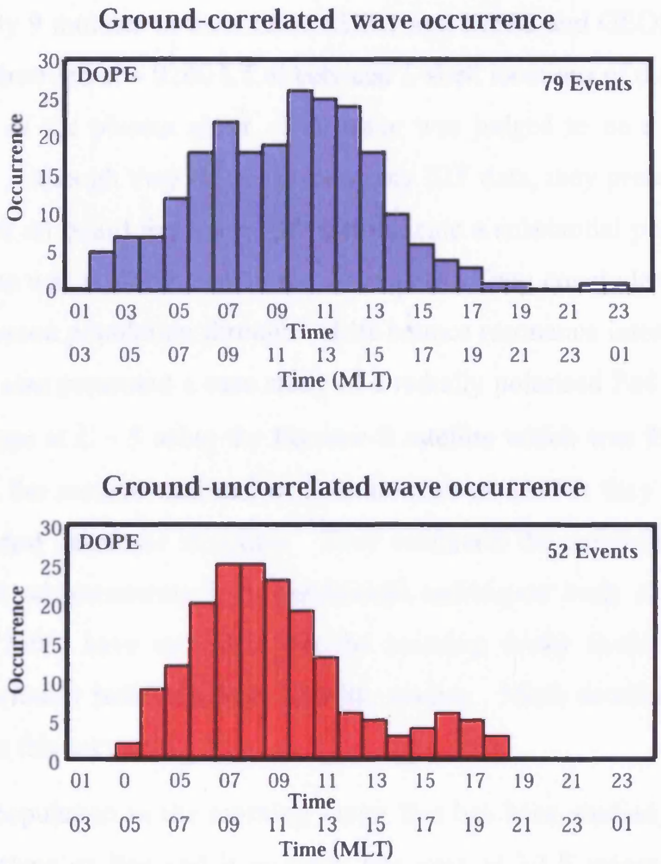

Figure 3.11. The distribution of events observed by the DOPE HF sounder as a function of MLT and UT. (a) indicates the distribution of the 79 events which possessed a conjugate ground signature. (b) indicates the distribution of the 52 events which, due to their small scale size, did not possess any conjugate ground signature, (taken from *Yeoman et al.*, 2000).

separated by only 9 minutes in their orbit; ISEE1 and ISEE2 and GEOS 1. The 11 mHz Pc4 wave was observed at ~ 0200 LT at between L-shell locations of 6 and 9, close to the inner boundary of the plasma sheet. The wave was judged to be a second harmonic standing wave. Although they do not present any IDF data, they present evidence from particle detectors on board the spacecraft that indicate a substantial population of ~ 5 to > 10 keV protons was co-located with the wave field. They conclude that the wave was driven by this proton population through a drift-bounce resonance interaction. *Cramm et al.* (2000) have also presented a case study of a radially polarised Pc4 wave observed in the morning sector at $L \sim 5$ using the Equator-S satellite which was 9° off the magnetic equator. Using the method outlined in *Takahashi et al.* (1990) they speculate that the wave has a second harmonic structure. They estimated the azimuthal m number was ~ -150. Recent advancements in observational techniques such as that outlined by *Yeoman et al.* (2000) have indicated that the morning sector could be a more fertile region than previously indicated from satellite studies. More detailed observations are clearly needed in this sector.

The Pc4 wave population in the morning sector that has been studied in the most detail are Giant Pulsations or Pgs and it possibly this area of ULF waves that thus far has received the most attention and thus the most debate. Pgs will be discussed in detail in section 3.6.

3.4.4. Case Studies of Afternoon Sector ULF Waves

The majority of statistical studies utilising ground based systems has focused on the post-noon sector. The statistical studies outlined earlier also identified the primary region of ULF wave generation as the post-noon sector, although the preliminary study of *Yeoman et al.* (2000) has indicated that new instrumentation with optimal spatial and temporal resolution such as the DOPE sounder could indicate the morning sector is equally as fertile. In this section ground based statistical studies which focus purely on the post-noon sector will be discussed.

Yeoman and Wright (2001) have previously presented a study of three waves observed in artificial induced HF radar backscatter using the CUTLASS radar which occurred in the post-noon sector. The interval studied is shown in figure 3.12. The figure shows the line-of-sight velocity plots for the (a) beam 5 of the Finland radar and (b) beam 15 of the Iceland radar. The radar fields-of-view are orientated such that the two beams overlay in

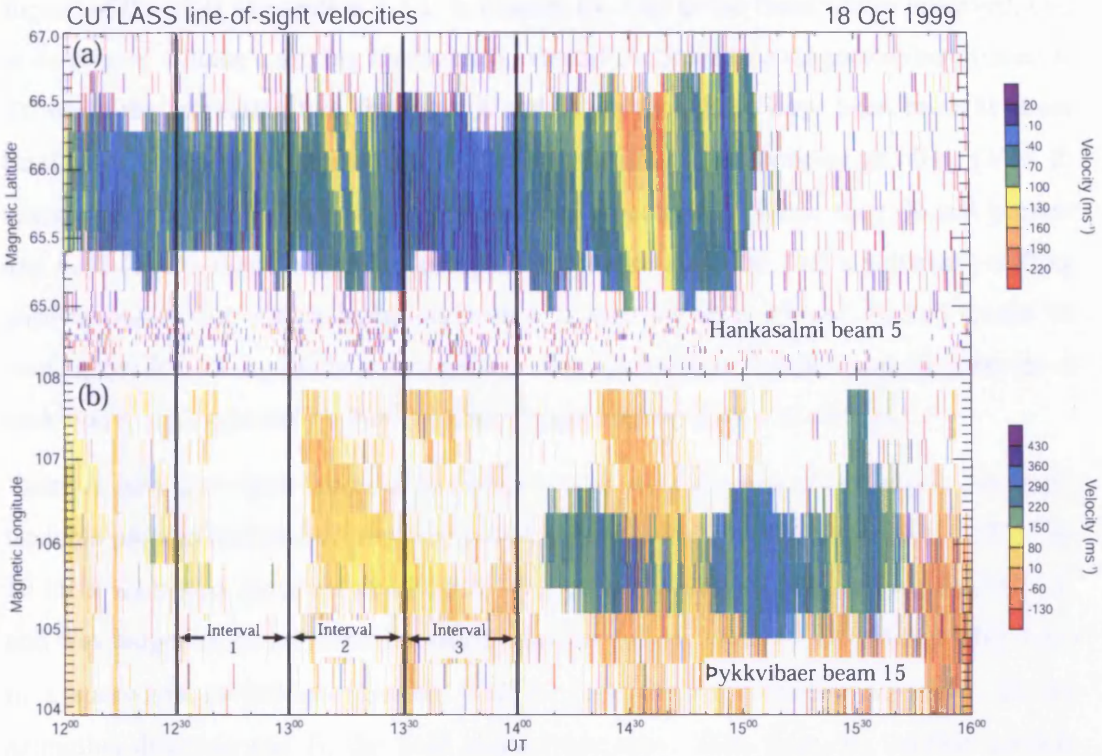

	Interval 1	Interval 2	Interval 3
Frequency (mHz)	5.7	3.8	14.3
m number	$+6 \pm 3$	-35 ± 6	-35 ± 6
Interpretation	Large-scale fundamental toroidal FLR	Fundamental poloidal drift resonance	Second harmonic drift-bounce resonance
Inferred proton energy (keV)		47 ± 10	34 ± 10

Table 3.2

Figure 3.12. Waves observed in artificially generated backscatter observed by the CUTLASS radars. The data from (a) beam 5 of the Finland radar and (b) beam 15 of the Iceland radar are shown. Three different waves are observed in the Hankasalmi data; the interval of each marked with the vertical solid black lines. The wave characterstics and hypothetical generation mechanims are listed in table 3.2. below, (taken from *Yeoman and Wright*, 2001)

the region where the irregularities are observed (for a more detailed discussion about the format of the plots see section 1.2.1. in chapter 6). Out of the three waves observed, one is concluded to have a driving mechanism external to the Earth's magnetosphere (interval 1), while the remaining two (intervals 2 and 3) are thought to have been brought about through wave-particle interactions. The mechanisms are identified as drift (N = 0) resonance and drift-bounce (N = 1) resonance respectively. While they do not present any particle data they do surmise, using the resonance equation, that a westward drifting particle population with a bump-on-the-tail located between 35 and 45 keV could be responsible for driving the later two waves. The azimuthal m numbers and frequencies of each wave, accompanied by their inferred eigenmode are shown in table 3.2.

There is only one observation of a ULF wave in the post-noon sector and a conjugate unstable particle distribution function which was presented by *Hughes et al.* (1978). The 10 mHz wave was observed at 1500 LT by three spacecraft; SMS 1, SMS 2 and ATS 6, and was judged to be a second harmonic standing mode. Figure 3.13 indicates the wave in a spacecraft co-ordinate system, with B_r indicating the radial component, B_ϕ the azimuthal direction and B_z the field aligned direction. Data from the satellite particle detectors also indicated the driving particle population, in the form of a bump on tail IDF, to be that of 10 keV protons, as shown in figure 3.14. The wave mode, frequency and driving particle energy inferred a drift-bounce resonance interaction.

Hughes et al. (1979) described multiple satellite observations of a high frequency (18.2 mHz) Pc4 compressional wave at geostationary orbit. The authors deduced that the wave was a second harmonic standing wave which led to their interpretation of the driving mechanism being a bounce resonance interaction with ring current protons. The wave number, m, was calculated to be 100.

3.5. Storm time Pc5 Pulsations

Storm time Pc5 pulsations have been seen in STARE (the Scandinavian Twin Auroral Radar Experiment; *Greenwald et al.*, 1978) data (*Allan et al.*, 1982, 1983). They are compressional waves of high m number (m = -20 – -80 and frequency in the Pc5 range (1.7 - 6.7 mHz) which are observed in the dusk sector during magnetically disturbed intervals. They have been related primarily to fundamental mode interaction mechanisms such as the drift resonance interaction (e.g. *Allan et al.*, 1983). An example of these types of waves is shown in figure 3.15 which was studied in detail by *Allan et al.* (1982).

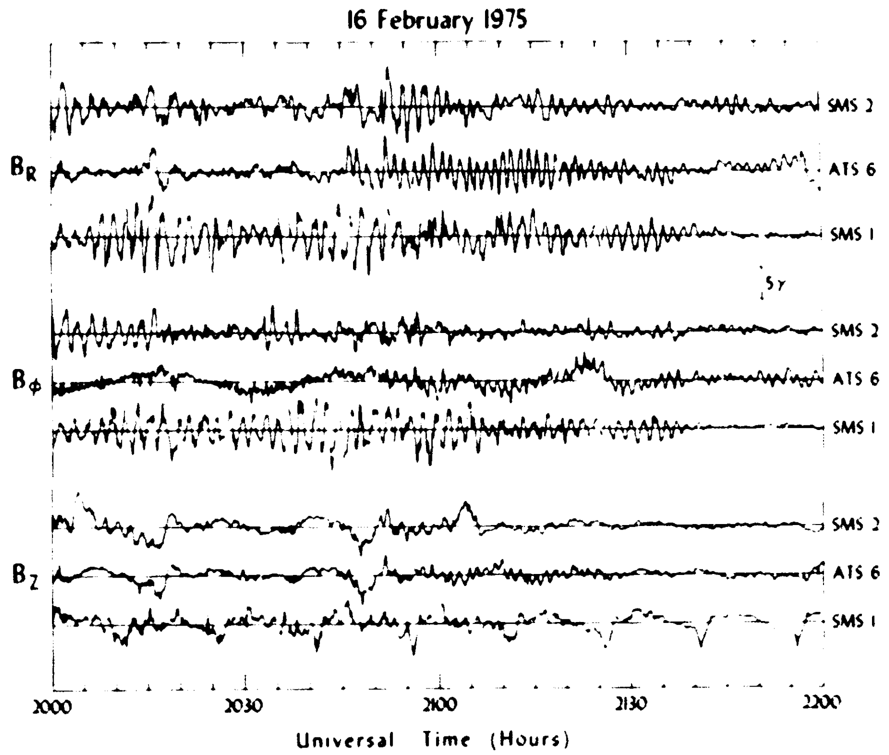

Figure 3.13. Radially polarized Pc4 waves seen in the magnetic field data from SMS 1, ATS 6 and SMS 2 at about 1500 LT. The data are presented in a spacecraft co-ordinate system, B_Z is field aligned, B_ϕ in the azimuthal direction and B_r in the radial direction. The data has been high pass filtered with a cut off at a period of 10 minutes, (taken from *Hughes*, 1978).

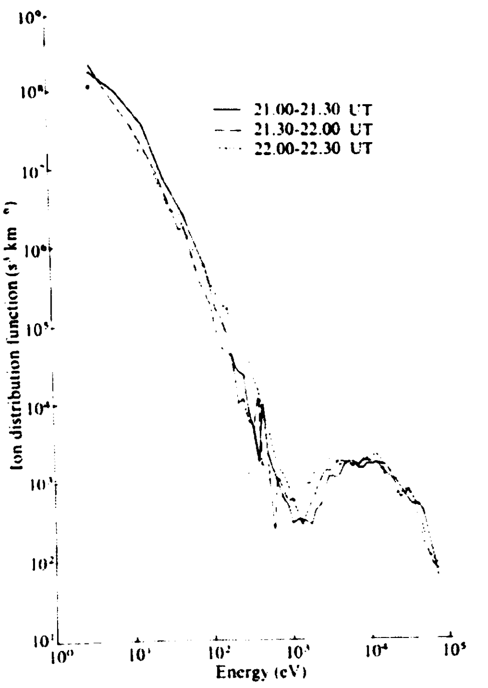

Figure 3.14. Ion velocity distribution functions measured on ATS 6 during the three half hour periods during which the oscillations are apparant in figure 3.13. The instrument cannot distinguish ion species directly, they are assumed to be protons. This is the direct evidence of generation of hydromagnetic waves through a bounce resonance interaction with a non-Maxwellian distribution function, (taken from H*ughes et al.,* 1978).

Panel (a) indicates the geographic north-south components of the **E**$\wedge$**B** drift velocity versus geographic latitude and UT. The wave signature is clearly seen from ~1115 to ~1415 UT. Panel (b) indicates the amplitude of the geographic north-south drift velocity component versus geographic longitude and UT. The northerly component is shown in green and the southerly component in red. The azimuthal *m* number varied between ~-25 and -50 to keep the azimuthal phase velocity approximately constant at a given latitude. This event was also contained in a larger dataset studies by *Kremser et al.* (1981) using the GEOS 2 satellite. The authors noted the ULF waves signatures in energetic particle flux oscillations. Most of the events occurred between 1400 and 2000 MLT.

Allan et al. (1983) also noted that the mapped equatorial velocity of the waves observed by STARE related to proton energies of 35 – 70 keV. Similar waves, but with an equatorward phase motion, have been observed by the SABRE (the Sweden And Britain auroral Radar Experiment; *Nielsen et al.*, 1983) coherent radar system in the dusk sector by *Yeoman et al.* (1992). They observed 26 events all with frequencies in the Pc5 range and with *m* numbers ranging from -5 to -36.

Yeoman et al. (1992) noted that unlike traditional storm time Pc5s which generally have only a small latitudinal phase change (< 90°, e.g. *Allan et al.*, 1983) the pulsations observed by SABRE displayed latitudinal phase changes of 180° or more. The authors also note that the STARE radar is located at higher latitudes than the SABRE radar. However, they go on to state that despite the differences in phase change magnitude between the two populations they believe the waves have similar generation mechanisms.

Equatorward propagating features have also been observed by observed in the dusk sector by *Grant et al.* (1992) using the BARS radar which is at higher latitudes than the SABRE radar. The observed waves displayed higher azimuthal *m* numbers than those measured by the SABRE radar (*m* ~ -25 to -60) suggesting a less energetic particle population. The overall picture gained from the studies which have focused purely on the afternoon sector indicates that the majority of compressional Pc5 waves are associated with recently-injected drifting particles during intervals of disturbed magnetic activity. Additionally there have been direct measurements of a particle injection associated with a storm time Pc5 wave made by the Explorer 45 satellite (*Engebretson and Cahill*, 1981).

Takahashi et al. (1990) utilised the AMPTE spacecraft to detect a radially polarised Pc5 wave located at 6.7 R_E at an MLT of 1300. The azimuthal *m* number was calculated to

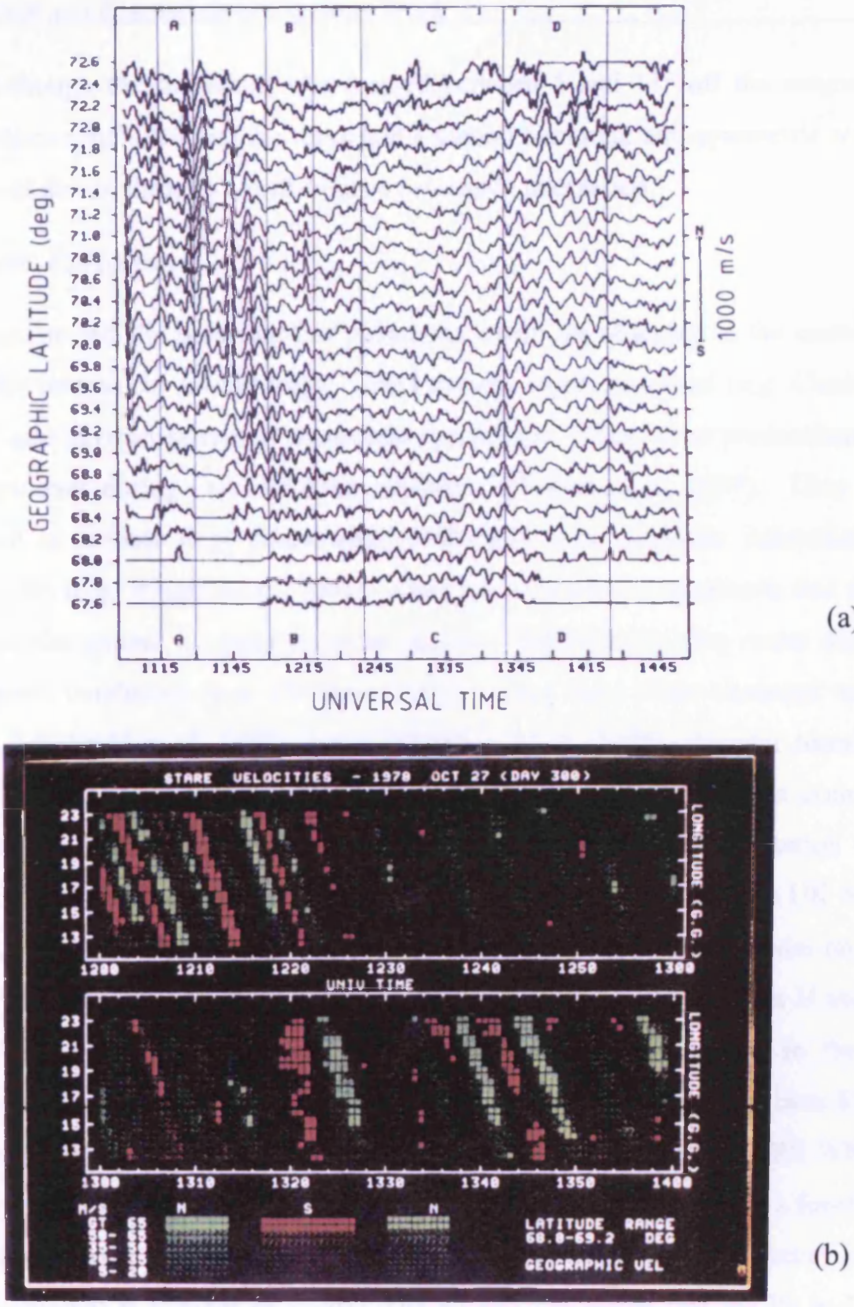

Figure 3.15. An example of a stormtime Pc5 pulsation observed in the STARE radar. Panel (a) indicates the geographic north-south components of the **E**∧**B** drift velocity versus geographic latitude and UT. The wave signature is clearly seen from ~11.15 to ~14.15. Panel (b) indicates the amplitude of the geographic north-south drift velocity component versus geographic longitude and UT. The northerly component is shown in green and the southerly component in red, (taken from *Allan et al.,* 1982).

be ~ -100. Although the spacecraft was located between 5 and 11° off the magnetic equator the authors concluded that the wave had a second harmonic anti-symmetric wave structure and was driven through a drift-bounce resonance interaction.

3.6. Giant Pulsations

Giant Pulsations are radially polarised Pc4 pulsations which are observed in the morning sector. They are unusual in several ways. They are very rarely observed (e.g. *Chisham and Orr* 1991) and have an extremely sinusoidal appearance. They occur predominantly around the equinoxes during years of solar minimum (*Brekke et al.,* 1987). They are highly localised in latitude (e.g. *Glassmeier,* 1980) and have moderate azimuthal *m* numbers (*m* ~ -30) (e.g. *Wright et al.*, 2001). They are of sufficient amplitude that they are observed on the ground by magnetometer stations. Additionally they occur during quiet geomagnetic conditions (e.g. *Chisham,* 1996). They have been observed using satellites (e.g. *Takahashi et al.*, 1992), radars (*Chisham et al.*, 1992), Doppler sounders (*Wright et al.,* 2001) and ground magnetometers (*Glassmeier et al.*, 1999). An example of a Pg detailed by *Chisham et al.* (1992) is shown in figure 3.16. The pulsation was observed by the EISCAT magnetometer cross (see chapter 4), SAMNET (the UK Sub-Auroral Magnetometer NETwork, e.g. *Yeoman et al.*, 1990) and the SABRE radar on the 29th December 1987. Figures 3.16 (a) and (b) indicate the wave signature in the H and D component of 6 ground magnetometers. The pulsation is more evident in the D component, (which is consistent with an internally driven ULF pulsation) and lasts for ~ 1.5 hours. Figure 3.17 indicates the same pulsation event observed in the SABRE WICK radar. The two panels show the line-of-sight velocity measured by the radar as a function of (a) geographic latitude and (b) geographic longitude. The wave had a frequency of 9 mHz and an azimuthal *m* number of ~ -20. The authors calculated that the Pg had an anti-symmetric eigenmode and was driven through a drift-bounce resonance interaction with ~15 keV protons from a substorm particle injection.

Takahashi et al. (1992) used data from the AMPTE/CCE spacecraft to determine the eigenmode of a Pg. They based their conclusions on the fact that an odd mode wave has node of the transverse component and an antinode of the compressional component at equator, while an even mode has the opposite. They observed a morning sector wave which had oscillations purely in the compressional component when the spacecraft was within 5° of the magnetic equator which had a conjugate ground signature. Figure 3.18

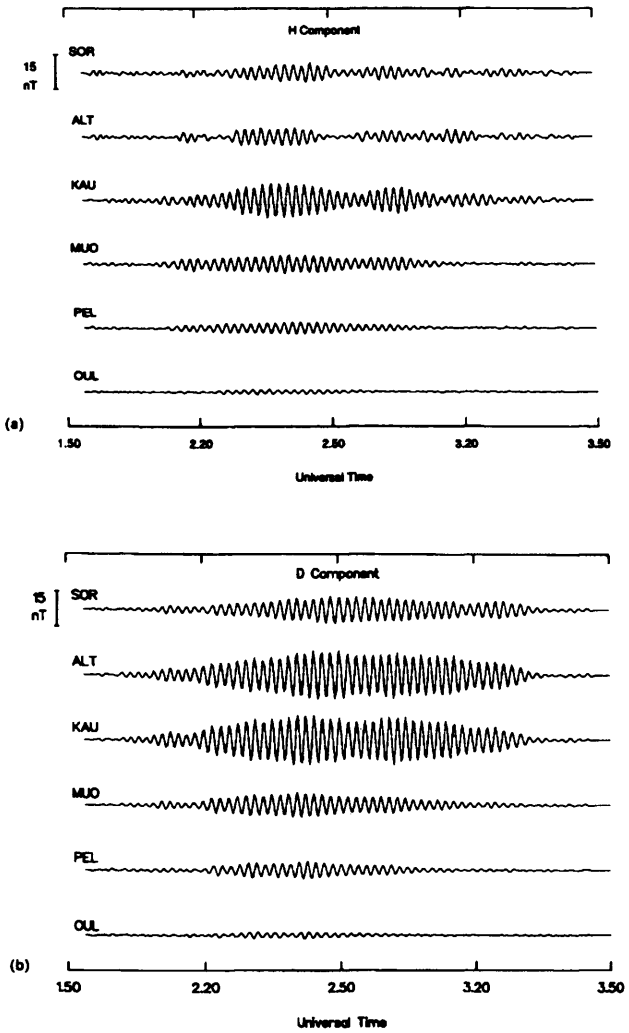

Figure 3.16. (a) The *H* component and (b) the *D* component of the Giant Pulsation event measured by the latitudinal chain of the EISCAT magnetometer cross and OUL from SAMNET. The data are filtered between 80 and 190 s (5.3 to 12.5 mHz), (taken from *Chisham et al.,* 1992).

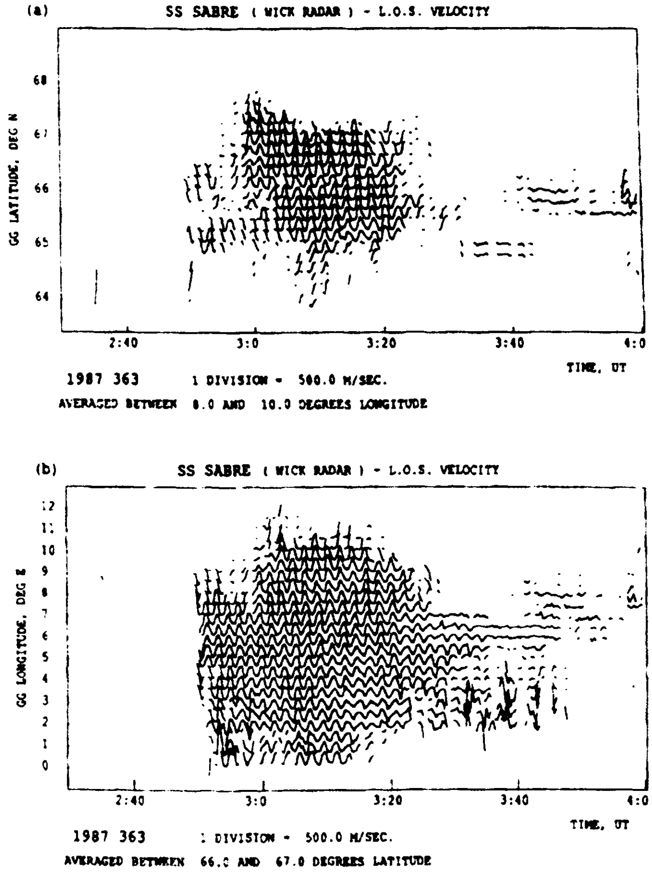

Figure 3.17. SABRE WICK radar line-of-sight velocity for the Giant Pulsation event. (a) plotted every 0.2^{o} of geographic latitude and averaged between 8^{o} and 10^{o} geographic longitude. (b) Plotted every 0.5^{o} of geographic longitude and averaged between 66^{o} and 67^{o} geographic latitude (taken from *Chisham et al.,* 1992).

indicates the data from the spacecraft (panels (a) and (b)), with B_z indicating the compressional component. Panels (c) and (d) indicate the signature in the D (Y) component at two ground magnetometer stations; one at HUS (Husafell) in Iceland and one at PEL (Pello) in Scandinavia. Using the ground magnetometer stations the azimuthal *m* number was obtained to be ~ -30. The satellite observations suggested that the Pg was an odd mode standing wave. The authors suggest that the Pg could either be a fundamental or a third harmonic eigenmode driven by either an $N = 0$ or $N = 2$ drift-bounce resonance instability respectively.

Thompson et al. (2001) utilised near conjugate observations of a Pg using magnetometers in Iceland and Antarctica to infer an odd mode standing wave structure. The authors also utilised geosynchronous proton fluxes as measured by the Los Alamos National Laboratory (LANL) spacecraft. They noted proton fluctuations in the 104-125 keV and 125-153 keV channels at a frequency identical to the Pg. They concluded that the Pg was the result of a drift resonance interaction between an odd mode standing wave and ~100 keV protons. Previous work into Pg eigenmodes by *Annexstad and Wilson* (1968) inferred an even mode structure while *Green* (1979) inferred an odd mode structure despite both using the same method. *Green* (1979) suggested the Pg was driven through the drift wave instability. *Hillebrand et al.* (1982), using the same method as *Takahashi et al.* (1992), also identified a Pg as an odd mode standing wave.

There have been only two publications which present conjugate ground based observations of a Pg and satellite observations of the driving particle population. A recent paper by *Wright et al.* (2001) reported multi-instrument observations of a Pg pulsation. The wave was detected simultaneously on the ground by the International Monitor for Auroral Geomagnetic Effects (IMAGE) magnetometer network and in the ionosphere by DOPE. Shortly before the commencement of the Pg, the particle instruments onboard the *Polar* spacecraft detected a non-Maxwellian or 'bump–on–the -tail' proton distribution drifting westward. By solving the resonance equation (equation 2.55) they conclude that the Pg is likely to be the result of a drift-bounce resonance interaction between an even mode standing wave and energetic particles of around 7keV, at the lower energy edge of the observed unstable distribution.

Controversially, a recent paper by *Glassmeier et al.* (1999) presented direct measurements of drifting non-Maxwellian particle populations made by the GEOS 2 spacecraft and ground observations from the Scandinavian Magnetometer Array in the

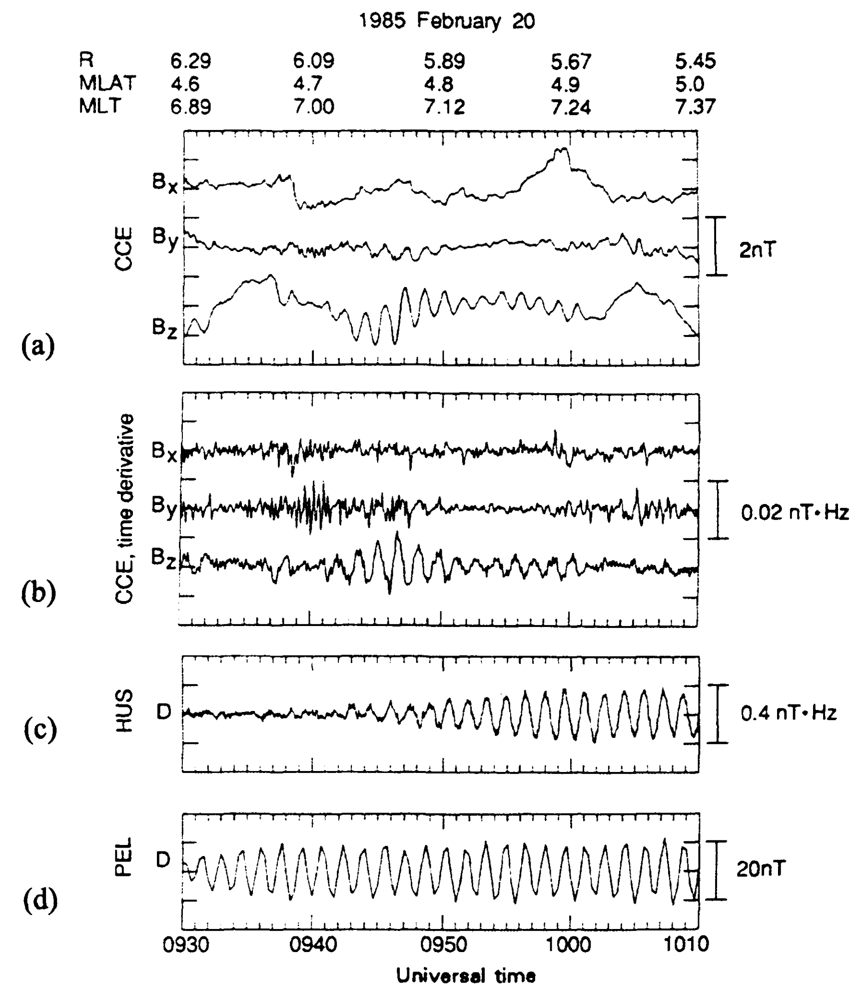

Figure 3.18. Data from the (a) and (b) AMPTE/CCE spacecraft indicating a Giant Pulsation event, with B_Z indicating the compressional component. Panels (c) and (d) indicate the signature in the *D* (Y) component at two ground magnetometer stations; one at HUS (Husafell) in Iceland and one at PEL (Pello) in Scandinavia. The location of the spaceraft is shown above panel (a), (taken from *Takahashi et al.,* 1992).

morning sector. In the paper they inferred that the resonance equation could be satisfied by a non-integer value of N if the equation was modified slightly, thus invoking an odd-mode fundamental field line oscillation interaction. The comment by *Mann and Chisham* (2000) which followed suggested that the 'real' bump on tail was located outside the energy range of the particle detector and that the Pg observed could be driven though either an interaction with 12 keV or 250 keV protons and thus be an even or odd mode standing wave respectively.

Chisham and Orr (1991) presented a statistical study of 34 of these events observed on the EISCAT magnetometer cross in northern Scandinavia. They found a peak in occurrence of these waves in the dawn / pre-noon sector while no events were observed in the afternoon. They deduced that Pgs are second harmonic (even mode) standing wave oscillations. The average value of the azimuthal wave number, m was ~ -26 for the 34 events.

Chisham (1996) has proposed an explanation of the characteristics of Pgs based upon the expected behaviour of westward drifting protons at energies 5-30 keV. In chapter 2 of this thesis the various particle motions were introduced and discussed. The two main particle drift motions in the magnetosphere are $\mathbf{E}\wedge\mathbf{B}$ drift and gradient curvature drift. The $\mathbf{E}\wedge\mathbf{B}$ drift dominates for low energy particles (< 50 keV). For higher energy particles the gradient curvature drift dominates. Particles generally lose energy as they drift to higher L shells. This accentuates the influence of the $\mathbf{E}\wedge\mathbf{B}$ drift and can lead to low energy particles leaving the magnetosphere through the dayside magnetopause. In his model *Chisham* (1996) assumed a guiding centre approximation (whereby the particle's cyclotron radius is much smaller than the scale size of the system) and a time-stationary dipolar magnetospheric **B** field. He considered results only in the dayside magnetosphere at L shell locations < 8. The model started the particle drifts from 2100 MLT with an initial pitch angle, $\alpha = 45°$ and the model ran till the particles reached 0300 MLT. The results of the simulation indicated that for the low energy particles thought to be responsible for Pg generation (< 50 keV) to reach the dawn side of the magnetosphere the magnetosphere must be geomagnetically quiet (i.e. with small convection electric fields) and there must be very little large amplitude wave activity. The model successfully explained other interesting features of Pgs, such as that they have a tendency to occur on successive days, 24 hours apart and that Pg activity is quashed during a substorm. The overall picture that emerged is that after an initial geomagnetically active period during which the driving particle population is injected onto the nightside, the magnetosphere must be geomagnetically quiet to allow the particles to drift round to the dawn side.

Since Pgs have been related to resonance interaction mechanisms with both symmetric (e.g. *Takahashi et al.*, 1992; *Thompson et al.*, 2002) and anti-symmetric (e.g. *Chisham and Orr*, 1991; *Wright et al.*, 2001) wave modes, the wave-particle interaction responsible for their generation and eigenmode thus remains controversial.

3.7. Thesis Aims

This chapter of the thesis has highlighted previous research into ULF waves and also highlighted several unanswered questions. The aim of this thesis is to provide a better understanding as to the dominance of any generation mechanism and any specific wave eigenmode. Particular attention will be paid to giant pulsations. This thesis will present two case studies and also various statistical studies utilising a new analysis method which investigates the amount of energy transferred from the driving ring current particle population, into the wave field, and ultimately into the ionosphere. Such a study has never before been undertaken and the results have suggested the dominant interaction mechanism for Pgs. This thesis will also be the first to investigate the magnetospheric ring current population using Ion Distribution Functions (IDFs) in a statistical manner, the results of which indicate the dominance of particular particle energies in different sectors of the magnetosphere. It will also present the first large scale statistical study of ULF waves measured in the ionosphere using the new multi-path DOPE system.

Chapter 4

Instrumentation and Experimental Techniques

4. Introduction

Many differing opinions still exist as to the exact wave mode of these small scale internally driven ULF waves and thus the energy requirements for the 'bump-on-tail' of any interacting particle population. The resonance equation (equation (2.55)) itself can only provide a number of particle energy requirements for any interacting particle population. It also cannot indicate whether free energy is available to the wave: i.e. it provides a necessary but not sufficient condition for wave growth. Thus, for a given azimuthal wave number m, and frequency ω_{wave}, there are a number of potential solutions, each relating to a different wave mode. Only observational evidence enables the actual wave mode and particle energy to be determined. As pointed out in section 4.1 of chapter 3, satellites traversing an active region, often at great speed, are rarely the optimal instrument to study small scale waves. Therefore, this thesis only employs satellite observations for the driving magnetospheric particle populations, and uses a multi-instrument approach to separately characterise the wave field.

When considering ground observations, such factors as limited instrumentation coverage and spatial and temporal resolution must be considered. The ground magnetic field is dominated by the effect of the E-region Hall currents. Ground magnetometers work by averaging information from an ionospheric region whose scale size is similar to the height of the E-region. This act of spatial integration introduces problems when observing high m waves (see chapter 2), which means that ground magnetometer data alone is far from optimal for this study. ULF waves are, however, more commonly observed in the E- and F- region ionosphere by VHF and HF radars respectively, where spatial resolution is better (15 – 45 km).

The most accurate method of deducing the exact generation mechanism is through conjugate radar observations of the wave in the ionosphere and satellite data of the driving particle population in the magnetosphere. This chapter introduces and explains the various instruments, both ground and space based, utilised in this study and also outlines the experimental techniques employed. Ground based radar measurements of plasma flows in the high latitude ionosphere due to ULF wave activity are made using both the CUTLASS HF (Co-Operative UK Twin Located Auroral Sounding System, *Milan et al.*, 1997) coherent radars, which are part of the SuperDARN (Super Dual Auroral Radar Network, *Greenwald et al.*, 1995) array and also the EISCAT (European Incoherent Scatter; *Rishbeth and Williams*, 1983) UHF incoherent scatter radar. The EISCAT radar can provide additional parameters e.g. the ionospheric conductivities, albeit in a limited spatial region. Additional ionospheric measurements can be made using the DOPE (the DOppler Pulsation Experiment, e.g. *Wright et al.*, 1997) HF Doppler sounder. Data from the IMAGE (International Monitor for Auroral Geomagnetic effects, *Lühr et al.*, 1994) ground magnetometer array are also utilised when available. Satellite observations are made of particle populations in the magnetosphere using the CAMMICE (Charge And Mass Magnetospheric Ion Composition Experiment) (MICS) (Magnetospheric Ion Composition Sensor; e.g. *Wilken et al.*, 1992) and TIMAS (the Toroidal Imaging Mass-Angle Spectrograph, *Shelley et al.*, 1995) instruments on board the *Polar* spacecraft.

4.1. Ground Based Instruments

4.1.1. The IMAGE Magnetometer Array

The main function of the magnetometer array in the context of this thesis is to discern whether or not any pulsations observed in the ionosphere displayed a conjugate ground signature. This allows the pulsations to be more easily identified. Large scale FLRs are toroidal mode waves with magnetic perturbations in the azimuthal direction. Due to the rotational effect of the ionosphere described in chapter 2 the largest perturbation on the ground are observed in the North - South or X component. In comparison Pgs are small scale poloidal mode waves with the magnetic oscillations contained in a meridian plane, which results in a ground magnetic perturbation dominated by the East - West or Y component. As mentioned earlier in this chapter, the majority of high *m* pulsations are undetectable by ground magnetometers due to their large spatial integration of the data. Whilst this does reduce the amount of available data for an individual event, it can also provide useful information on the wave type.

The magnetometer data utilized in this thesis is from the IMAGE magnetometer array. The array consists of 27 magnetometer stations located in northern Scandanavia. The original array of 7 magnetometers, the EISCAT cross (see figure 4.1 (a)), was erected in 1982 and

The EISCAT Magnetometer Cross

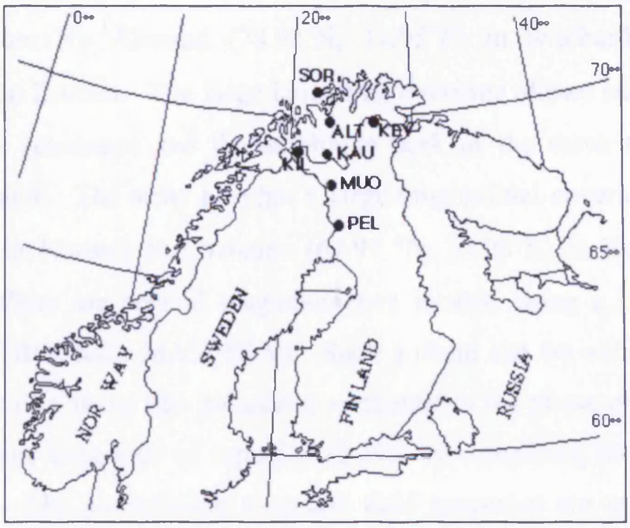

(a)

The IMAGE Magnetometer Network

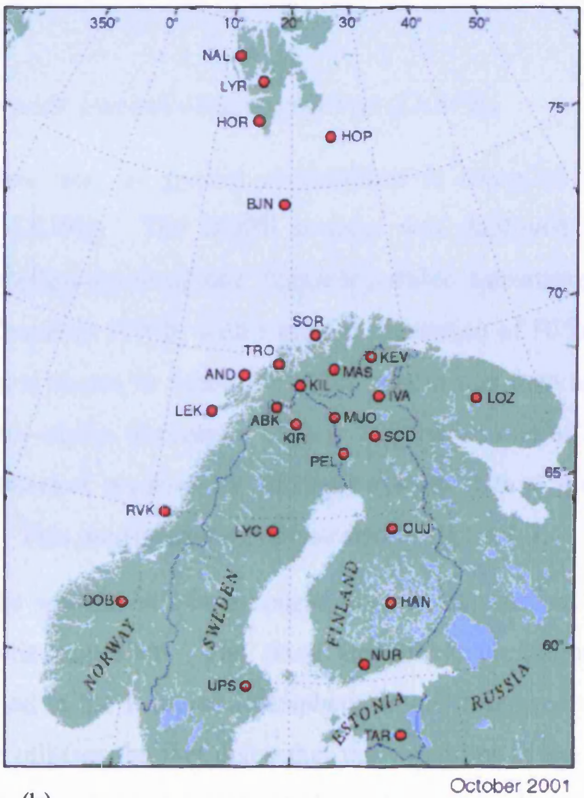

(b)

Figure 4.1. (a) The location of the magnetometers which formed the EISCAT magnetometer Cross. This system ran from 1982 - 1991 before being extended to form (b) the IMAGE magnetometer network.

this was extended in 1991 to form what is now the IMAGE array (see figure 4.1 (b)). The network extends from Ny Ålesund (78.92°N, 11.95°E) in Svalbard down to Tartu (58.26°N, 26.46°E) in Estonia. The large latitudinal coverage allows such features as the phase change across resonance and the amplitude peak of the wave to be observed if ground data is available. The array also has a large longitudinal coverage, from Dombås (62.07 °N, 9.11°E) in Norway to Lovozero (67.97 °N, 35.08°E) in Russia. IMAGE is arranged such that there are several magnetometers located along a line of ~ constant latitude (i.e. AND, TRO, KIL, MAS, KEV). Such a chain can be utilised to deduce the azimuthal m number of a wave (the parameter m quantifies the phase change of the wave per degree of magnetic longitude cf. equation (2.39)) by comparing the wave phase data from these stations. The perturbation magnetic field measured are in geographical co-ordinates: X (north), Y (east), Z (downwards) at a resolution of 0.1nT, with a sampling of 10 seconds. The Tromsø (69.66°N, 18.94°E) magnetometer in particular is utilised due to its conjugate location with the DOPE sounder, the EISCAT heater and also the CUTLASS radars.

4.1.2. The DOppler Pulsation Experiment (DOPE)

The main statistical data base of ground observations is compiled using the DOppler Pulsation Experiment (DOPE). The DOPE sounder was deployed in May 1995 near Tromsø in an initial configuration of one frequency-stable transmitter (*Chapman* 1995, 1997a) and receiver (*Chapman* 1997b) with a ground separation of 50 km. A picture of the DOPE system receivers is shown in figure 4.2. This system was then upgraded in October 1998 to a four frequency-stable transmitter (two at Seljelvnes, one at Skibotn and one at Kilpisjarvi) and four channel receiver (at Tromsø) system with a ground separation of between 40 and 90 km. This configuration is illustrated in figure 4.3.

The configuration of the sounder allows propagation of a near vertical radio path roughly aligned on the magnetic meridian. The fixed frequency, continuous wave signal is transmitted then reflected in the F-region ionosphere before being received at the ground. The Doppler technique utlilises the fact that either the variations in the refractive index or bulk motion of the plasma along the path of the radio wave cause small shifts in the received frequency due to changes in the phase path of the wave. The frequency shift is given by

Figure 4.2. A picture of the DOppler Pulsation Experiment (DOPE) receiver system located at the EISCAT radar mainland site near Tromsø, northern Norway.

DOPE Experimental Configuration 1998 ->

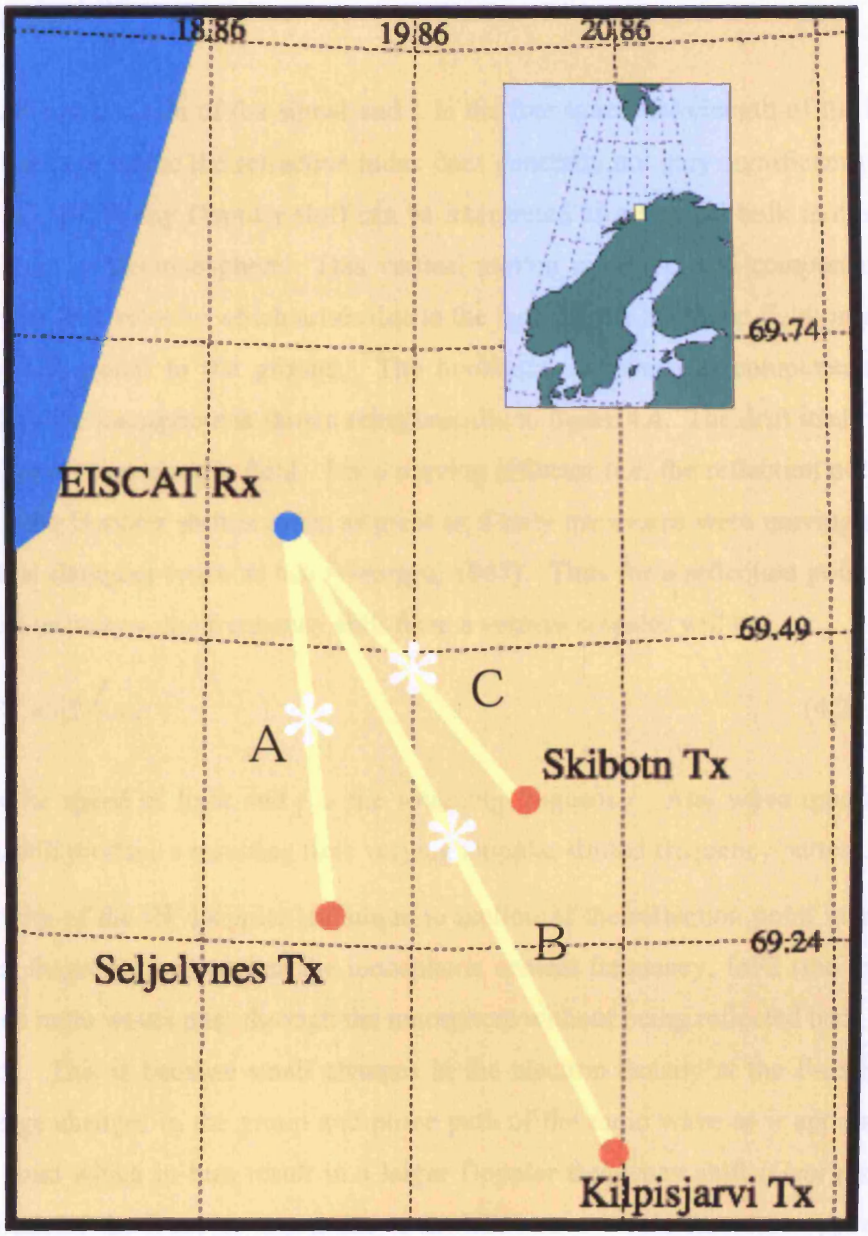

Figure 4.3. The location of the transmitters and receiver system for the DOppler Pulsation Experiment (DOPE). Two transmitters are located at Seljelvnes and one each at Kilpisjarvi and Skibotn. The approximate ionospheric reflection locations are marked by white stars on the beam paths.

$$\Delta f = -\frac{1}{\lambda}\frac{\mathrm{d}P}{\mathrm{d}t}, \tag{4.1}$$

where P is the phase path of the signal and λ is the free space wavelength of the Doppler signal. In the case where the refractive index does generally not vary significantly in time (*Wright et al.*, 1997) any Doppler shift can be interpreted as a vertical bulk motion of the reflection point in the ionosphere. This vertical motion is the vertical component of the $\mathbf{E} \wedge \mathbf{B}$ plasma drift velocity which arises due to the fact that the magnetic field lines are not completely orthogonal to the ground. The horizontal and vertical components of the $\mathbf{E} \wedge \mathbf{B}$ drift in the ionosphere is shown schematically in figure 4.4. The drift itself is due to the wave perturbation electric field. For a moving reflector (i.e. the reflection point in the ionosphere) the Doppler shift is twice as great as if only the source were moving since the path length is changing twice as fast (*Georges,* 1967). Thus for a reflection point moving with vertical velocity v, the frequency shift from a vertical sounder will be

$$\nabla f = -2\frac{f}{c}v, \tag{4.2}$$

where c is the speed of light and f is the sounding frequency. Any wave motion in the ionosphere will produce a resulting time varying Doppler shifted frequency pattern.

The sensitivity of the HF Doppler technique to motion of the reflection point increases as the sounder frequency approaches the ionospheric critical frequency, foF2 (the frequency above which radio waves pass through the ionosphere without being reflected back towards the ground). This is because small changes in the electron density at the F-region peak result in large changes in the group and phase path of the radio wave as it approaches its reflection point which in turn result in a larger Doppler frequency shift (*Georges,* 1967). The amplitude of the Doppler signal due to an ULF wave would therefore appear larger when the HF reflection point is nearer the F-region peak, which would effect the number of wave observations throughout the day (*Wright,* 1996). The spatial resolution is determined by the area over which the instrument integrates data. This is given, to a first approximation, by the region of specular reflection of the HF radio wave from the ionosphere which is equal to the area of the first Fresnel zone of the reflecting plane of the ionosphere (*Wright et al.*, 1997). A simplified relation for the radius of the first Fresnel zone which assumes an idealized mirror reflection is given by (*Georges*, 1967),

$$R = \sqrt{\lambda h}, \tag{4.3}$$

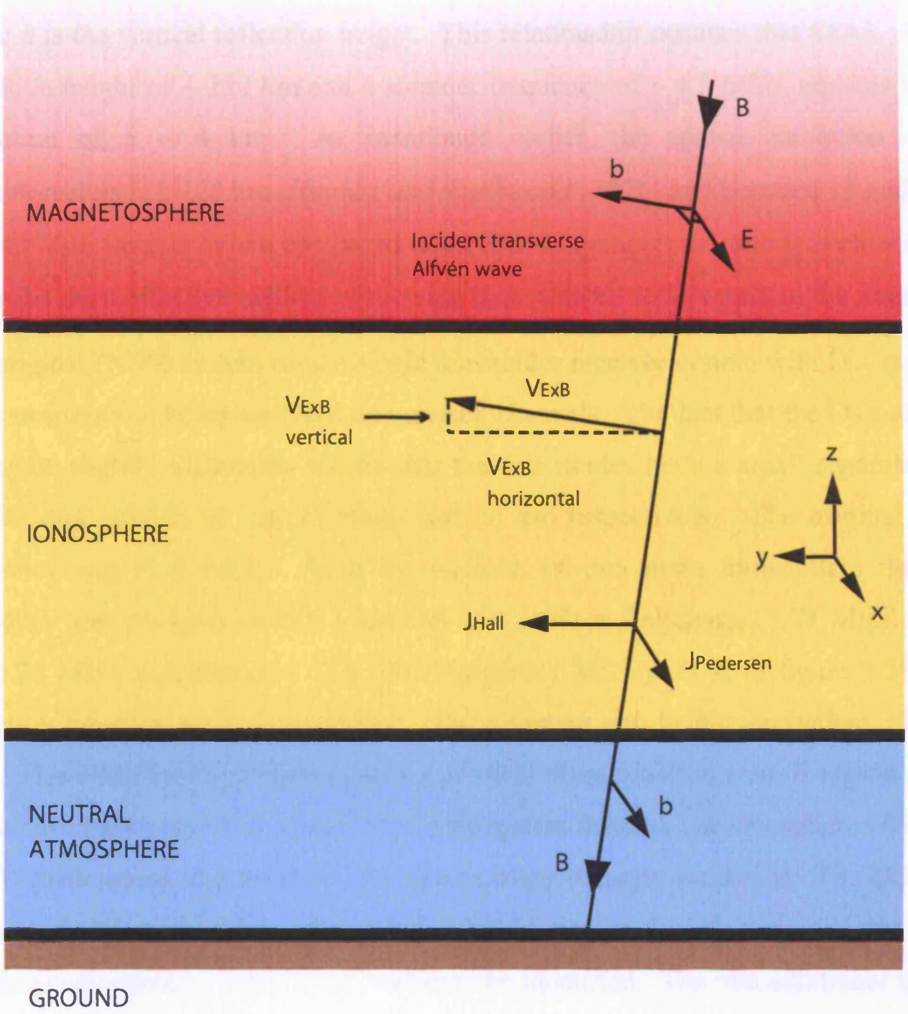

Figure 4.4. Schematic indicating the vertical and horizontal components of the **E**∧**B** drift in the ionosphere which arises due to the fact that the magnetic field lines are not completely orthogonal to the ground

where h is the vertical reflection height. This relationship assumes that $h \gg \lambda$. A F-region reflection height of ~ 250 km and a sounder frequency of ~ 4.5 MHz, equates to a spatial resolution of $R \sim 4$ km. As mentioned earlier, the spatial resolution of ground magnetometers is ≥ 120 km (*Hughes and Southwood*, 1976) and between 15 and 45 km for HF and VHF radars. When compared to the DOPE spatial resolution it is clear that DOPE offers the most effective method of viewing high m small scale waves in the ionosphere.

The original DOPE system used a single transmitter receiver system with O – mode and X-mode propagation being analysed on separate channels. The fact that the O- and X- modes propagate slightly differently means that the two modes have a small separation in both altitude and latitude of up to 50km and 20 km respectively. The original diagnostic frequency was 4.45 MHz. With the addition of two more transmitters the sounding frequency was changed to 4.16 MHz and 5.25 MHz at Seljelvnes, 5.73 MHZ at Skibotn, and 5.26 MHz at Kilpisjarvi. The dual frequency path (path A in figure 4.3) gives two reflection points separated in altitude, thus allowing any height dependent effects to be seen. This allows the elimination of any possible contamination from E-region reflections. There have been reports of sound wave propagation through the ionosphere (*Wright et al.*, 1997) which would also result in ULF waves being wrongly identified. The DOPE system has never witnessed such a phenomenon, but again the dual frequency paths allow any possible contamination from sound waves to be identified. The two additional transmitters are azimuthally spaced to allow a direct measurement of ULF wave m number in the ionosphere, (paths B and C in figure 4.3). The system parameters are listed in table 4.1. The received data are sampled at 40 Hz and passed through a filter with a cut off of 15 Hz at the 3 dB level before being passed through a Fast Fourier Transform (FFT) routine to produce a 'Doppler Trace'. The temporal resolution of the DOPE data is 12.8 s, ideal for ULF wave observations. An example of a Doppler trace is shown in figure 4.5 (a). The plots show 90 minutes of data from 11:00 UT to 12:30 UT on the 20th January 1999. The four Doppler traces clearly show the presence of a ULF wave. Figure 4.5 (b) indicates a peak trace plot for the same data. This is achieved by joining together spectral maxima for consecutive integration intervals. The peak trace thus returns a single Doppler shift value for each point in time allowing a more accurate analysis to be undertaken. By analysing the phase difference between the paths the azimuthal m number can be obtained, which is necessary for determining the wave generation mechanism.

Locations of the DOPE transmit, receive and reflection points

Site	Geographic Latitude (North) (°)	Geographic Longitude (East) (°)	Magnetic Latitude (AACGM North) (°)	Magnetic Longitude (AACGM East) (°)
Receiver Ramfjordmoen (EISCAT) (R)	69.59	19.22	66.88	104.49
Transmitter Seljelvnes (Sj)	69.25	19.43	66.52	104.34
Transmitter Skibotn (Sk)	69.35	20.37	66.57	105.15
Transmitter Kilpisjarvi (K)	69.05	20.79	66.23	105.21

Path	Path Length, km	Midpoint Latitude (Geographic North) (°)	Midpoint Longitude (Geographic East) (°)	Midpoint Latitude (AACGM North) (°)	Midpoint Longitude (AACGM East) (°)
R-Sk	52	69.47	19.80	66.73	104.83
R-K	86	69.32	20.02	66.56	104.86
R-Sj	38	69.42	19.33	66.71	104.42

Path Midpoint Pair	Separation, km	Bearing from North (°)	Azimuthal Separation (AACGM Longitude) (°)
RSk-RK	18.5	152	0.04
RSk-RSj	18.9	254	0.4
RSj-RK	29.0	112	0.44

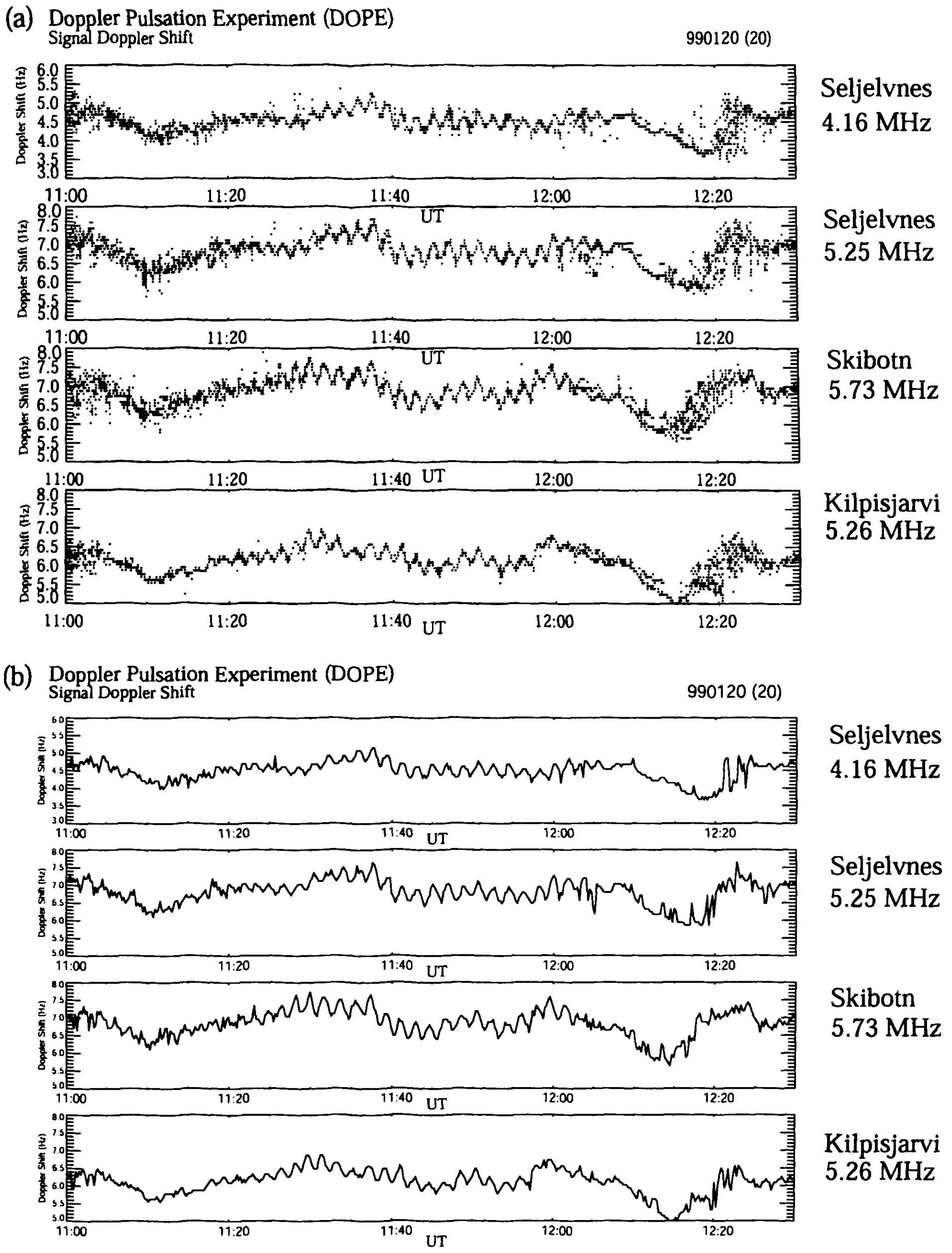

Figure 4.5. (a) An example of a doppler trace obtained using DOPE. Figure (b) indicates a peak trace plot for the same data. A high m ULF wave is clearly visible in all four traces between 11.20 and 12.10 UT. By utilising the four beam paths, the azimuthal *m* number can be obtained.

4.1.3. The CUTLASS Radars

The CUTLASS radars are located at Hankasalmi (62.3°N, 26.6°E) in Finland and Þykkvibær (63.8°N, 20.5°W) in Iceland, forming the easternmost part of the SuperDARN array and have been operational since the end of February 1995 and mid-November 1995, respectively. The radars are shown in figure 4.6. The radars comprise two arrays of log-periodic antennas, a main array of 16 antennas, able to both transmit and receive information, and an interferometer array of 4 antennas, able to receive only. The radars can operate in the HF band between 8 MHz and 20 MHz, though the usual operating frequency is close to 10 MHz. The antennas in each array are phased with relationship to one another to form an antenna pattern in which the maximum gain (beam position) has one of 16 azimuthal pointing directions separated by approximately 3.2°, distributed symmetrically about the radar boresites of −12° (i.e. west of north) and 30° (east of north) for the Finland and Iceland radars respectively. In the normal scan mode of the radars, the 16 beams are sounded with a dwell time of either 7 s or 3 s, producing field-of-view maps of backscatter, with an azimuthal coverage of over 50°, every 1 or 2 minutes. Typically, 75 range gates are sampled for each beam, with a pulse length of 300 μs, corresponding to a gate length of 45 km, and a lag to the first gate of 1200 μs (180 km). In this configuration the maximum range of the radars is approximately 3550km, with each field-of-view containing 1200 cells (*Milan et al.*, 1997). Additional scan modes are also employed to improve both spatial and temporal resolution. The data in this thesis is from a special scan mode developed for viewing ULF waves called SP-UK-OUCH (Observations of ULF waves Using CUTLASS and the Heater, *Wright and Yeoman*, 1999). The pulse scheme remains the same as normal scan mode, however the pulse length is reduced to 100 μs, corresponding to higher spatial resolution gate length of 15 km. The beam integration time can also be reduced to a minimum of 1 s, thus providing higher temporal resolution scans. The exact OUCH scan mode is described in greater detail in chapter 6.

The fields-of-view of the two radars are shown in figure 4.7. The radars measure 4 principal parameters through which investigations into the large-scale magnetospheric-ionospheric coupling can be undertaken. These are, (i) backscatter power, (ii) line-of-sight velocity of scattering irregularities, (iii) spectral width imposed on the spectra and (iv) the altitude of the irregularities via the angle of arrival of the received HF rays.

(a)

(b)

Figure 4.6. Pictures of the CUTLASS (Co-operative UK Twin Located Auroral Sounding System) HF radars located at (a) Hankasalmi in Finland and (b) Þykkvibær in Iceland.

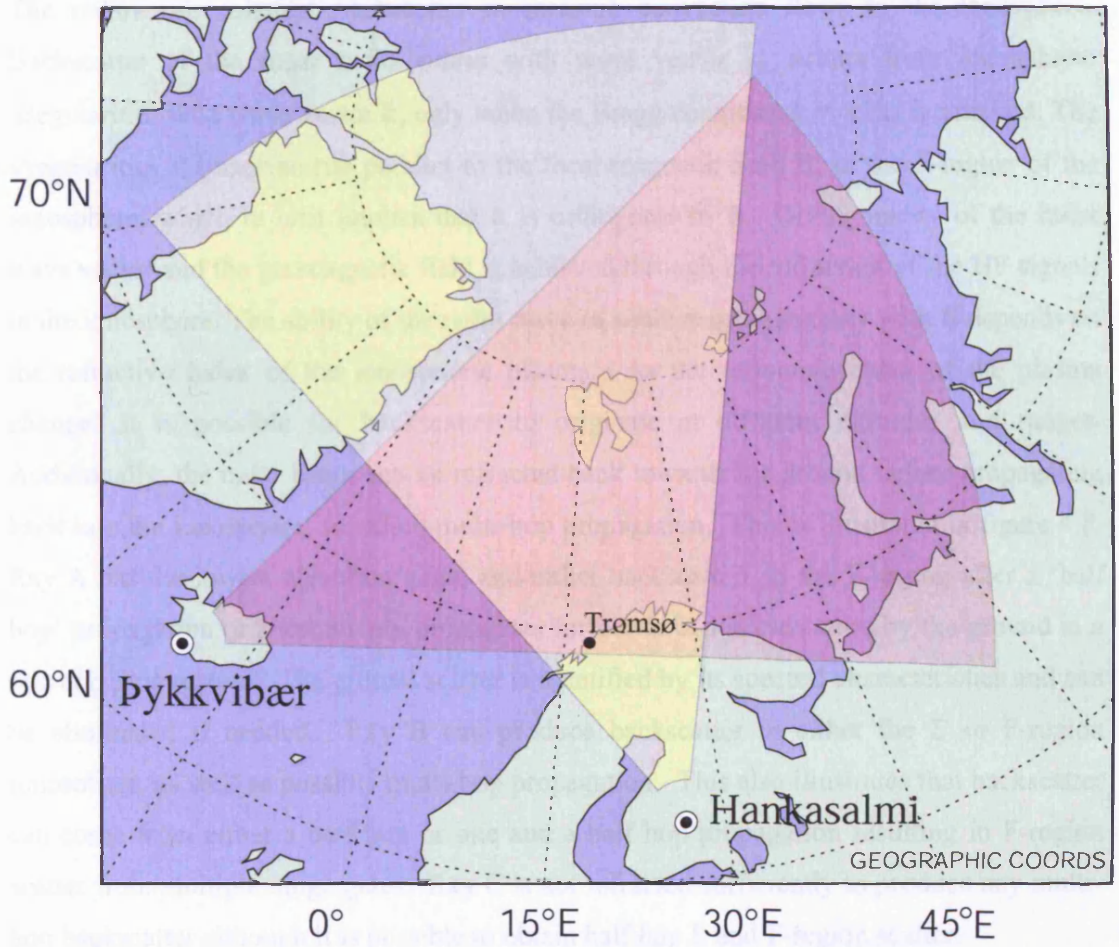

Figure 4.7. The fields of view of the CUTLASS HF radars. Tromsø is also marked on the map as it is the location of many of the other instuments utilised in this thesis (from *Wild* 2000)

The radars use coherent backscatter to measure convection flows in the ionosphere. Backscatter of the radar radio waves with wave vector $\mathbf{k_r}$, occurs from ionospheric irregularities with wave vector **k**, only when the Bragg condition $\mathbf{k} = \pm 2\mathbf{k_r}$ is satisfied. The irregularities themselves run parallel to the local magnetic field **B**, in the F-region of the ionosphere, which in turn implies that **k** is orthogonal to **B**. Orthogonality of the radar wave vector and the geomagnetic field is achieved through the refraction of the HF signals in the ionosphere. The ability of the radio wave to achieve orthogonality with **B** depends on the refractive index of the ionospheric plasma. As the refractive index of the plasma changes it is possible for backscatter to originate at different altitudes and ranges. Additionally, the radar beam can be refracted back towards the ground before propagating back into the ionosphere, so called multi-hop propagation. This is illustrated in figure 4.8. Ray A has the lowest elevation angle and either backscatters in the E-region after a 'half hop' propagation or alternatively propagates further to be backscattered by the ground in a one hop propagation. The ground scatter is identified by its spectral characteristics and can be eliminated if needed. Ray B can produce backscatter in either the E or F-region ionosphere, as well as possible multi-hop propagation. This also illustrates that backscatter can come from either a half hop or one and a half hop propagation resulting in F-region scatter from multiple range gates. Ray C is not refracted sufficiently to produce any multi-hop backscatter although it is possible to obtain half hop E and F-region scatter.

4.1.4. The EISCAT Radars

The EISCAT facility consists of three UHF (931MHz) and one VHF (224 MHz) radar systems. Two of the UHF facilities are located on the island of Svalbard in the Arctic Ocean. This thesis utilizes data from the mainland UHF system only. The UHF mainland system consists of three 32m fully steerable parabolic dishes, one which can transmit and receive, located at Tromsø and shown in figure 4.9, Norway and two receivers located at Sodankyla, Finland and Kiruna, Sweden. Although the effective radiated power is in gigawatts (10^9W), the returned signal is only picowatts (10^{-12}W) in strength and thus large high-gain antennas (typically at least 1000 m^2 in area) and sensitive receivers are necessary for the successful detection of the echoes received from the ionosphere. The 'incoherent' scatter echo is the result of the scattering of the radar signal by electrons in the ionospheric plasma, which are themselves controlled by the much slower moving ions. The received power is due to scattering from thermal electron density fluctuations caused by the

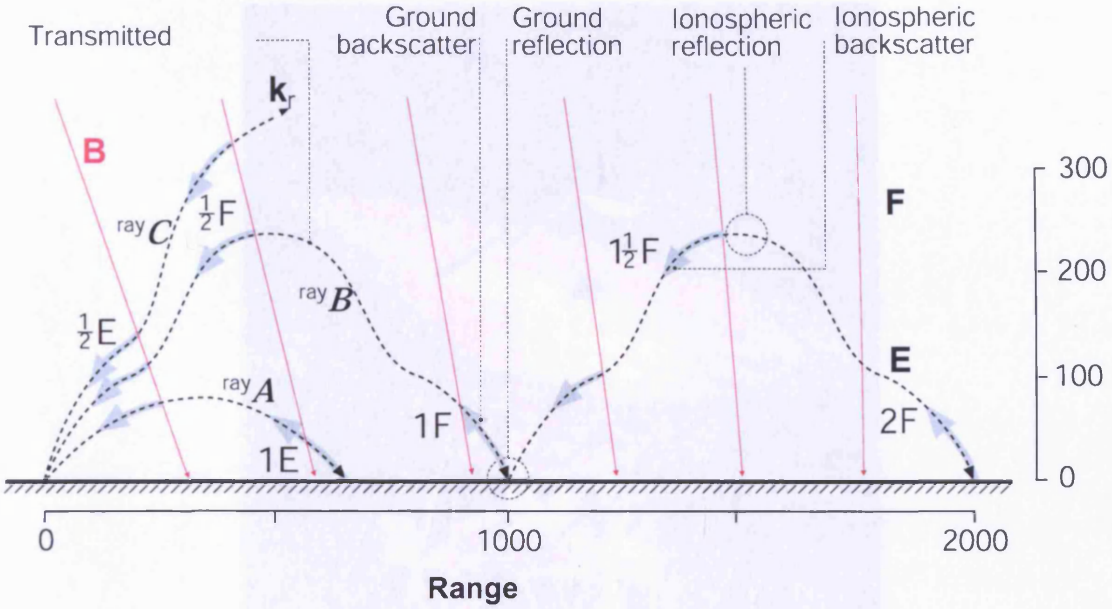

Figure 4.8. Possible propagation paths for the HF radar beams. Backscatter detected from field aligned irregularities in both the E- (ray A) and F-region (ray B) ionosphere is illustrated as well as backscatter from the ground, so called ground scatter. Ray C penetrates the ionosphere completely (from *Milan et al.*, 1997).

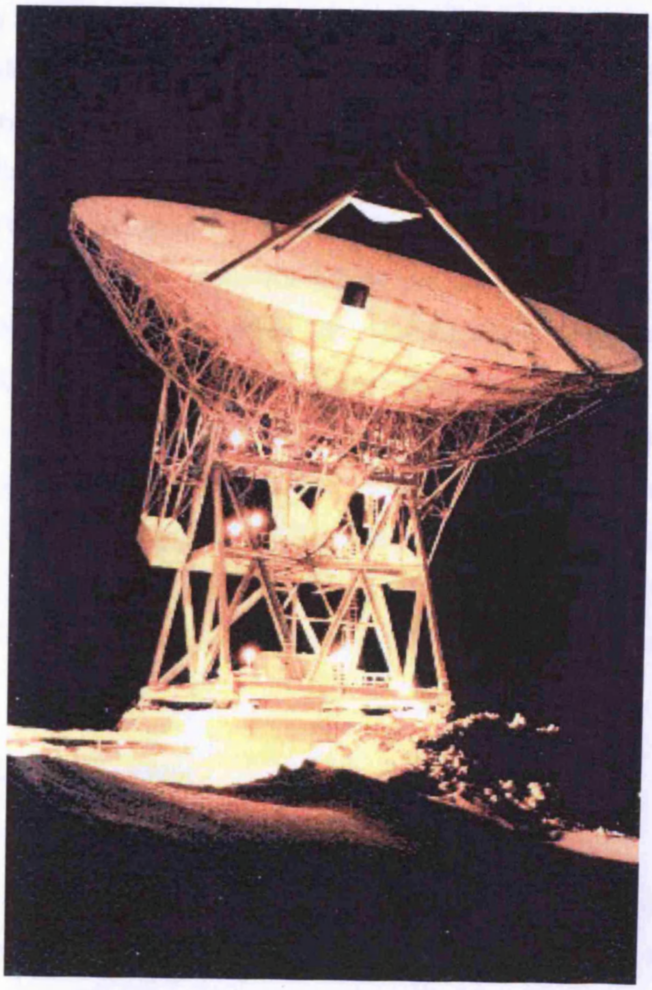

Figure 4.9. The EISCAT (European Incoherent Scatter, *Rishbeth and Williams* 1983) UHF (931MHz) radar located at Tromsø, Norway. The 32m dish is fully steerable and is capable of both transmitting and receiving.

presence of these ions and the frequency spectrum of the received signal provides information about their temperature, composition and velocity. The received signal takes the form of a double-peaked ion-line spectrum. The total returned power depends on the number of electrons and gives an estimate of the ionospheric electron density; the width of the spectrum depends on the ratio of the ion temperature to ion mass, and the overall shift of the spectrum corresponds to the bulk motion of the ions. The shape of the ion line spectrum is also a function of the ratio of the electron and ion temperatures. Besides the ion-line, the incoherent scatter spectrum also contains two weaker components; the plasma lines. These represent scattering processes where the electrons act as if the ions were absent. With suitable assumptions about the concentrations of different ions in the ionosphere, the basic parameters of electron density, electron temperature, ion temperature and ion velocity can be obtained. From these basic results, many further ionospheric and upper atmospheric parameters can be deduced. These include: ion composition, electric field strength, conductivity and current, Joule and particle heating rates and electric current density in the direction of the magnetic field. The radars can currently make measurements from about 50 km to more than 2500 km in altitude and resolve structures on scales of 100's of meters.

4.1.5. The Heater Facility

The EISCAT Heating facility located at Tromsø, Norway (*Rietveld et al.*, 1993) is capable of generating artificial field-aligned irregularities using high power HF radio waves (e.g. *Robinson*, 1989) that are detectable by both coherent and incoherent scatter radars (e.g. *Robinson et al.,* 1997). The heater consists of three antenna arrays which cover the frequency range 3.9 to 8 MHz. Figure 4.10 outlines the array configurations and also shows the location of the heater with respect to the EISCAT radars at Tromsø. Array 1 is the largest array, consisting of 12 rows of 12 antennas and scanning in the frequency range 5.5 to 8 MHz. Arrays 2 and 3 each contain 6 rows of 6 antennas covering the frequency ranges 3.9 to 5.6 MHz and 5.5 to 8 MHz respectively. The heater produces artificial electron density irregularities at the upper hybrid height in the F region ionosphere. This height is such that the plasma density is optimal for wave-wave coupling between the electromagnetic heater wave and Langmuir or electrostatic waves and irregularities are generated along the field lines which act as targets for the CUTLASS HF radar. This is shown schematically in figure 4.11 (a). The artificial targets have been demonstrated to

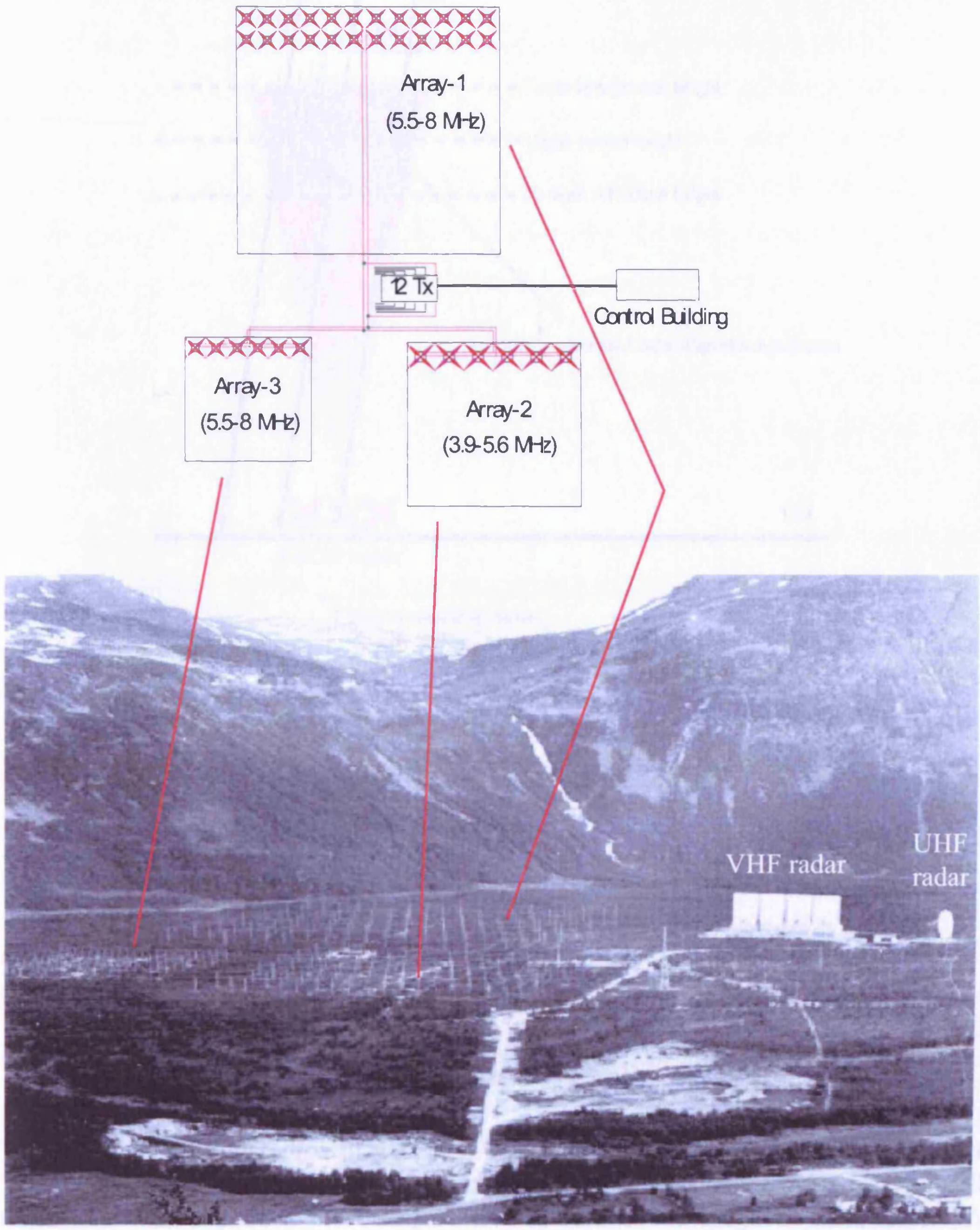

Figure 4.10. The three arrays that make up the EISCAT heating facility, with the control building also indicated. The photograph shows the heater location with respect to the EISCAT UHF and VHF radars at Tromsø.

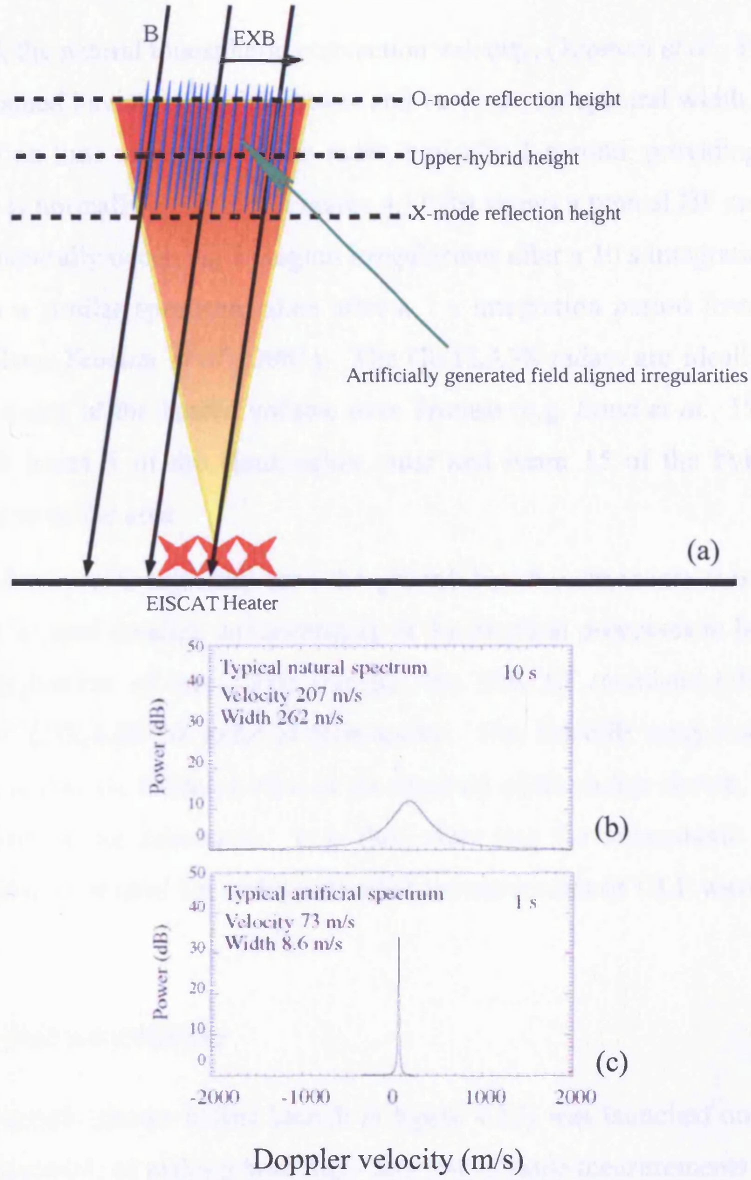

Figure 4.11. (a) An illustration of the EISCAT heater generating field aligned irregularities. The irregularities are generated at the upper-hybrid height through a wave - wave coupling process and naturally track the background ExB drift of the magnetic field lines. (b) A typical HF radar spectrum using an integration period of 10 s. (c) A similar spectrum but this time obtained from a 1 s integration from a heated F region (adapted from *Yeoman and Wright*, 2001).

accurately track the natural ionospheric convection velocity, (*Yeoman et al.*, 1997) with the backscatter obtained having very high power and very narrow spectral width. This allows a short integration time to be run on the radar, typically 1 second, providing higher time resolution than is normally available. Figures 4.11 (b) shows a typical HF radar spectrum, obtained from naturally occurring F- region irregularities after a 10 s integration period and 4.11 (c) shows a similar spectrum taken after a 1 s integration period from a heated F-region (taken from *Yeoman et al.*, 2001). The CUTLASS radars are ideally situated for making observations of the heated volume over Tromsø (e.g. *Bond et al.*, 1997; *Eglitis et al.*, 1998), with beam 5 of the Hankasalmi radar and beam 15 of the Þykkvibær radar aligning exactly over the area.

Figure 4.12 indicates schematically how the ground based instruments complement each other and allow a more detailed understanding of the physical processes to be obtained. It shows the configuration of the DOPE sounder, the EISCAT mainland UHF radars and heater, and the CUTLASS HF radar at Hankasalmi. The IMAGE magnetometer array is also co-located within the fields-of-view of the majority of the radars shown, although they are not indicated on the schematic. It is thus clear that the ionospheric region above northern Scandinavia is ideal for making detailed measurements of ULF wave processes in the ionosphere.

4.2. Satellite Instrumentation

The *Polar* spacecraft (shown before launch in figure 4.13) was launched on February 24, 1996 with the objective of making both high- and low-altitude measurements of the Earth's polar regions. The spacecraft describes a highly elliptical orbit, with apogee at 9 Earth radii (R_E), perigee at 1.8 R_E geocentric and an inclination of 86°. The orbital period is about 18 hours with a spacecraft spin period of 6 seconds. Initially apogee was over the northern polar region, but apogee has been moving towards the equator at about 18° per year. Figure 4.14 shows 6 single orbits of the spacecraft each separated by one month from February 1997 to July 1997 in solar magnetic (SM) co-ordinates. Figure 4.14 (a) indicates the precession of the orbit as viewed in the X-Y plane (i.e. looking down on the polar cap) and shows how the spacecraft can cover all MLTs. Figure 4.14 (b) and (c) indicate how the orbit processes in 6 months in the X-Z and Y-Z plane. The spacecraft's orbit is fixed with respect to the sun, and thus traverses north to south in the daytime magnetosphere during autumn and vice-versa during spring. The spacecraft spin axis is normal to the

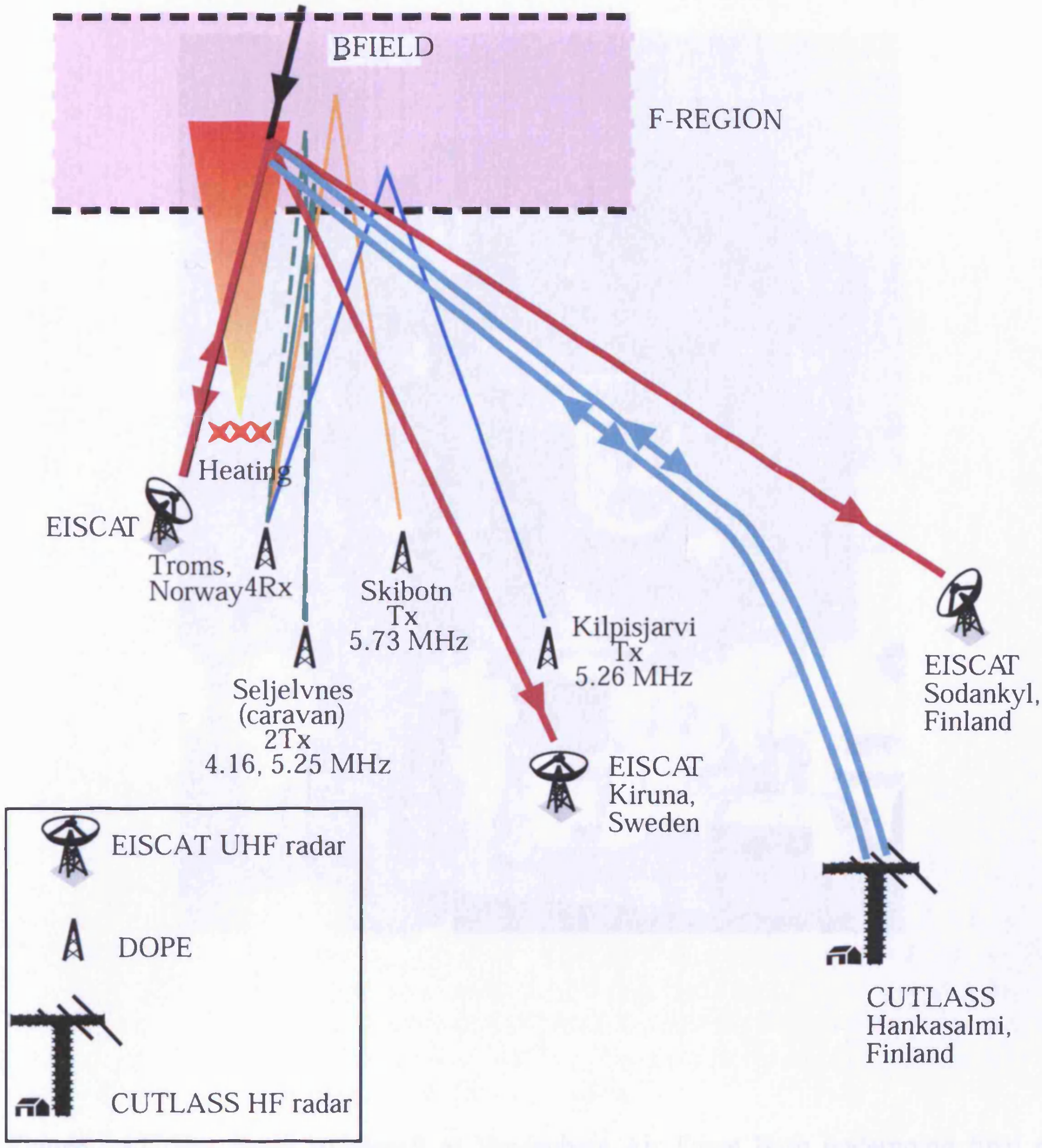

Figure 4.12. Some of the ground based instrumentation utilised in this thesis. The diagram indicates the EISCAT heater and UHF radars, the DOPE system and also the CUTLASS Finland HF radar. In addition to these instuments there are also conjugate ground magnetometers from the IMAGE network. The fantastic overlap in instrument coverage makes Scandanavia an ideal location for studying ULF waves.

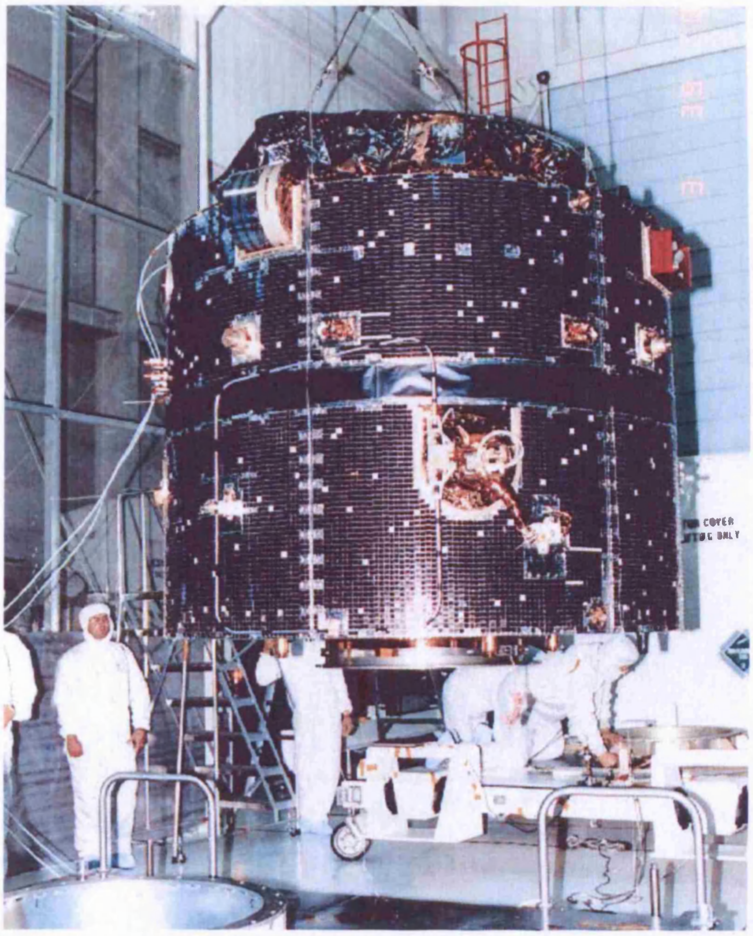

Figure 4.13. The *Polar* spacecraft at Vandenberg Air Force Base undergoing final pre-launch testing.

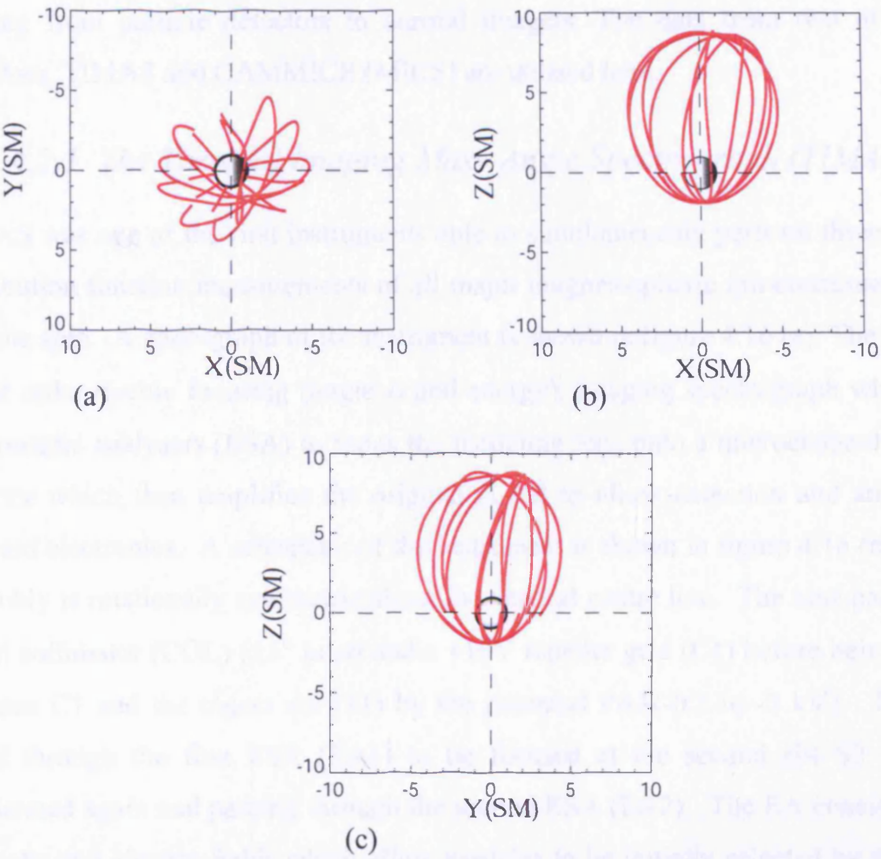

Figure 4.14. Six single orbits of the *Polar* spacecraft each separated by one month from February 1997 to July 1997 in solar magnetic (SM) co-ordinates. Figure (a) indicates the precession of the orbit as viewed in the X-Y plane (i.e. looking down on the polar cap) and shows how the spacecraft can cover all MLTs. Figures 4.13 (b) and (c) indicate how the orbit processes in 6 months in the X-Z and Y-Z plane.

orbital plane to allow a despun platform for the auroral imagers and to enable the particle instruments to map out the full 4π steradian distribution functions. In total, *Polar* contains 12 instrument sets consisting of 27 separate sensors, (shown schematically in figure 4.15) ranging from particle detectors to auroral imagers. The data from two of the particle detectors, TIMAS and CAMMICE (MICS) are utilised here.

4.2.1. The Toroidal Imaging Mass-Angle Spectrograph (TIMAS)

TIMAS was one of the first instruments able to simultaneously perform three-dimensional distribution function measurements of all major magnetospheric ion constituents twice per satellite spin. A photograph of the instrument is shown in figure 4.16 (a). The instrument is a first order double focusing (angle α and energy), imaging spectrograph which uses two electrostatic analysers (ESA) to focus the incoming ions onto a microchannel plate (MCP) detector which then amplifies the original signal to allow detection and analysis by the onboard electronics. A schematic of the instrument is shown in figure 4.16 (b). The entire assembly is rotationally symmetric about the vertical centre line. The ions pass through an initial collimator (COL) ($\pm 5°$ in α) and a +10V repeller grid (C1) before being accelerated between C1 and the object slit (S1) by the potential PA1(-0.2 to -3 kV). The ions then travel through the first ESA (EA1) to be focused at the second slit S2 before being accelerated again and passing through the second ESA (EA2). The EA consists of crossed magnetic and electric fields which allow particles to be initially selected by their velocity. The centripetal force experienced by the ions must balance the Lorentz force exerted by the magnetic field (strength B, radius r) for it to be focussed onto the double focussing point. This allows particles of a given mass to charge ratio (m/q), or energy to be selected. A post acceleration potential U is then applied between the ESA and the detector system to improve the sensitivity of the instrument for low energy particles. The detected particle energy, E is then $E = E_0 + Uq = q(E_0/q + U)$, where E_0 is the incident particle energy. Mass per charge is dispersed radially on an annular microchannel plate detector and the azimuthal position on the detector is a map of the instantaneous 360° field of view. The 3-D ion distributions are measured with approximately 11° angular resolution over the energy per charge range from 15 eV/q to 32 keV/q which is covered in 28 steps. Each energy step is sampled for approximately 20 ms; 14 step (odd or even numbered) energy sweeps are completed 16 times per spin (every 6 seconds).

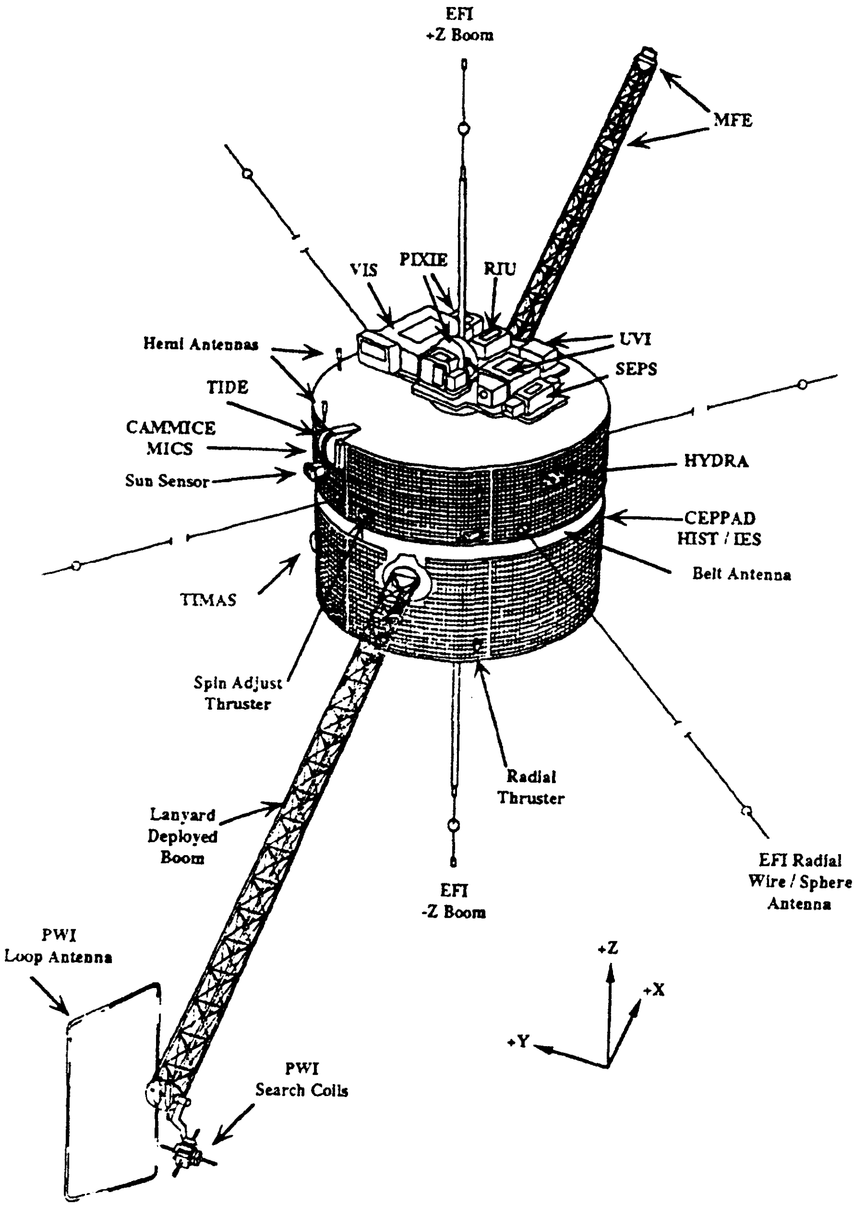

Figure 4.15. The *Polar* spacecraft contains 12 instrument sets consisting of 27 separate sensors, ranging from particle detectors to auroral images . The data from two of the particle detectors, TIMAS and CAMMICE are utilised in this thesis.

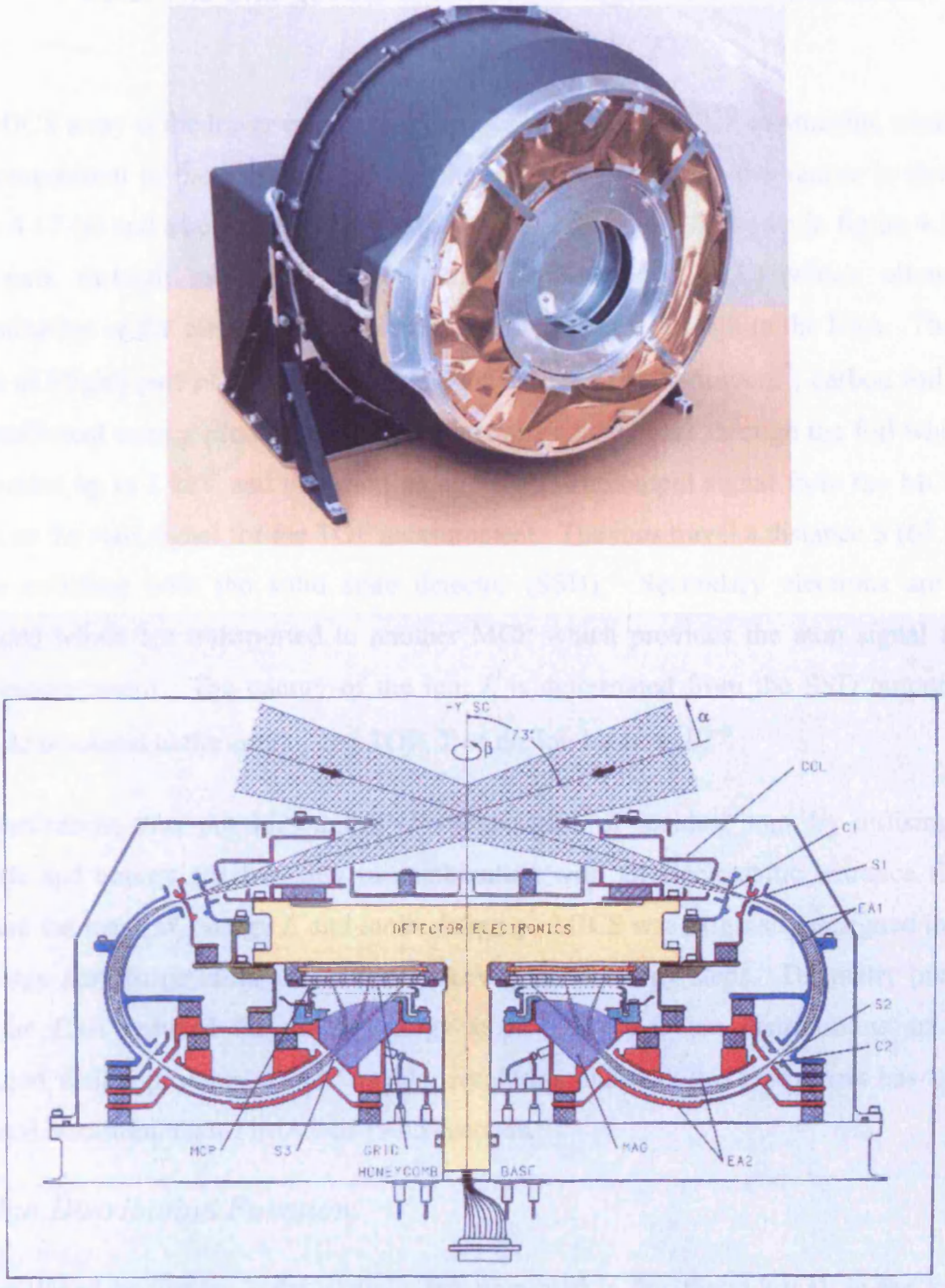

Figure 1

Figure 4.16. (a) A photograph of the TIMAS instrument. (b) A schematic of the instrument. The entire assembly is rotationally symmetric about the vertical centre line.

4.2.2. The Charge And Mass Magnetospheric Ion Composition Experiment (CAMMICE)

The MICS array is the lower energy range sensor of the CAMMICE instrument, measuring ion composition in the 1 to 425 keV/q range. A photograph of the sensor is shown in figure 4.17 (a) and a schematic of the MICS detector assembly is shown in figure 4.17 (b). Ions pass through an initial narrow angle collimator (COLL) which allows the determination of the pitch angle distribution before passing through to the ESA. The TOF (Time of Flight) part of the instrument is shielded by a thin (~5μg/cm^2) carbon foil. Ions with sufficient energy produce secondary electrons as they pass through the foil which are accelerated up to 1 keV and collected on an MCP. The output signal from the MCP then serves as the start signal for the TOF measurement. The ions travel a distance S (63.5 mm) before colliding with the solid state detector (SSD). Secondary electrons are again produced which are transported to another MCP which provides the stop signal for the TOF measurement. The energy of the ion, E is determined from the SSD output. The mass, M is related to the energy and TOF, T of the ion by $M \propto ET^2$.

The instrument thus provides a full characterisation of incident ions by utilising TOF analysis and energy spectroscopy in combination with an electrostatic entrance filter to measure the mass M, energy E and ionic charge q. MICS was originally designed to cover an energy per charge range of 1.2 to 427 keV/q in 32 energy steps. Telemetry problems with the ESA reduced this to 24 energy steps. The 3-D ion distributions are again measured with approximately 11° angular resolution although this instrument has a larger temporal resolution than TIMAS of 197.5 seconds.

4.3. Ion Distribution Functions

As mentioned in chapter 2, the particle data presented in this thesis are all in the form of ion distribution functions (IDFs), which are a 7-D quantity which considers the number of particles in a unit of spatial volume, r^3 which are also in a unit volume of velocity space, v^3 at a particular time t, $f(\mathbf{r},\mathrm{v},t)$. The TIMAS and CAMMICE (MICS) instruments measure the particle count rate. This can be converted to a differential number flux, dn/dE if the instrument geometry and efficiency factors are known.

Differential number flux is generally given in units of $s^{-1}cm^{-2}sr^{-1}eV^{1}$ in comparison to the units of IDFs which are $km^{-6}s^3$. A detector of area dA observes a velocity space volume,

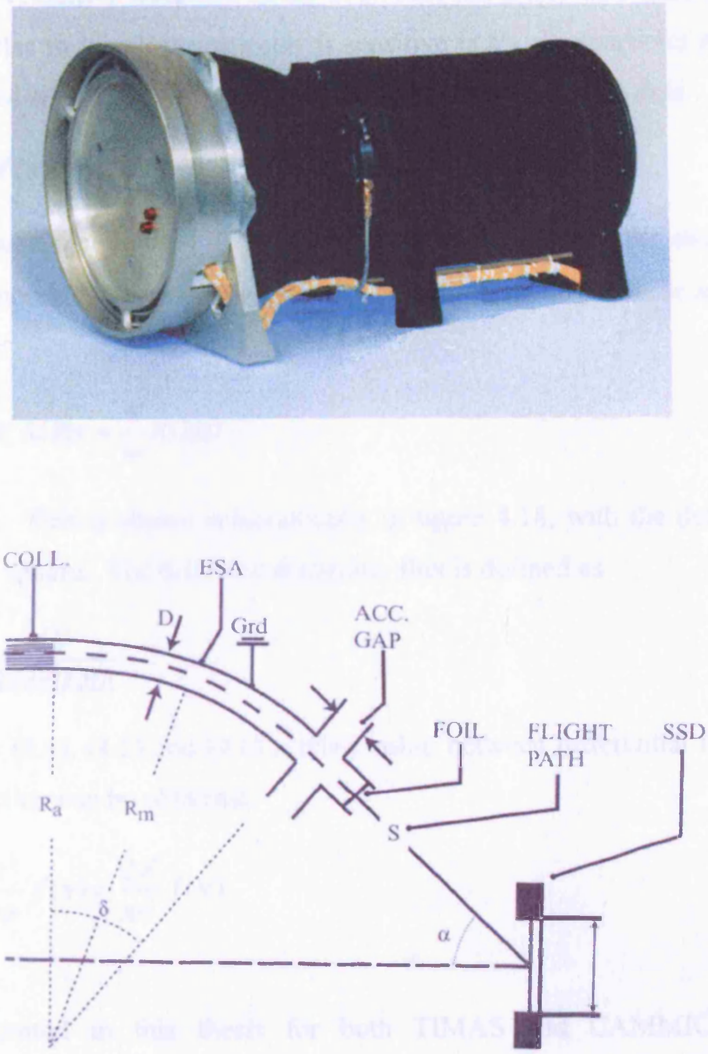

Figure 4.17. (a) A photograph of the CAMMICE (MICS) instrument. (b) A schematic of the instrument.

d^3v centred on a velocity v where the distribution function is $f(\mathrm{v})$ for a time dt. The number density of particles to which the detector is sensitive is $f(\mathrm{v})d^3\mathrm{v}$ (particles m^{-3}), the flux is $\mathrm{v}f(\mathrm{v})d^3\mathrm{v}$ (particles $\mathrm{m}^{-2}\mathrm{s}^{-1}$) and the number of particles counted in time dt is

$$\mathrm{d}N = \mathrm{v}f(\mathrm{v})\mathrm{d}^3\mathrm{v}\mathrm{d}A\mathrm{d}t. \tag{4.4}$$

If the detector sweeps out a solid angle $d\Omega$ with particles filtered in the energy passband E to $E+dE$, corresponding to velocity v to v+dv, the corresponding volume in velocity space is

$$\mathrm{d}^3\mathrm{v} = \mathrm{v}^2\mathrm{d}\Omega\mathrm{d}\mathrm{v} = \frac{\mathrm{v}}{m}\mathrm{d}\Omega\mathrm{d}E. \tag{4.5}$$

since $m\mathrm{v}\mathrm{d}\mathrm{v}=\mathrm{d}E$. This is shown schematically in figure 4.18, with the detector located at the centre of the sphere. The differential number flux is defined as

$$\frac{\mathrm{d}n}{\mathrm{d}E} = \frac{\mathrm{d}N}{\mathrm{d}A\mathrm{d}t\mathrm{d}\Omega\mathrm{d}E}. \tag{4.6}$$

Using equations (4.4), (4.5) and (4.6) a relationship between differential number flux and distribution function can be obtained,

$$\frac{\mathrm{d}n}{\mathrm{d}E} = \frac{\mathrm{v}^2}{m}f(\mathrm{v}) = \frac{2E}{m^2}f(\mathrm{v}). \tag{4.8}$$

The IDFs presented in this thesis for both TIMAS and CAMMICE (MICS) are omnidirectional in nature.

4.4. Summary

This chapter has detailed the instruments utilised in this thesis. Both ground and space based data sets are studied in the following chapters. The complementary locations of the ground based facilities means that any ULF wave structures can be studied simultaneously by a wide variety of instruments. The *Polar* spacecraft provides IDFs over the energy range of particles which could drive ULF waves through either drift or drift-bounce resonance interaction. This allows a complete study to be carried out into the possible dominance of either interaction mechanism. The precession of the *Polar* spacecraft also means that the particle populations of the magnetospheric ring current can be studied at all MLTs.

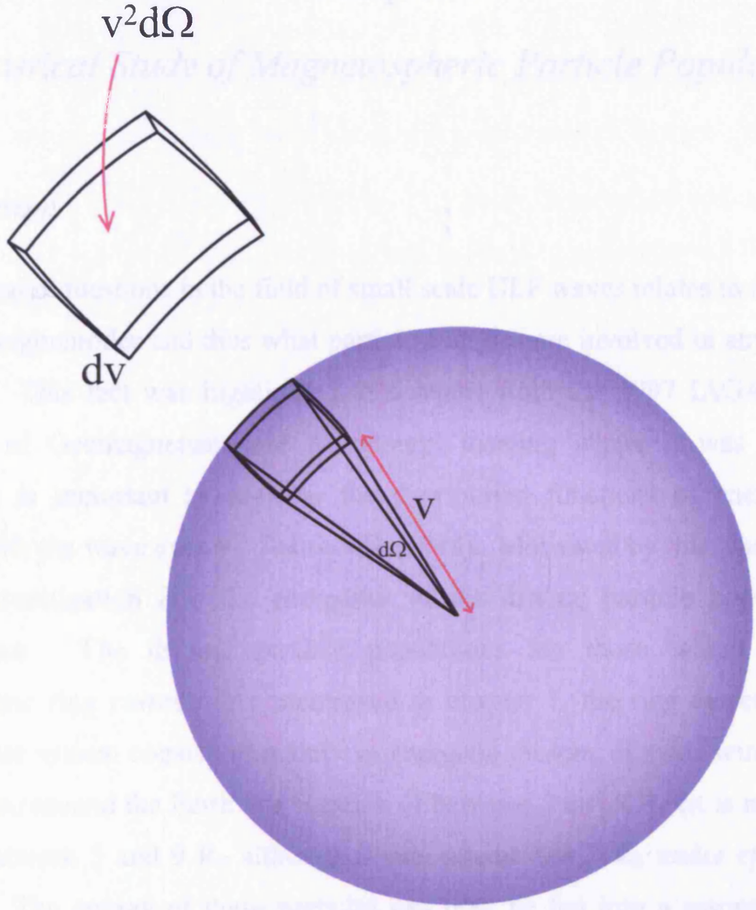

Figure 4.18. Scematic of the volume in velocity space observed by a detector which sweeps out a solid angle dΩ, with particles filtered in the velocity passband, v to v+dv.

Chapter 5

Statistical Study of Magnetospheric Particle Populations

5. Introduction

One of the major questions in the field of small scale ULF waves relates to the exact nature of the wave eigenmodes and thus what particle energies are involved in any wave-particle interactions. This fact was highlighted in a report from the 1997 IAGA (International Association of Geomagnetism and Aeronomy) meeting where it was noted that 'in particular, it is important to examine the distribution functions of energetic particles associated with the wave events', *Takahashi*, (1998). Motivated by this, chapter 5 presents a detailed investigation into the energetics of the driving particle populations in the magnetosphere. The driving particle populations are those which make up the magnetospheric ring current. As mentioned in chapter 1, the ring current is a toroidal shaped current system consisting mainly of energetic protons of solar wind origin which flow westward around the Earth at a location of between 2 and 9 R_E (it is more commonly located at between 5 and 9 R_E although it can extend into 2 R_E under extremely active conditions). The energy of these particles can then be fed into a resonant wave mode through inverse Landau damping. This chapter will present a statistical study of the driving particle populations in the ring current. Such a study has never before been undertaken and so will establish the general importance and occurrence rates of such wave-particle interactions.

The particle populations studied are all in the form of Ion Distribution Functions (IDFs). This format allows identification of any possible free energy, which manifests itself as a positive gradient region in the IDF, which could be fed into a resonant wave mode. Knowledge pertaining to the particle energies involved in any resonant interaction will place constraints on the specific wave eigenmode into which energy may be fed. Knowledge of the wave characteristics then offers an unambiguous determination of the wave-particle interaction driving the wave. This is usually only possible when conjugate wave and particle data are used in combination. If both the particle energy and amount of available free energy are known, further constraints can be added in connecting a particular driving population to a specific pulsation. As discussed in chapter 2 of this thesis, for a given wave frequency ω_{wave} and azimuthal m number there are a number of solutions, as a consequence of the resonance equation (equation 2.55), each relating to a different wave mode. These solutions reveal that in general a resonant interaction with a fundamental mode requires particles of higher energies than with a second harmonic mode.

This chapter will detail a statistical study of dayside magnetospheric particle data to discover the prevalence of these 'bump-on-tail' particle distributions which can feed free energy into a resonant wave mode.

5.1. Free Energy Calculation

To determine if a particle population induces wave growth or damping its particle distribution function f, must be analysed as a function of particle energy, W (see section 8 in chapter 2). The gradient of the particle distribution function governs the direction of energy transfer. A negative gradient, $df/dW < 0$, (see section 8 in chapter 2) implies energy will be transferred from the wave to the particles, inducing wave Landau damping, while $df/dW > 0$ implies energy may be transferred from the particles to the wave, thus inducing wave growth. This technique allows the identification of any populations that contain free energy which manifest themselves as a 'bump' or positive gradient region, $df/dW > 0$, in the IDF which elsewhere follows a monotonic power law distribution. If this occurs in a region where the particle azimuthal drift velocity is close to that of the wave azimuthal phase velocity, then free energy is available to the wave and thus wave growth may occur. Chapter 2 detailed how energy exchange occurs between the wave mode and the particles and theorized as to how much free energy was available. However, the parameters required for such a complex theoretical approach, such as knowledge of the individual particle trajectories in velocity space with respect to the overall population, are unobtainable. Thus, this chapter details a new method to obtain the approximate quantity of free energy available utilising the quantities measurable by spacecraft traversing the ring current.

The IDFs measured by both TIMAS and CAMMICE (MICS) used here are omnidirectional in nature. A particle population in a given finite velocity range (and therefore a given energy range) will occupy a volume in velocity space ($km^{-6}s^{3}$) given by

$$\mathrm{Vol_V} = \frac{4\pi}{3}(V_U{}^3 - V_L{}^3), \tag{5.1}$$

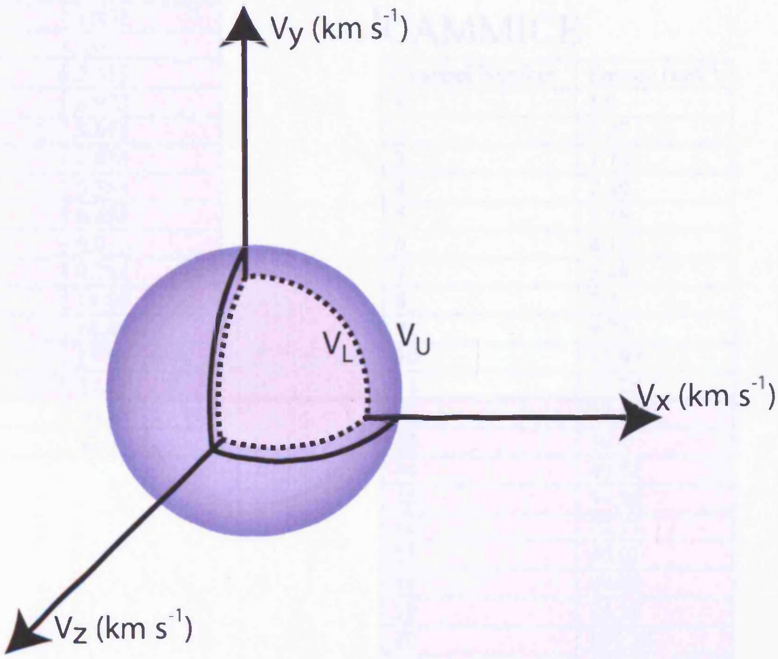

Figure 5.1. A particle population distribution in velocity space (Vx, Vy, Vz) centered on the origin. The sphere will occupy a volume defined by the particle velocities. Any spherical surface of the sphere represents particles of a constant total velocity. V_U represents the upper limit of the particle velocity in the population. V_L represents the particle velocity at a lower limit. Using these two limits, a particle population with between specific velocities and thus energies can be examined.

TIMAS

Channel Number	Energy (keV)
1	0.025
2	0.045
3	0.068
4	0.0925
5	0.125
6	0.171
7	0.2326
8	0.3162
9	0.43
10	0.5848
11	0.7953
12	1.082
13	1.471
14	2.0
15	2.438
16	2.972
17	3.623
18	4.416
19	5.384
20	6.653
21	8.0
22	9.752
23	11.89
24	14.49
25	17.67
26	21.53
27	26.25
28	32.0

CAMMICE

Channel Number	Energy (keV)
1	1.0
2	1.27
3	1.78
4	2.39
5	3.16
6	4.11
7	5.48
8	7.3
9	9.73
10	12.97
11	17.28
12	23.03
13	30.7
14	40.92
15	54.55
16	72.71
17	80.01
18	88.06
19	99.26
20	109.24
21	123.13
22	138.79
23	152.72
24	172.17
25	189.48
26	213.58
27	240.75
28	264.95
29	298.65
30	328.67
31	370.47
32	407.71
33	448.69

Table 5.1. Energy channels for the TIMAS and CAMMICE particle detectors. The study utilises TIMAS data in the energy range 1.082 to 21.53 keV and CAMMICE data in the energy range 23.03 to 328.67 keV (the channels highlighted in red).

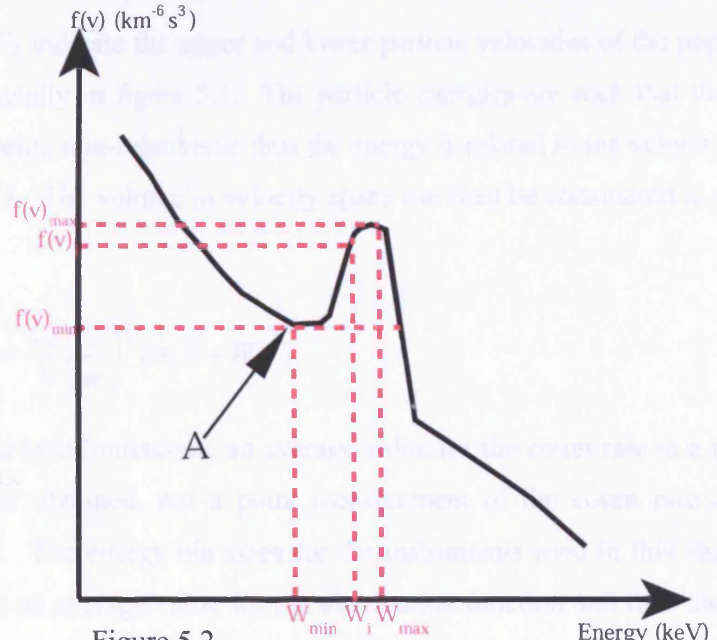

Figure 5.2

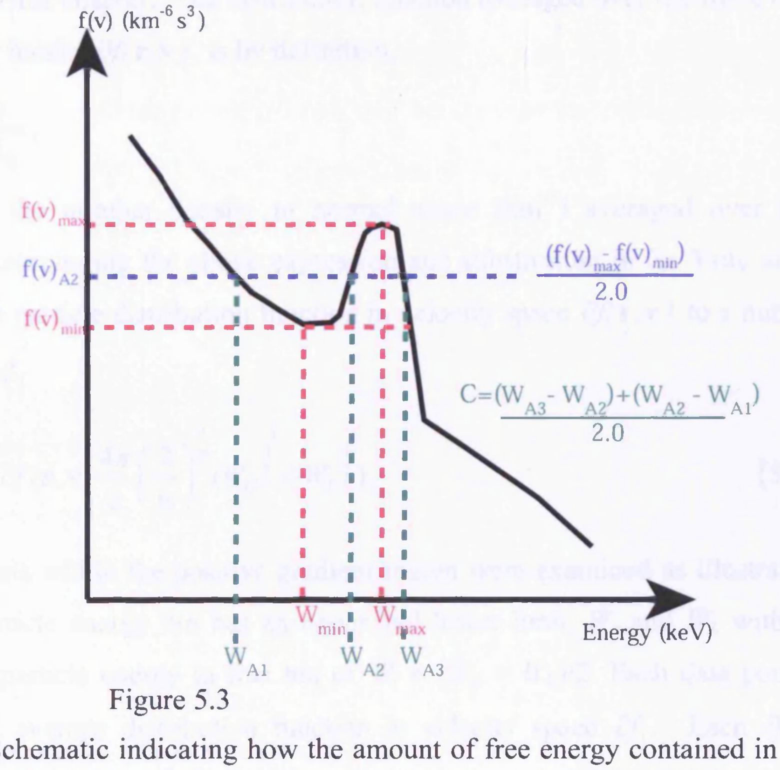

Figure 5.3

Figure 5.2. Schematic indicating how the amount of free energy contained in the 'bump' is calculated for the statistical study. The point A represents the location in phase space the particles which contain free energy are transposed to.

Figure 5.3. A more rigorous method of the calculation which transposes the particles located above $f(v)_{A2}$ by an energy amount defined by the parameter C. Although this method produced results consistent with the method outlined in figure 5.2 it also applied greater constraints on the quality of data and reduced the database considerably.

where V_U and V_L indicate the upper and lower particle velocities of the population. This is shown schematically in figure 5.1. The particle energies are such that the system can be considered as being non-relativistic thus the energy is related to the velocity of the particles using $W = mv^2/2$. The volume in velocity space can then be considered in terms of particle energy,

$$\mathrm{Vol_V} = \frac{4\pi}{3}\left(\frac{2}{m}\right)^{\frac{3}{2}}(W_U^{\frac{3}{2}} - W_L^{\frac{3}{2}}). \tag{5.2}$$

Given the instrument limitations, an average value for the count rate in a particular energy bin can only be obtained, not a point measurement of the count rate of particles of a specific energy. The energy bin sizes for the instruments used in this study are shown in table 5.1. Thus an average value for the distribution function and thus the number density of particles which occupy that finite volume of phase space is what is utilized in the calculations in this chapter. The distribution function averaged over the finite energy width of the detector bands, $\partial f(\mathbf{r},\mathbf{v})$, is by definition,

$$\partial f(\mathbf{r},\mathbf{v}) = \frac{\partial n}{\mathrm{Vol_V}},$$

where ∂n is the number density in normal space (km^{-3}) averaged over the detector badnwidth. Rearranging the above expression and substituting in for $\mathrm{Vol_V}$ an expression that relates the particle distribution function in velocity space $\partial f(\mathbf{r},\mathbf{v})$ to a number density can be obtained,

$$\partial n = \partial f(\mathbf{r},\mathbf{v})\frac{4\pi}{3}\left(\frac{2}{m}\right)^{\frac{3}{2}}(W_U^{\frac{3}{2}} - W_L^{\frac{3}{2}}). \tag{5.3}$$

Only data points within the positive gradient region were examined as illustrated in figure 5.2. Each particle energy bin has an upper and lower limit, W_u and W_L with an average value for the particle energy in that bin of $W_i = (W_u + W_L)/2$. Each data point W_i, has a corresponding average distribution function in velocity space ∂f_i. Each ∂f_i was then transformed back from velocity space to real space, to determine the average number density of particles, ∂n_i, at that particular energy. It was then assumed that all particles with free energy (i.e. in the positive gradient region) would return to some predefined minimum, (W_{min}, f_{min}) which is set by the location of the initial point of the positive gradient region in each particle distribution (marked point A on figure 5.2). This can be thought of as a conservative estimate as to the energy release needed for the population to return to a completely monotonic distribution which is given by

$$E = \sum_{i}(\partial n_i - \partial n_{min})(W_i - W_{min}). \qquad (5.4)$$

This returns an energy in units of J km^{-3}. where A is the area of dissipation in the ionosphere, typically 1° latitude by 5° of longitude for a high m wave at $L \sim 6$, By numerical integration of a dipole field an estimate can be made of the corresponding flux tube volume, V which the particle population occupies and thus the total amount of free energy available to a possible resonant wave on that flux tube can be quantified,

$$E_{total} = \mathrm{V} * \sum_{i}(\partial n_i - \partial n_{min})(W_i - W_{min}). \qquad (5.5)$$

The flux tube volume calculation utilised an ionospheric flux tube footprint area of 1° latitude by 5° of longitude, which is a typical spatial extent when considering high m wave at $L \sim 6$ (e.g. *Chisham*, 1996; *Yeoman et al.* 2001) and a co-latitudinal extent of ± 30°.
An alternative method which utilizes a different W_{min} and ∂n_{A2} was also examined as shown in figure 5.3. In this case the point ∂n_{A2} was defined as the halfway point between the start and end of the positive gradient region, $\partial n_{A2} = (\partial n_{max} + \partial n_{min})/2$. Instead of transporting the particles to a predefined minimum point as in equation (5.5) the particles were shifted in energy by an amount C which is defined in figure 5.3. The method examined the total number of particles above this new minimum ∂n_{A2} and how much energy would be released if they were moved to a lower energy state determined by the new corresponding formula,

$$E_{total} = \mathrm{V} * \sum_{i}(\partial n_i - \partial n_{A2})(W_i - C). \qquad (5.6)$$

However, this method applied greater constraints on the quality of data and reduced the database considerably. Nevertheless, the results obtained from this more rigorous alternative method were consistent with the results using the original method giving confidence in the original approximations.

This process of IDF 'energy draining' out of the positive gradient region has been reported in a paper by *Wright et al.* (2001) in which a Pg pulsation is observed simultaneously on the ground by the IMAGE magnetometer network and in the ionosphere by DOPE. Conjugate observations taken by both the CAMMICE (MICS) and TIMAS instruments onboard *Polar* revealed a driving particle population with a positive gradient region at the

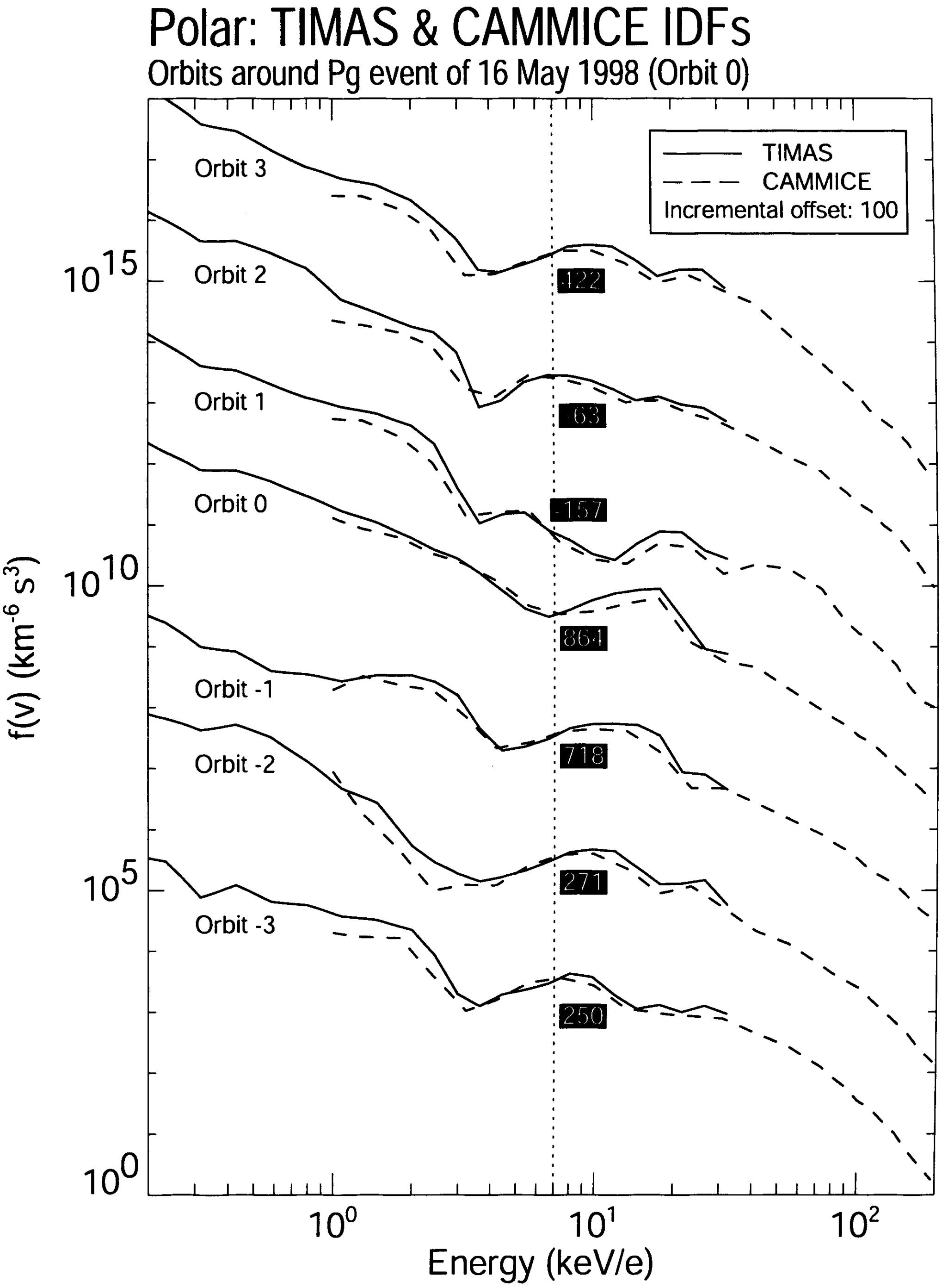

Figure 5.4. Taken from *Wright et al.*, (2001). IDFs derived from the TIMAS and CAMMICE (MICS) instrument on seven sequential orbits of the *Polar* spacecraft. The IDFs were derived over MLTs and L shells in the ranges 0930-1000 hours and 6.5 - 8.5 respectively. The vertical dotted line marks 7 keV, the energy of the interacting particles. The values given in the black boxes indicate the gradient of each distribution function (*df/dW* in units $km^{-6}s^3\ keV^{-1}$) of each distribution function in the energy range 7 - 10 keV. The positive gradient region can clearly be seen growing in magnitude, before maximizing on the orbit of the Pg onset (Orbit 0). For the orbits following the Pg onset, the positive gradient region disappears, as the free energy is transferred from the particle population to the resonant wave,

correct energy to drive the wave through a drift – bounce resonance interaction. In addition, the IDF evolution was observed over seven consecutive eighteen hour orbits, (see figure 5.4 taken from *Wright et al.*, 2001). The positive gradient region can clearly be seen growing in magnitude, before maximizing on the orbit of the Pg onset (orbit 0). For the two orbits following the Pg onset, the positive gradient region disappears, as the free energy is transferred from the particle population to the resonant wave, thus returning the IDF to an approximate power law.

5.2. Statistical Database

The database used for the study comprises omnidirectional IDFs measured using the particle detectors on board the *Polar* spacecraft. A full description of the instruments can be found in chapter 4. The TIMAS instrument measures the lower energy protons from ~ 0.025 keV to 32 keV, while the CAMMICE (MICS) instrument extends to higher energies, 1 keV to 328 keV. Table 5.1 shows the energy channels of both the TIMAS and CAMMICE (MICS) instruments. The original energy limit of CAMMICE (MICS) was 448 keV, however problems with the instrument reduced this range to 328keV. The orbit of *Polar* is highly elliptical allowing the spacecraft to sample the inner magnetospheric particle population, more specifically, populations located in the ring current. The study used data from L – shell locations of between 5 and 9 R_E. The precession of the orbit also allows the entire magnetosphere to be sampled (see figure 4.14). The database comprises of ~2500 IDFs amassed over a 2.5 year period from May 1996 to December 1998. This data interval was chosen due to the limitations in the TIMAS database introduced by telemetry problems and a high voltage breakdown which occurred in the instrument. The data were firstly binned into hourly MLT bins to examine the overall data coverage. Figure 5.5 indicates this coverage for all MLTs in the form of a (a) histogram plot and also as a (b) coloured occurrence plot. The occurrence plot in (b) is a view orientated with midday at the top of the plot, looking down onto the Polar cap. It can be seen that there is excellent data coverage throughout the magnetosphere, with the distribution maximising at ~13MLT. In all there are ~ 100 IDFs in each bin from 07 – 16 and 18 – 06 MLT, with ~ 70 data points in each bin in the early morning and late evening sectors.

The populations were investigated, firstly to ascertain the prevalence of the bump-on-tail IDFs, secondly, to quantify the amount of free energy available in the positive gradient region and thirdly to ascertain over what particle energy range it occurs. Various criteria

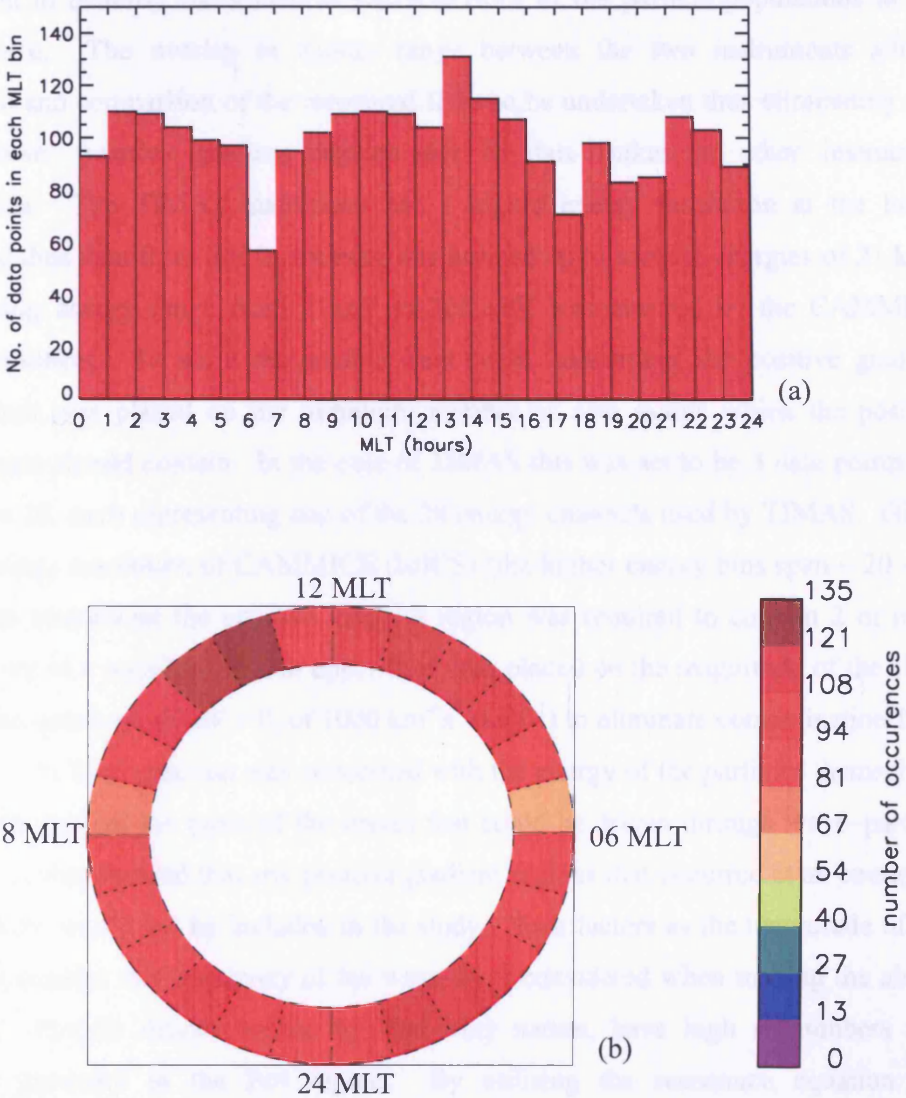

Figure 5.5. (a) Histogram of the number of Ion Distribution Functions (IDFs) in each MLT bin. (b) coloured occurence plot for the number of IDFs in each MLT bin. The view is orientated with midday MLT at the top of the plot, looking down onto the polar cap.

were applied to quantify the statistical characteristics of the particle populations in the magnetosphere. The overlap in energy range between the two instruments allows confirmation and comparison of the measured IDFs to be undertaken thus eliminating any possible 'false' positive gradient regions due to data spikes or other instrument contamination. The TIMAS instrument has a higher energy resolution at the lower energies and thus data from this instrument was utilized up to particle energies of 21 keV. The remaining energy range from 21keV to 328 keV was covered by the CAMMICE (MICS) instrument. To set a discernable limit when concerning the positive gradient region, a limit was placed on the minimum number of data points which the positive gradient region should contain. In the case of TIMAS this was set to be 3 data points out of a possible 28, each representing one of the 28 energy channels used by TIMAS. Given the lower energy resolution of CAMMICE (MICS) (the higher energy bins span ~ 20 – 40 keV) for this instrument the positive gradient region was required to contain 2 or more data points out of a possible 32. An upper limit was placed on the magnitude of the slope of the positive gradient, $df/dW > 0$, of 1000 $km^{-6}s^3$ (keV^{-1}) to eliminate contamination from data spikes. The final criterion was concerned with the energy of the particles themselves. After consideration of the types of the waves that could be driven through wave–particle interactions, it was decided that any positive gradient regions that occurred at an energy of less than 1 keV would not be included in the study. Such factors as the magnitude of the azimuthal *m* number and frequency of the wave were considered when making the above assumption. Particle driven waves, by their very nature, have high *m* numbers and frequencies generally in the Pc4 region. By utilising the resonance equation the characteristics of the types of wave that can be driven by a positive gradient region located below 1 keV may be determined. The waves would either have to have a small *m* number, which would in turn imply that it was not particle driven due to its large spatial size, or, given a large *m* value, an unrealistic oscillation frequency when considered alongside observational data.

For this study, the two parameters W_{min} and W_{max} are used to quantify the particle range over which free energy is available. Consider an IDF which contains a positive gradient which extends from < 1 keV to ~ 5keV; this would be excluded from the study if only the W_{min} parameter was considered, as the positive gradient extends to energies thought to be too low to provide enough energy to any resonant wave, even though particles of 5 keV are involved also in any resonant interaction. However, an IDF which contains a positive gradient which extends only from 1.5 keV to 2keV would be considered given the W_{min} criteria only even though the population as a whole is at a very low energy. Various methods were considered and it was decided that the average energy location of the positive gradient ($W_{av}=(W_{min}+W_{max})/2$) for each IDF would be used to determine if the energy location exceeds the 1 keV threshold.

Examples of IDFs from the database are shown in figure 5.6. The plots are all in a log – log format with the x-axis indicating the energy of the particles, *W* from 0.1 keV to 328 keV, and the y-axis the corresponding distribution function, *f*(*W*). The blue lines on each plot represent data from the TIMAS instrument with the red lines representing data from the CAMMICE (MICS) instrument. It can be see that there is a reassuringly excellent agreement between the two instruments. Figure 5.6 (a) illustrates an IDF without a positive gradient region and thus would not be considered as a candidate for a wave energy source. Figure 5.6 (b) indicates an IDF that was omitted from the study due to the low energy location of the positive gradient region. Figures 5.6 (c) to (e) indicate IDFs that would be suitable wave energy sources and thus would be included in the study. The W_{min} and W_{max} parameters are indicated in figures 5.6 (c) to (e). The statistical analysis proved to be very challenging. The fact that all of the IDFs are unique made ascertaining a fair test parameter by which to analyse the population very difficult. Many of the IDFs contain multiple positive gradient regions. In this situation the positive gradient regions were all included in the study if they were deemed suitable through the selection process described above.

5.3. Free Energy Statistics

Using the method detailed in section 5.1 the amount of free energy available was calculated for each IDF. The results are shown in figures 5.7 (a) and (b). The results have been divided into hourly MLT bins depending on the location of the particle populations. The graph is orientated such that the view is of the magnetosphere looking down onto the equatorial plane, with 06 MLT on the right hand side, 12 MLT at the top, 18 MLT on the left hand side and 24 MLT at the bottom. In figure 5.7 (a) as the radial distance from the centre of the circle is increased the amount of free energy available increases from 0 to $1.8\text{x}10^{11}$ J on a linear scale in increments of $1.2\text{x}10^{10}$ J. In figure 5.7 (b) the scale is from 0 to $0.23\text{x}10^{11}$ on a linear scale in increments of $1.2\text{x}10^{9}$ J allowing a more detailed look at the structure of the amount of free energy available. No low energy threshold when

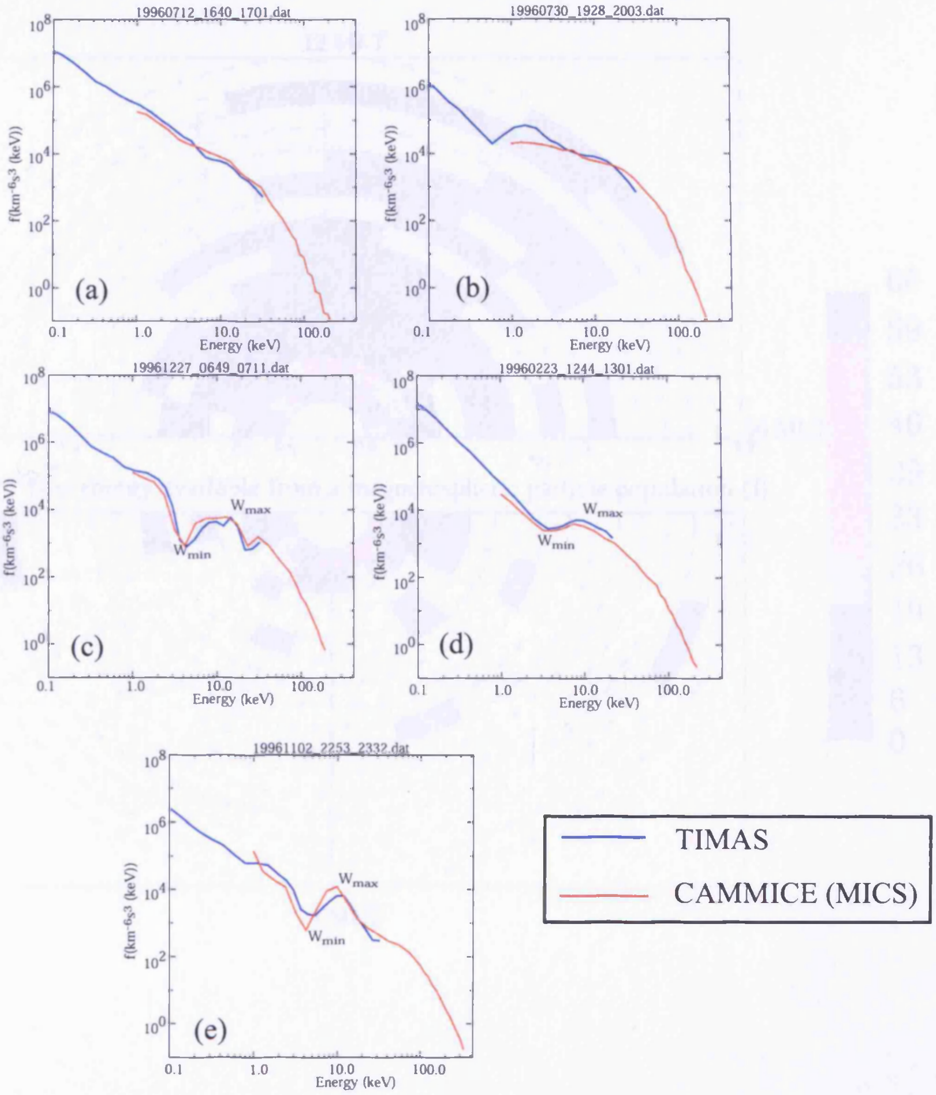

Figure 5.6 Example IDFs from the statistical database. TIMAS data is shown in blue and CAMMICE (MICS) data is shown in red. Figure (a) illustrates an IDF without a positive gradient region and thus would not be considered as a candidate for a wave energy source. Figure (b) indicates an IDF that was omitted from the study due to the low energy location of the positive gradient region. Figures (c) to (e) indicate IDFs that would be suitable wave energy sources and thus would be included in the study. Two further parameters are indicated in figures (c) to (e) which are later used to indicate over what particle energy range the positive gradient region and thus free energy is located; W_{min} and W_{max}. W_{min} indicates the lower energy location of the positive gradient region, while W_{max} indicates its upper energy limit.

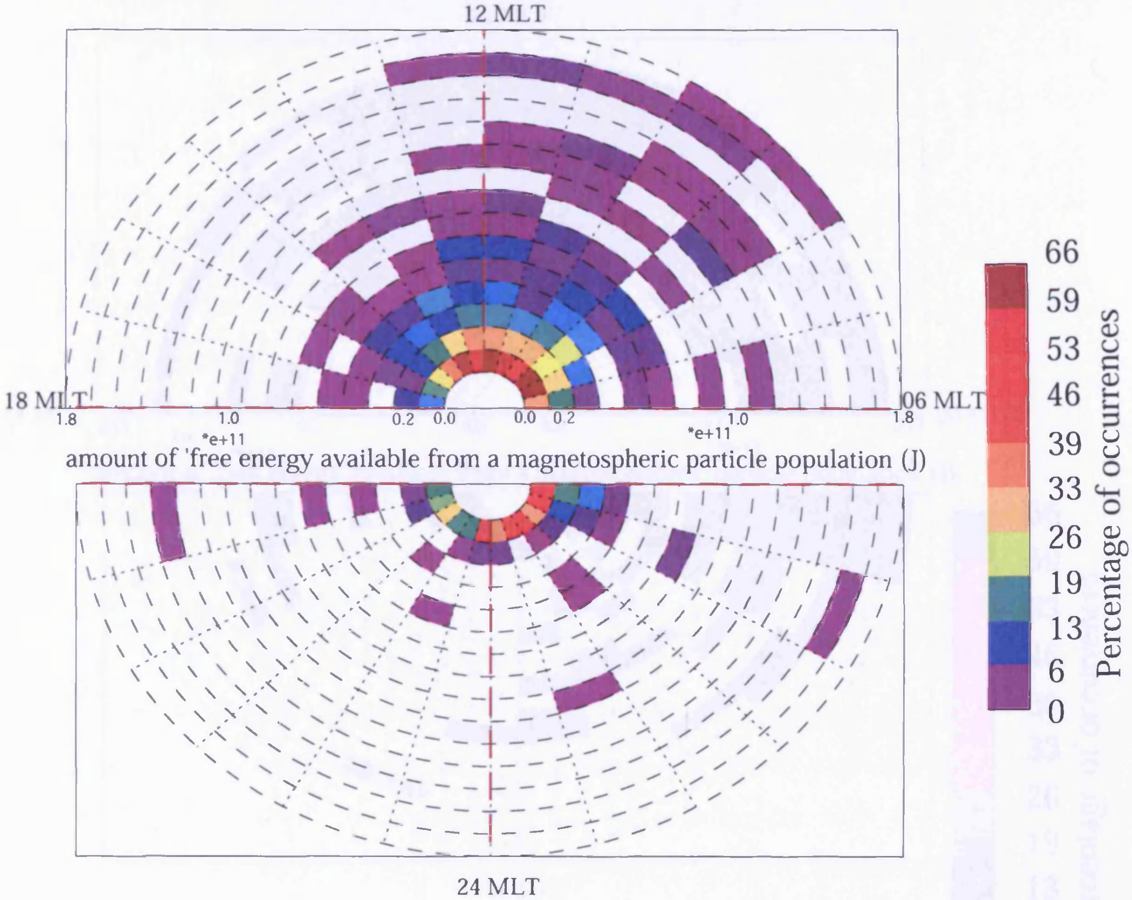

Figure 5.7(a). Results from a statistical study of magnetospheric particle populations, using the TIMAS and CAMMICE (MICS) instruments. Two years of data were binned according to MLT location and also according to the amount of free energy each IDF contained in the form of a positive gradient region. The radial distance from the centre of the circle indicates increasing amounts of free energy available up to a maximum of 1.8×10^{11} J in bin increments of 1.2×10^{10} J. The data bins are colour coded as a percentage occurrence in that MLT bin.

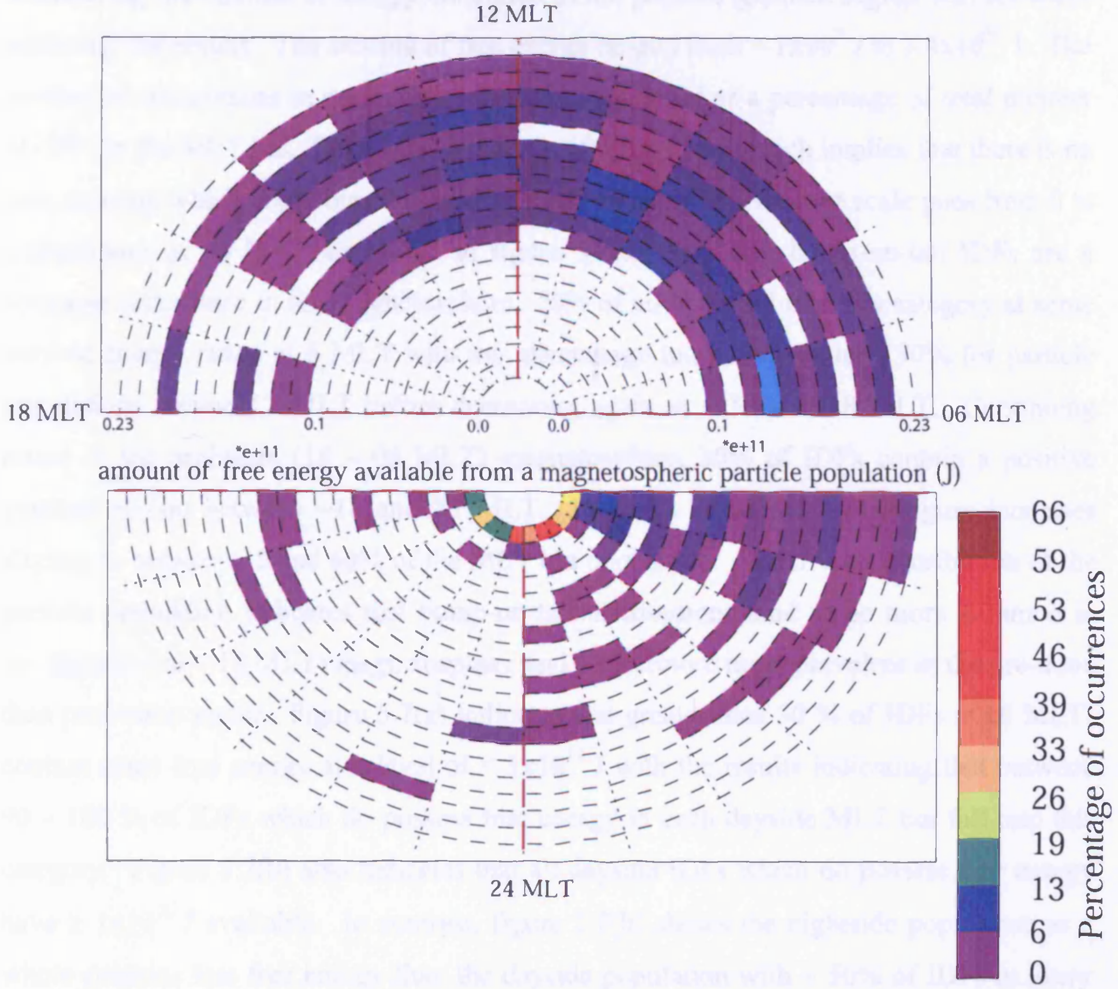

Figure 5.7(b). The plot is the same format as figure 5.7(a) except that the radial scale of the plot has changed. The radial distance from the centre of the circle indicates increasing amounts of free energy available up to a maximum of 0.23×10^{11} J in bin increments of 1.2×10^{9} J. The data bins are colour coded as a percentage occurrence in that MLT bin.

considering the amount of energy contained in the positive gradient region was set when analysing the results. The amount of free energy ranged from ~ 1×10^7 J to 3.4×10^{11} J. The number of occurrences in each energy bin is colour-coded as a percentage of total number of IDFs in the MLT bin. Each MLT bin has ~ 100 IDFs in it which implies that there is no data skewing which could bias the results. The percentage occurrence scale goes from 0 to a maximum of 66 %. The results in figure 5.7(a) show that bump-on-tail IDFs are a common occurrence in the magnetosphere. 50% of all IDFs fall into this category at some particle energy range at 6 MLT with this percentage increasing up to ~ 90% for particle populations around 12 MLT before decreasing again to ~ 30% at 18 MLT. Continuing round to the nightside (18 – 06 MLT) magnetosphere, 30% of IDFs contain a positive gradient region between ~18 and 23 MLT. From 23 to 06 MLT this figure increases slightly to between 35 and 60% of the MLT bin population. The overall distribution of the particle population indicates that bump-on-tail distributions tend to be more common in the dayside (06 – 18 MLT) magnetosphere and furthermore more prevalent in the pre-noon than post-noon sector. Figure 5.7(a) indicates that greater than 30 % of IDFs at all MLTs contain some free energy at a level of $< 1 \times 10^{11}$ J with the results indicating that between 90 – 100 % of IDFs which do possess free energy in each dayside MLT bin fall into this category. Figure 5.7(b) also indicates that all dayside IDFs which do possess free energy have $\geq 1 \times 10^{10}$ J available. In contrast, figure 5.7(b) shows the nightside population as a whole contains less free energy than the dayside population with ~ 50% of IDFs in every MLT bin indicating $< 1.2 \times 10^9$ J available. When considering larger amounts of free energy ($>1 \times 10^{11}$ J) the pre-noon sector population is dominant with IDFs containing this larger amount concentrated between 8 and 13 MLT. What is also of interest is that the occurrence of this increased amount of free energy is very rare. Only ~ 10 – 15 % of particle populations in each MLT bin measured between 8 and 13 MLT contain a positive gradient region with this increased amount of free energy.

5.4. Energy of Particles in the Positive Gradient Region

The energy of the particles resonantly driving the wave was also examined by investigating the location along the x-axis of the IDF of the positive gradient region (i.e. the W_{av} parameter). Particle-driven ULF waves have been linked to driving particle populations of between 10 and 100's keV depending on the resonant wave mode. By examining the IDFs in a statistical fashion the prevalence of such particles can be ascertained and thus provide evidence as to the statistical likelihood of any wave modes being driven by these particles in both the pre- and post-noon sectors.

The results (shown in figure 5.8) have again been divided into hourly MLT bins depending on the location of the particle populations and the graph is orientated such that the view is of the magnetosphere looking down onto the equatorial plane, with 06 MLT on the right hand side, 12 MLT at the top, 18 MLT on the left hand side and 24 MLT at the bottom. In this part of the analysis, the data from the TIMAS and the CAMMICE (MICS) instrument were dealt with separately. The red semicircular line indicates the divide between the TIMAS and CAMMICE (MICS) data, with TIMAS data located in the inner semicircles. As the radial distance from the centre of the circle is increased the energy of the particles which posses free energy (the E_{av} parameter) increases. TIMAS data were examined for positive gradient regions between 1 and 21 keV and CAMMICE (MICS) data were examined in a similar manner for regions between 10 and 325 keV. The overlap in energy was utilised to provide additional confirmation that any positive gradient regions were real and not an artefact of the particle detectors. The data bin sizes on the graph are the actual detector bin sizes (see table 5.1) and the plot is in a log format to allow the full energy range of both detectors to be covered. The bins are colour coded as a function of percentage of the number of IDFs in each MLT bin. It is encouraging to see that in the overlap energy range of ~10 – 20 keV both TIMAS and CAMMICE (MICS) are in excellent agreement. On the dayside, both instruments indicate the majority of IDFs have free energy available for a possible resonant interaction with ~ 10 – 40 keV protons. This trend is strongest in the dawn sector with ~ 60% of IDFs falling into this category. The trend continues slightly into the dusk sector although again the percentage of IDFs containing free energy is reduced. On the nightside the overall number of occurrences is far less than that of the dayside. Most of the IDFs here display positive gradient regions at energies of between 75 and 300 keV, except at 04 – 06 MLT where the distribution resembles that of the dayside pre-noon distributions. What is most surprising is the small number of IDFs which contain particles with free energy above ~ 75 keV. In all dayside MLT bins < 10% of the particle populations indicate the presence of 75 keV protons with free energy to feed to a possible wave modes. This figure is only slightly larger on the nightside with up to ~25% of IDFs in each MLT bin indicating the presence of a positive gradient region between 75 and 300 keV.

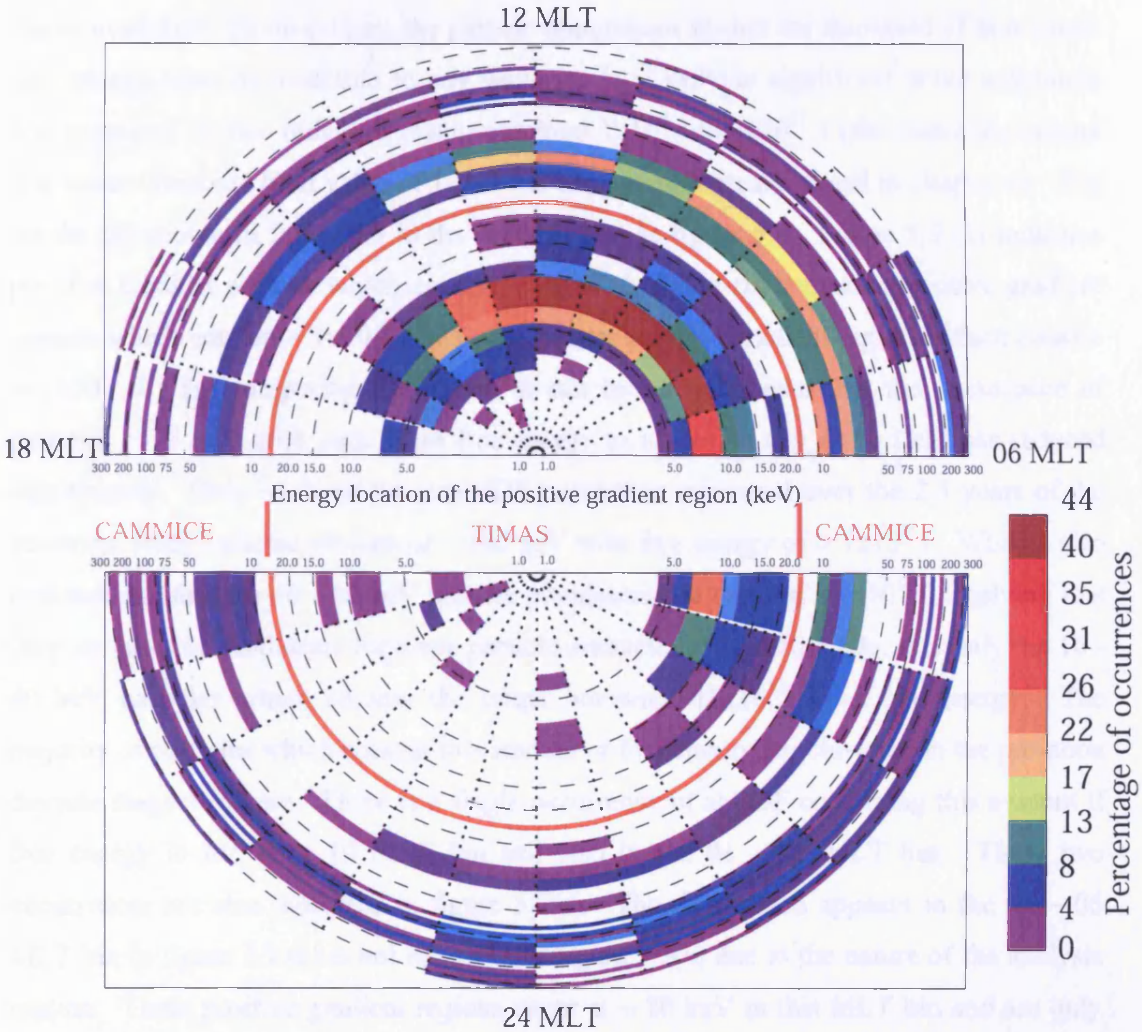

Figure 5.8 Results of the study into the energy of the particles which contain free energy. As the radial distance from the centre of the circle is increased the energy of the particles which posses free energy (the E_{AV} parameter) increases. TIMAS data were examined for positive gradient regions between 1 and 21 keV and CAMMICE (MICS) data were examined in a similar manner for regions between 10 and 325 keV. The scale is logarithmic and the bin sizes are that of the instruments. The red line indicates the divide between the two instruments. Note there is an energy overlap between the two instruments. The data were binned according to MLT location. The data bins are colour coded as a percentage occurrence in that MLT bin.

In figure 5.8 all data has been included, regardless of how small the amount of free energy that is available. To investigate the particle populations further the threshold of how much free energy must be available to any wave mode to provide significant wave amplitude was increased by two orders of magnitude from 1×10^9 J to 1×10^{11} J (the reasoning behind this lower threshold limit value of 1×10^9 J is explained in greater detail in chapter 6). The results are shown in figure 5.9 in the same format as figure 5.8. Figure 5.9 (a) indicates positive gradient regions which contain > 1×10^9 J, figure (b) indicates positive gradient regions which contain > 1×10^{10} J and (c) indicates positive gradient regions which contain > 1×10^{11} J. By comparing the figures it can instantly be seen that the occurrence of particles > 75 keV with significant free energy to impart to any wave field has reduced significantly. Only ~1 % of the total IDF population measured over the 2.5 years of the statistical study indicate protons of ~ 100 keV with free energy of > 1×10^9 J. What is also noticeable is that the 10 - 40 keV particle populations do contain > 1×10^9 J, implying that they are suitable candidates for wave particle interactions. Additionally, it is only the 10 - 40 keV particles which contain the larger amounts, >1×10^{11} J, of free energy. The majority of particles which contain this amount of free energy are clustered in the pre-noon dayside magnetosphere. There is a single occurrence of an IDF containing this amount if free energy in the 18 – 19 MLT bin and also in the 01 – 02 MLT bin. These two occurrences are also indicated in figure 5.7(a). The data which appears in the 05 – 06 MLT bin in figure 5.9 (c) is not indicated in figure 5.7(a) due to the nature of the analysis routine. These positive gradient regions occur at ~ 20 keV in this MLT bin and are only registered by the analysis software for the CAMMICE (MICS) instrument. In figures 5.7(a) and (b), CAMMICE (MICS) data is only utilised for particles of > 21 keV, thus these positive gradient regions are not registered here. In figures 5.8 and 5.9 CAMMICE (MICS) data is utilised from 10 keV as both TIMAS and CAMMICE (MICS) data can be plotted separately on these plots.

5.5. Free Energy as a Function of Particle Energy

The dependence of the quantity of free energy as the energy of the particles which provide this energy revealed in figure 5.9 may be examined directly. The results for the dayside magnetosphere (06 – 18 MLT) are shown in figure 5.10 (a) and for the nightside magnetosphere (18 – 06 MLT) in figure 5.10 (b). The x-axis indicates the energy of the particles which possess free energy, the E_{av} parameter. The y-axis indicates the amount of

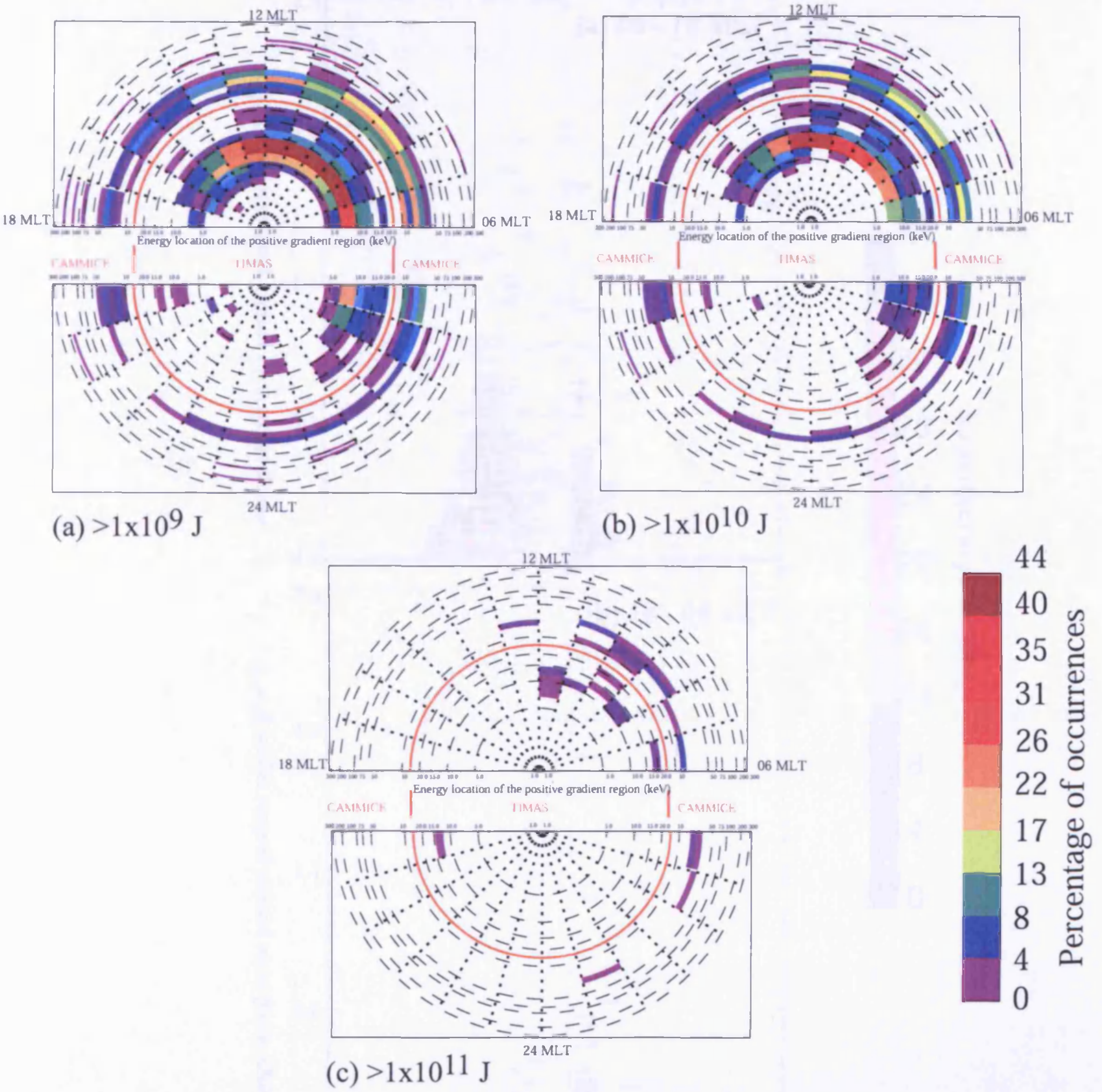

Figure 5.9 The format of the plots are the same as for figure 5.8. In this figure the amount of free energy contained in the positive gradient region must be greater than or equal to (a) $1x10^9$J, (b) $1x10^{10}$J and (c) $1x10^{11}$J. This has the effect of reducing the amount of occurrences at higher particle energies.

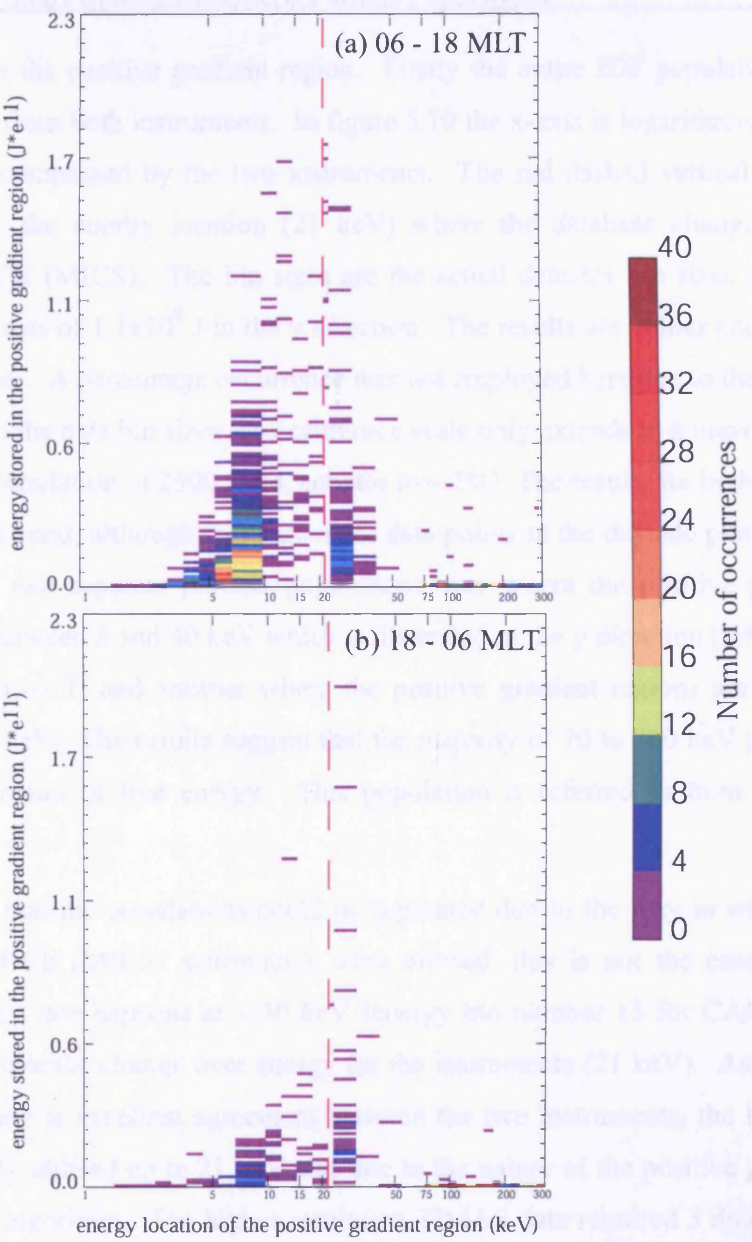

Figure 5.10. Occurrence plot indicating the free energy in the IDF as a function of the particle energy for (a) 06 - 18 MLT and (b) 18 - 06 MLT. The x-axis represents the energy location of the positive gradient region in the IDF, i.e. the energy of the particles. This axis is logarithmic, with the red dashed vertical line indicating the transition from TIMAS data at lower energies to CAMMICE (MICS) data at higher energies. The y-axis is a linear scale indiating the amount of free energy contained in the IDF. The data bins are 1.1x10^9 J in size in the y direction and the energy bin sizes of the instruments (see table 5.1) in the x direction. The bins are colour coded as a number of occurrences given on the scale on the right hand side. The data from all MLTs are included in this plot.

free energy stored in the positive gradient region. Firstly the entire IDF population was analysed, using data from both instruments. In figure 5.10 the x-axis is logarithmic due to the energy range encompassed by the two instruments. The red dashed vertical line in each plot represents the energy location (21 keV) where the database changes from TIMAS to CAMMICE (MICS). The bin sizes are the actual detector bin sizes in the x direction and increments of 1.1×10^{9} J in the y direction. The results are colour coded as a number of occurrences. A percentage occurrence was not employed here due to the format of the results. Due to the data bin sizes the occurrence scale only extends to a maximum of 40 which, in a total population of 2500 IDFs, equates to ~ 2%! The results for both (a) and (b) indicate a similar trend, although there are more data points in the dayside plot. There is the possibility of two separate particle populations, one where the positive gradient regions are located between 3 and 40 keV which is distended in the y direction (referred to from now as population 1) and another where the positive gradient regions are located between 75 and 300 keV. The results suggest that the majority of 70 to 300 keV particles contain a similar amount of free energy. This population is referred to from now as population 2.

Although it appears that the populations could be separated due to the way in which the TIMAS and CAMMICE (MICS) instruments were utilised, this is not the case as the increase in occurrence rate happens at ~ 30 keV (energy bin number 13 for CAMMICE (MICS)) which is above the change over energy for the instruments (21 keV). As seen in figures 5.7 to 5.9 there is excellent agreement between the two instruments, the fact that TIMAS data was only utilised up to 21 keV was due to the nature of the positive gradient region identification algorithm. The higher resolution TIMAS data required 3 data points to be located in the positive gradient region. For the free energy calculation an additional data point at the first energy channel above the positive gradient region was used. This meant that for positive gradient regions located > 21 keV, although TIMAS detected them, the analysis software was unable to calculate the free energy, thus discarding valuable data. An example of this is shown in figure 5.11. Both TIMAS and CAMMICE (MICS) detect the positive gradient and are both in excellent agreement as to its shape and energy location, however given the nature of the analysis, only CAMMICE (MICS) will have indicated its presence. Additionally, the energy resolution of TIMAS and CAMMICE (MICS) at ~ 21 keV are approximately the same thus eliminating any biasing due to discrepancies in bin sizes between the two instruments.

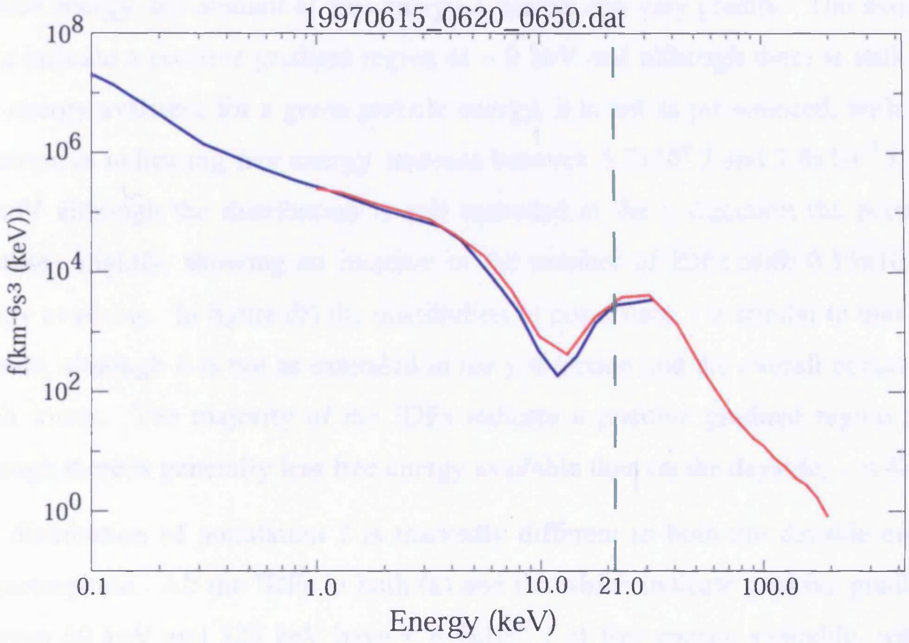

Figure 5.11. An example of an IDF which contains a positive gradient region. Both the TIMAS and CAMMICE (MICS) instruments are in excellent agreement as to the shape of the IDF. The analysis procedure used in this study means that because the region extends to the highest energy measurable by TIMAS the amount of free energy cannot be obtained. Thus the CAMMICE (MICS) instrument was utlilised for any positive gradient regions that extended to above 21 keV. The green vertical dashed line represents this cut off energy imposed on the TIMAS data (equivalent to the red dashed line in figure 7.10).

In figure 5.10 (a), as the particle energies increase in population 1 from 3 keV to 20 keV the occurrence distribution becomes extended in the y direction, indicating larger amounts of free energy, peaking at ~ 1.8×10^{11} J. Between particle energies of 10 to 20 keV, the distribution becomes more evenly spread in the y direction, indicating that for a given particle energy, the amount of free energy available can vary greatly. The majority of the IDFs indicate a positive gradient region at ~ 9 keV and although there is still a spread in free energy available for a given particle energy, it is not as pronounced, with the bulk of occurrences indicating free energy amounts between 5.7×10^9 J and 2.8×10^{10} J. At ~ 30 – 40 keV although the distribution is still extended in the y direction the occurrence rate increases slightly, showing an increase in the number of IDFs with 0.15×10^{11} J of free energy available. In figure (b) the distribution of population 1 is similar to that seen on the dayside, although it is not as extended in the y direction and the overall occurrence rate is much lower. The majority of the IDFs indicate a positive gradient region at ~ 9 keV although there is generally less free energy available than on the dayside; ~ < 4.4×10^9 J.

The distribution of population 2 is markedly different in both the dayside and nightside magnetosphere. All the IDFs in both (a) and (b) which indicate positive gradient regions between 60 keV and 325 keV have < 4.5×10^{10} J of free energy available, with ~95% of population 2 IDFs containing < 1×10^9 J. As seen also in figure 5.8 the majority of IDFs observed on the nightside which contain a positive gradient region, do so at higher energies than on the dayside.

The data were further investigated by looking at the distribution of data in the pre and post noon sector and also the pre and post midnight sectors separately. This was done to ascertain whether particles of certain energies containing certain amounts of free energy displayed any preferential MLT location. The plot axes remain unchanged from figure 5.10. The results are shown in figure 5.12 (a) for the pre-noon magnetosphere and 5.12 (b) for the post-noon magnetosphere. Figure 5.12 (a) indicates that the pre noon sector has the most occurrences out of the two dayside data plots and also the largest amount of free energy available. There is also evidence that the amount of free energy possessed by particles populations of between ~ 10 and 40 keV can vary greatly between ~ 10^9 and 10^{11} J although the majority of particles in this energy range contain ~ 10^{10} J of free energy. There seems to be no MLT dependence on the number of IDFs which contain a positive gradient region at particle energies > 60 keV. Figure 5.13 indicates the results for the (a) pre-midnight and (b) post-midnight sector. Both the amount of free energy

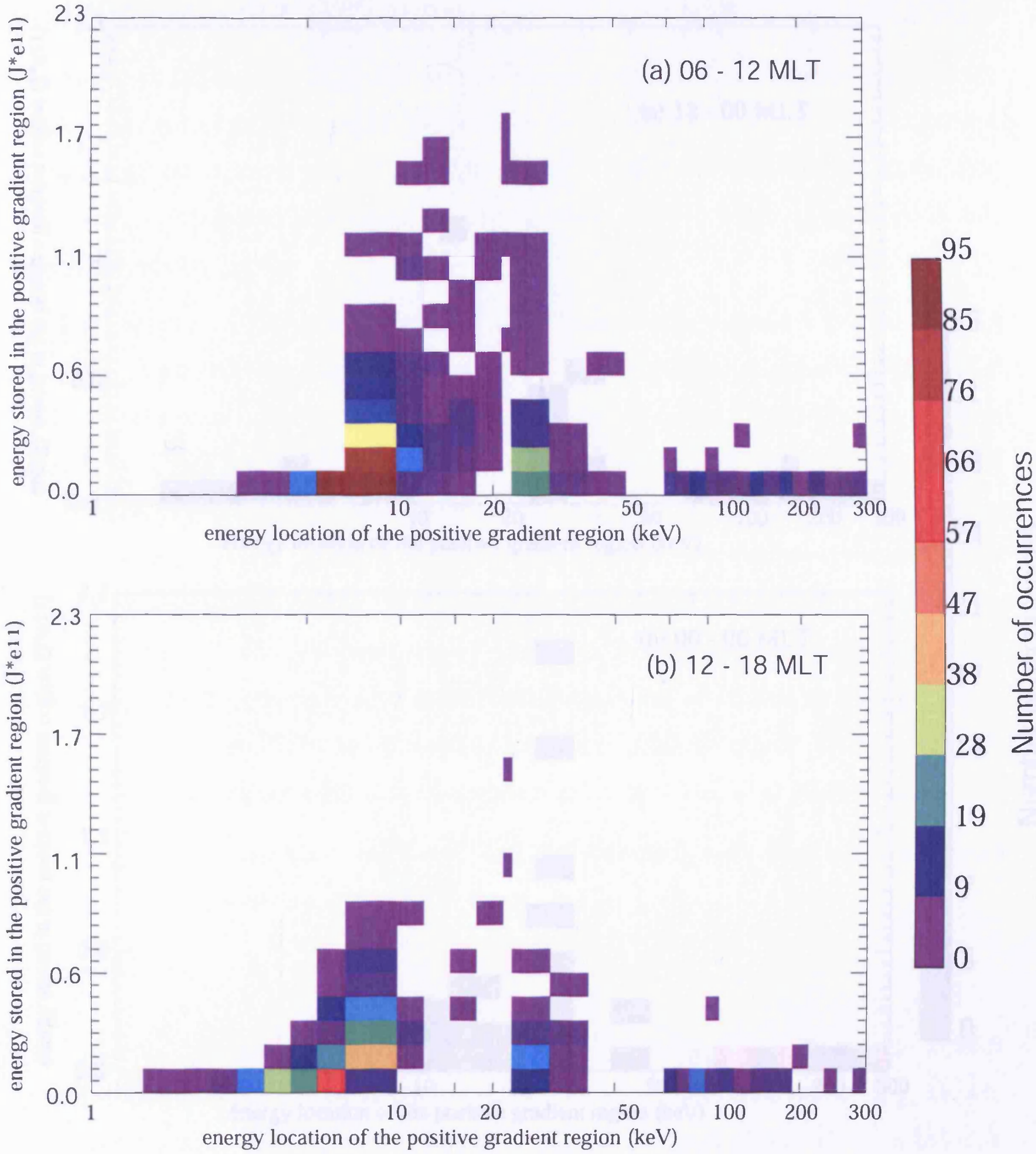

Figure 5.12. 6 hourly MLT plots using data from 06 - 18 MLT of the same format as in figure 5.10. Panel (a) shows data from 06 - 12 MLT and panel (b) shows data from 12 - 18 MLT. Both TIMAS and CAMMICE (MICS) data are included on all plots.

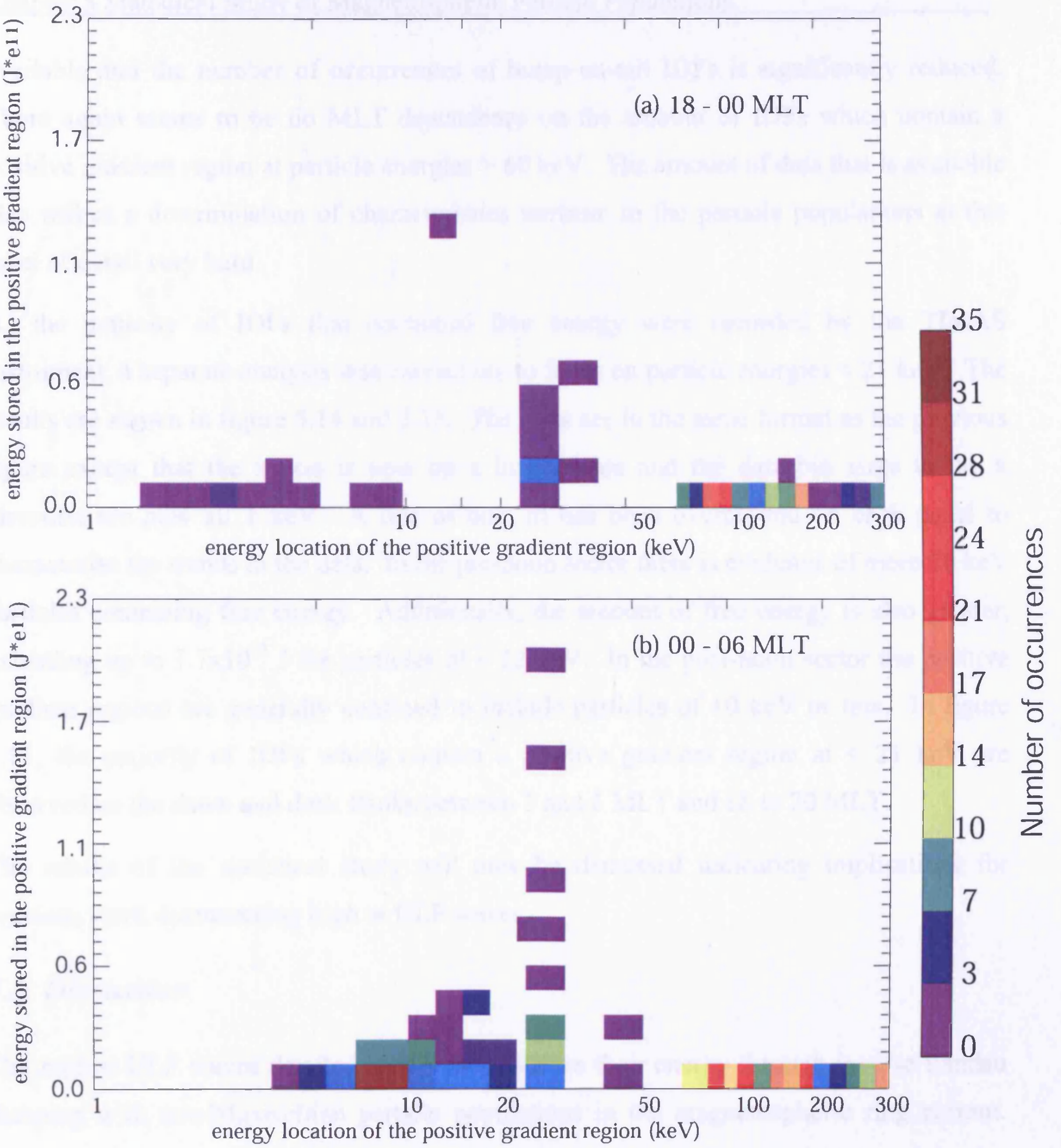

Figure 5.13. 6 hourly MLT plots using data from 18 - 06 MLT of the same format as in figure 5.12. Panel (a) shows data from 18 - 00 MLT and panel (b) shows data from 00 - 06 MLT. Both TIMAS and CAMMICE (MICS) data are included on all plots.

available and the number of occurrences of bump-on-tail IDFs is significantly reduced. There again seems to be no MLT dependence on the amount of IDFs which contain a positive gradient region at particle energies > 60 keV. The amount of data that is available also makes a determination of characteristics intrinsic to the particle populations at this level of detail very hard.

As the majority of IDFs that contained free energy were recorded by the TIMAS instrument, a separate analysis was carried out to focus on particle energies < 21 keV. The results are shown in figure 5.14 and 5.15. The plots are in the same format as the previous figure except that the x-axis is now on a linear scale and the data bin sizes in the x direction are now all 1 keV. A line of best fit has been overplotted on each panel to characterise the trends in the data. In the pre-noon sector there is evidence of more 20 keV particles containing free energy. Additionally, the amount of free energy is also greater, extending up to 1.7×10^{11} J for particles of ~ 12 keV. In the post-noon sector the positive gradient regions are generally confined to include particles of 10 keV or less. In figure 5.15, the majority of IDFs which contain a positive gradient region at < 21 keV are observed on the dawn and dusk flanks between 3 and 6 MLT and 18 to 20 MLT.

The results of the statistical study will now be discussed indicating implications for previous work documenting high *m* ULF waves.

5.6. Discussion

The high *m* ULF waves detailed in this thesis derive their energy through inverse Landau damping with non-Maxwellian particle populations in the magnetospheric ring current. The statistical study detailed in this chapter examined 2.5 years of particle data from the TIMAS and CAMMICE (MICS) particle detectors on board the *Polar* spacecraft to ascertain the prevalence of such driving ring current particle populations. Such a study has never previously been undertaken. Several interesting conclusions can be drawn about the possible dominant interaction mechanism and thus wave eigenmode at different MLT locations.

5.6.1. Morning Sector and Giant Pulsation (Pg) Observations

A major topic of debate in the field of particle-driven ULF waves is the energy of the interacting proton populations that drive morning sector waves, particularly Pgs. Previous work has cited 10 – 40 keV protons (*Wright et al.*, 2001 and *Chisham,* 1996) and 100 –

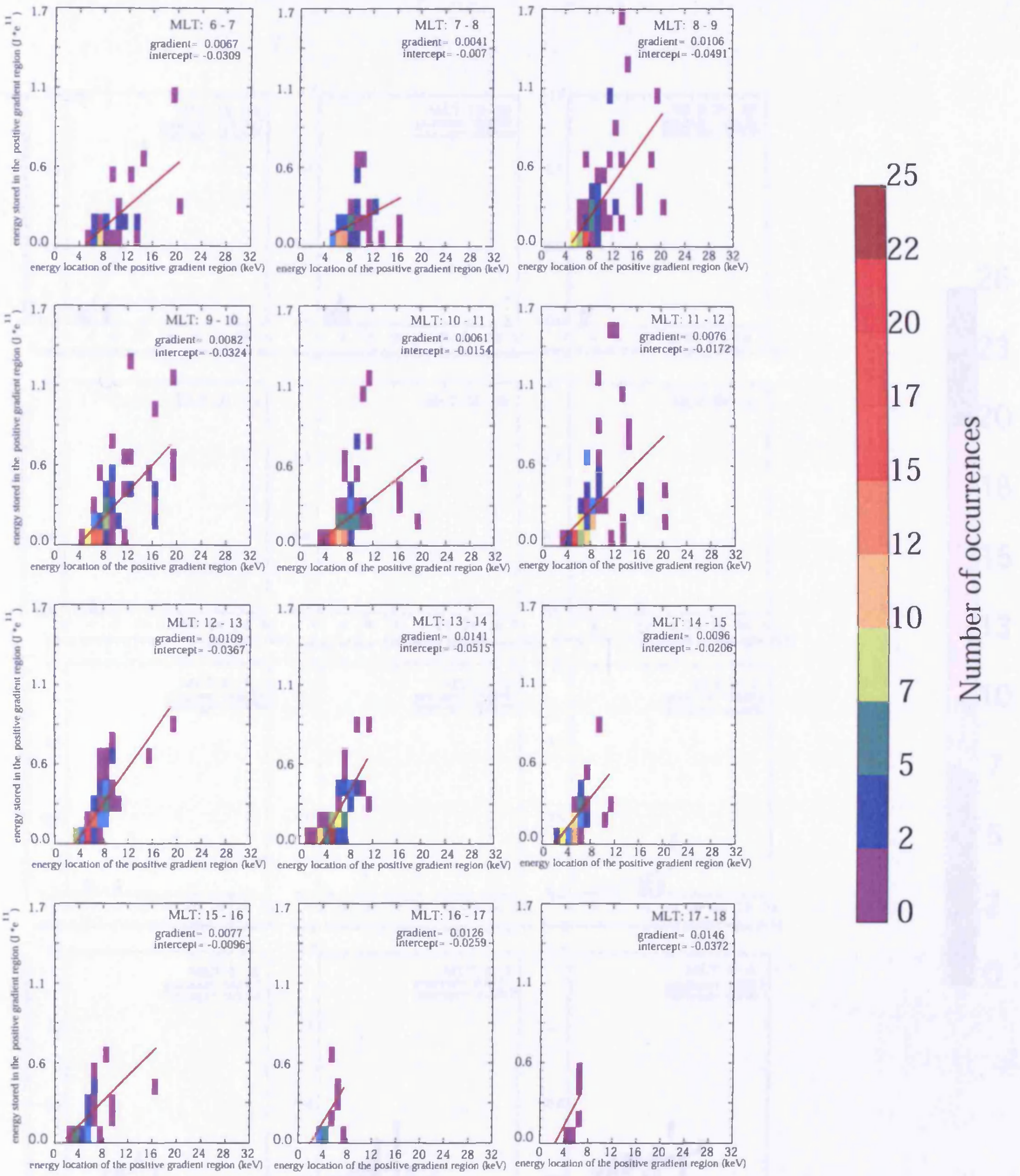

Figure 5.14. The plots are in the same format as figure 5.12 for 06 - 18 MLT except the x axis is now a linear scale. The plots are all for TIMAS data only, with an energy range of 0 to 32 keV. The red line on each plot indicates the line of best fit to the data with a numerical value for both the gradient and y intercept shown at the top right hand corner of each plot. The bin sizes are 1 keV in the x direction and 1.1×10^{10} J in the y direction. The bins are colour coded as a function of occurrence, with the scale shown on the right hand side.

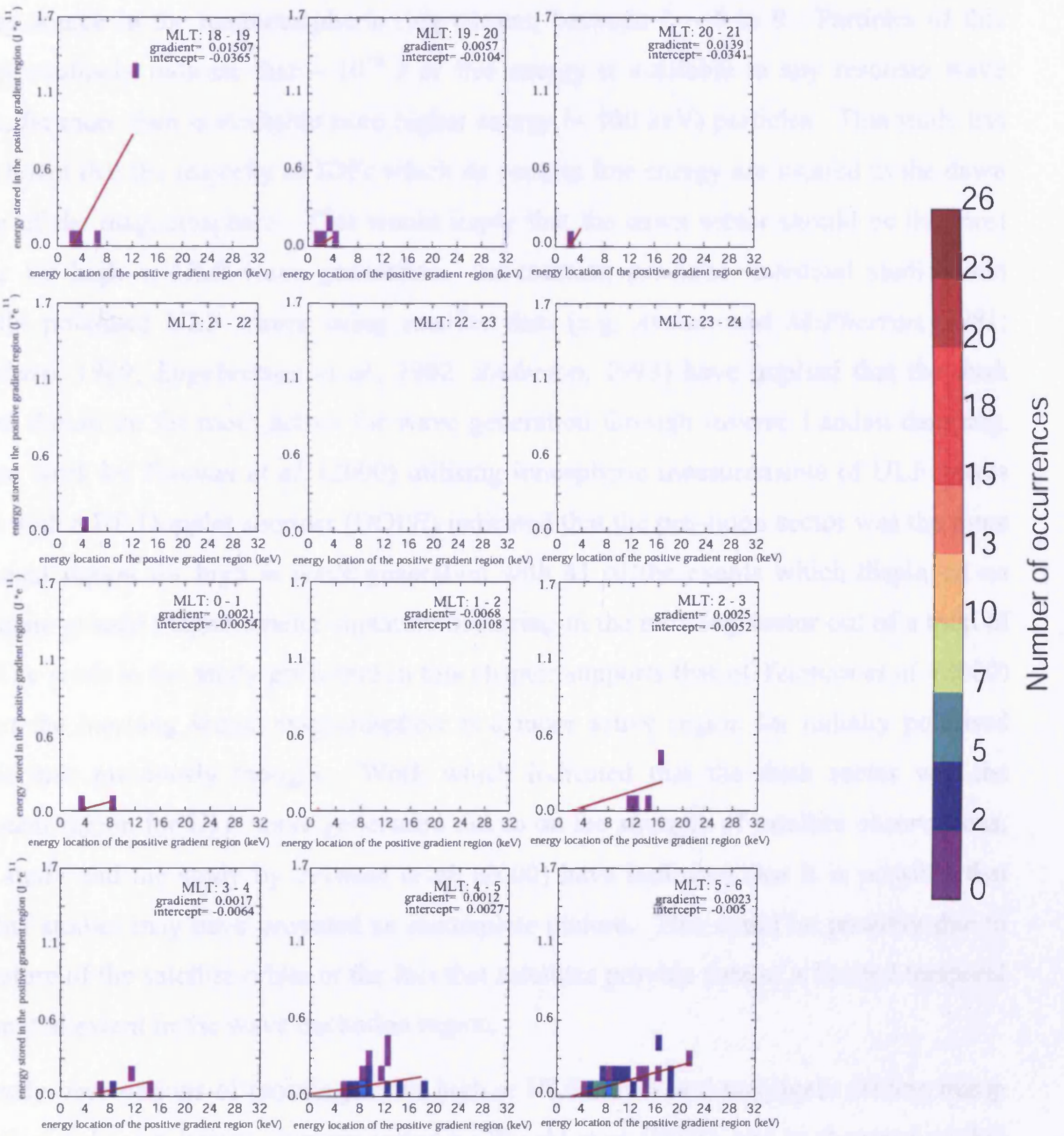

Figure 5.15. The plots are in the same format as figure 5.14, for 18 - 06 MLT. The plots are all for TIMAS data only, with an energy range of 0 to 32 keV. The red line on each plot indicates the line of best fit to the data with a numerical value for both the gradient and y intercept shown at the top right hand corner of each plot. The bin sizes are 1 keV in the x direction and 1.1×10^{10} J in the y direction. The bins are colour coded as a function of occurrence, with the scale shown on the right hand side.

150 keV protons (*Thompson et al.,* 2001) as the driving particle populations for Pgs. This study has shown that low energy particles, between ~ 10 and 40 keV are the dominant energy source in the magnetospheric ring current, between $L \sim 6$ to 9. Particles of this energy routinely indicate that ~ 10^{10} J of free energy is available to any resonant wave mode, far more than is available from higher energy (~ 100 keV) particles. This study has also shown that the majority of IDFs which do contain free energy are located in the dawn sector of the magnetosphere. This would imply that the dawn sector should be the most fertile for high *m* ULF wave generation. In contrast, previous statistical studies into radially polarised ULF waves using satellite data (e.g. *Arthur and McPherron,* 1981; *Kokuburn,* 1989; *Engebretson et al.*, 1992; *Anderson,* 1993) have implied that the dusk region should be far more active for wave generation through inverse Landau damping. Recent work by *Yeoman et al.* (2000) utilising ionospheric measurements of ULF waves made with a HF Doppler sounder (DOPE) indicated that the pre–noon sector was the more dominant region for high *m* wave generation with 41 of the events which displayed no conjugate ground magnetometer signature occurring in the morning sector out of a total of 52. The work in the study presented in this chapter supports that of *Yeoman et al.* (2000) in that the morning sector magnetosphere is a more active region for radially polarised waves than previously thought. Work which indicated that the dusk sector was the dominant region for ULF wave generation did so on the strength of satellite observations. This study and the study by *Yeoman et al.* (2000) have indicated that it is possible that satellite studies may have provided an incomplete picture. This could be possibly due to the nature of the satellite orbits or the fact that satellites provide data of a limited temporal and spatial extent in the wave excitation region.

The only observations of morning sector high *m* ULF waves and conjugate driving bump on tail particle populations were presented by *Wright et al.* (2001), and in chapter 6 of this thesis, and have indicated driving particle populations of ~ 10 keV. There has been no published observational evidence of such a bump on tail particle population of ~ 100 keV. Publications which have stated that the driving particle population was ~ 100 keV protons have done so on the basis of other, more circumstantial evidence such as observed particle modulations detected in the vicinity of the wave with the same frequency or by utilising either spacecraft measurements of the magnetic field in the equatorial plane or near conjugate inter-hemispheric ground magnetometer stations to infer the wave eigenmode. *Thompson et al.* (2001) utilised near conjugate observations of a Pg using magnetometers in Iceland and Antarctica to infer on odd mode standing wave structure. This method of inferring the wave eigenmode utilizing inter-hemispheric magnetometer data may be unreliable. Previous work into Pg eigenmodes by *Annexstad and Wilson* (1968) inferred an even mode structure while *Green* (1979) inferred an odd mode structure despite both using this same method. The main problem in this method is the fact that the locations of the magnetometers are judged to be conjugate using internal magnetic field models, (e.g. *Tsyganenko* 1989). As pointed out by *Takahashi et al.* (1992) different field models can produce discrepancies as large as ~ 4° in longitude between them. When considering Pgs, which have large phase changes over a small longitudinal extent, this difference can result in supposed conjugate magnetometer phase data being wrongly compared resulting in an inaccurate eigenmode deduction. *Thompson et al.* (2001) also utilised geosynchronous proton fluxes as measured by the Los Alamos National Laboratory (LANL) spacecraft. They noted proton fluctuations in the 104-125 keV and 125-153 keV channels at a frequency identical to the Pg. They concluded that the Pg was the result of a drift resonance interaction between an odd mode standing wave and ~100 keV protons. While it is entirely plausible that the wave field was indeed modulating the proton flux, this does not imply that this was the particle population which provided the free energy. Evidence from this extensive statistical study indicates that not only are 100 keV protons which contain free energy very rare in the pre-noon sector, they also contain very meagre amounts of free energy. This would indicate that it is highly unlikely that Pgs can be driven through a drift resonance interaction such as that cited by *Thompson et al.* (2001).

Glassmeier et al. (1999) suggested a resonant interaction with particles of ~67 keV measured by the GOES 2 spacecraft were responsible for driving a Pg observed in magnetometer data from the Scandinavian magnetometer array. The IDFs presented by *Glassmeier et al.* (1999) as the driving magnetospheric population are now compared to two example IDFs from this study. Figure 5.16 (c) and (d) indicate the IDFs which *Glassmeier et al.* (1999) stated could drive the observed Pg. Figure 5.16 (a) and (b) shows two IDFs from this study which contain a bump on tail located at ~ 12 keV. They also contain some secondary bumps on tail at ~ 70 keV which are located at approximately the same phase space density and energy as the one presented by *Glassmeier et al.* (1999). The dashed green lines align the y-axes between the plots presented by *Glassmeier et al.* (1999) and the ones from this statistical study. The free energy available from ~ 12 keV protons shown in figures (a) and (b) clearly dominates over any possible free energy from

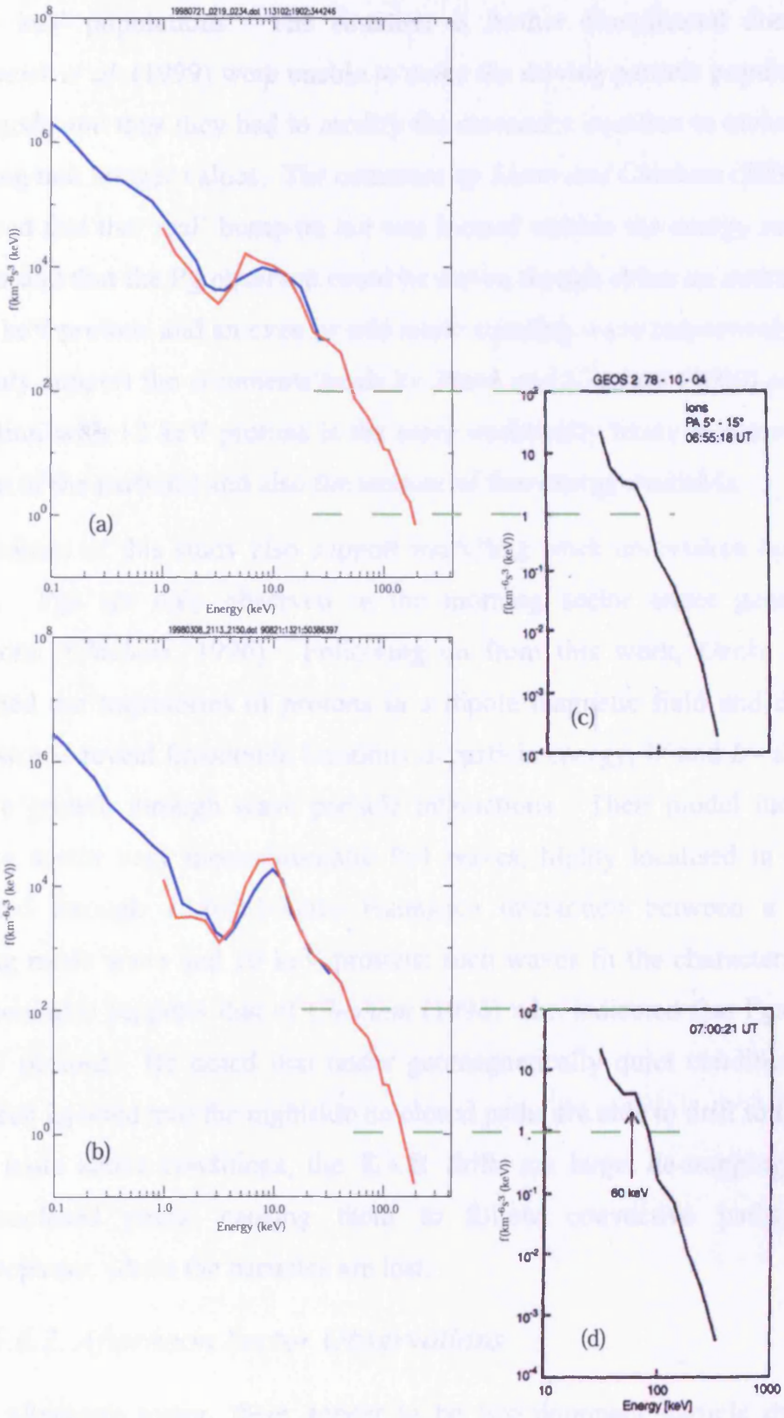

Figure 5.16. (a) and (b) show example IDFs from this statistical study. Both contain a primary bump at ~ 10 keV and both display evidence of a secondary much smaller bump at ~ 100 keV. (c) and (d) are taken from *Glassmeier et al.*, (1999) and indicate the 'bump-on-tail' cited as driving a Pg. All plots are on the same scale with the green lines between the plots indicate the same values of *f*(v). The amount of free energy contained in (c) and (d) is insignificant when placed along side the amount of free energy available from the primary bumps in (a) and (b).

the 70 keV populations. The situation is further complicated due to the fact that *Glassmeier et al.* (1999) were unable to make the driving particle population fit a resonant wave mode and thus they had to modify the resonance equation to include all values of N, including non integer values. The comment by *Mann and Chisham* (2000) which followed suggested that the 'real' bump on tail was located outside the energy range of the particle detector and that the Pg observed could be driven though either an interaction with 12 keV or 250 keV protons and an even or odd mode standing wave respectively. The findings of this study support the comments made by *Mann and Chisham* (2000) and indicate that an interaction with 12 keV protons is the more statistically likely in terms of both the MLT location of the particles and also the amount of free energy available.

The findings of this study also support modelling work undertaken by *Ozeke and Mann* (2001). Pgs are only observed in the morning sector under geomagnetically quiet conditions (*Chisham*, 1996). Following on from this work, *Ozeke and Mann* (2001) calculated the trajectories of protons in a dipole magnetic field and developed a model which would reveal favourable locations in particle energy, W and L - shell space for high m wave growth through wave particle interactions. Their model indicated that in the morning sector very monochromatic Pc4 waves, highly localised in latitude would be generated through a drift-bounce resonance interaction between a second harmonic standing mode wave and 10 keV protons; such waves fit the characteristics of Pgs. The work here also supports that of *Chisham* (1996) who indicated that Pgs are driven by 5 – 30 keV protons. He noted that under geomagnetically quiet conditions are ions which have been injected into the nightside on closed paths are able to drift to the morning sector. Under more active conditions, the $\mathbf{E} \wedge \mathbf{B}$ drifts are large, de-trapping the protons from their enclosed paths, causing them to follow convective paths to the dayside magnetopause, where the particles are lost.

5.6.2. Afternoon Sector Observations

In the afternoon sector, there appear to be two dominant particle driven wave types; radially polarised Pc4 pulsations which have been observed during geomagnetically quiet times and compressional Pc5 pulsations, so called storm time Pc5s, which have been observed during geomagnetically active times. *Engebretson et al.* (1992) utilised geosynchronous satellite observations to observe 21 pulsation events in the dayside magnetosphere. They concluded that the Pc4 pulsations occurred primarily in the dusk sector and surmised that the waves were driven through a resonant interaction with 100 keV protons. Storm time Pc5 pulsations have been seen in STARE (the Scandinavian Twin Auroral Radar Experiment; *Greenwald et al.*, 1978) data (*Allan et al.*, 1982, 1983). They are compressional waves of high m number ($m \sim$ -7 to -80) which are observed in the dusk sector during magnetically disturbed intervals. The wave onsets are closely associated with enhancements in the ring current as a result of newly injected plasma from the magnetotail (e.g. *Engebretson and Cahill,* 1981; *Allan et al.*, 1982) and it is agreed that they derive their energy through wave-particle interactions. They have been related to particle energies of between 10 and 70 keV, and it is generally agreed that they have an odd mode standing structure and are generated through a drift resonance interaction, (e.g. *Allan et al.*, 1982, 1983). Similar waves, termed 'diamagnetic class' waves have been observed in the dusk sector by *Woch et al.* (1990) who favoured an even mode standing structure using measurements from the GOES 2 satellite and a drift mirror mode instability, although they did not specify the energy of the interacting particle population. The authors suggest that the waves are related to the classical storm time Pc5s. Similar high m waves, but with an equatorward phase motion, have been seen in SABRE (the Sweden And Britain auroral Radar Experiment; *Nielsen et al.,* 1983) and BARS (Bistatic Auroral Radar System; *McNamara et al.*, 1983) coherent radar systems also in the dusk sector by *Yeoman et al.* (1992) and *Grant et a*l. (1992) respectively. They also suggested that these waves derive their energy from energetic particle populations. More recently, *Yeoman et al.* (2001) have observed high m Pc4 waves in the post-noon sector using the CUTLASS radars. They suggested the waves were driven through both drift and drift-bounce resonance with 37 – 57 keV and 35 – 41 keV protons respectively. In all cases the authors cited in this section have indicated further research must be undertaken as no one generation mechanism can fully explain their observations. Results from the study presented in this chapter indicate that in the post-noon sector there are populations of 10 -50 keV ions which contain free energy. Additionally, from figure 5.9, the populations do contain significant (>1×10^{10} J) free energy which would identify them as suitable candidates for driving any resonant wave mode. Only ~1 % of the total IDF population measured over the 2.5 years of the statistical study indicate protons of ~ 100 keV with free energy of > 1×10^{9} J. This figure increases to ~ 80% when considering 30 – 60 keV protons. The results from this statistical study thus support the findings of *Allan et al.* (1982, 1983) and also *Yeoman et al.* (2001).

5.6.3. Satellite Observations

Several authors have identified Pc4 waves as odd mode wave structures on the basis of magnetic field measurements made by satellites in the equatorial region (e.g. *Hillebrand et al.*, 1982; *Takahashi et al.*, 1992; *Cramm et al.*, 2000) and also compressional Pc5 waves as even mode structures (e.g. *Woch et al.*, 1990; *Takahashi et al.*, 1987). This method is notoriously difficult. The technique relies on the fact that an odd mode standing wave will have a node of the transverse component at the equator and an antinode of the compressional component, while a second harmonic mode will have the opposite configuration. Recent work by *Ozeke and Mann* (Dr. I. Mann, private communication) has suggested that any asymmetry in ionospheric conductivities could result in the node of the wave shifting out of the equatorial plane. This was examined by *Glassmeier* (1999) although this treatment of the electric field structure of the wave was questioned by *Mann and Chisham* (2000) due to the resulting non-integer N solution to the resonance equation. A universally acceptable model for the electric field structure has yet to be agreed on. If the possibility exists for the wave mode to shift out of the equatorial plane, then results which depend solely on this method of identification must be re-examined.

This study has indicated that very few ~100 keV particles possess significant amounts of free energy to impart to any resonant waves field at all MLTs. If these higher energy particles play a role in wave generation then either they do so under extremely rare occasions or they cannot be detected by current instruments, possibly due to pitch angle effects. The *Polar* spacecraft utilised in this study has a highly elliptical orbit and as such it is possible that it cannot detect particles with large pitch angles which would remain close to the equatorial plane in the magnetosphere. The European Space Agency's (ESA) Double Star mission which involves two spacecraft, one in a polar orbit and one in an equatorial orbit, will allow particle populations at different positions along the field line to be viewed simultaneously, thus allowing the plasma environment of the wave field to be more thoroughly examined.

5.7. Summary

This chapter has presented a statistical study of magnetospheric ring current ion populations using 2.5 years of IDFs. The IDFs were examined to ascertain the statistical likelihood of specific particles containing free energy and also how much free energy the populations contained. A study of this manner has never been undertaken. The results of this study indicate that lower energy (10 – 45 keV) protons are the dominant non-Maxwellian populations for any interacting wave mode. Not only is the occurrence of these particles dominant, they also routinely contain the largest amount of free energy (>10^{10} J). Particles of higher energies (>100 keV) are rarely observed to contain significant amounts of free energy (<10^9 J). This has proved a vital result in understanding the generation mechanism of high *m* ULF waves. Although this study alone cannot indicate the eigenmode structure of any interacting wave, when combined with previous work certain conclusions can be drawn. More IDFs containing free energy were observed in the dawn sector which, in agreement with the work of *Yeoman et al.* (2000), indicates that the dawn sector could be a more fertile region for high *m* ULF wave generation than previously thought. Additionally this work suggests that Pgs are more likely to be an even mode structure driven by a drift-bounce resonance interaction with 10 – 45 keV protons. The fact that this study has revealed very few possible sources of free energy from protons with energies > 45 keV indicates that it is highly unlikely that Pgs can be driven through a drift resonance interaction such as that cited by *Thompson et al.* (2001) and *Glassmeier et al.* (1999). This work supports the work of *Allan et al.* (1982, 1983) and *Yeoman et al.* (2001) in identifying pulsations in the dusk sector such as storm time Pc5 pulsations as fundamental mode oscillations which may be driven by particles in the 30 – 60 keV energy range in the dusk sector. This work has also indicated possible incompatibilities with work which utilises spacecraft data to identify the wave mode and on this data alone infers the driving particle population, which is generally calculated to be ~ 100 keV protons. As shown in this study, particles of higher energies (~ 100 keV) are rarely observed to contain significant amounts of free energy (<10^9 J). Possible flaws in this method of wave identification using spacecraft data have been outlined, which when combined with the results of this study imply that some wave events may have been mis-identified. It is also possible, however, that the higher energy particles (~100 keV) are not detected by the *Polar* spacecraft, possibly due to the high latitude location of the space craft which precludes measurements of particles with large pitch angles which would be confined to the equatorial regions of the magnetosphere. Further investigation is certainly needed utilising multi-satellite particle observations from projects such as Cluster or Double Star.

Chapter 6

Observations of a Morning Sector, Uncorrelated, High m Wave; Energy Considerations and Comparisons with Giant Pulsations

6. Introduction

Whilst it is generally agreed that ULF waves with a high azimuthal wavenumber (*m*) have their energy source in wave-particle interactions, many questions still remain as to their exact generation mechanism. In this chapter, two case studies are presented of a ULF wave which was observed in artificially generated irregularities using the CUTLASS HF radar and also by the EISCAT UHF radar. Conjugate measurements made by the CAMMICE (MICS) particle detector onboard the *Polar* spacecraft indicate a driving non - Maxwellian particle population. This is one of only three ever recorded examples of an event in which the wave was observed in the ionosphere and a driving particle population was observed in the magnetosphere. The first case study details the interaction mechanism which drives the wave. Statistical data are also presented from the TIMAS particle detector also on board the *Polar* spacecraft, but with a slightly lower energy range than that of CAMMICE (MICS). The statistical study adds weight to the conclusion that the wave was a second harmonic standing poloidal mode wave driven through the drift-bounce resonance mechanism.

The second case study quantifies the energy source of two classes of high *m* wave, by examining magnetospheric driving particle population and directly comparing these with the wave energy dissipated into the conjugate ionosphere. The calculations are undertaken for the wave described in case study 1 and an event detailed in a paper by *Wright et al.* (2001). This is the first time this amount of energy has been quantified and reveals experimentally that this process is a major route through which solar energy can enter into and effect the Earth's atmosphere.

6.1. Case Study 1 – Morning Sector Drift-Bounce Resonance Driven ULF Wave Observed in Artificially-Induced HF Radar Backscatter

6.1.1. Instrumentation

6.1.1.1. CUTLASS

The radar data presented here result from the generation of artificial ionospheric HF coherent backscatter. It has been previously documented that the EISCAT Heating facility located at Tromsø, Norway (*Rietveld et al.*, 1993) is capable of generating artificial field-aligned irregularities using high power HF radio waves (e.g. *Robinson*, 1989) that are detectable by both coherent and incoherent scatter radars (e.g. *Robinson et al.*, 1997). Under favourable ionospheric conditions it is possible to modify the magnetosphere-ionosphere coupling conditions using the EISCAT Heater. This study involves unmodulated F region heating during quiet magnetospheric conditions, with the main electrojet currents lying north of Tromsø. The action of the heater is thus restricted to increasing the backscatter cross-section which the F region ionosphere offers to HF coherent radars. The CUTLASS (Co-operative UK Twin Located Auroral Sounding System) radar is an HF coherent backscatter radar system located at Hankasalmi, Finland and Þykkvibær, Iceland, and forms part of the SuperDARN array (*Greenwald et al.*, 1995). CUTLASS is ideally situated for making observations of the heated volume over Tromsø (*e.g. Bond et al.*, 1997; *Eglitis et al.*, 1998), as shown schematically in figure 6.1. Here data is presented from the SP-UK-OUCH (Observations of ULF waves with CUTLASS and the Heater; *Wright and Yeoman*, 1999) experiment. In this experiment the CUTLASS radars run in a high temporal and spatial resolution mode, with Hankasalmi running a 6-beam scan (scanning beams 7 through to 2, inclusive) with an integration time of 1 s, whilst Þykkvibær runs a 3-beam scan (beams 13 - 15) with a 2s integration period. Thus both radars produce data with a temporal resolution of 6s. Both run in a high spatial resolution mode, with each radar having 75 range gates of 15 km length, centred on the heated volume at Tromsø. For the interval discussed in this paper only data from Hankasalmi was available for analysis. The EISCAT heater was in continuous operation at 50% power (using 6 X 80 kW transmitters, an ERP of ~130 MW), at a frequency of ≈ 4 MHz for 4-hour intervals. The heater produces artificial electron density irregularities in the F region ionosphere, which act as targets for the HF radar. The artificial targets have

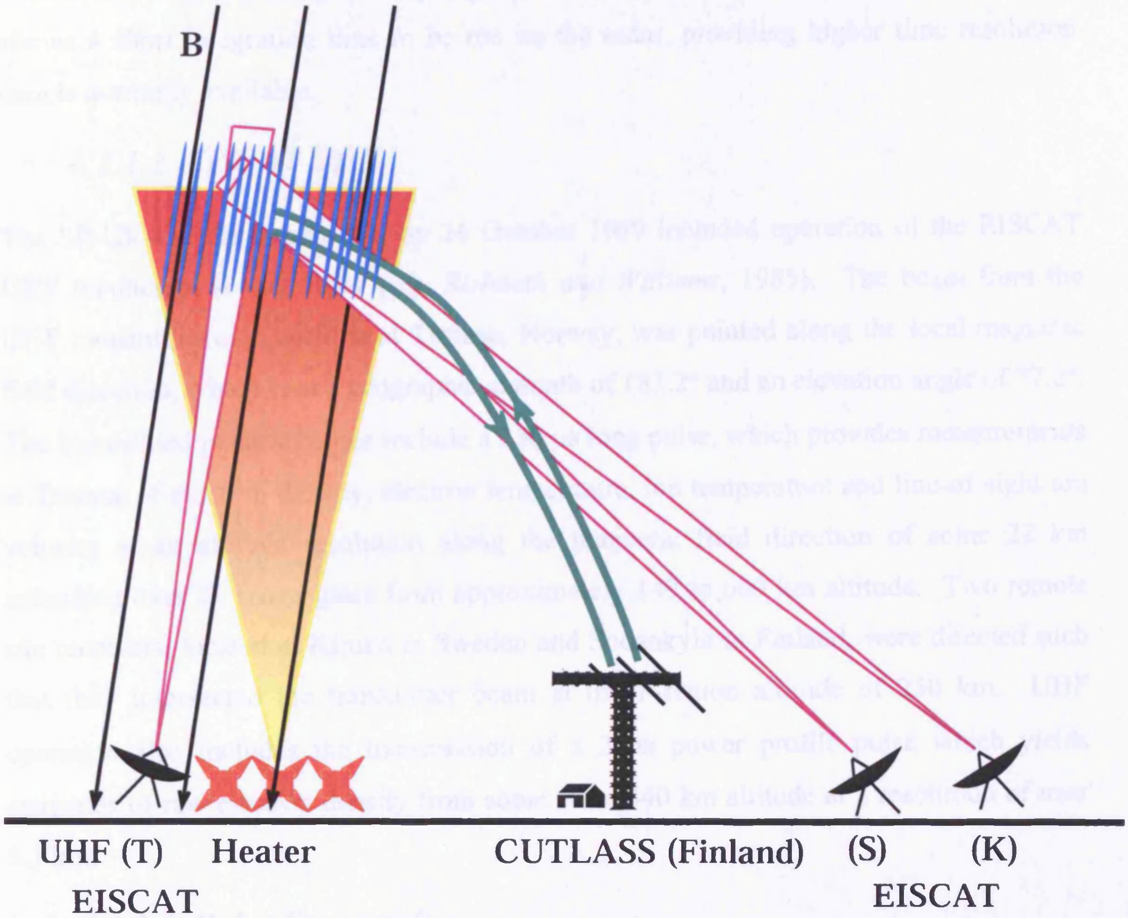

Figure 6.1. A schematic of the artificial backscatter experiment, SP-UK-OUCH. The Tromsø heater continuously heats the F region ionosphere, creating artificial ionospheric irregularities. Both the CUTLASS HF coherent backscatter radars, operating in a high temporal and spatial resolution mode, detect these irregularities. Measurements are also available from the EISCAT UHF incoherent scatter radar.

been demonstrated to accurately track the natural ionospheric convection velocity with the backscatter obtained being of very high power, and very narrow spectral width. This allows a short integration time to be run on the radar, providing higher time resolution than is normally available.

6.1.1.2. EISCAT UHF

The SP-UK-OUCH experiment on 26 October 1999 included operation of the EISCAT UHF incoherent scatter radar (e.g. *Rishbeth and Williams*, 1985). The beam from the UHF transmit/receive antenna at Tromsø, Norway, was pointed along the local magnetic field direction, which is at a geographic azimuth of 183.2° and an elevation angle of 77.2°. The transmitted pulse schemes include a 350 μs long pulse, which provides measurements at Tromsø of electron density, electron temperature, ion temperature and line-of-sight ion velocity at an altitude resolution along the magnetic field direction of some 22 km extending over 21 range gates from approximately 140 to 600 km altitude. Two remote site receivers, located at Kiruna in Sweden and Sodankylä in Finland, were directed such that they intersected the transmitter beam at the F-region altitude of 250 km. UHF operation also includes the transmission of a 21μs power profile pulse which yields estimates of raw electron density from some 60 to 340 km altitude at a resolution of near 3.1 km.

6.1.1.3. Polar Spacecraft

Data from the CAMMICE (MICS) and TIMAS instruments, which are two of the particle detectors onboard the *Polar* spacecraft are utilised for this study. A more detailed description of the satellite and its instruments can be found in chapter 4 of this thesis.

6.1.2. Observations

6.1.2.1. CUTLASS

During the experimental run of the SP-UK-OUCH, the artificial backscatter technique provided unprecedented spatial, temporal and electric field resolution. Figure 6.2 presents a colour-coded representation (flow away from the radars (negative velocities) are colour coded red, with flow towards the radars (positive velocities) colour-coded blue) of the l-o-s (line-of-sight) velocity measured by the CUTLASS Hankasalmi radar for radar range gates 20 through to 40. The experiment ran from 07:00 - 10:00 UT. The data shown are

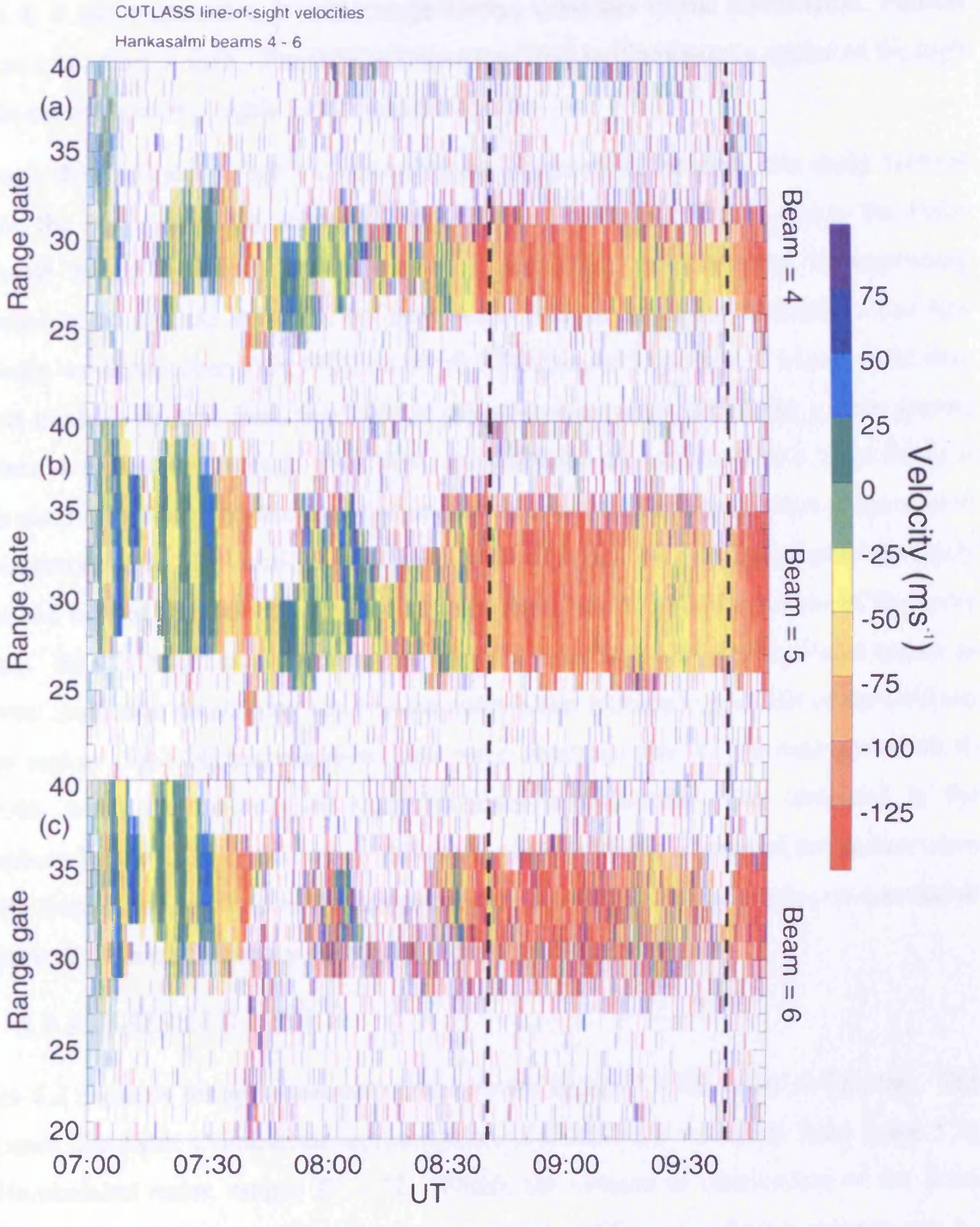

Figure 6.2. An overview of the CUTLASS line-of-sight velocity data for the SP-UK-OUCH experiment on 26 October 1999. The experiment ran from 07:00 - 10:00 UT. The data shown are Beams 4, 5 and 6 (panels a, b and c respectively) velocities of the Hankasalmi, Finland radar as a function of range gate. The velocities are colour-coded such that flow away from the radar (negative velocities) are indicated in red and flow toward the radar (positive velocities) are indicated in blue. The interval of data indicated with dashed vertical lines will be examined in detail in this chapter.

beams 4, 5 and 6 (panels a, b and c respectively) velocities of the Hankasalmi, Finland radar as a function of time. The EISCAT heater at Tromsø illuminates a region of the high latitude ionosphere of roughly one degree in latitude.

Although there are other, earlier, wave features observed in the data, this study focuses only on the later part of the interval from 08:40 to 09:40 UT. This is due to the *Polar* spacecraft being conjugate with Tromsø at this time and thus the corresponding magnetospheric particle data for the later wave interval has been obtained. The low frequency wave observed from 07:00 to 07:30 UT in beams 5 and 6 is of a large scale size, with an analysis of data from the IMAGE magnetometer array indicating a clear ground signature over this time period. Thus it is concluded that the earlier wave is most likely to be the result of a field line resonance or impulsive event with an energy source external to the magnetosphere. The details of this wave interval cannot be determined more precisely due to the limited number of wave cycles available, and the complex nature of the wave activity. By 07:18 UT clear evidence of a higher frequency wave, of the same nature as the event studied in detail here, can be seen in the lower latitude range cells of the artificial scatter region. IMAGE magnetometer data were examined also for the time period 08:40 – 09:40, when the majority of high frequency wave activity was observed in the ionosphere by the CUTLASS radar. Although some evidence is seen of the earlier wave activity from 07:00 to 07:30 in the magnetometer data as mentioned above, no conclusive evidence of the high frequency wave was viewed on the ground.

6.1.2.2. EISCAT UHF

Figure 6.3 presents the measurements taken by the EISCAT UHF radar at Tromsø. The top panel illustrates a timeseries representation of CUTLASS velocities from beam 5 of the Hamkasalmi radar, ranges 27 – 32. Within the volume of intersection of the three UHF receiver beams, the three measured components of line-of-sight ion velocity can be combined to provide the 3-dimensional ion velocity vector. In this case, the vector velocity, calculated at a temporal resolution of 15 seconds, has been resolved into components parallel and perpendicular to the local magnetic field direction. The field-perpendicular ion velocity has been further resolved into its component along and perpendicular to the direction of beam 5 of the CUTLASS Finland radar within range gate 28, this being the Finland range cell which corresponds magnetically to the UHF observation volume. These velocity components are illustrated in the bottom panel of

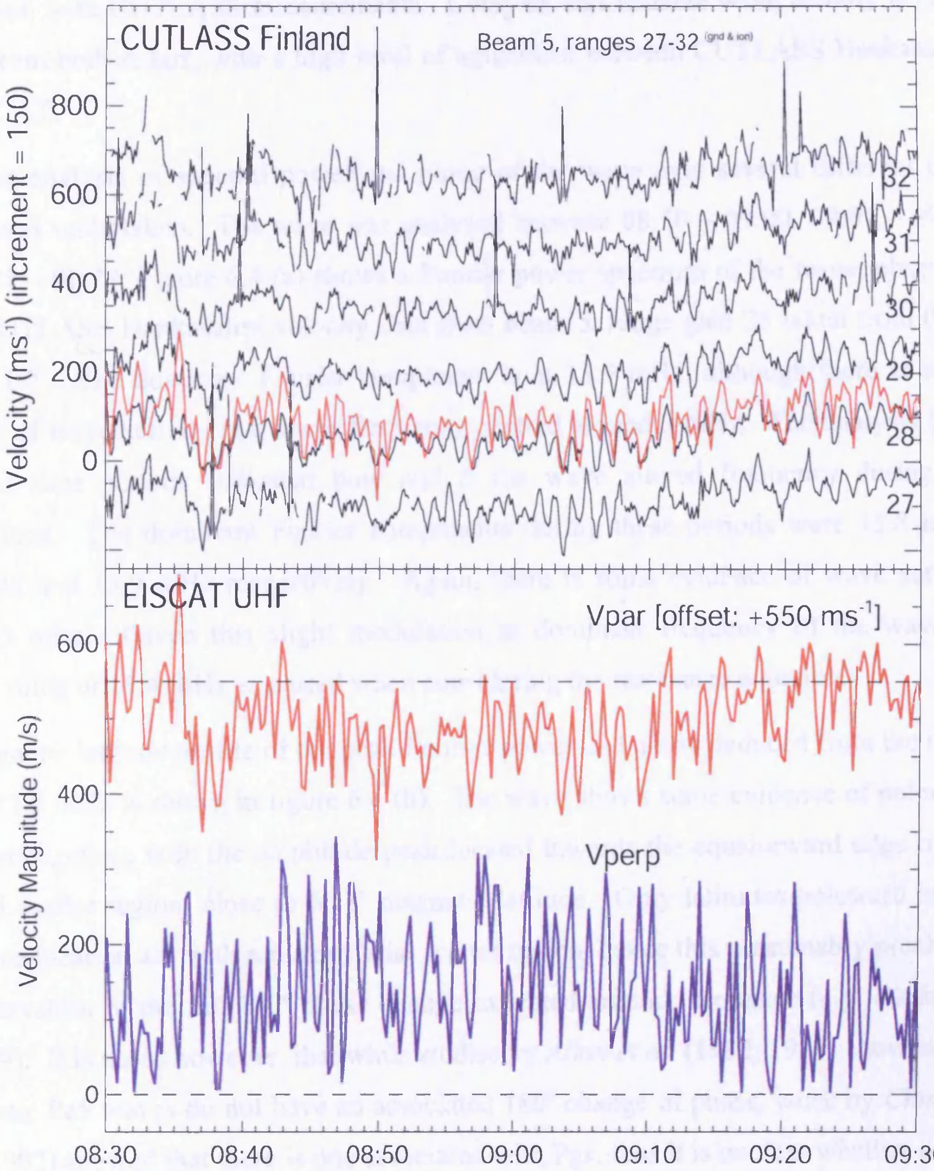

Figure 6.3. The top panel illustrates CUTLASS velocities from beam 5 of the Hankasalmi radar, ranges 27 - 32. The bottom panel illustrates the two field perpendicular components of the EISCAT radar tristatic velocity measurements, resolved parallel and perpendicular to the direction of CUTLASS beam 5, range gate 28. The parallel velocity is superimposed in red on the top panel to allow a direct comparison with CUTLASS measurements of the wave event shown in figure 2 and 3, using beam 5, range gate 28 for the interval 08:30 - 09:30 UT.

figure 6.3. The parallel velocity is superimposed in red on the top panel to allow a direct comparison with CUTLASS measurements. Complex and variable wave activity is clear in data from both radars, with a high level of agreement between CUTLASS Hankasalmi and EISCAT.

A Fourier analysis of spectral power and phase of the wave over several different time periods was undertaken. The wave was analysed between 08:50 – 09:00, 09:01 – 09:08 and 09:21 – 09:28. Figure 6.4 (a) shows a Fourier power spectrum of the wave; observed in the CUTLASS Hankasalmi velocity data from beam 5, range gate 28 taken from 0921 to 0928 UT. The dominant Fourier component is at 13.9 mHz, although there is some evidence of wave activity at a lower frequency centred around 3 mHz. The analysis from the other time periods indicated how and if the wave altered frequency during the observations. The dominant Fourier components during these periods were 15.8 mHz, 16.6 mHz and 13.9 mHz respectively. Again, there is some evidence of wave activity around 3 mHz. Given this slight modulation in dominant frequency of the wave an average value of 15.4 mHz was used when considering the resonance equation.

The magnetic latitude profile of the peak Fourier power and phase deduced from the radar data at 13.9 mHz is shown in figure 6.4 (b). The wave shows some evidence of poleward phase propagation, with the amplitude peak located towards the equatorward edge of the artificial scatter region, close to 66.3° magnetic latitude. Only latitudes poleward of the resonance location are within the artificial scatter region, hence this presumably precludes the observation of the full 180° phase change expected around resonance (e.g. *Walker et al.*, 1979). It is noted however, that while studies by *Allan et al.* (1982, 1983) showed that storm time Pc5 waves do not have an associated 180° change of phase, work by *Chisham et al.* (1992) showed that there is one associated with Pgs, thus it is unclear whether one is expected for this event. A comparison of beams 4 and 5 of the Hankasalmi radar, at the same magnetic latitude, which are thus separated in azimuth reveal that the wave has an azimuthal wavenumber, $m = -45\pm10$. The negative sign indicates that the wave displayed a westward phase propagation, in the same direction as gradient-curvature drifting protons.

An examination of estimates of the ionospheric Hall and Pedersen conductivities as derived from the EISCAT radar shows no significant modulations at the wave frequency for this event. Hence this small amplitude event does not modulate the ionospheric conductivity, unlike the large amplitude events studied by *Buchert et al.* (1999) and *Lester*

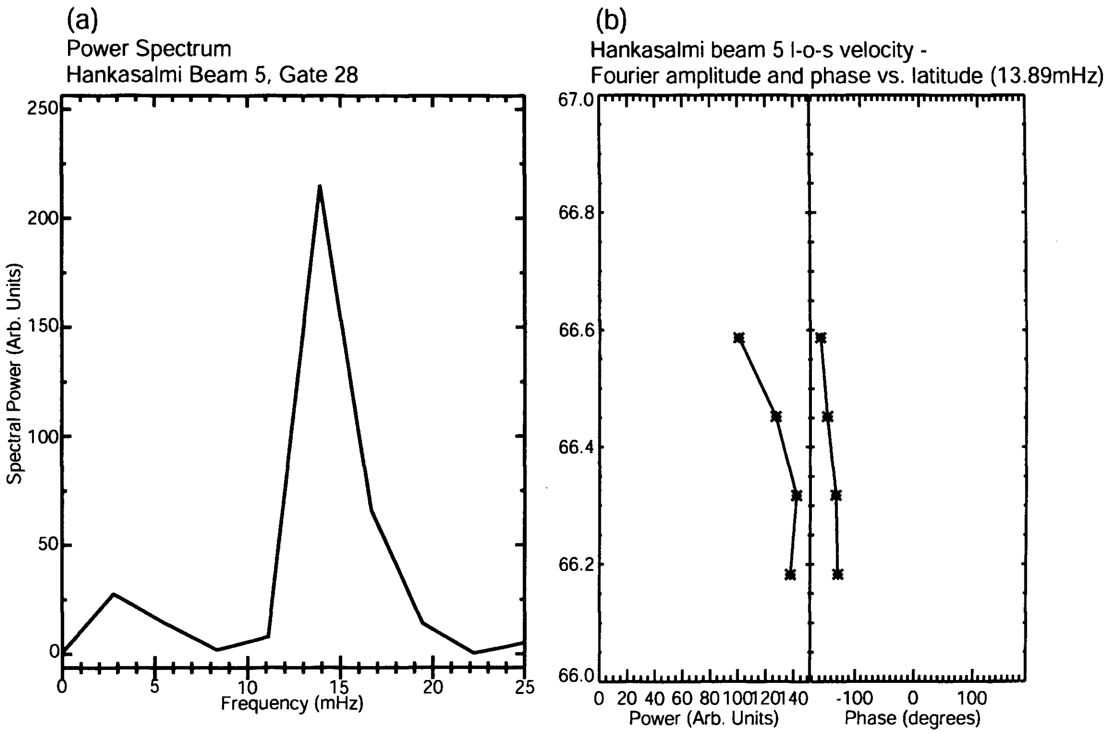

Figure 6.4. (a) Fourier power spectrum, (b) magnetic latitude profile of Fourier power and phase at 13.9 mHz over the same interval.

et al. (2000), which showed large ground magnetic field oscillations and accompanying conductivity modulations.

6.1.2.3. CAMMICE (MICS)

Figure 6.5 (a) defines the orbit of the *Polar* spacecraft, in SM coordinates. The specific interval studied in this paper is highlighted in grey. The footprint of the spacecraft mapped magnetically to Tromsø at a time of 09:05UT. Its on board instrumentation includes energetic particle detectors and magnetometers.

Figures 6.5 (b) and (c) show two particle distributions as measured by the CAMMICE (MICS) energetic particle instrument on board *Polar*, between a time of 09:00 and 09:10. The figures represent the ion distribution functions in phase space as a function of particle energy, and clearly demonstrate that an unstable (non-Maxwellian) population of protons with a positive gradient region in the energy range of 8 to 15 keV was observed on, or near the Tromsø fieldline. These measurements were made at a local time of 11:25 MLT as the spacecraft travelled southward in the Northern Hemisphere at an *L*-shell location of ~6. As mentioned earlier, this 'bump-on-the-tail' distribution implies that free energy is available to the wave if the resonance equation is satisfied at these energies.

6.1.3. Discussion

The wave presented in this chapter was observed to occur in the morning sector in artificially created field-aligned irregularities generated by the EISCAT heating facility located at Tromsø. Through an FFT analysis of line-of-sight velocity measurements made by the CUTLASS radar located at Hankasalmi the wave was shown to have a dominant frequency of ~ 15.4 mHz. A comparison of beams 4 and 5 of the Hankasalmi radar, at the same magnetic latitude, which are thus separated in azimuth reveal that the wave has an azimuthal wavenumber, $m = -45\pm10$. The characteristics of the wave are similar in nature to that of a Pg, however the magnitude of this wave is not sufficient enough for it to be detected on the ground. The negative sign of the m number indicates the wave has phase propagation, in the direction of gradient-curvature drifting protons that have been injected into the inner magnetosphere on the nightside.

Polar magnetic field observations reveal a short-lived wavepacket to exist as the spacecraft crosses the Tromsø field line. The frequency of the observed wave is consistent

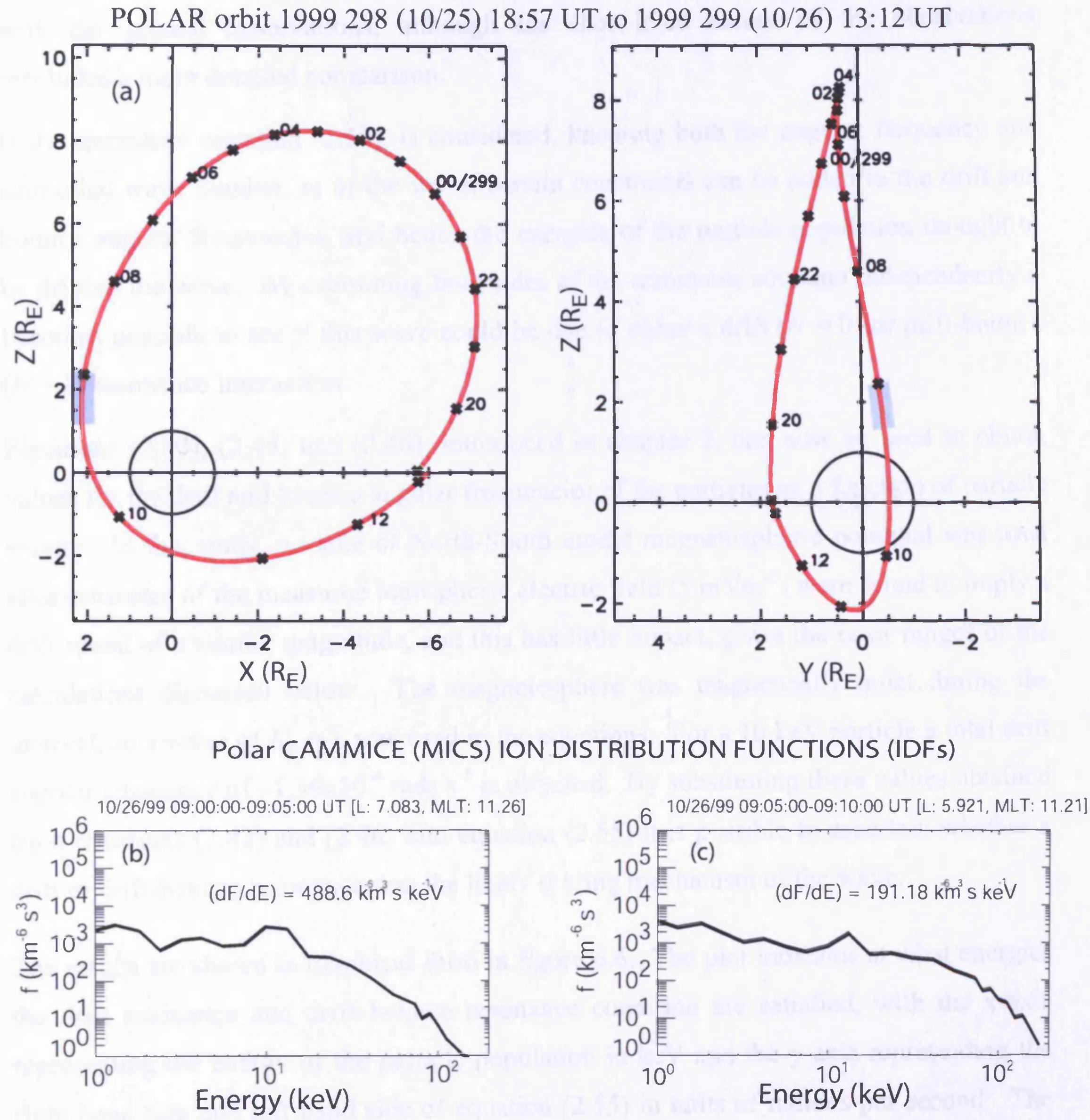

Figure 6.5. (a) A section of the orbit described by the Polar spacecraft on October 26, 1999 expressed in a Solar Magnetic coordinate frame. The shaded grey region indicates the interval where the ion distribution functions were derived from the on-board particle detector CAMMICE (MICS). (b) (c) Ion distribution functions, IDFs, derived from the CAMMICE (MICS) instrument for the intervals (a) 09:00:00-09:05:00 UT and (b) 09:05:00-09:10:00 UT. During this time the spacecraft traversed L shells 7.1 - 5.9 and 11:26 - 11:21 MLT.

with the ground observations, although the short-lived nature of the observations precludes a more detailed comparison.

If the resonance equation (2.55), is considered, knowing both the angular frequency and azimuthal wave number, m of the wave, certain constraints can be added to the drift and bounce angular frequencies, and hence the energies of the particle population thought to be driving the wave. By examining both sides of the resonance equation independently it becomes possible to see if this wave could be due to either a drift ($N = 0$) or drift-bounce ($N = 1$) resonance interaction.

Equations (2.42), (2.45) and (2.46), introduced in chapter 2, can now be used to obtain values for the drift and bounce angular frequencies of the particles as a function of particle energy. In this study, a value of North-South model magnetospheric potential was used after estimates of the measured ionospheric electric field (5 mVm^{-1}) were found to imply a drift speed of a similar magnitude, and this has little impact, given the error ranges of the calculations discussed below. The magnetosphere was magnetically quiet during the interval, so a value of $K_p = 2$ was used in the equations. For a 10 keV particle a total drift angular frequency of -1.36×10^{-4} rads s^{-1} is obtained. By substituting these values obtained from equations (2.42) and (2.46) into equation (2.55) it is possible to ascertain whether a drift or drift-bounce resonance was the likely driving mechanism of the wave.

The results are shown in graphical form in figure 6.6. The plot indicates at what energies the drift resonance and drift–bounce resonance condition are satisfied, with the x-axis representing the energy of the particle population in keV and the y-axis representing the right hand side and left hand side of equation (2.55) in units of radians per second. The blue areas indicate the right hand of the resonance equation, which deals with the contribution from the bounce angular frequency of the particles. Shown on the graph are the conditions for the $N = 0$, drift resonance and the $N = 1$, drift–bounce resonance condition. The pink area represents the left hand side of the resonance equation, which takes into account the angular frequency of the wave, the drift angular frequency of the particles and the azimuthal wave number m, of the wave. The spread in both the pink and blue lines represent the maximum errors brought about due to uncertainties in the parameters used to obtain values for ω_d, ω_b, m and ω_{wave}. Changes in the spacecraft location during the wave event, introduce errors in both L and φ. The largest errors come from the measurement of the angular frequency and m number of the wave and the value

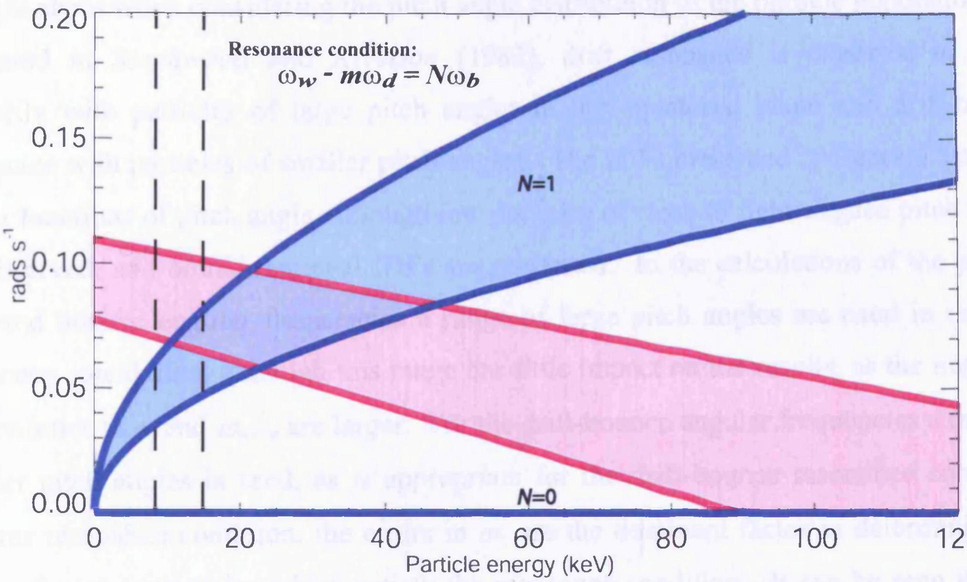

Figure 6.6. A graphical representation of the drift-bounce resonance condition (see text for details). It can be seen that the two shaded areas intersect at two locations, with these locations revealing the energies at which the resonance condition is satisfied. If free energy is available to the wave at these interaction energies in the form of a positive gradient in the IDF, then the particle population can provide energy for that wave mode. The dashed vertical lines represent the upper and lower particle energies of the positive gradient ($df/dW > 0$) as measured by the CAMMICE (MICS) instrument onboard the *Polar* spacecraft.

for particle pitch angle. As mentioned earlier in this chapter, the wave frequency does alter slightly during the period studied. When considering the resonance equation, values of the maximum and minimum frequency were used to ensure uncertainties were included. The *m* value of the wave also carries an error of +/- 10. Another source of errors is brought about when considering the pitch angle distribution of the particle population. As discussed in *Southwood and Kivelson* (1982), drift resonance is expected to occur primarily with particles of large pitch angles in the equatorial plane and drift-bounce resonance with particles of smaller pitch angles. The IDFs presented in figure 6.5 are not strong functions of pitch angle although few particles of close to field aligned pitch angles are observed, and omnidirectional IDFs are presented. In the calculations of the particle drift and bounce angular frequencies a range of large pitch angles are used in the drift frequency calculation, although this range has little impact on the results, as the impact of uncertainties in m and ω_{wave} are larger. For the drift-bounce angular frequencies a range of smaller pitch angles is used, as is appropriate for the drift-bounce resonance condition. For this resonance condition, the errors in ω_b are the dominant factor in determining the range of particle energies which satisfy the resonance condition. It can be seen that the lines intersect at two locations, with these locations revealing the energies at which the resonance condition is satisfied. If free energy is available to the wave at these interaction energies in the form of a positive gradient in the IDF then the particle population can drive that wave mode. From the graph it can be seen that a drift resonance process can be driven at ~ 110 keV or a drift-bounce resonance interaction at ~ 10 - 40 keV.

During the wave event, the CAMMICE (MICS) energetic particle instrument onboard the *Polar* spacecraft detected a non-Maxwellian population of protons drifting westward in the inner magnetosphere. The measurements were made at 09:05 – 09:10 UT (a local time of 11.25 MLT) as the spacecraft travelled equatorward through the Northern Hemisphere, crossing the Tromsø field line. The distribution had an energy range of 1-200 keV, with a clear bump-on-the-tail evident at an energy of ~8 – 15 keV. These energies overlap with the lower end of the predicted drift–bounce resonance condition presented in figure 6.6. It is thus clear that the wave observed by both the CUTLASS and EISCAT radars shows evidence of being generated by a drift-bounce resonance interaction between a second harmonic standing wave and a non-Maxwellian energetic particle population with a positive gradient located between 8 and 15 keV, but is not consistent with a drift resonance mechanism.

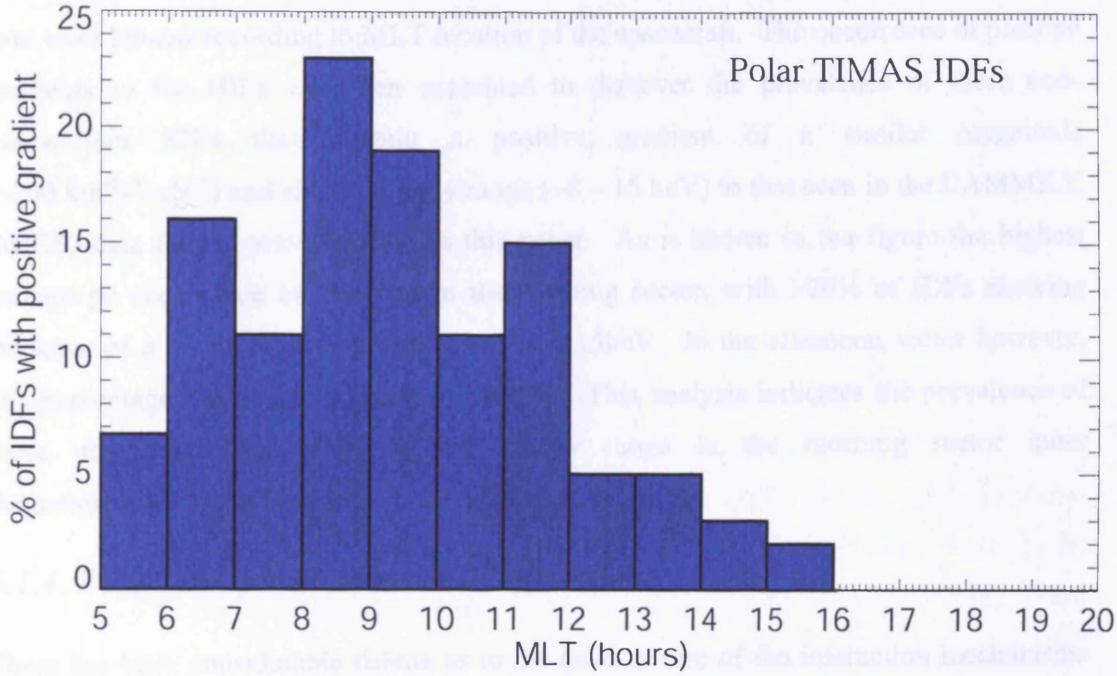

Figure 6.7. Results of a statistical analysis of almost three years of Polar TIMAS data from the Tromsø *L*-shell. The graph indicates the percentage occurrence of IDFs that contain a similar positive gradient over a similar energy range to the IDF seen in the CAMMICE (MICS) data in figure 6.5, as a function of magnetic local time.

Further analysis has been undertaken using 2.5 years (1996 – 1998), worth of data from the *Polar* TIMAS instrument (see chapter 5 for further details as to the statistical database). Intervals were considered when the spacecraft was located at a magnetic *L*-shell of between 5 and 8, and the orbits covered an MLT range of 06 – 18 MLT. Figure 6.7 describes results obtained in relation to the study of this morning sector wave. The data were binned according to MLT location of the spacecraft. The occurrence of positive gradients in the IDFs was then examined to discover the prevalence of these non-Maxwellian IDFs that contain a positive gradient of a similar magnitude (~300 $km^{-6}s^{3}keV^{-1}$) and similar energy range (~8 – 15 keV) to that seen in the CAMMICE (MICS) data for the wave studied in this paper. As is shown in the figure the highest percentage occurrence of this was in the morning sector, with ~20% of IDFs showing evidence of a positive gradient between 8 and 15keV. In the afternoon sector however, this percentage has decreased to less than 5%. This analysis indicates the prevalence of these non-Maxwellian IDFs at this energy range in the morning sector inner magnetosphere.

6.1.4. Relationship with Previous Observations

There has been considerable debate as to the exact nature of the interaction mechanisms for such wave particle interactions observed in the morning and afternoon sectors. Previous observations by *Yeoman and Wright* (2001), from the SP-UK-OUCH campaign have identified both drift (N = 0) and drift-bounce (N = 1) mechanisms as viable candidates for high m waves as observed in the high latitude ionosphere in the afternoon sector. In that paper evidence of a (N = 0) fundamental mode, which evolves into a (N = 1) second harmonic wave mode is presented. Here, I present evidence of a morning sector (N = 1) second harmonic drift-bounce resonance. While the characteristics of the wave discussed in this chapter are similar to those observed for Pgs, the amplitude of the wave is not large enough to be observed by ground magnetometers. Such Pg-like events in the morning sector have been demonstrated to be a common phenomenon (if a difficult one to observe), *Yeoman et al.* (2000). *Wright et al.* (2001) presented an example of a particle driven Pg. They present both data from the ground IMAGE magnetometer array and DOPE as well as conjugate particle data from *Polar*. In the paper they surmise that the wave was the result of wave–particle interactions between a non-Maxwellian particle population drifting westwards and a second harmonic standing wave through the drift-bounce ($N = 1$) resonance mechanism, the same interaction thought to be responsible for driving the wave presented in this paper. The azimuthal m number for the Pg is estimated to be -30±5. Results from chapter 8 of this thesis have indicated that both drift ($N = 0$) and drift-bounce ($N = 1$) mechanisms are evident in the afternoon sector of the magnetosphere, however, much controversy still surrounds the question of which is the dominant mechanism in the morning sector. There are conflicting theories as to the mechanism which drives the dawnside Pgs and other high m waves. Previous papers have cited both drift-bounce (second harmonic) resonance (*Chisham and Orr*, 1991) and drift (fundamental) resonance (*Takahashi et al.*, 1992). A recent paper by *Ozeke and Mann*, (2001) illustrates a model in which they reveal the energetically favourable locations in energy – L shell space where unstable particle distributions $df/dW > 0$ can occur. The model predicts the location of these particle populations by ascertaining the position where the open-closed orbit boundary of the azimuthally drifting particle population intersects a drift and drift-bounce resonance curve. During geomagnetically active times, closed orbit paths around the Earth become open and energetic particles can be injected onto them into the inner magnetosphere. If a period of low geomagnetic activity follows these paths become closed once more and the newly injected particles can drift round the Earth to the morning sector from their injection point on the nightside. In the morning sector they will on occasion match the local drift–bounce resonance condition. In their model, *Ozeke and Mann* (2001) show that only the $N = 1$ resonance curve crosses the open-closed westward orbit boundary in the morning sector. Thus they conclude that only the $N = 1$ resonance is a viable candidate to be driven by bump-on-the-tail distributions. The morning sector wave presented in this chapter is concluded to have similarly been brought about through the drift-bounce (N=1) resonance interaction mechanism. The model is thus in good agreement with the findings of this chapter.

At the low energy range of the positive gradient region in the IDF presented the drifting protons would have been strongly influenced by the dawn-dusk magnetospheric electric field. Due to the unpredictability of the drift paths of the protons under these conditions, it is very difficult to be able to identify an individual substorm particle injection event as a source of these particles. In fact, the energies are so low that the protons may not be the result of a substorm; rather the unstable population could be the result of other magnetospheric processes such as particle loss into the ionosphere or out of the magnetosphere through the dayside magnetopause. The magnetosphere was geomagnetically quiet for several hours before the wave on the 26th October 1999 was observed (an index of $K_p = 2$ was measured). Thus it is reasonable to hypothesise that the protons thought to be driving the wave are of low enough energy that they could have drifted, in the ring current from the nightside around to the morning sector, without being scattered out of the magnetosphere, again fitting in with the model of *Ozeke and Mann* (2001).

6.1.5. Summary

Data from both the CUTLASS HF radars and the EISCAT UHF radar have been analysed to investigate ULF wave processes observed in the morning sector of the inner magnetosphere. HF radar backscatter, which has been artificially-induced by the high power RF facility at Tromsø, provided ionospheric electric field data of unprecedented temporal resolution and accuracy. Data from the SP-UK-OUCH experiment have revealed small scale waves with an azimuthal wave number, $m = -45\pm10$, in the morning sector. An FFT analysis of the data revealed the angular frequency of the wave to be ~15.4 mHz. Conjugate observations from the *Polar* CAMMICE (MICS) instrument indicate the presence of a non-Maxwellian IDF, with evidence that free energy was available to the wave between 8 and 15 keV. An analysis of the resonance equation supports the conclusion that the wave observed was the result of a drift-bounce ($N = 1$) resonance interaction between a second harmonic standing wave and the non-Maxwellian particle population. Further statistical analysis was undertaken using the *Polar* TIMAS instrument to reveal the prevalence and magnitude of the non-Maxwellian energetic particle populations thought to be responsible for generating these wave types. It was seen that ~20% of all IDFs contain a positive gradient over a similar energy range as that seen in the data for the wave discussed here, in the morning sector only. The evidence presented suggests that the drift-bounce resonance condition, with particle populations of relatively low energy (~10keV) is the most likely mechanism for the bulk of such high m morning sector waves.

A statistical analysis of TIMAS and CAMMICE (MICS) data is presented in chapter 5 with the aim of discovering how prevalent non-Maxwellian IDFs are in both the morning and evening sectors of the magnetosphere, in addition to quantifying the magnitude and energy of the 'bump-on-the-tail' events. Chapter 7 will combine this statistical data base with ground based measurements to obtain evidence as to the exact nature of the energy generation mechanism for these high *m* waves observed in both the morning and afternoon sector magnetosphere.

6.2. Case Study 2 – Energy Considerations in Morning Sector particle-Driven High m ULF Waves

Through wave-particle interactions, energy is extracted from the magnetospheric particle population and ultimately dissipated into the ionosphere by the wave electric field through Joule heating (e.g. *Newton et al.*, 1977). Here, this amount of energy has been quantified for the first time by examining the energy available to the wave from the collisionless plasma of the ring current and comparing this to the energy dissipation due to the wave in the collisional ionospheric plasma. The calculations are undertaken for two case studies, typical of two classes of high *m* wave; (1) a wave that displays no corresponding ground magnetometer signature, a so-called uncorrelated wave (UW) which is detailed in case study 1 and (2) a giant pulsation or Pg, which, due to its large amplitude and modest azimuthal wave number, does have a corresponding ground magnetic signature. In addition, I present a statistical study using data from both the TIMAS and CAMMICE (MICS) instruments onboard the *Polar* spacecraft identifying the MLT distribution of such particle populations containing free energy. This statistical study provides a natural explanation for the both the rarity of Pgs (e.g. *Chisham*, 1996) and the ubiquity of other high *m* waves in this region.

6.2.2. Analysis Procedure

6.2.2.1. Energy Available from the Driving Particle Population

The theory and method used to obtain the amount of free energy possessed by the driving magnetospheric particle population is described in detail in chapter 5.

6.2.2.2. Energy Dissipated into the Ionosphere

To quantify the amount of energy dissipated in the ionosphere the method employed by *Greenwald and Walker* (1980) is used here. As explained in section 2.9.1 of this thesis, there exists a balance between the magnitude of the averaged downward wave Poynting flux into the ionosphere and the Joule dissipation rate within it;

$$\frac{1}{\mu_0}Eb = J_P E = \Sigma_P E^2, \qquad (6.4)$$

where μ_0 is the permeability of free space, J_P is the Pedersen current, Σ_P is the height integrated Pedersen conductivity, E is the magnitude of the wave electric field and b is the magnitude of the wave magnetic field. The total amount of energy dissipated into the ionosphere, P, can then be quantified by,

$$P = 2A\Sigma_P E^2 T_1, \qquad (6.5)$$

where A is the area of dissipation in the ionosphere, typically 1° latitude by 5° of longitude for a high m wave at $L \sim 6$, (see case study 1) and T_1 is the duration of the wave. The factor of 2 arises from the fact that the wave energy is dissipated simultaneously into both the northern and southern hemisphere ionospheres. In the calculations for the wave sink and source, the area of ionospheric dissipation and the flux tube volume calculations were identical, thus eliminating errors due to any potential underestimate of the spatial extent of the wave. In both the waves considered in this paper ground observations were made at Tromsø; an L-shell location of ~ 6.3.

6.2.3. Results

Here we have chosen two examples of high *m,* particle-driven waves. The first is an UW observed by both the CUTLASS and EISCAT radars in an experiment utilising the heating facility at the EISCAT Tromsø site (see case study 1). The second is a Pg observed by the DOPE system and the IMAGE magnetometer array (see *Wright et al.,* 2001). In both cases conjugate particle data from *Polar* particle instruments were available.

6.2.3.1. Case 1 – Uncorrelated Wave Observed on 26th October 1998

The details of the experimental set up and a full analysis of this wave event are available in section 6.1. The Pc4 wave had a measured frequency of ~ 14 mHz, and an azimuthal wave number, m of – 45 and was observed using the CUTLASS Hankasalmi radar in artificially generated backscatter during a special mode from 0840 – 0940 UT (1040 – 1140 MLT) on 26th October 1999. Figure 6.8 (a) indicates the line of sight velocities for individual range gates, (27-29) for beam 5 of the radar as a time series. Figures 6.8 (b) and 6.8 (c) indicate the X and Y magnetic field components, as measured by the IMAGE magnetometer at Tromsø and reveal that the wave has no associated ground signature.

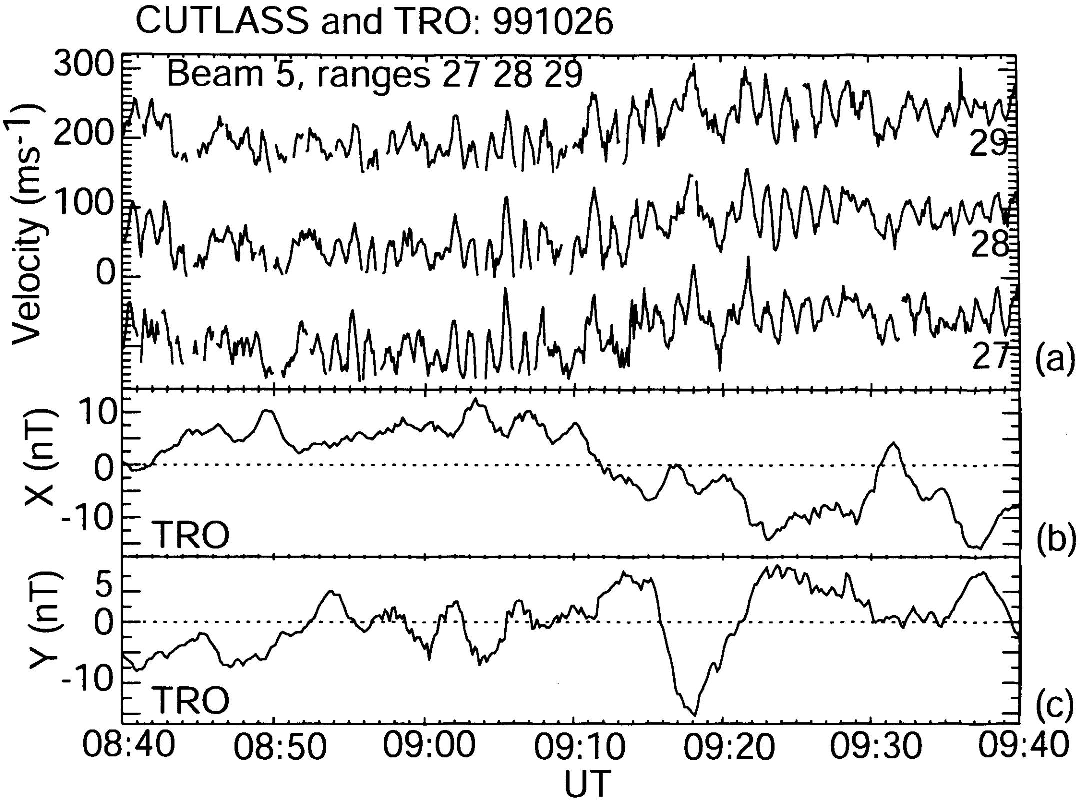

Figure 6.8 Data from the SP-UK-OUCH experiment on 26th October 1999, described as case study 1 in chapter 6. (a) CUTLASS stack plot for beam 5, range gates 27 - 29. (b, c) Conjugate measurements of the ground magnetic field as measured by the Tromsø magnetometer, for both the X (b) and Y (c) components.

The CUTLASS Hankasalmi and EISCAT Tromsø radars were utilized to obtain values for the ionospheric electric field, *E*, (5 mV m^{-1}) and the height integrated Pedersen conductivity, Σ_P (3 mho). By inserting these measured values for Σ_P and *E* into equations (6.4) and (6.5) it can be calculated that ~10^{10} J of energy was dissipated into the ionosphere during this wave event, at a dissipation rate of 7.5×10^{-5} W m^{-2}. Figures 6.5 (b) and 6.5 (c) show conjugate particle data for this event from the CAMMICE (MICS) instrument. This particle data revealed that free energy was available in the form of a positive gradient region at the correct energy to drive the observed UW, which was the result of a second harmonic standing wave interacting with protons of ~10 keV via the drift-bounce resonance interaction. Calculations utilizing equation (6.5) revealed that in this case there was ~10^{10} J of free energy available to the wave from the driving magnetospheric particle population.

6.2.3.2. Case 2 – Giant Pulsation (Pg) Observed on 16th May 1998

The details of the experimental set up and a full analysis for this event are available in *Wright et al.* (2001). The Pg had a measured frequency of ~6 mHz and an *m* number of ~ -30 and was observed using the DOPE system (figures 6.9 (a) and 6.9 (b)) on the 16th May 1998 at ~0600 UT (0800 MLT), lasting for approximately 3 ½ hours. Measurements made by the IMAGE network of magnetometers (figures 6.9 (c) and 6.9 (d)), revealed that the wave was of large enough amplitude to have a magnetic ground signature, most prominently in the Y component, with the peak amplitude of the magnetic oscillations occurring south of Tromsø. Unfortunately for this event, direct measurements of the electric field and height integrated Pedersen conductivities were unavailable. DOPE measurements imply an electric field of 8 mVm^{-1} at Tromsø (see *Wright et al.,* 1998 for details of the technique employed), suggesting an electric field of 15 mVm^{-1} at the Pg peak. Similar values were obtained by the SABRE radar (*Chisham et al.*, 1992) in one of only two radar detections of Pg pulsations ever recorded. This value is three times that measured for a UW. A typical value of the height integrated Pedersen conductivity was also used, $\Sigma_P \sim 3$ mho. Using equations (6.4) and (6.5) it was revealed that for this larger amplitude wave ~10^{11} J of energy was dissipated into the ionosphere at a local dissipation rate of 6.8×10^{-4} W m^{-2}, ten times more than that for the UW. Figure 6.10 (b) shows conjugate particle data for this event from both the TIMAS and CAMMICE (MICS) instruments. This particle data revealed that free energy was available in the form of a positive gradient region at the correct energy to drive the observed Pg, which was the

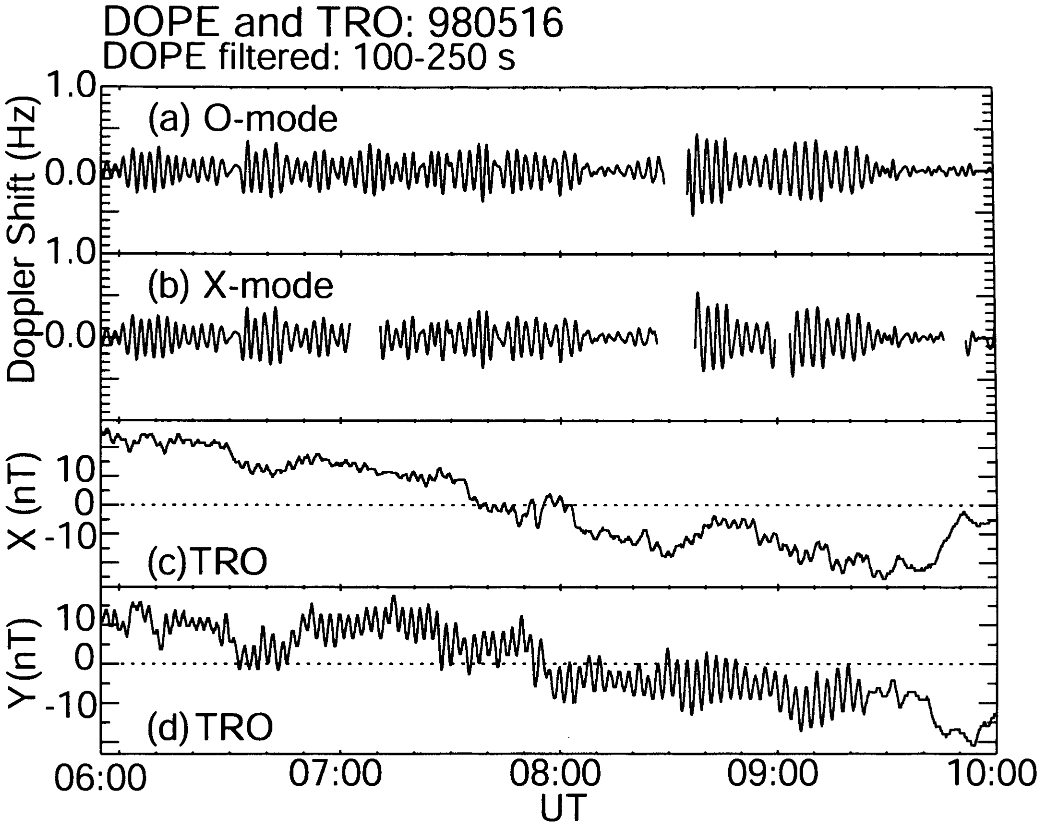

Figure 6.9. Taken from *Wright et al.* 2001, described as case 2 in chapter 6. (a) 0- and (b) X- mode, HF Doppler sounder data from DOPE and (c) X and (d) Y component ground magnetometer data from Tromsø (TRO) for 0600 - 1000 on 16th May, 1998 during the occurrence of a giant pulsation (Pg).

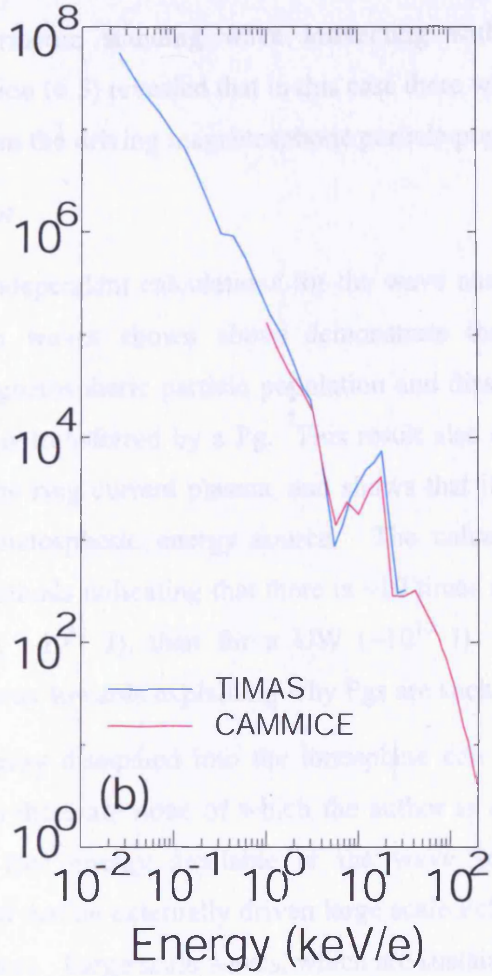

Figure 6.10. The conjugate driving ion distribution functions, IDFs, derived from the TIMAS and CAMMICE (MICS) instruments for the interval on 16th May 1998, 03:30 - 03:45 UT.

result of a second harmonic standing wave interacting with protons of ~7 keV. Calculations using equation (6.5) revealed that in this case there was $\sim 10^{11}$ J of free energy available to the wave from the driving magnetospheric particle population.

6.2.4. Discussion

For the first time, the independent calculations for the wave energy source and sink for morning sector high *m* waves shown above demonstrate that $\sim 10^{10}$J of energy is transferred from the magnetospheric particle population and dissipated in the ionosphere in a UW, whilst $\sim 10^{11}$J is transferred by a Pg. This result also quantifies the amount of energy extracted from the ring current plasma, and shows that it represents a major sink for this important magnetospheric energy source. The calculations are in excellent agreement, with both methods indicating that there is ~10 times more energy required for a Pg to be generated ($\sim 10^{11}$ J), than for a UW ($\sim 10^{10}$ J). This additional energy requirement goes some way towards explaining why Pgs are such a rare phenomenon.

Only values for the energy dissipated into the ionosphere can be directly compared to previous publications as there are none of which the author is aware which numerically detail the amount of free energy available at the wave source. *Greenwald and Walker* (1980) calculated that an externally driven large scale Pc5 wave dissipated $\sim 10^{13}$ J of energy in the ionosphere. Large scale waves, which are sustained by an external energy source, such as the Kelvin-Helmholtz instability or solar wind buffeting clearly involve larger energies than the internally driven waves examined here.

Allan and Poulter (1984) reported observations of a storm time Pc5 pulsation and also a Pg using the STARE radar, both wave types being driven by wave-particle interactions. They estimated that $\sim 10^{10}$ J dissipated into the ionosphere for the storm time Pc5; identical to the estimate made here for the UW, as detailed in case 1. In the case of the Pg, they also infer that the wave was the result of an even mode standing wave interacting through a drift-bounce resonance interaction with 10 keV protons, the same mechanism as proposed for the Pg detailed in case 2, and also ascertained that $\sim 10^{11}$ J was dissipated in the ionosphere, a value consistent with the calculations undertaken in this chapter.

6.2.4.1. Complementary Particle Statistical Study

In addition to the two studies, we also present a statistical study of the driving magnetospheric particles. The data base used here comprises of 2.5 years of IDF

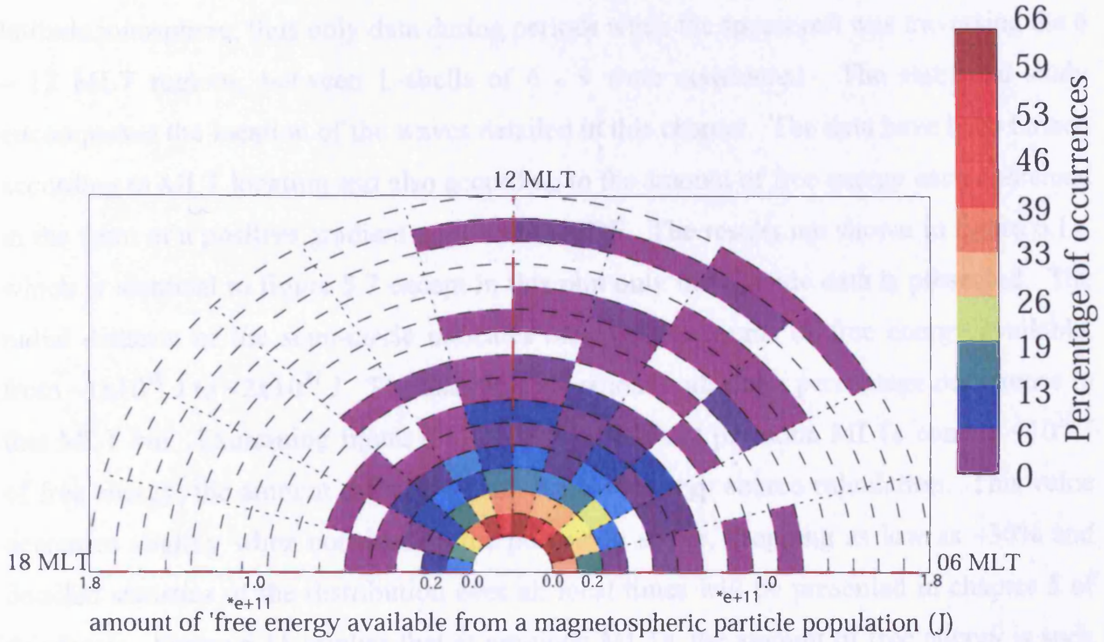

Figure 6.11. (Dayside section of figure 5.7) Results from a statistical study of magnetospheric particle populations, using the TIMAS and CAMMICE (MICS) instruments. Almost three years of data were binned according to MLT location and also according to the amount of free energy each IDF contained in the form of a positive gradient region. The radial distance from the centre of the semi-circle indicates increasing amounts of free energy available up to a maximum of 1.8×10^{11} J in bin increments of 1.2×10^{10} J. The data bins are colour coded as a percentage occurrence in that MLT bin.

measurements (in total ~ 2500 IDFs, with ~ 100 in each MLT bin) measured by both the TIMAS and CAMMICE (MICS) instruments, from March 1996 to December 1998. The particle energy range encompassed in this data base ranges from 1 to 328 keV. The data were selected according to spacecraft location in both MLT and L-shell. A more detailed description of this database can be found is chapter 5 of this thesis. The study presented here focuses on the dawn sector dayside magnetosphere which maps down to the high latitude ionosphere; thus only data during periods when the spacecraft was traversing the 6 – 12 MLT regions, between L-shells of 6 - 9 were considered. The statistical study encompasses the location of the waves detailed in this chapter. The data have been binned according to MLT location and also according to the amount of free energy each contained in the form of a positive gradient region in the IDF. The results are shown in figure 6.11, which is identical to figure 5.7 except in this plot only the dayside data is presented. The radial distance of the semi-circle indicates increasing amounts of free energy available, from ~1×10^{10} J to ~2×10^{11} J. The data bins are colour coded as a percentage occurrence in that MLT bin. Examining figure 6.11, ~65 % of IDFs at pre-noon MLTs contain ~10^{10} J of free energy; the amount consistent with the UW energy source calculation. This value decreases slightly when considering the post-noon sector, dropping as low as ~30% and detailed statistics of the distribution over all local times will be presented in chapter 5 of this thesis. Figure 6.11 implies that at pre-noon MLTs, the amount of free energy is such that UWs can be frequently generated via wave particle interactions if the resonance condition matches a field line eigenmode.

6.2.5. Summary

Calculations undertaken in this chapter indicate that ~10^{11} J is transferred from the ring current particle population into the ionosphere by a Pg. Examining figure 6.11 it is clear that less than 10% of the observed particle populations contain this amount of free energy. Pgs have been related to drift and drift-bounce resonance mechanisms with both fundamental (e.g; *Thompson et al.*, 2001) and second harmonic (e.g. *Wright et al.,* 2001) wave modes respectively. The two examples of Pgs discussed in this chapter (Case 2 here and the example from *Allan and Poulter,* 1984) both suggest a drift-bounce resonance interaction between a second harmonic standing mode and particles of energy of ~10 keV. For case 2 in this chapter, conjugate particle data were available which did indeed reveal a positive gradient region at ~10 keV. The statistical particle data presented here, thus suggests that even if the resonance conditions are met, Pgs will be a rare, morning phenomena due to the small statistical probability of a particle population containing enough free energy to drive the wave.

The statistical study undertaken also suggests that the conjugate existence of an IDF containing not only a positive gradient region at the correct particle energy, but also enough free energy to drive the Pg (*Wright et al.*, 2001) is very unlikely to be coincidental given the small probability of such an IDF existing in the magnetospheric particle population. This additional statistical evidence strongly supports the work of *Wright et al.* (2001) that the ~ 10 keV particle population was indeed the driving source of the Pg via the drift-bounce resonance interaction and is thus strongly supportive of a causal link between unstable IDFs in the magnetospheric ring current and high *m*, small scale waves in the magnetosphere.

The approach taken in this study demonstrates quantitatively how important ULF waves are when considering energy transport from the magnetospheric ring current into the high latitude ionosphere. Additionally, it offers a greater insight into the generation mechanism of the waves and allows a stronger case to be put forward for a preferential wave mode and particle energy. The technique is further enhanced by the complementary statistical study which, as shown here, strongly supports the conclusions drawn from previous observations that energy is fed to the Pg via the drift-bounce resonance interaction.

Chapter 7

Statistical Study of Ionospheric Signatures of ULF Waves

7. Introduction

The most accurate method of determining the wave eigenmode and interaction mechanism of a high *m* wave is through conjugate ground – satellite observations of a ULF wave and its driving particle population. The paucity of such observations (only three have been reported, one of which is detailed in chapter 6) has meant that there is much conjecture over the dominance of any particular generation mechanism and eigenmode, particularly in the morning sector. Additionally, in many publications, (e.g. *Engebretson et al.*, 1992; *Anderson*, 1993; *Yeoman et al.,* 2001) the authors do not have conjugate particle data and thus must speculate as to the nature of the interaction, in many cases stating that the waves are generated through interactions where free energy from an unstable, but unobserved, particle population in the magnetospheric ring current is fed into the wave mode. While theoretically a great deal of work has been done into examining the interaction mechanisms (e.g. *Southwood,* 1976; *Southwood and Kivelson*, 1982; *Cheng* 1982; *Pokhotelov et al.*, 1986; *Hasegawa,* 1991; *Cheng and Qian* 1994) the hypothesis that the waves are driven in this manner has rarely been experimentally tested. This chapter will firstly statistically test the assumption that the majority of high *m* ULF waves are indeed driven by unstable particle populations in the magnetospheric ring current using conjugate measurements of driving magnetospheric particle populations made by the *Polar* spacecraft and ionospheric wave observations made by the DOPE HF sounder. It will secondly present ionospheric observations of high *m* waves and ascertain, on a statistical basis, the more likely generation mechanism utilising the particle data presented in chapter 5.

The DOPE HF Sounder, located near Tromsø, Norway has been operational since May 1995 and is designed to make measurements of ionospheric signatures of ULF waves at high latitudes (see chapter 4 for a more detailed instrument description). The excellent ionospheric spatial resolution (of the order of 3 – 4 km for F-region reflection height, *Wright et al.*, 1997) and continuous operation of the instrument gives unprecedented observations of high *m* small spatial scale waves. Additionally, the location of the instrument is such that the observed waves are on field lines which map to the equatorial ring current, the major energy source for such pulsations. The system had an initial configuration of one frequency-stable transmitter and receiver with a ground separation of 50 km. While this original DOPE system still provided an excellent tool for detecting small scale waves in the ionosphere, only the wave frequency was able to be obtained. The lack of knowledge about the spatial scale of the wave in azimuth, due to the fact that only two beams in the same meridian (which were height separated) were in operation, meant that m numbers of the waves were not known. A statistical study using this original single path DOPE system was presented by *Yeoman et al.* (2001). They also presented the first measurement of a single high m wave using the new multi-path DOPE system ($m \sim -90$). Using this single measurement from the new DOPE system they inferred the azimuthal m number using a method outlined by *Yeoman et al.* (1992) of the ULF waves measured using the original DOPE system. In the study they demonstrated the existence of a possible new population of previously undetected waves in the pre-noon sector. In the first study presented in this chapter a Monte Carlo method is employed to test if the particle populations observed during conjugate ionospheric high m wave events have more free energy available than populations extracted at random from the database.

Previous statistical studies of ULF waves have utilised primarily satellite observations (e.g. *Arthur and McPherron*, 1981; *Kokubun et al.*, 1989; *Anderson et al.*, 1990; *Woch et al.* 1990; *Takahashi and Anderson*, 1992; *Anderson*,1993; *Cao et al.*, 1994). The main reason for using satellites was the difficulty in observing such small scale waves both in the ionosphere and on the ground using the instrumentation available. These studies have mainly focused on identifying the occurrence distribution of each type of wave as classified in the Pc scale (see table 3.1) and indicating those waves that were driven through wave-particle interactions. However, as detailed in chapter 3,satellites traversing an active region, often at great speed, are not always the optimal instrument to study the phenomena, and as such can often give an incomplete picture of the occurrence of highly localized, small scale waves. Although waves have been observed in the dawn sector of the magnetosphere, the studies all conclude that the dusk region is the dominant region for internally generated ULF waves. The eigenmodes of the waves have often been inferred using a single spacecraft measurement which therefore has very limited spatial information. This has lead to significant debate as to the dominant eigenmode of ULF wave populations (if one exists) in both the dawn and dusk sector. Knowledge as to the eigenmode structure of the wave is vital if the interaction mechanism is to be more fully understood (see section 3.2 for a more detailed discussion). The second study in this chapter will detail a statistical study using the new DOPE system which was upgraded in October 1998 from the single path system to a four frequency-stable transmitter (two at Seljelvnes, one at Skibotn and one at Kilpisjarvi) and four channel receiver (at Tromsø) system with a ground separation of between 40 and 90 km. This new system allows direct measurement of the azimuthal *m* number due to its multi path configuration. This chapter will present the most accurate ionospheric measurements of ULF waves utilising this new multi-path DOPE system. This study will be the first to statistically detail only high *m* waves where a direct measurement of the azimuthal *m* is made in the ionosphere. By obtaining measurements of the wave azimuthal *m* number and angular frequency, the resonance equation (equation 7.2) has been solved resulting in a hypothetical IDF with free energy available to either drive the wave through a drift or drift-bounce resonance interaction. The possible dominant eigenmode can then be inferred in a statistical nature when combined with the statistical particle data presented in chapter 5.

7.1. Statistical Study 1 - Monte Carlo Investigation

7.1.1. Particle Population database

The particle populations studied are all in the form of Ion Distribution Functions (IDFs). This format allows identification of any possible free energy, which manifests itself as a positive gradient region in the IDF, which could be fed into a resonant wave mode. The database used for the study comprises omnidirectional IDFs measured using the particle detectors on board the *Polar* spacecraft. A full description of the instruments can be found in chapter 4. A more detailed discussion of IDFs can be found in chapter 2, with details of the method utilised to obtain the amount of free energy available in chapter 7.

7.1.2 ULF wave database

The conjugate ground-satellite study presented here utilises the old single path DOPE system. This was due to fact that from October 1998 the data from the TIMAS particle instrument onboard *Polar* became unreliable. During this time, from May 1995 to October 1998, DOPE measured ~ 130 events. An example of a Doppler trace utilised in the study is shown in figure 7.1. The sounding frequency for the two frequency separated traces are

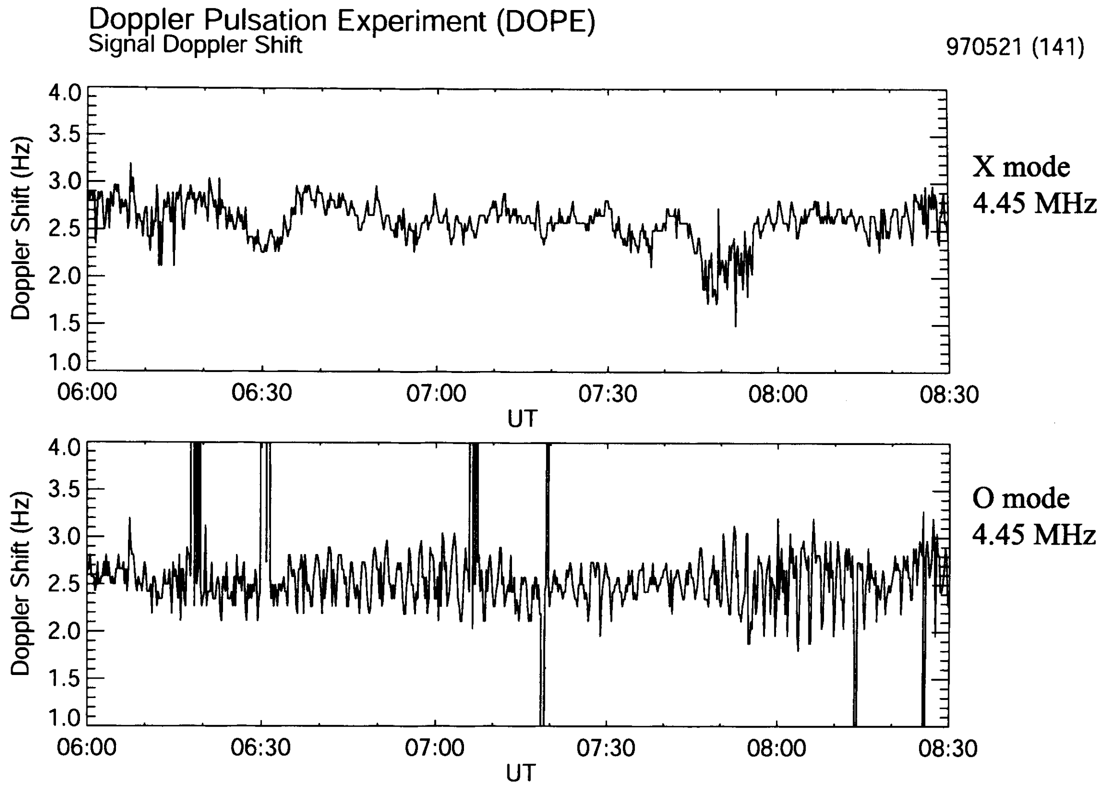

Figure 7.1. An example of a Doppler trace using the original 2 beam DOPE system. A ULF wave signature is seen in both channels, although predominently in channel 2 (O mode), between 0630 to 0820 UT. The DOPE sounding frequencies are shown to the right of each trace.

shown next to each plot. Both traces indicate the presence of a ULF wave from ~ 0630 to 0820 UT. The signal is larger in panel (b). Both traces show unfiltered data and as such there are data spikes, possibly due to an external source, in panel (b).

7.1.3. Statistical analysis

A spectral analysis was undertaken on ground magnetometer data to ascertain whether the wave displayed a conjugate ground signature. An example of this analysis is shown in figure 7.2. The filtered Doppler data from figure 7.1 is shown in panel (a). The data, from channel 2 presented in figure 7.1, has been filtered between 50 s and 300 s to remove the data spikes. Conjugate magnetometer data from the TRO magnetometer is also presented. The results of the spectral analysis undertaken on both the DOPE and magnetometer data are shown in figures (c) and (d). Figure 7.2 (c) indicates the wave observed by DOPE had a frequency ~ 8 mHz. Figure (d) indicates a ~ 3 mHz wave was observed in both the X and Y components of the TRO magnetometer data. The wave is classed as uncorrelated as there is no evidence of an 8 mHz wave in the magnetometer data. *Cummings et al.* (1969) presented tabulated frequencies for the first 6 harmonics for radial plasma density models r^{-n}, where $0 \leq n \geq 6$. The frequency ratio of the two waves presented here resembles that predicted by *Cummings et al.* (1969) for a toroidal fundamental eigenmode (~ 3 mHz) and a poloidal second harmonic eigenmode (~ 8 mHz) so it is possible that the two waves are harmonically related. A similar event has been documented by *Wright and Yeoman* (1999a).

Both databases were examined to obtain ULF waves events which displayed no ground magnetometer signature for which conjugate particle and wave data was available. As detailed in section 2.10, the majority of high *m* pulsations do not display a ground signature. The parameters imposed were that the particle data was obtained within a window of +/- 3 hours in UT of a wave being observed by DOPE. This amalgamation of databases resulted in only 7 wave events observed by DOPE for which particle data was available. Figure 7.3 shows the 7 IDFs for which a wave was observed at the conjugate point in the ionosphere. All the IDFs contain free energy in the form of a positive gradient region. To ascertain if there is a statistical cause and effect relationship between the driving particle populations and the waves, these 7 IDFs were examined and compared to the entire database. The positive gradient regions in the 7 conjugate IDFs occurred between particle energies of ~ 2 keV and ~ 15 keV and a spatial location of between 9 and

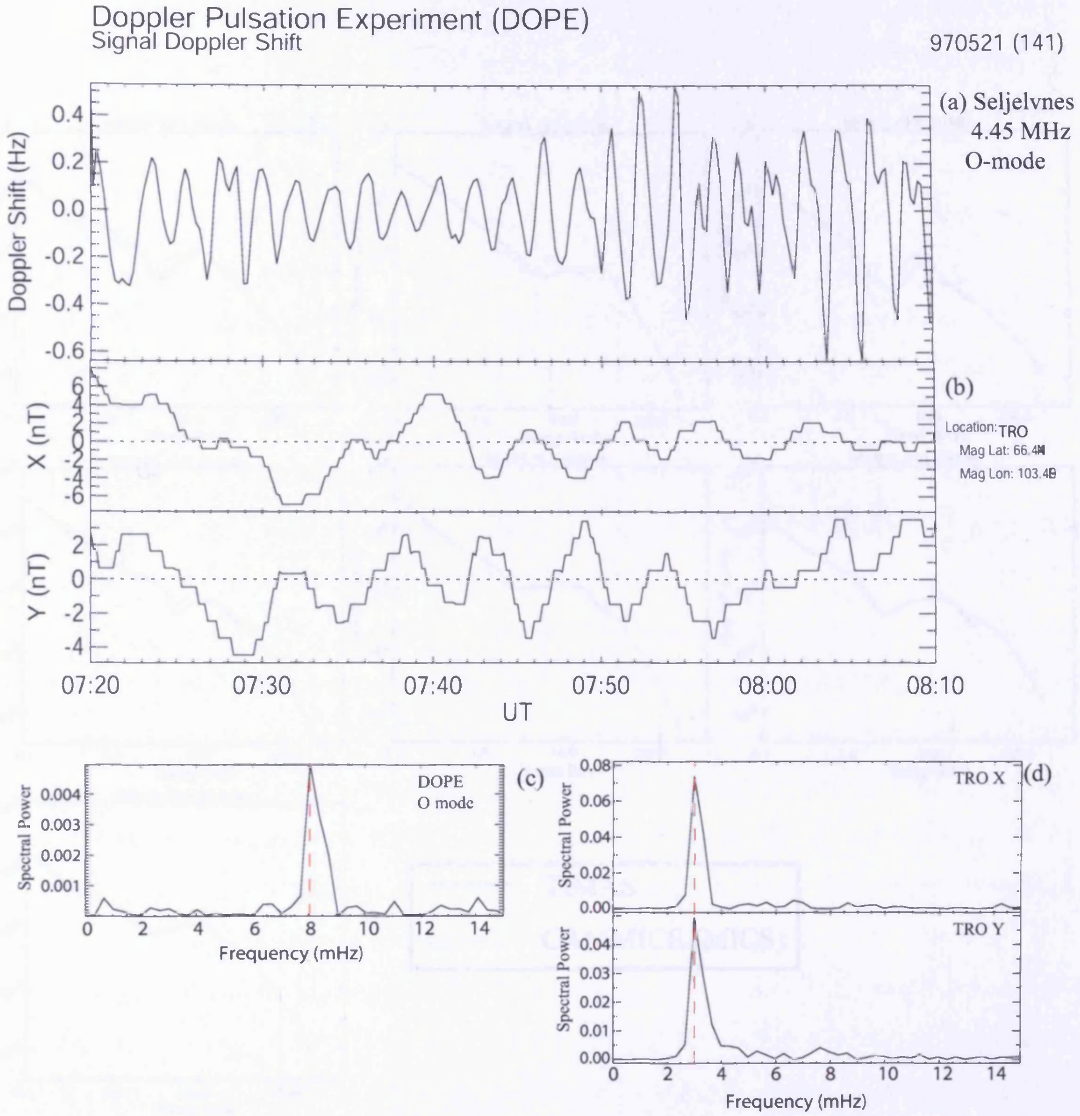

Figure 7.2. (a) The filtered O mode DOPE trace from figure 7.1 and (b) conjugate ground magnetometer data (X and Y components) from the TRO magnetometer. Results from a spectral analysis of both datasets indicates a 8 mHz wave is observed in the ionosphere and 3 mHz wave is observed on the ground in both the X and Y compnents. The ionospheric wave is classed as uncorrelated as there is no signature of it in the magnetometer data. The two waves however could be harmonically related.

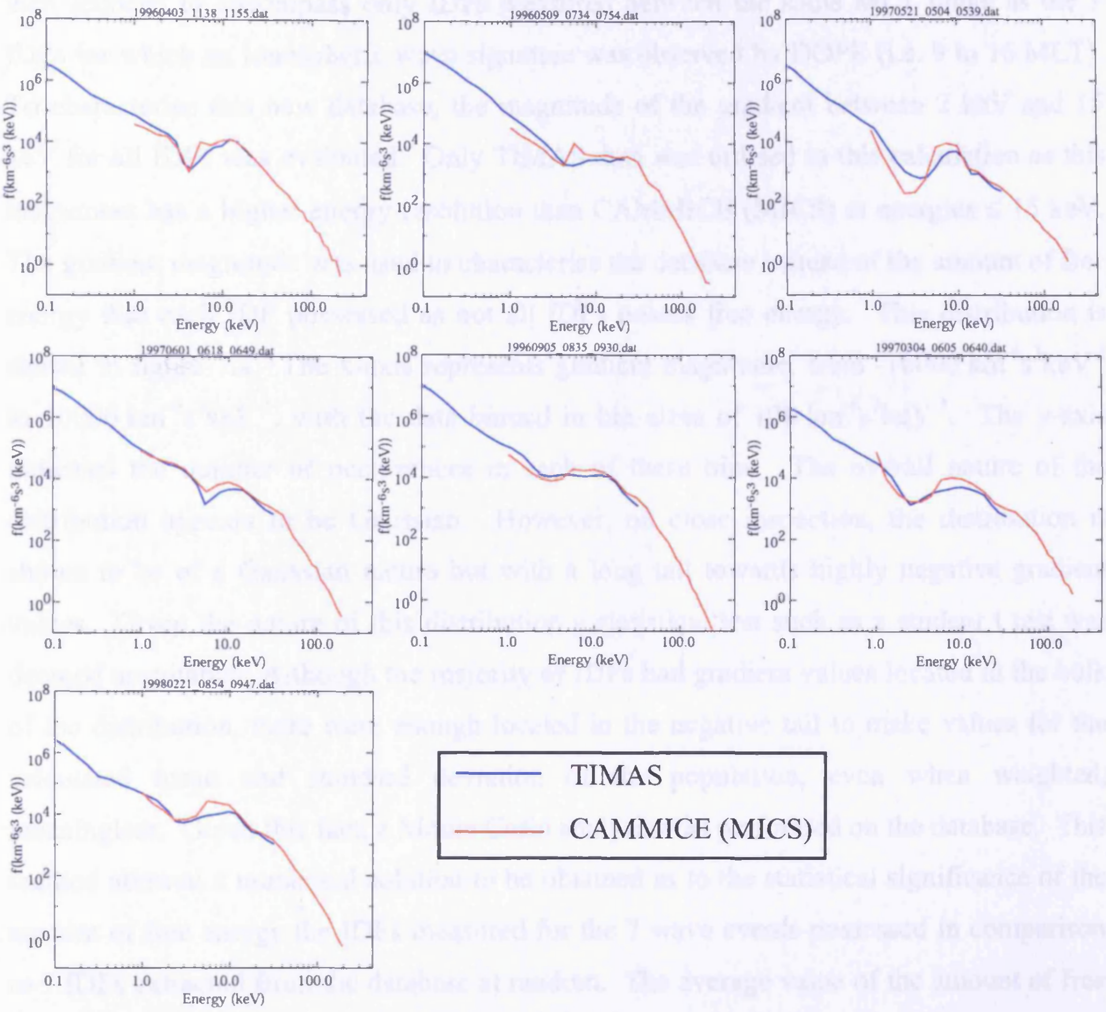

Figure 7.3. The 7 IDFs measured by the TIMAS and CAMMICE (MICS) instruments for which there was conjugate ionospheric wave observations from the DOPE HF sounder.

16 MLT. Using the method outline in chapter 5, the average amount of free energy available from these 7 IDFs was calculated to be ~$3\text{x}10^{10}$ J. The total IDF database was then reduced to encompass only IDFs measured between the same MLT range as the 7 IDFs for which an ionospheric wave signature was observed by DOPE (i.e. 9 to 16 MLT). To characterise this new database, the magnitude of the gradient between 2 keV and 15 keV for all IDFs was evaluated. Only TIMAS data was utilised in this calculation as this instrument has a higher energy resolution than CAMMICE (MICS) at energies ≤ 15 keV. The gradient magnitude was used to characterise the database instead of the amount of free energy that each IDF possessed as not all IDFs posses free energy. This distribution is shown in figure 7.4. The x-axis represents gradient magnitude, from -10000 $\text{km}^{-6}\text{s}^{3}\text{keV}^{-1}$ to 10000 $\text{km}^{-6}\text{s}^{3}\text{keV}^{-1}$, with the data binned in bin sizes of 100 $\text{km}^{-6}\text{s}^{3}\text{keV}^{-1}$. The y-axis indicates the number of occurrences in each of these bins. The overall nature of the distribution appears to be Gaussian. However, on close inspection, the distribution is shown to be of a Gaussian nature but with a long tail towards highly negative gradient values. Given the nature of this distribution a statistical test such as a student t test was deemed unsuitable. Although the majority of IDFs had gradient values located in the bulk of the distribution, there were enough located in the negative tail to make values for the calculated mean and standard deviation of the population, even when weighted, meaningless. Given this fact, a Monte Carlo analysis was performed on the database. This method allowed a numerical solution to be obtained as to the statistical significance of the amount of free energy the IDFs measured for the 7 wave events possessed in comparison to 7 IDFs extracted from the database at random. The average value of the amount of free energy possessed by these 7 randomly chosen IDFs was then obtained. In the case where the IDF possessed no free energy in the form of a positive gradient region between 2 and 15 keV a value of 0 J was recorded. The operation was performed 10000 times. The results are displayed in figure 7.5. The average amount of free energy possessed by 7 randomly extracted IDFs is shown on the x-axis in bin sizes of $2.8\text{x}10^{10}$ J with a percentage occurrence rate for each bin shown on the y-axis. The average amount of free energy available from the 7 IDFs for which a wave event was recorded ($3\text{x}10^{10}$ J) is marked with a red vertical dashed line.

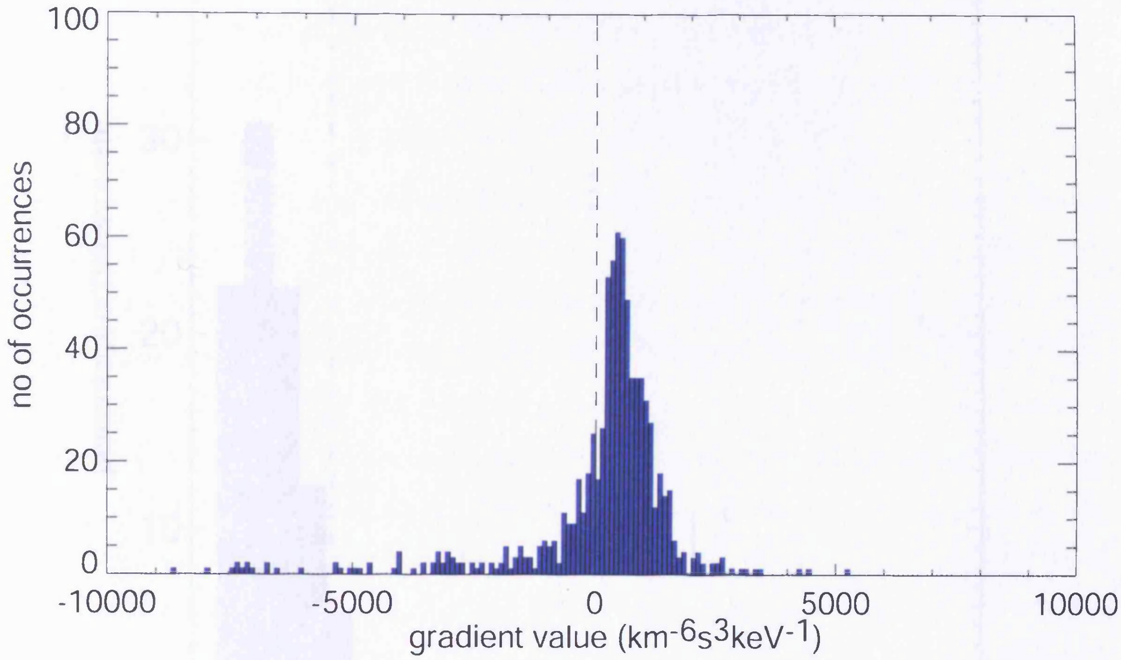

Figure 7.4. Distribution of the gradient magnitude measured between ~ 2 keV and 15 keV for all IDFs measured between 9 and 16 MLT.

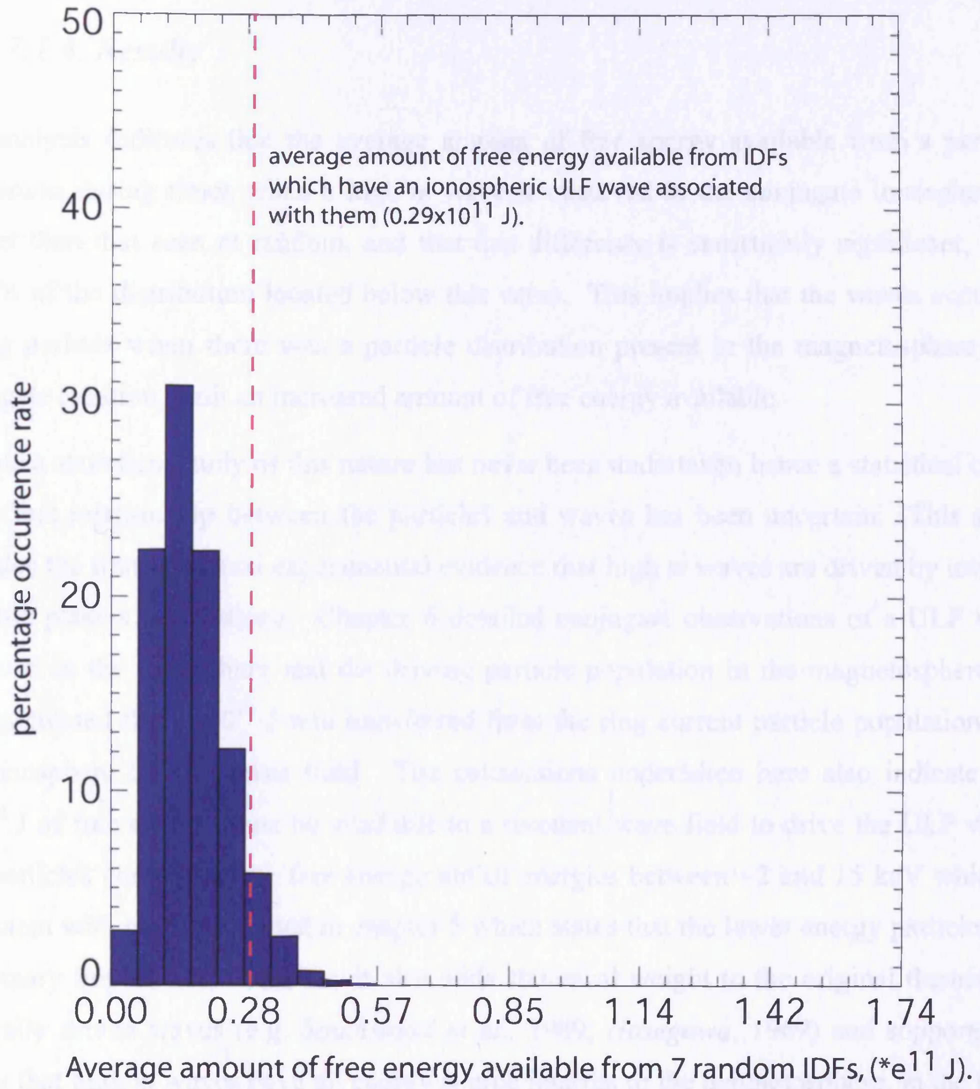

Figure 7.5. The distribution of the average amount of free energy available from a sample of 7 random IDFs extracted from the database described in this chapter. The average amount of free energy for the 7 IDFs for which a conjugate ionospheric ULF wave was detected by DOPE is marked with a vertical red dashed line. 89.5% of the distribution lies below this redline indicating a statistical cause and effect relationship between the driving particle populations and the ULF waves.

7.1.4. Results

The analysis indicates that the average amount of free energy available from a particle population during times when a high *m* wave is observed in the conjugate ionosphere is greater than that seen at random, and that this difference is statistically significant, with 89.5 % of the distribution located below this value. This implies that the waves occurred during periods when there was a particle distribution present in the magnetosphere at a conjugate location, with an increased amount of free energy available.

To date a statistical study of this nature has never been undertaken hence a statistical cause and effect relationship between the particles and waves has been uncertain. This study provides the first statistical experimental evidence that high *m* waves are driven by internal unstable plasma populations. Chapter 6 detailed conjugate observations of a ULF wave observed in the ionosphere and the driving particle population in the magnetosphere. It was calculated that $\sim 10^{10}$ J was transferred from the ring current particle population into the ionosphere by the wave field. The calculations undertaken here also indicate that $\sim 10^{10}$ J of free energy must be available to a resonant wave field to drive the ULF wave. The particles containing the free energy are of energies between ~2 and 15 keV which is consistent with work presented in chapter 5 which states that the lower energy particles are of primary importance. This result also adds statistical weight to the original theories of internally driven waves (e.g. *Southwood et al.,* 1969; *Hasegawa,* 1969) and supports the notion that high *m* waves have an energy source internal to the magnetosphere, in the form the magnetospheric ring current.

7.2. Statistical Study 2 - New DOPE statistics

7.2.1. Statistical database and analysis technique

This study focuses on 27 pulsation events measured by the new multi-path DOPE system between October 1998 and March 2002. During this period the DOPE system measured ~ 160 pulsation events in total. The 27 included in this study were extracted due to a simple selection criterion, that a clear wave signature that consisted of at least 10 full wave cycles was observed in all four paths. An example of a wave Doppler trace included in the study is shown in figure 7.6. The four panels, (a) to (d), indicate the Doppler trace for each of the paths. The sounding frequency is also shown along with the transmitter station location on the right hand side of each trace. A ULF wave is observed between ~ 11.30

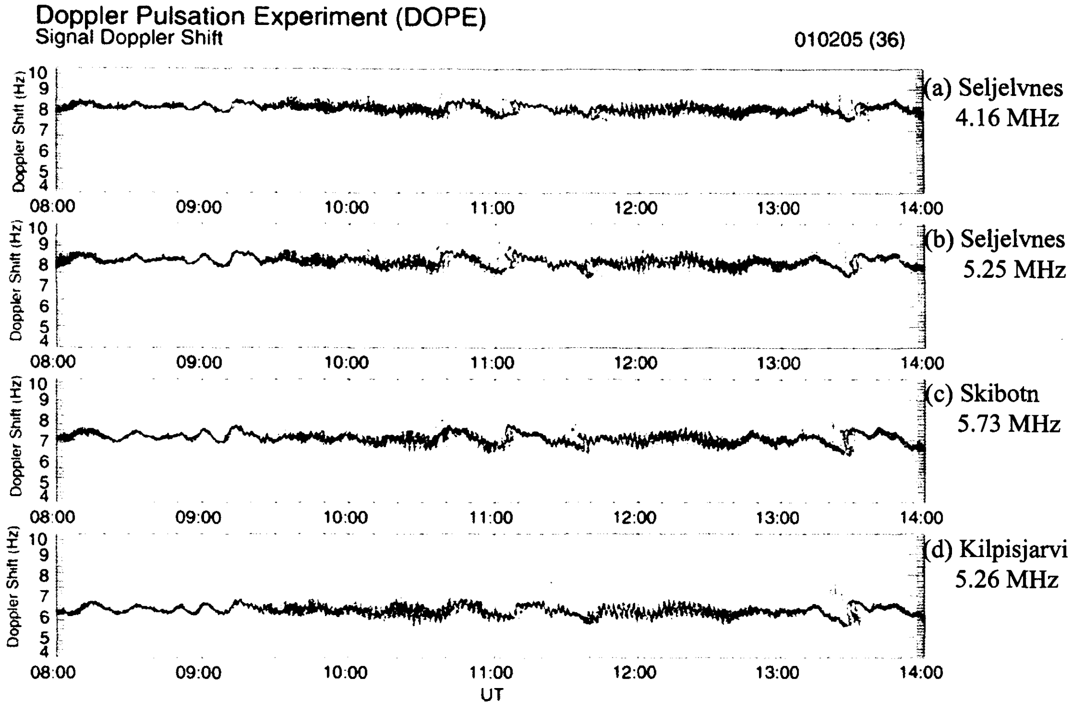

Figure 7.6. An example of a Doppler trace from the new multipath DOppler Pulsation Experiment (DOPE). The four traces are at different sounding frequencies and locations, as shown on the right hand side of each plot. A ULF wave signature is clearly visible between ~ 11.30 and 12.30 UT. There is also an Atmospheric Gravity Wave (AGW) signature in the trace between 10.30 and 14.00 UT.

and 12.30 UT. There is also an atmospheric gravity wave (AGW) signature in the trace from ~10.30 UT to 14.00 UT. Figure 7.7 indicates a peak trace plot for the same interval. This is achieved by joining together spectral maxima for consecutive integration intervals. The peak trace thus returns a single Doppler shift value for each point in time allowing a time series analysis to be undertaken. The data were filtered with a low cut off of 20 s and a high cut off of 500 s (50 mHz to 2 mHz) to remove the effects of the AGW from the trace. The wave can now be seen more clearly and this process also highlights the problem of obtaining a definite start time for the wave. Figure 7.7 (d) shows the wave more clearly than the other three traces and indicates a start time of ~ 10.00 UT. Although the wave is also seen in figure 7.7 (a) its amplitude is half that of figure 7.7 (d) and the start time is ~ 11.50 UT.

For all 27 events the average UT was obtained from the start and end times of all four traces. This was then translated into an MLT location where MLT = UT+2.0 for DOPE. The data were then passed through an FFT routine to obtain the dominant frequency of the wave. Figure 7.8 shows the frequency analysis results for each of the Doppler traces in figure 7.7. The FFT analysis used unfiltered data to reduce the chance of any false spectral peaks due to the filtering process. The time range over which the FFT analysis was undertaken was the same for each Doppler trace (11.40 – 12.30 UT). The plots are all in the form of frequency (mHz) vs. spectral power. There is evidence of smaller peaks located at ~ 1 mHz, possibly due to the AGW. The dominant peak in all four traces is at 8 mHz, placing the wave in the Pc4 class.

The phase of the wave at the peak spectral power was also obtained for each trace. The first two DOPE traces are from the same transmit - receive system (Seljelvnes to Tromsø) at different frequencies and hence have different reflection altitudes but should have similar phase values. By comparing the phase difference between the paths the azimuthal *m* number can be obtained. This phase difference is illustrated in figure 7.9. The trace is over the time period for which the FFT analysis was undertaken and is filtered between 2 and 33 mHz. The two red lines indicate points at the same phase of the wave cycle on each of the traces and indicates a phase lag between the different paths. Figure (a) indicates the trace from Seljelvnes while figure (d) indicates the trace from Kilpisjarvi. The slope of the red lines indicate that the wave is westward propagating as it is observed first by the path between Kilpisjarvi and Tromsø. This calculation was undertaken for various combinations of stations to allow a comparison of the different *m* values. For the

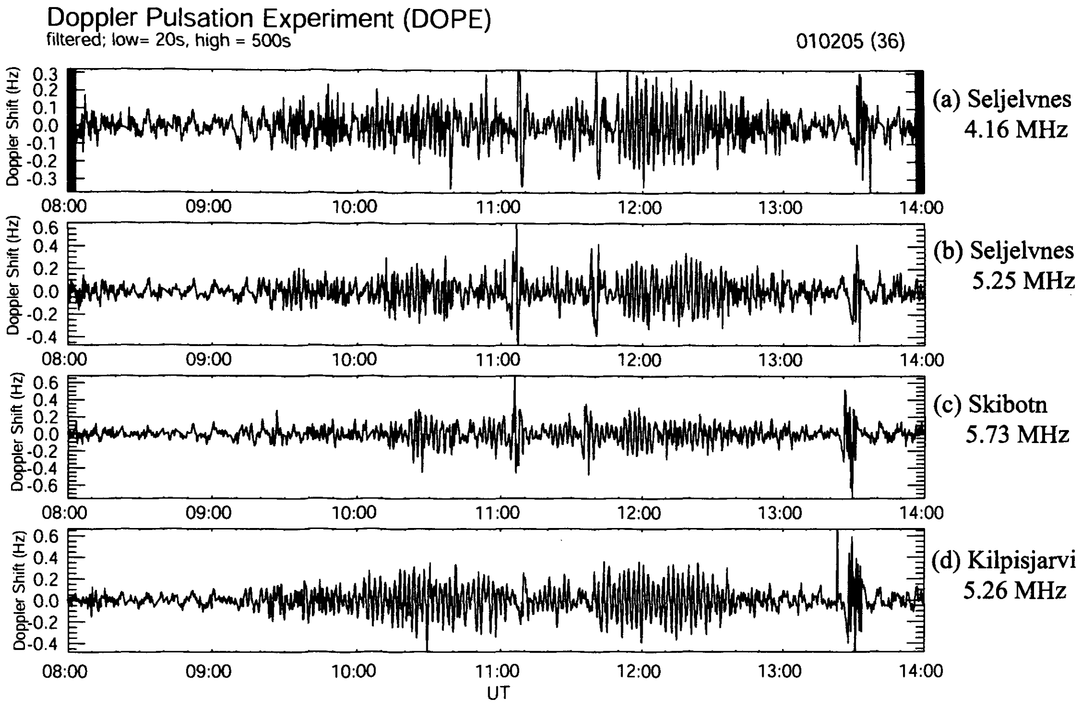

Figure 7.7. The peak trace for the same interval presented in figure 7.6. The peak trace is achieved by joining together spectral maxima for consecutive integration intervals, thus returning a single Doppler shift value for each point in time allowing a more accurate analysis to be undertaken. The data were filtered with a low cut off of 20 s and a high cut off of 500 s (50 mHz to 2 mHz) to remove the effects of the AGW from the trace.

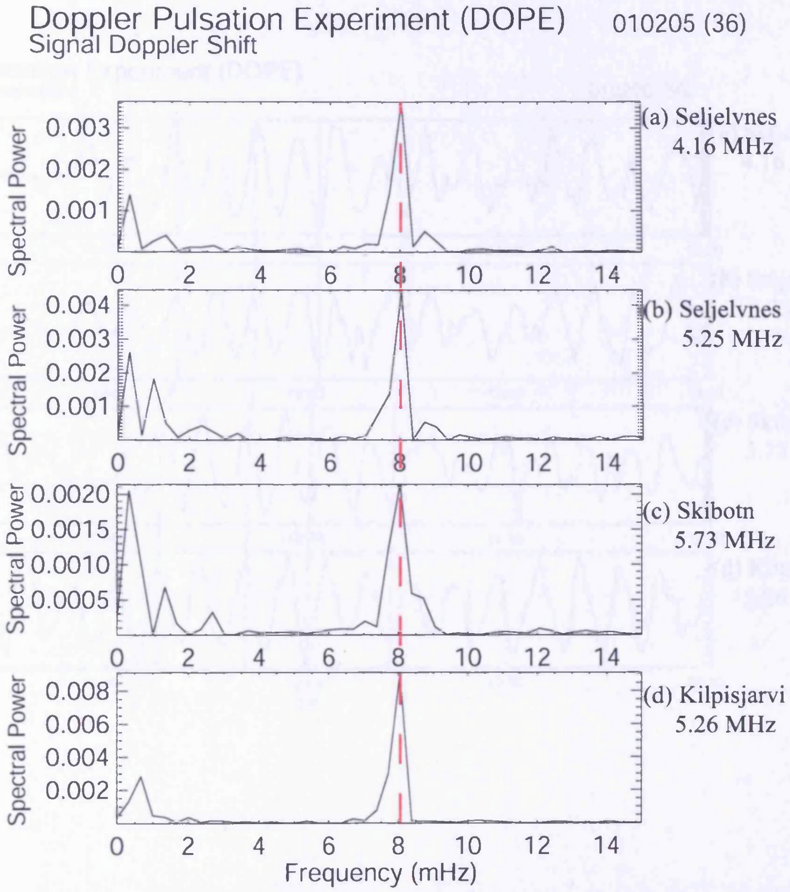

Figure 7.8. The frequency analysis results for each of the Doppler traces in figure 7.7. The FFT analysis used unfiltered data to reduce the chance of any false spectral peaks due to the filtering process. The time range over which the FFT analysis was the same for each Doppler trace (11.40 - 12.30 UT). The plots are all in the form of frequency (mHz) vs. spectral power. There is evidence of smaller peaks located at ~ 1 mHz, possibly due to the AGW. The dominant peak in all four traces is at 8 mHz, placing the wave in the Pc4 class.

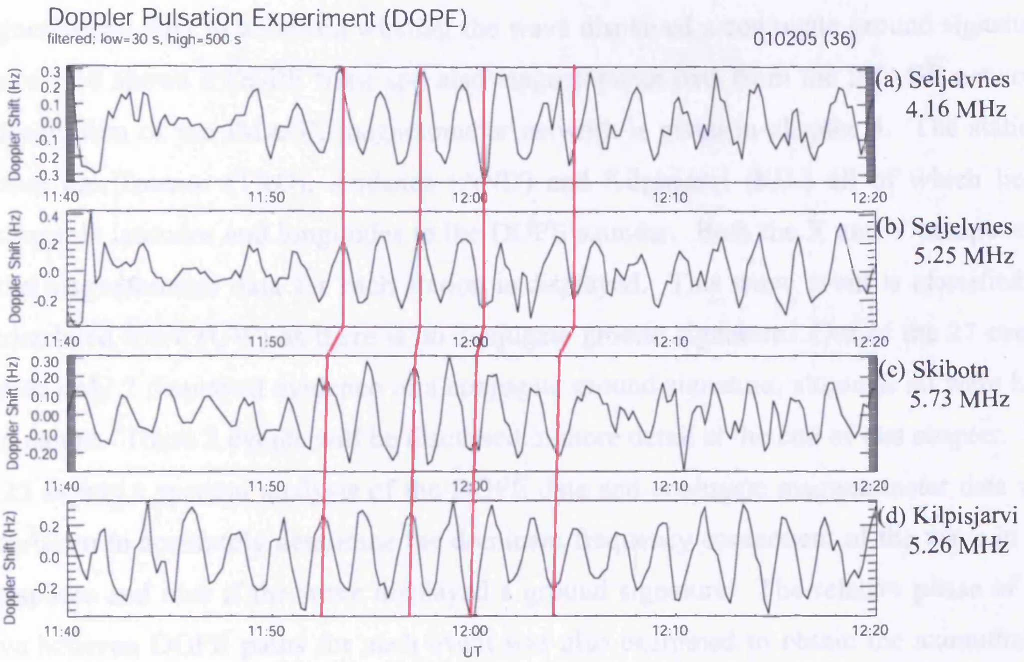

Figure 7.9. The trace is over the time period the FFT analysis was undertaken and is filtered between 2 and 33 mHz. The two red lines indicate points at the same phase of the wave cycle on each of the traces and indicates a phase lag between the different paths. Figure (a) indicates the trace from Seljelvnes while figure (d) indicates the trace from Kilpisjarvi. The slope of the red lines indicate that the wave is westward propagating as it is observed first by Kilpisjarvi.

event presented in figure 7.9 the *m* number was calculated to be ~-200. A calculation was not undertaken between the Skibotn and Kilpisjarvi traces due to the fact that the latitudinal spacing of their ionospheric reflection points (0.17°) is four times that of their longitudinal spacing (0.04°). A spectral analysis was also undertaken on ground magnetometer data to ascertain whether the wave displayed a conjugate ground signature. Figure 7.10 shows a DOPE trace and also magnetometer data from the IMAGE network. A description of the IMAGE magnetometer network is given in chapter 4. The stations utilised are Tromsø (TRO), Andenes (AND) and Kilpisjarvi (KIL) all of which lie at comparable latitudes and longitudes to the DOPE sounder. Both the X and Y components of the magnetometer data for each station is displayed. This wave event is classified an uncorrelated wave (UW) as there is no conjugate ground signature. Out of the 27 events studied only 2 displayed evidence of a conjugate ground signature, although all were high *m* in nature. These 2 events will be discussed in more detail at the end of this chapter. For all 27 events a spectral analysis of the DOPE data and conjugate magnetometer data was undertaken to accurately determine the dominant frequency component of the wave in the ionosphere and also if the wave displayed a ground signature. The relative phase of the wave between DOPE paths for each event was also examined to obtain the azimuthal *m* number.

7.2.2. Results of Statistical Study

For each wave event MLT location, frequency and azimuthal *m* number were obtained. All the waves were westward propagating and as such had negative *m* numbers. The DOPE system cannot discern if the waves are radially polarized or compressional in nature. However, the fact that they all possess such high *m* numbers and are observed in the ionosphere indicates that they posses significant radial components. The theory outlined in chapter 2 describes that such small scale waves are thought to derive their energy from instabilities in the westward flowing magnetospheric ring current. To maximize the interaction time between the wave and particle population the waves would also be westward propagating. The fact that propagation is opposite to the solar wind flow direction in the dusk sector implies that solar wind generation mechanisms, such as the Kelvin Helmholtz instability or solar wind buffeting of the magnetopause, are unlikely. If the waves had an external generation mechanism then the propagation direction would be expected to possess a phase structure related to the solar wind flow direction. Figure 7.11 (a) indicates the *m* number magnitude distribution of the events as an occurrence

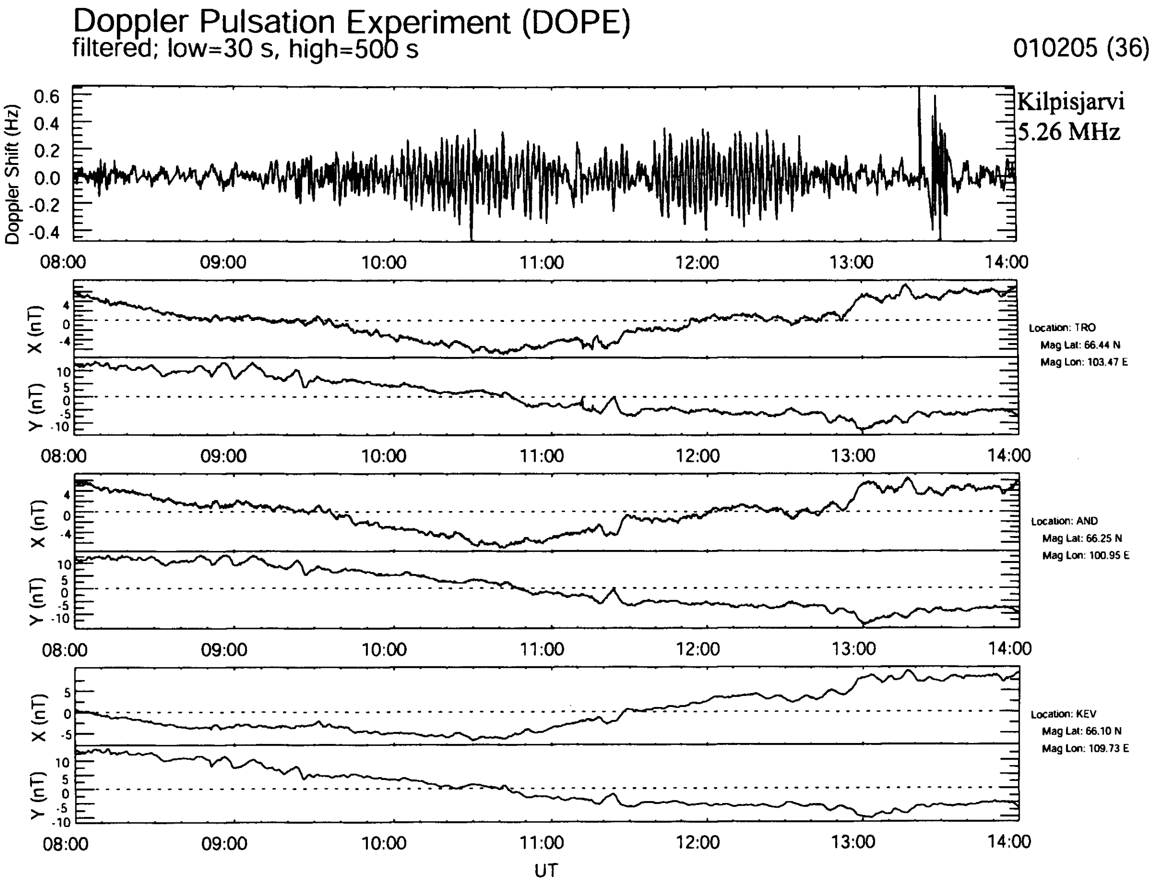

Figure 7.10. **A** DOPE trace (Kilpisjarvi trace from figure 7.7(d)) and also magnetometer data from the IMAGE network. The stations utilised are Tromsø (TRO), Andenes (AND) and Kilpisjarvi (KIL) all of which lie at comparable latitudes and longitudes to the DOPE sounder. Both the X and Y components of the magnetometer data for each station are displayed. This wave event is classified as uncorrelated as there is no conjugate ground signature.

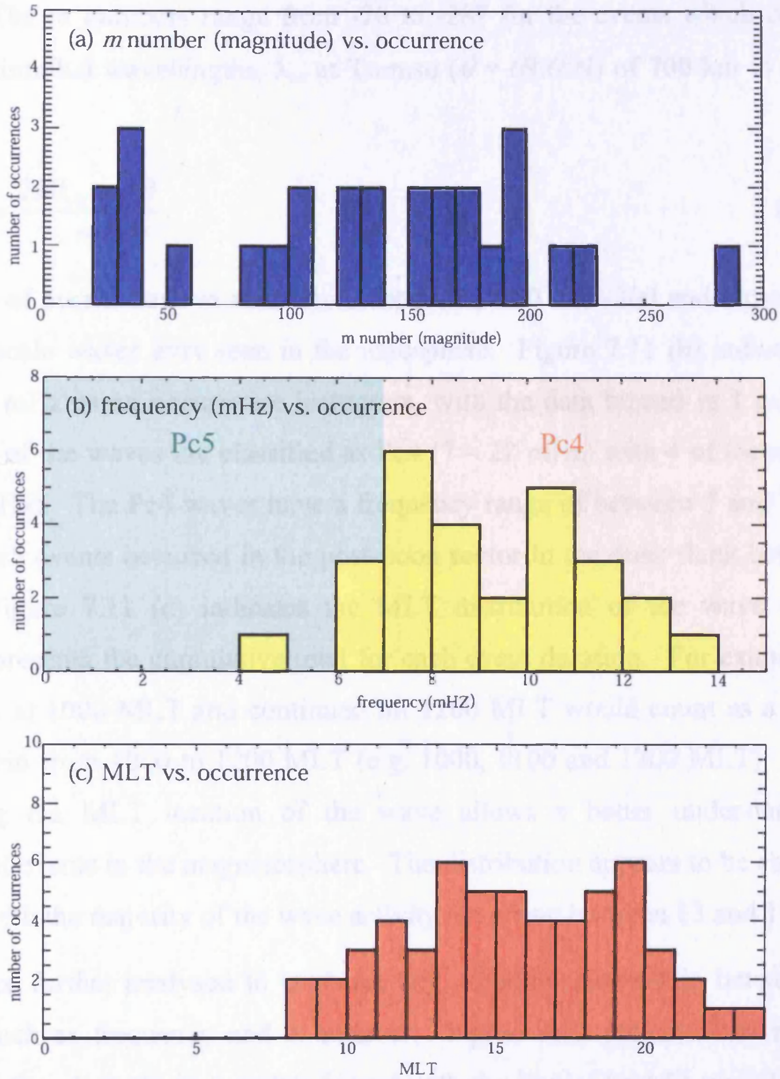

Figure 7.11. Occurrence statistics of the 27 pulsation events observed by DOPE.

histogram. The m numbers range from -20 to -287 for the events which correspond to equivalent azimuthal wavelengths, λ_{az} at Tromsø (θ = 69.6°N) of 700 km to 48 km using the fact that

$$\lambda_{az} = \frac{2\pi R_E \cos\theta}{m}. \tag{7.1}$$

The majority of events have m numbers of between -100 and -200 and represent some of the smallest scale waves ever seen in the ionosphere. Figure 7.11 (b) indicates the wave frequency in mHz as an occurrence histogram, with the data binned in 1 mHz bin sizes. The majority of the waves are classified as Pc4 (7 – 22 mHz) with 4 of them classified as Pc5 (2 – 7 mHz). The Pc4 waves have a frequency range of between 7 and 14 mHz. All four of the Pc5 events occurred in the post-noon sector in the dusk flank between 14 and 19 MLT. Figure 7.11 (c) indicates the MLT distribution of the wave events. The histogram represents the cumulative total for each event duration. For example, an event which started at 1000 MLT and continued till 1200 MLT would count as a data point in each hourly bin from 1000 to 1200 MLT (e.g. 1000, 1100 and 1200 MLT). This method of displaying the MLT location of the wave allows a better understanding of the distribution of events in the magnetosphere. The distribution appears to be centered on the dusk sector with the majority of the wave activity occurring between 13 and 19 MLT.

The data were further analysed to establish any possible relationship between the wave parameters such as frequency and m number. Figure 7.12 indicates the results of the analysis. All the plots are in a scatter format with the line of best fit overplotted through the data. Figure 7.12 (a) indicates MLT location of the wave against wave frequency (mHz), figure 7.12 (b) indicates MLT location against the azimuthal m number and figure 7.12 (c) indicates wave frequency vs. m number. Out of the three plots only figure 7.12 (a) shows strong evidence of a relationship. Although there are distinct gradients in the line of best fit in the other two plots, the scatter of the actual points is enough to discount any statistically significant relationship. There is however evidence of a relationship between MLT location and wave frequency; the wave frequency decreases as the MLT location increases from dawn, through midday and round to dusk. This is consistent with the fact that the four lower frequency Pc5 waves are located on the dusk flank.

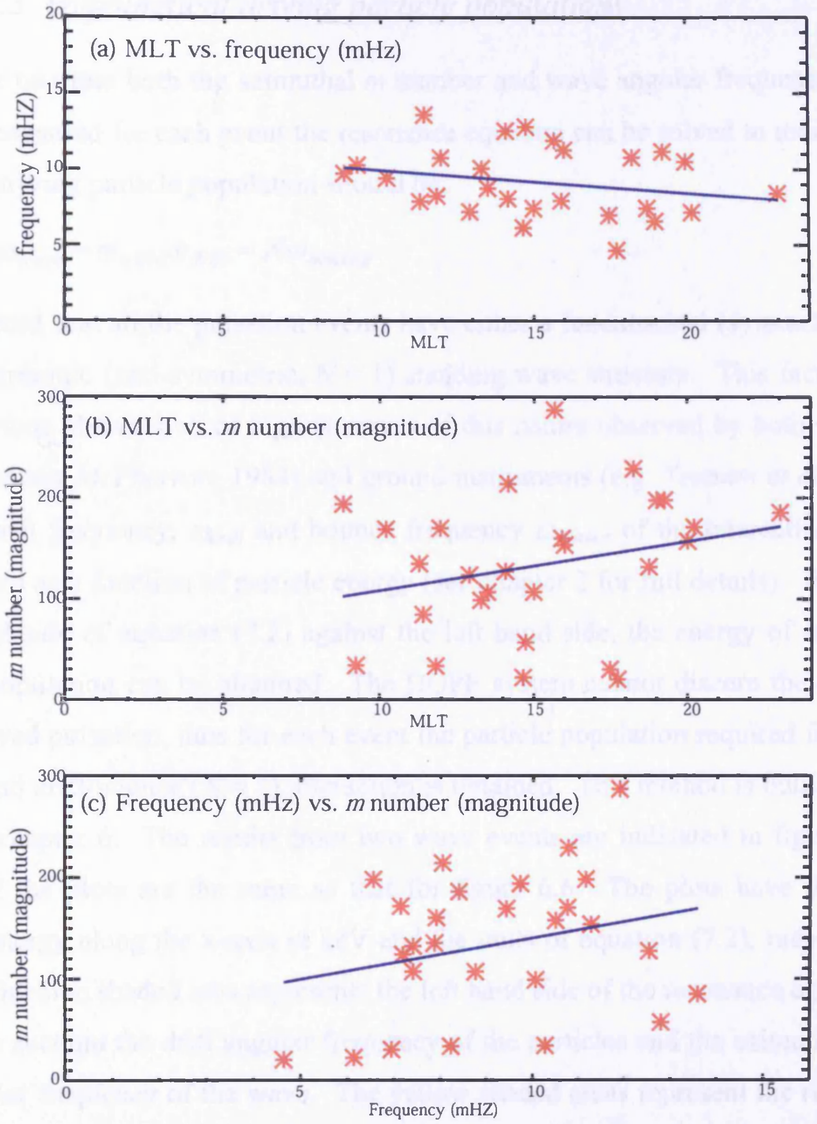

Figure 7.12. Scatter plots of the wave parameters. A line of best fit has been overplotted on each plot.

7.2.3. Hypothetical driving particle populations

Given the fact that both the azimuthal *m* number and wave angular frequency, ω_{wave} were directly measured for each event the resonance equation can be solved to indicate what the required driving particle population should be,

$$\omega_{wave} - m_{wave}\omega_{drift} = N\omega_{bounce}. \tag{7.2}$$

It is assumed that all the pulsation events have either a fundamental (symmetric, $N = 0$) or second harmonic (anti-symmetric, $N = 1$) standing wave structure. This fact is consistent with previous observation of high *m* waves of this nature observed by both satellites (e.g. *Takahashi and McPherron*, 1984) and ground instruments (e.g. *Yeoman et al.*, 2001). The angular drift frequency, ω_{drift} and bounce frequency ω_{bounce} of the interacting protons can be obtained as a function of particle energy (see chapter 2 for full details). By plotting the right hand side of equation (7.2) against the left hand side, the energy of any interacting particle population can be obtained. The DOPE system cannot discern the eigenmode of the observed pulsation, thus for each event the particle population required for both a drift ($N = 0$) and drift-bounce ($N = 1$) interaction is obtained. This method is outlined in greater detail in chapter 6. The results from two wave events are indicated in figure 7.13. The format of the plots are the same as that for figure 6.6. The plots have the interacting particle energy along the x-axis in keV and the units of equation (7.2), rads s^{-1}, along the y-axis. The blue shaded area represents the left hand side of the resonance equation, which takes into account the drift angular frequency of the particles and the azimuthal *m* number and angular frequency of the wave. The yellow shaded areas represent the right hand side of the equation, which deals with contributions from the bounce angular frequency of the particles. The curved yellow shaded area represents the $N = 1$ (drift-bounce resonance) solution and the yellow horizontal line represents the $N = 0$ (drift resonance) solution. The spread in the yellow and blue areas represent the maximum error brought about due to uncertainties in the parameters used to obtain values for ω_{bounce}, ω_{drift} and ω_{wave}. The azimuthal *m* number was estimated to be calculated with 10% accuracy. As discussed in *Southwood and Kivelson* (1982), drift resonance is expected to occur primarily with particles of larger pitch angles in the equatorial plane and drift-bounce resonance with particles of smaller pitch angles due to the nature of the electric field structure for each eigenmode. Pitch angle values utilized were, 45° to 20° when considering a drift-bounce interaction and ~ 70° when considering a drift interaction. The largest errors come from

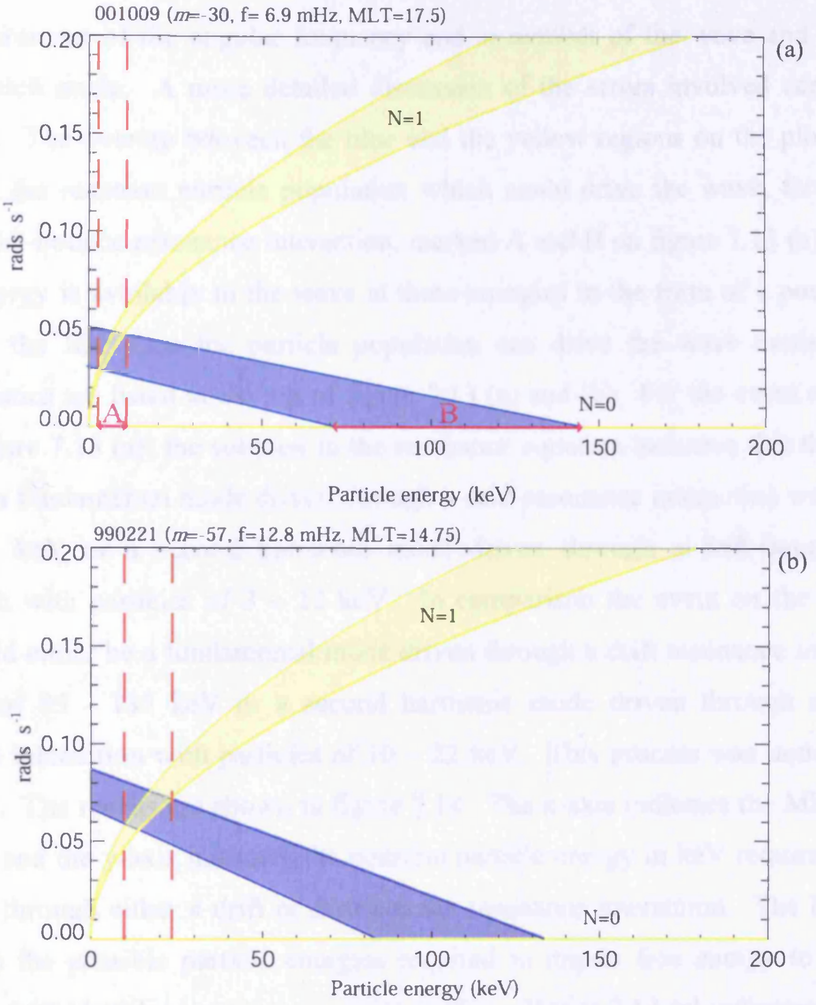

Figure 7.13 A graphical representation of the drift-bounce resonance condition (see text for details). It can be seen that the two shaded areas intersect at two locations, with these locations revealing the energies at which the resonance condition is satisfied. If free energy is available to the wave at these interaction energies in the form of a positive gradient in the IDF, then the particle population can provide energy for that wave mode. Particles of energy A on panel (a) represent those which could drive the wave through a drift-bounce resonance interaction while those of energy B could drive the wave through a drift resonance. Panels (a) and (b) represent the possible solutions for two different wave events.

the measurement of the angular frequency and m number of the wave and the value for particle pitch angle. A more detailed discussion of the errors involved can be found in chapter 6. The overlap between the blue and the yellow regions on the plot indicate the energy of the resonant particle population which could drive the wave, through either a drift or drift-bounce resonance interaction, marked A and B on figure 7.13 (a) respectively. If free energy is available to the wave at these energies in the form of a positive gradient region in the IDF then the particle population can drive the wave mode. The wave characteristics are listed at the top of figure 7.13 (a) and (b). For the event on 9th October 2000, (figure 7.13 (a)) the solution to the resonance equation indicates that the wave could either be a fundamental mode driven through a drift resonance interaction with particles of 70 - 145 keV or a second harmonic mode driven through a drift-bounce resonance interaction with particles of 3 – 12 keV. In comparison the event on the 21st February 1999 could either be a fundamental mode driven through a drift resonance interaction with particles of 85 - 135 keV or a second harmonic mode driven through a drift-bounce resonance interaction with particles of 10 – 22 keV. This process was undertaken for all 27 events. The results are shown in figure 7.14. The x-axis indicates the MLT location of the event and the y-axis indicates the possible particle energy in keV required to drive the pulsation through either a drift or drift-bounce resonance interaction. The blue (red) line represents the possible particle energies required to impart free energy to the pulsation through a drift (drift-bounce) resonance interaction. Figure 7.14 (a) indicates the full range of particle energies required for all events and figure 7.14 (b) is a more detailed look at particle energy requirements below 60 keV (indicated on figure 7.14 (a) by the green box). For all events higher energy particles are required for a drift resonance than a drift-bounce resonance interaction. There is no obvious relationship between the MLT location of the pulsation and the energy requirements of the interacting particles. The majority of events indicate a driving particle population of energy < 60 keV, regardless of the interaction mechanism. The events which require particles of > 100 keV for a drift resonance interaction have the lowest m numbers (m = -20 to -56) of the population and 4 out of the 6 events occur in the dusk sector. While the results in figure 7.13 indicate the structure of the IDF thought to be driving these waves for either a drift or drift-bounce resonance mechanism, it cannot predict which of the mechanisms is actually driving each wave. Without *in situ* particle measurements, only a statistical likelihood for the two mechanisms can be demonstrated.

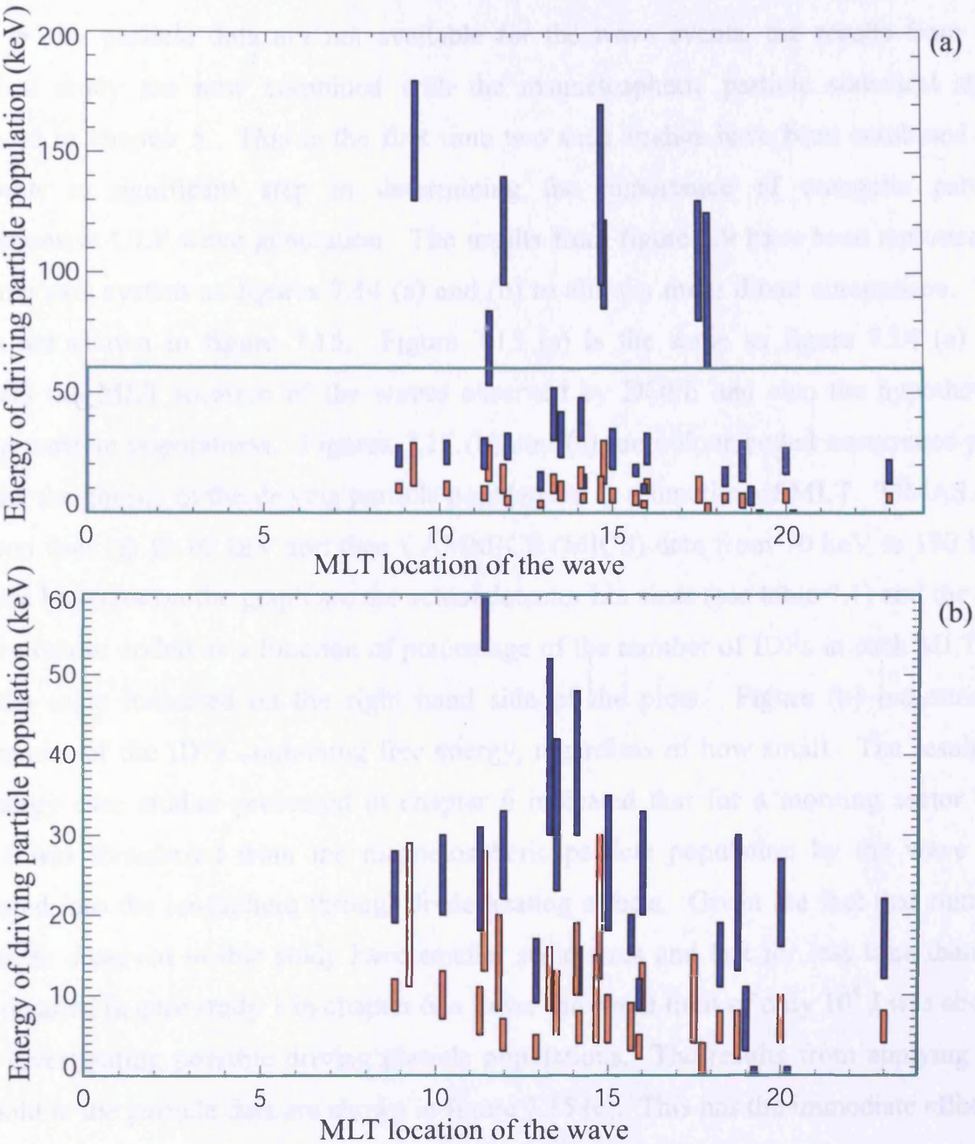

Figure 7.14. The energy of the particles which could provide free energy to the resonant wave field for each of the pulsation events observed by DOPE. For each event the MLT location was noted and the possible particle energy for a drift or drift-bounce resonance interaction is indicated in blue and red respectively. (a) indicates all particle energies up to 200 keV. (b) is a larger picture of the green box area indicated in (a), encompassing particle energies of up to 60 keV.

7.2.4. Comparison with statistical study of driving particle population

Since *in situ* particle data are not available for the wave events, the results from this statistical study are now combined with the magnetospheric particle statistical study presented in chapter 5. This is the first time two such studies have been combined and represents a significant step in determining the importance of energetic particle populations in ULF wave generation. The results from figure 5.9 have been replotted on the same axis system as figures 7.14 (a) and (b) to allow a more direct comparison. The results are shown in figure 7.15. Figure 7.15 (a) is the same as figure 7.14 (a) and indicates the MLT location of the waves observed by DOPE and also the hypothetical driving particle populations. Figures 7.15 (b) and (c) are colour coded occurrence plots showing the energy of the driving particle populations as a function of MLT. TIMAS data has been used up to 10 keV and then CAMMICE (MICS) data from 10 keV to 190 keV. The data bin sizes on the graph are the actual detector bin sizes (see table 7.1) and the data bins are colour coded as a function of percentage of the number of IDFs in each MLT bin with the scale indicated on the right hand side of the plots. Figure (b) indicates all occurrences of the IDFs containing free energy, regardless of how small. The results of the energy case studies presented in chapter 6 indicated that for a morning sector UW $\sim 10^{10}$ J was transferred from the magnetospheric particle population by the wave and dissipated into the ionosphere through Joule heating effects. Given the fact that some of the waves observed in this study have smaller scale sizes and last for less time than the wave detailed in case study 1 in chapter 6, a lower threshold limit of only 10^9 J was chosen when investigating possible driving particle populations. The results from applying this threshold to the particle data are shown in figure 7.15 (c). This has the immediate effect of eradicating the majority of higher energy (>70 keV) particles which posses free energy. This implies that any wave which requires a possible drift resonance interaction with particles of energies > 70 keV is statistically unlikely to be generated by such a mechanism. This includes the majority of the relatively low *m* (~-20 to -50) waves observed in the dusk sector. The particle population below 60 keV was examined in more detail as the majority of the observed waves do require energies of this order. Figure 7.16 is in the same format as figure 7.15 but the y-axis in all plots only extends to 60 keV. In figures 7.16 (b) and (c) the energy requirements of the wave events are overlayed onto the particle data. The particle data for figure 7.16 (b) and 7.16 (c) is almost identical despite the increase in the amount of free energy threshold imposed on figure (c). This reiterates

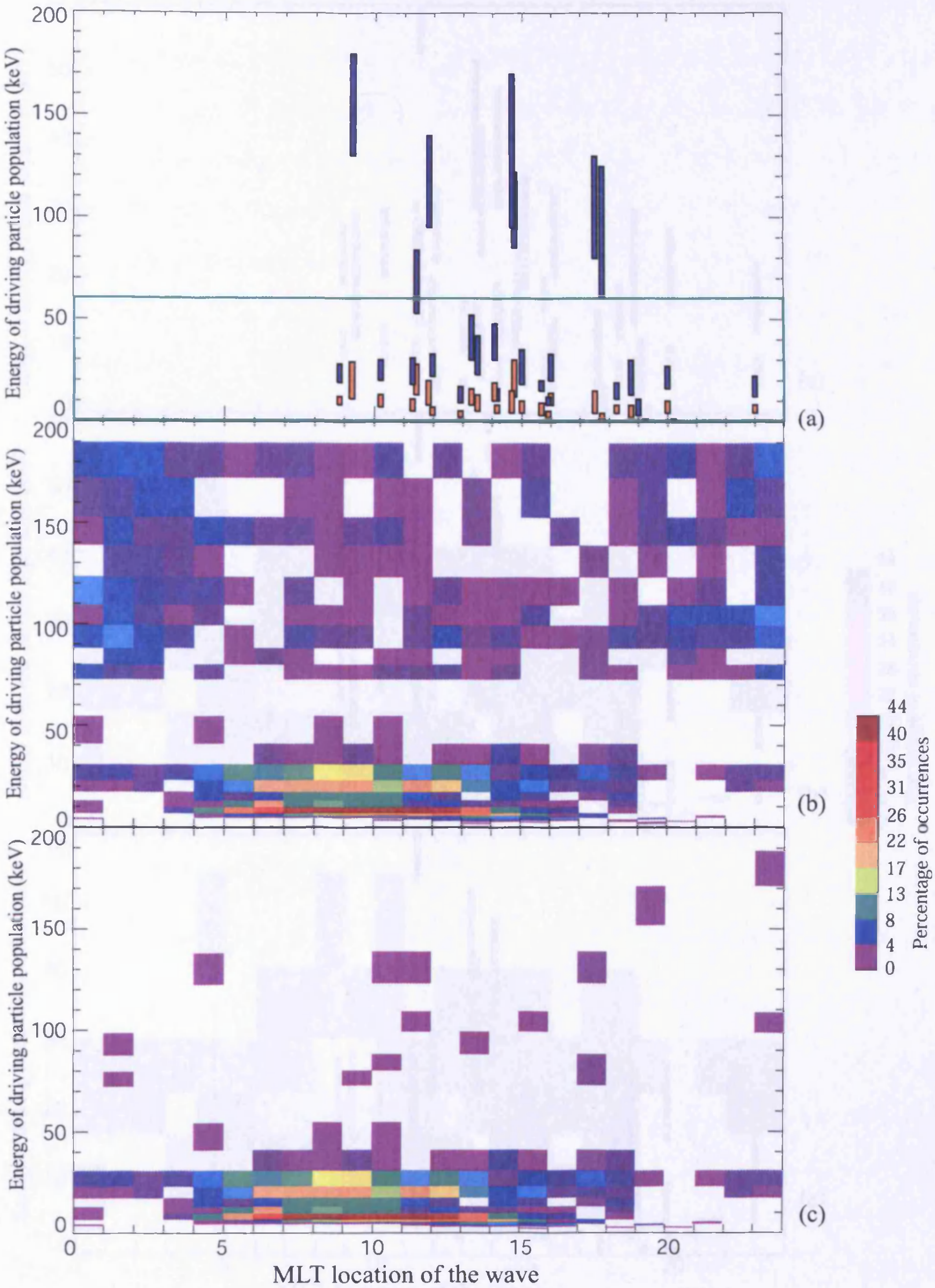

Figure 7.15. (a) the particle requirements to drive the wave through either a drift or drift-bounce resonance interaction, (same as figure 7.14 (a)). (b) and (c) indicate the statistical probability of a particle population of a specific energy exisitng in the magnetosphere. The figures are colour coded occurrence plots showing the energy of the driving particle populations as a function of MLT. TIMAS data has been used up to 10 keV and then CAMMICE (MICS) data from 10 keV to 190 keV. The data bin sizes on the graph are the actual detector bin sizes (see table 5.1) and the data bins are colour coded as a function of percentage of the number of IDFs in each MLT bin with the scale indicated on the right hand side of the plots. (b) indicates the distribution of free energy, regardless of how small an amount. (c) only indicates particles which have > 1×10^9 J of free energy available. (plots (b) and (c) are analogous to figures 5.8 and 5.9).

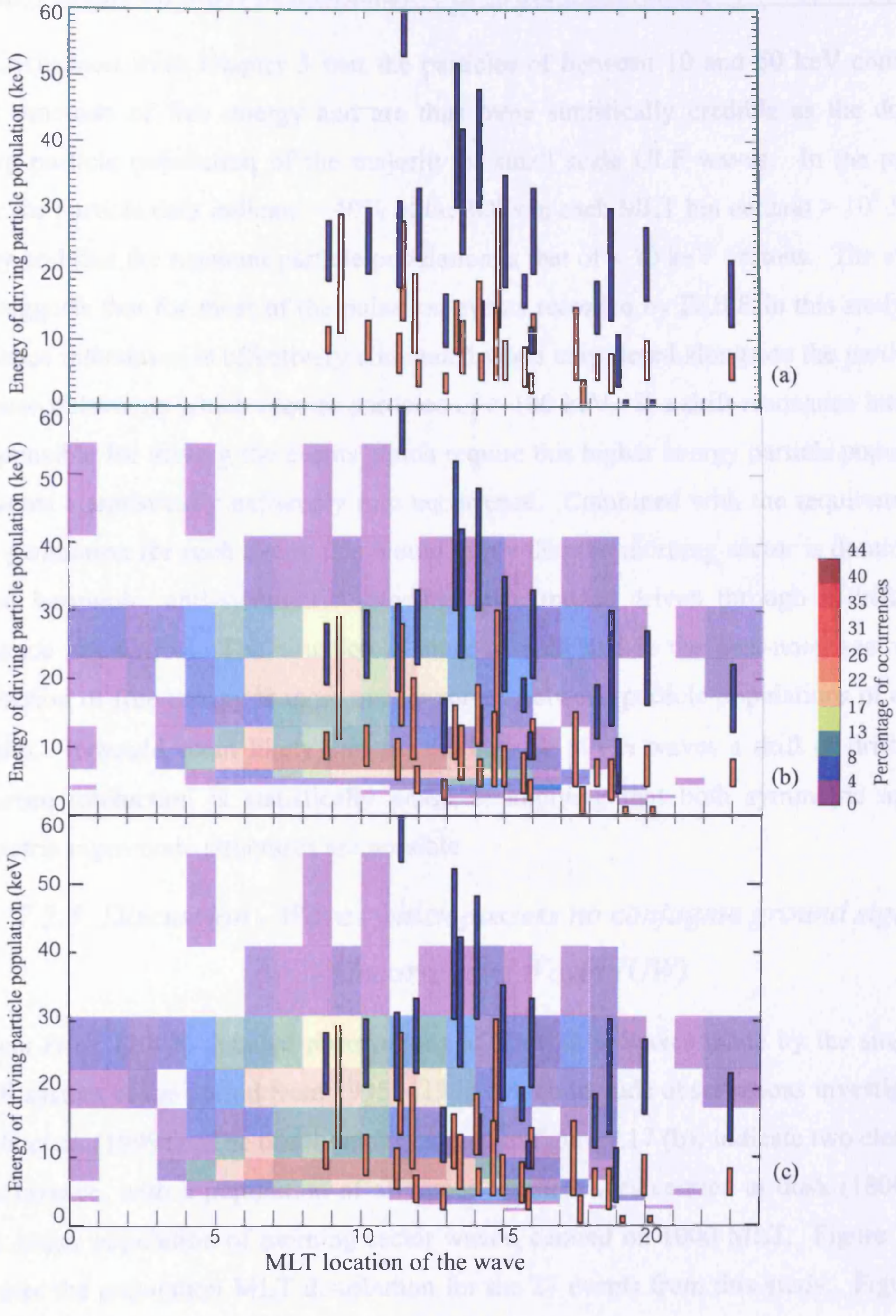

Figure 7.16. (a) the particle requirements to drive the wave through either a drift or drift-bounce resonance interaction, for particles < 60 keV (same as figure 7.14 (b)). (b) and (c) are the same as figure 7.15 (b) and (c) but only for particle energies < 60 keV. In this figure the energy requirements of the wave are overplotted on figures (b) and (c) for an easier comparison.

the conclusions from chapter 5 that the particles of between 10 and 50 keV contain the larger amounts of free energy and are thus more statistically credible as the dominant driving particle population of the majority of small scale ULF waves. In the pre-noon sector the particle data indicate ~ 40% of the IDFs in each MLT bin contain > 10^9 J of free energy and that the resonant particle population is that of ~ 10 keV protons. The evidence thus suggests that for most of the pulsation events recorded by DOPE in this study a drift resonance interaction is effectively eliminated when considered alongside the particle data for those pulsations which require particles of > 100 keV. If a drift resonance interaction is responsible for driving the events which require this higher energy particle population it represents a statistically extremely rare occurrence. Combined with the requirements for wave generation for each event, this would imply that the morning sector is dominated by second harmonic, anti-symmetric standing wave modes driven through a drift-bounce resonance interaction. The situation is more complicated in the post-noon sector as the distribution of free energy is more evenly spread between particle populations of different energies. It would seem likely that for the high (≥ 60) *m* waves a drift or drift-bounce resonance interaction is statistically possible, implying that both symmetric and anti-symmetric eigenmode structures are possible.

7.2.5. Discussion - Waves which possess no conjugate ground signature - Uncorrelated Waves (UW)

Yeoman et al. (2000) detailed observations of 52 high *m* waves made by the single path DOPE system in the period from 1995 – 1998, which include observations investigated by *Wright et al.* (1999a). The observations (shown in figure 7.17 (b)) indicate two clear peaks in occurrence, with a population of afternoon sector waves centred at dusk (1800 MLT) and a larger population of morning sector waves, centred on 1000 MLT. Figure 7.17 (a) indicates the population MLT distribution for the 27 events from this study. Figure 7.17 (c) has combined the results from both the study presented here and also the study by *Yeoman et al.* (2000). In the study by *Yeoman et al.* (2000) the morning sector waves, which included 41 of the 52 waves, were then analysed further and were shown to have a sharply peaked frequency distribution, centred on 6 mHz. This distribution is shown in figure 7.17 (d) and has been modified to include the findings of this study for morning sector UWs. *Yeoman et al.* (2000) estimated expected *m* values for this morning population using the methods of *Allan et al.* (1982, 1983) and *Yeoman et al.* (1992) to be in

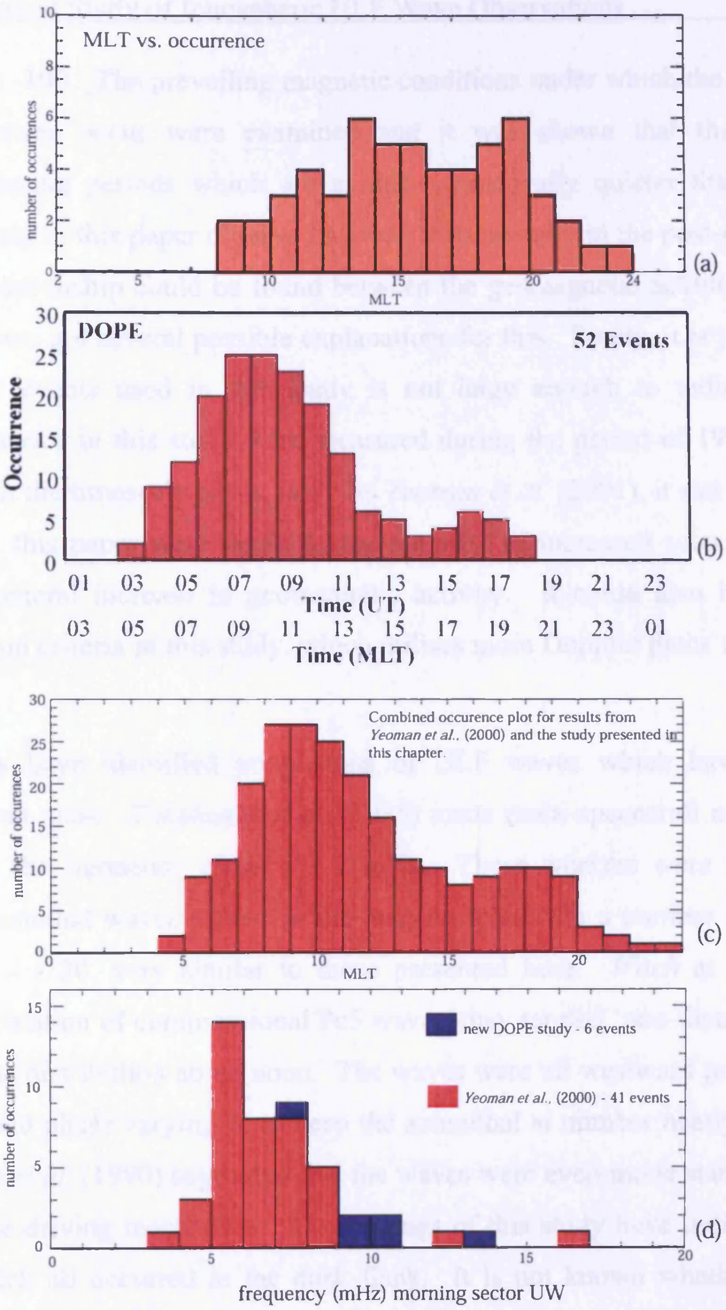

Figure 7.17. (a) MLT location of the 27 wave events observed using the new DOPE system. (b) 52 wave events which displayed no correlative ground signature observed using the old DOPE system (taken from *Yeoman et al.,* 2000) (c) the occurence statistics from panel (b) with the 25 uncorrelated events from panel (a) included. (d) the frequency distribution for the 41 uncorrelated morning sector events observed by *Yeoman et al.,* (2000) and the 5 uncorrelated morning sector events observed in the study presented here.

the range -40 to -100. The prevailing magnetic conditions under which the morning sector uncorrelated waves occur were examined and it was shown that the waves occur preferentially during periods which are a little magnetically quieter than average. In contrast, the study in this paper observed waves predominantly in the post-noon sector and no statistical relationship could be found between the geomagnetic activity and the wave occurrence. There are several possible explanations for this. Firstly, it is possible that the database of 27 events used in this study is not large enough to indicate this trend. Secondly, the waves in this study were measured during the period of 1998 – 2002. By comparison with the timescale of the study by *Yeoman et al.* (2001), it can be seen that the observations in this paper were made during a period of increased solar activity, which would imply general increase in geomagnetic activity. It could also be due to more rigorous selection criteria in this study, which utilises more Doppler paths than the original study.

Several authors have identified populations of ULF waves which have a symmetric distribution about noon. *Takahashi et al.* (1985) made multi-spacecraft measurements of ULF waves in the frequency range 1 - 3 mHz. These workers were able to directly measure the azimuthal wavenumbers in the magnetosphere for a number of wave events, finding m=-40 - -120, very similar to those presented here. *Woch et al.* (1990) also identified a population of compressional Pc5 waves, they termed 'non-diamagnetic' which had a symmetric distribution about noon. The waves were all westward propagating, with the frequency and phase varying so to keep the azimuthal m number nearly constant, with $m \sim -70$. *Woch et al.* (1990) suggested that the waves were even mode standing waves but did not state the driving mechanism. The findings of this study have indicated only four Pc5 waves which all occurred in the dusk flank. It is not known whether these waves would be classified as compressional waves, however the fact that they are observed in the ionosphere implies they have a significant radial component. In the statistical study outlined in this paper there is evidence that the waves that occur in the post-noon sector have lower frequencies than those that occur in the pre-noon sector. This supports work that both drift and drift-bounce resonance interaction mechanism is dominant in the post-noon sector, with the pre-noon sector preferentially supporting drift-bounce interactions. Drift resonance involves a fundamental poloidal mode wave, which in comparison, has a lower frequency than the second harmonic poloidal mode waves that are involved in drift-bounce resonance.

7.2.5.1. Morning Sector

The results of this statistical study have shown 7 morning sector waves, 6 of which display no conjugate ground signature. The combination of this study with the particle statistical study in chapter 5 have indicated that, given the energy requirements of the interacting particle population, the majority of the waves are driven through a drift-bounce resonance interaction by ~ 10 to 30 keV protons. This is in good agreement with modelling work undertaken by *Ozeke and Mann* (2001) which suggests that in the morning sector very monochromatic Pc4 waves, highly localised in latitude would be generated through a drift-bounce resonance interaction between a second harmonic standing mode wave and ~ 10 keV protons. The results also agree with the case study of conjugate wave-particle observations in the morning sector presented in chapter 6 which concluded that the observed pulsation was a second harmonic wave driven by ~ 10 keV protons through a drift-bounce resonance interaction. Additional observations of a second harmonic wave observed in the morning sector thought to be generated through drift-bounce resonance interaction such as that presented by *Hughes and Grard* (1984) are also in good agreement.

7.2.5.2. Post-noon sector

The majority (20 out of 27 observations) waves in this statistical study were observed in the dusk sector. All the Pc5 waves observed in this study were also observed in the dusk flank. The statistical studies indicated that for the Pc4 waves observed a drift or drift-bounce resonance interaction was equally possible with particle energies of < 70 keV. This is consistent with previous results by *Yeoman et al.* (2001) which gave evidence of post-noon high m waves driven through both the $N = 0$ drift resonance mechanism and the $N = 1$ drift-bounce resonance mechanism with particles of between 37 and 57 keV or 24 and 44 keV respectively. Overall they surmised that an IDF with a positive gradient region located between ~35 and 45 keV could be providing energy for both waves. The modelling work by *Ozeke and Mann* (2001) also indicates that the dusk region can support waves driven through drift and drift-bounce resonance mechanisms. Previous studies using both satellite and ground observations, (*Kokubun,* 1985; *Anderson et al.,* 1990; *Engebretson et al*., 1992 and *Lessard et al.,* 1999) have identified the post-noon sector as the dominant region of the magnetosphere for ULF wave generation. The types of pulsation fall into two categories; storm time Pc5 waves and quiet time Pc4 waves. Storm time Pc5's are modes with large compressional components which are observed during geomagnetically active conditions in the dusk flank. *Allan et al.* (1982, 1983) presented observations of storm time Pc5s using the STARE (Scandinavian Twin Auroral Radar Experiment) radar. The azimuthal *m* numbers were measured between -7 and -80. Although the driving mechanism is thought to be an instability in the ring current plasma the exact nature of the interaction is not fully understood and as such storm time Pc5s have been related to both a drift and drift-bounce resonance interaction. Similar waves but with an equatorward propagation have also been observed by *Yeoman et al.* (1992). The 26 events were all in the Pc5 range with *m* obtained from measurements to be -5 to -36. Although the observations were at lower latitudes than those of *Allan et al.* (1982, 1983), *Yeoman et al.* (1992) suggest they have a similar generation mechanism. The results in this study indicated the presence of four Pc5 waves observed in the dusk flank, with *m* numbers ranging from -20 to -56. The events did not occur during geomagnetically active conditions with Dst < -20 nT for 24 hours before and during each interval. Due to the ionospheric nature of the observations it is not known whether the waves possessed a significant compressional component. The particle statistical data would also suggest that the waves were driven through a drift-bounce resonance interaction with particles < 70 keV. It would seem likely that these waves are not storm time Pc5 pulsations as classified by *Allan et al.* (1983). Waves of the type presented in this study have been observed by spacecraft (e.g. *Takahashi et al.*, 1990). They observed a radially polarised Pc5 wave at 1300 MLT. The *m* number was measured to be ~ 100. They concluded that this wave was a second harmonic wave driven through a drift–bounce resonance interaction with 100 keV protons. The findings of this study indicate that Pc5 waves of this nature are statistically more likely to be a second harmonic mode structure but that the interaction would be with lower energy particles. This is consistent with the only observation of a ULF wave in the post-noon sector and a conjugate unstable particle distribution function which was presented by *Hughes et al.* (1978). The 10 mHz wave was observed at 1500 LT and judged to be a second harmonic standing mode. Data from the satellite particle detectors also indicated the driving particle population, in the form of a bump on tail IDF, to be that of 10 keV protons. The wave mode, frequency and driving particle energy suggested a drift-bounce resonance interaction.

The majority of the waves observed in this study have frequencies in the Pc4 range. Particle data would also suggest that the driving population is that of < 70 keV protons. The waves could be a similar population to those described *by Engebretson et al.* (1992). The authors noted 21 events using three satellites. The majority of the waves were radially polarised Pc4 waves which were observed in the post-noon sector of the magnetosphere. The events occurred during geomagnetically quiet conditions, usually after a magnetic storm. The authors suggest that the waves were associated with the refilling of the plasmasphere which caused the necessary plasma instabilities to form resulting in free energy. They theorized that ~ 100 keV protons as the driving particle population through the Drift-Alfvén-Ballooning-Mirror instability, which requires an anti-symmetric standing wave structure, (*Chen and Hasegawa,* 1991). The findings of this study indicate that the driving population would most likely be that of <70 keV protons, but that the wave structures could be anti-symmetric. The azimuthal *m* numbers of the Pc4 waves presented in this study are exceptionally high (m ~ -100 to -200) representing some of the smallest scale waves ever seen both in the ionosphere and the magnetosphere. Given the fact that the majority of previous statistical studies have focused on satellite observations, the results of this new study utilising ionospheric measurements could represent a significant step in understanding the generation mechanisms and fundamental role ULF waves play in the global magnetospheric system. The waves detailed here all derive their energy from the magnetospheric ring current and as such represent a significant energy sink.

7.2.6. Waves which possess a conjugate ground signature

As mentioned in section 7.1.2, two of the waves presented in this study possessed a conjugate ground magnetic signature. One event occurred in the morning sector and one in the post-noon sector. These events will now be presented in more detail and compared to previous results, both observational and theoretical.

7.2.6.1. Morning sector - Giant Pulsations?

The most controversy regarding morning sector waves is related to the standing wave mode and driving particle population of giant 'Pg' pulsations. These waves are long lived, highly monochromatic Pc4 oscillations which occur during geomagnetically quiet times. Pgs are an example of a particle-driven ULF wave which may be studied with ground based magnetometers due to their large amplitude although they have also been observed by orbiting satellites. They have been related to drift-bounce resonance mechanisms with both symmetric (e.g. *Takahashi et al.*, 1992; *Glassmeier et al.*, 1999) and anti-symmetric (e.g. *Chisham and Orr*, 1991) wave modes, hence the wave-particle interaction responsible for their generation remains controversial.

In the statistical database presented here, one of the morning sector waves which occurred on the 19th February 2001 does have a conjugate ground signature. Figure 7.18 indicates that the wave was observed by DOPE (panel (a)) between 0930 and 1400 MLT and by the Tromsø magnetometer (panel (b)) between ~1020 and 1140 UT (1220 to 1340 MLT). The MLT location of the wave, frequency (~ 8.2 mHz) and azimuthal m number ($m \sim -33$) of the wave are consistent with previous observations of Pgs. A further FFT analysis was undertaken using magnetometer stations from the IMAGE array to determine the latitudinal extent of the wave. Figure 7.19 (a) indicates the DOPE observations of the wave from 0940 UT to 1140 UT. Panels (b) to (k) indicate the X and Y components of IMAGE magnetometer traces from a latitude of 66.1°N to 63.34°N. The station names and co-ordinates are shown to the right of each panel. The wave is highly localised in latitude (~3°) and also is dominant in the Y magnetometer component, indicating the small scale size and radially polarised nature, both traits also consistent with Pgs. The panels to the right of the magnetometer and DOPE traces show the result of a FFT analysis undertaken of the DOPE data and the Y component of the magnetometer data. The dominant frequency component is at ~ 8.2 mHz for all the traces, although there is a slight shift to lower frequencies at SOD and PEL. It should be noted that the wave trace at both these stations is small compared to the other stations. The hypothetical IDFs required to drive this wave indicated either a drift resonance with 90 – 140 keV protons or drift-bounce resonance with 8 – 20 keV protons. From the particle statistical study, the most probable driving particle population would be the 8 – 20 keV protons. *Chisham* (1996) proposed that an injection of particles in the tail region followed by a period of reduced geomagnetic activity is required to allow this lower energy driving proton population to traverse to the morning side magnetosphere. To examine this for this event, the Dst index was also examined for the 48 hours before wave onset. The Dst is a geomagnetic index which monitors the world wide magnetic storm level. It is constructed by averaging the horizontal component of the geomagnetic field from mid-latitude and equatorial magnetometers from all over the world. Negative Dst values indicate a magnetic storm is in progress, the more negative Dst is the more intense the magnetic storm. The negative deflections in the Dst index are caused by the storm time ring current which flows around the Earth. The results are presented in figure 7.20. A value > - 20 nT in the Dst index is considered geomagnetically quiet. For the entire 48 hour period prior to wave onset the magnetosphere is quiet, the 24 hour period directly before wave onset is exceptionally

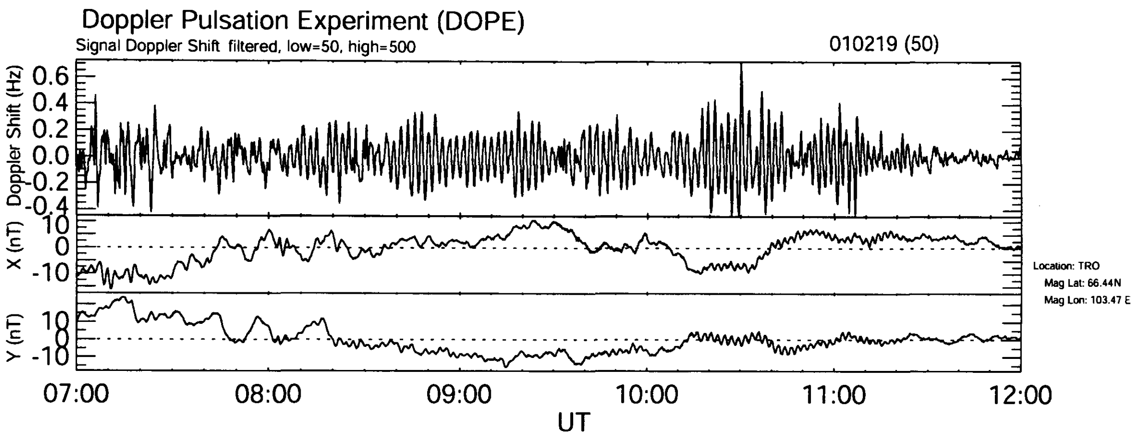

Figure 7.18. (a) indicates a Doppler trace from the DOPE HF sounder for the event on the 19th February 2001. (b) indicates conjugate magnetometer data from the TRO station. The X and Y components are both shown. Figure (a) indicates that the wave was observed by DOPE between 0930 and 1400 MLT and panel (b) indicates the wave observed by the Tromsø magnetometer between 1020 and 1140 UT (1220 to 1340 MLT). The MLT location of the wave, frequency (8.2 mHz) and azimuthal m number (m ~ -33) of the wave are consistent with previous observations of Pgs.

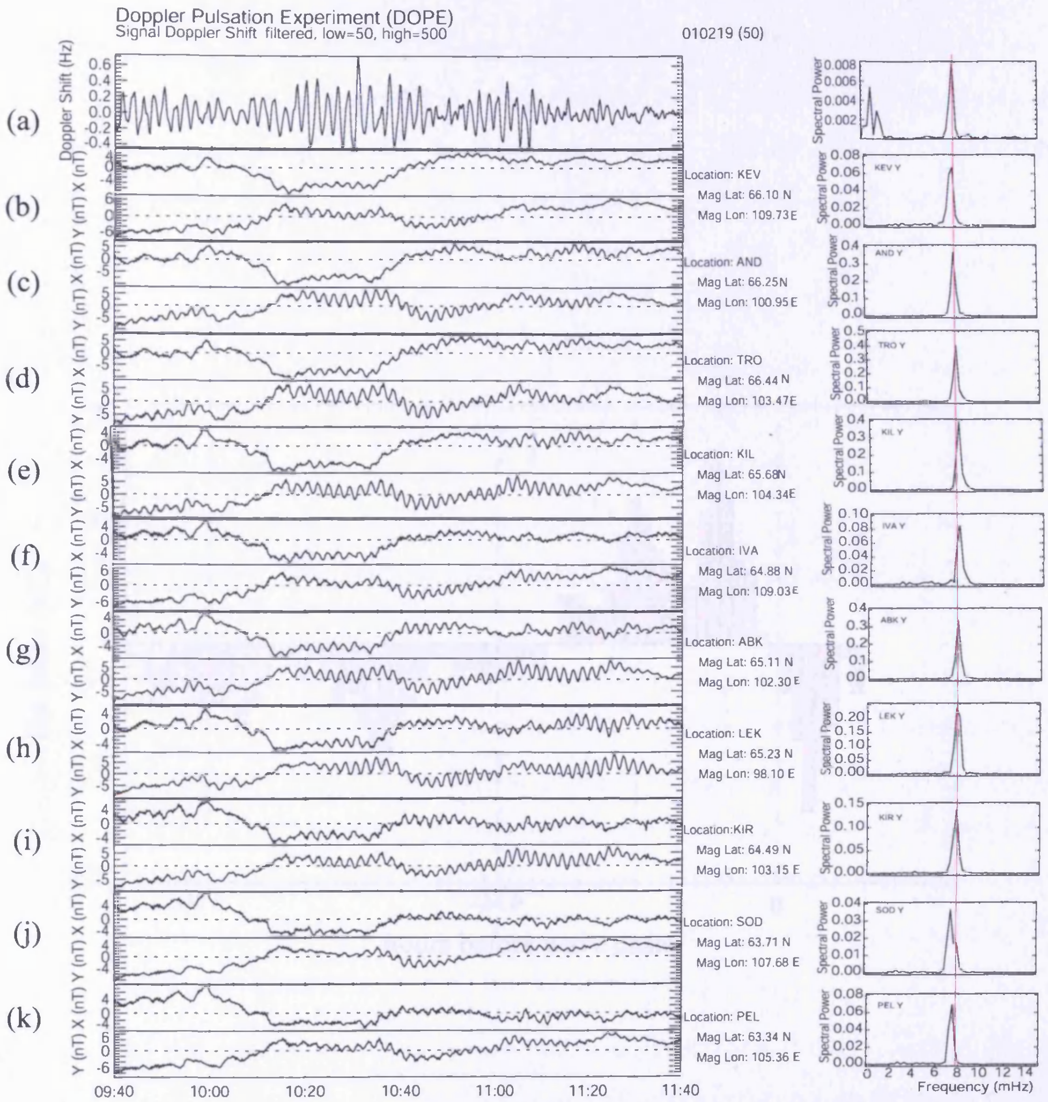

Figure 7.19. (a) indicates the DOPE observations of the wave from 0940 UT to 1140 UT. Panels (b) to (k) indicate the X and Y components of IMAGE magnetometer traces from a latitude of 66.1 N to 63.34 N. The station names and co-ordinates are shown to the right of each panel. The wave is highly localised in latitude (~3^{o}) and also is dominant in the Y magnetometer component, indicating the small scale size and radially polarised nature, both traits also consistent with Pgs. The panels to the right of the magnetometer and DOPE traces show the result of a FFT analysis undertaken of the DOPE data and the Y component of the magnetometer data. The dominant frequency component is at ~ 8.2 mHz for all the traces, although there is a slight shift to lower frequencies at SOD and PEL.

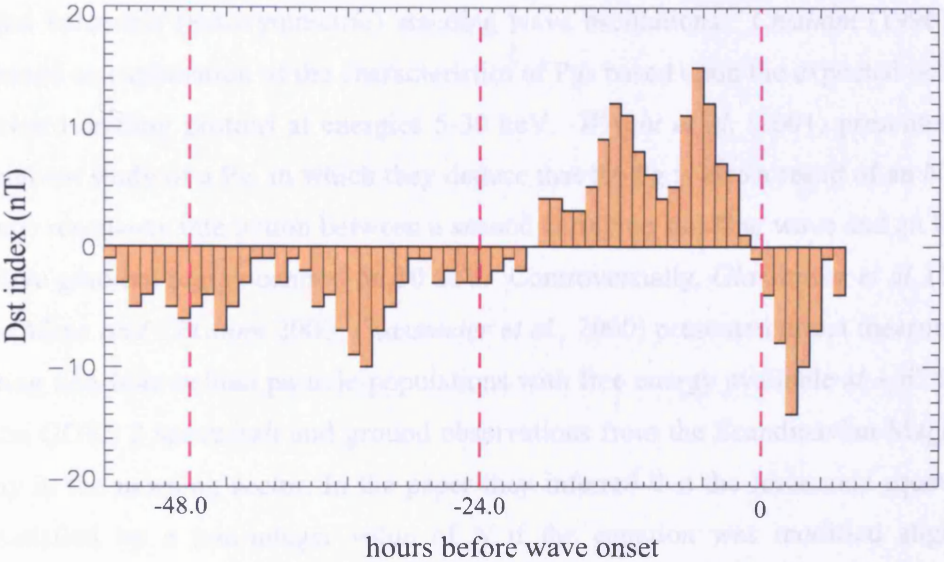

Figure 7.20. A superposed epoch analysis of the Dst index for ~ 48 hours before the wave observed on the 19th February 2001. The magnetosphere was quiet throughout the entire interval, although in the 20 hours preceeding wave onset the Dst index indicates the magnetopshere was at its quietest.

quiet. This implies that particles of the required energies (8 – 20 keV) would be able to travel round to the dawn sector without being deflected out of the dayside magnetosphere. It is likely that this pulsation could be classified as a Pg. The evidence presented here, both in a case study and statistical nature indicate that it is likely to be a second harmonic standing mode driven through a drift-bounce resonance interaction with 8 – 20 keV protons.

Chisham and Orr (1991) presented a statistical study of 34 Pgs which were deduced to be second harmonic (anti-symmetric) standing wave oscillations. *Chisham* (1996) has also proposed an explanation of the characteristics of Pgs based upon the expected behaviour of westward drifting protons at energies 5-30 keV. *Wright et al.* (2001) presented a multi-instrument study of a Pg, in which they deduce that the Pg is also a result of an $N = 1$ drift-bounce resonance interaction between a second harmonic standing wave and an IDF with a positive gradient region centred on 10 keV. Controversially, *Glassmeier et al.* (1999), see also (*Mann and Chisham* 2000; *Glassmeier et al.,* 2000) presented direct measurements of drifting non-Maxwellian particle populations with free energy available at ~ 67 keV made by the GOES 2 spacecraft and ground observations from the Scandinavian Magnetometer Array in the morning sector. In the paper they inferred that the resonance equation could be satisfied by a non-integer value of N if the equation was modified slightly, thus invoking an odd-mode fundamental field line oscillation interaction.

The evidence presented in this chapter, both statistically and the case study discussed in this section suggests that Pgs are second harmonic standing mode waves driven through a drift–bounce resonance interaction with 10 – 40 keV protons.

7.2.6.2. Post-noon sector

In the statistical database presented here, one of the Pc5 waves observed on the 27th March 2002 transforms into a Pc4 wave. The DOPE trace for this event is shown in figure 7.21. The waves are observed in all four paths. The initial Pc5 wave, has a frequency of 4.6 mHz, an azimuthal *m* number of ~ -20 and is observed between ~1430 and 1640 UT. Immediately after this is a much smaller scale Pc4 wave with a frequency of 11.1 mHz, and azimuthal *m* number of ~ -198 which lasts for ~ 1.5 hours. The conjugate magnetometer data indicates the Pc5 wave is observed on the ground. This is shown in figure 7.22 with an accompanying spectral analysis plot indicating the frequency of the wave in both the ionosphere and on the ground. Interestingly, the Pc5 wave has a

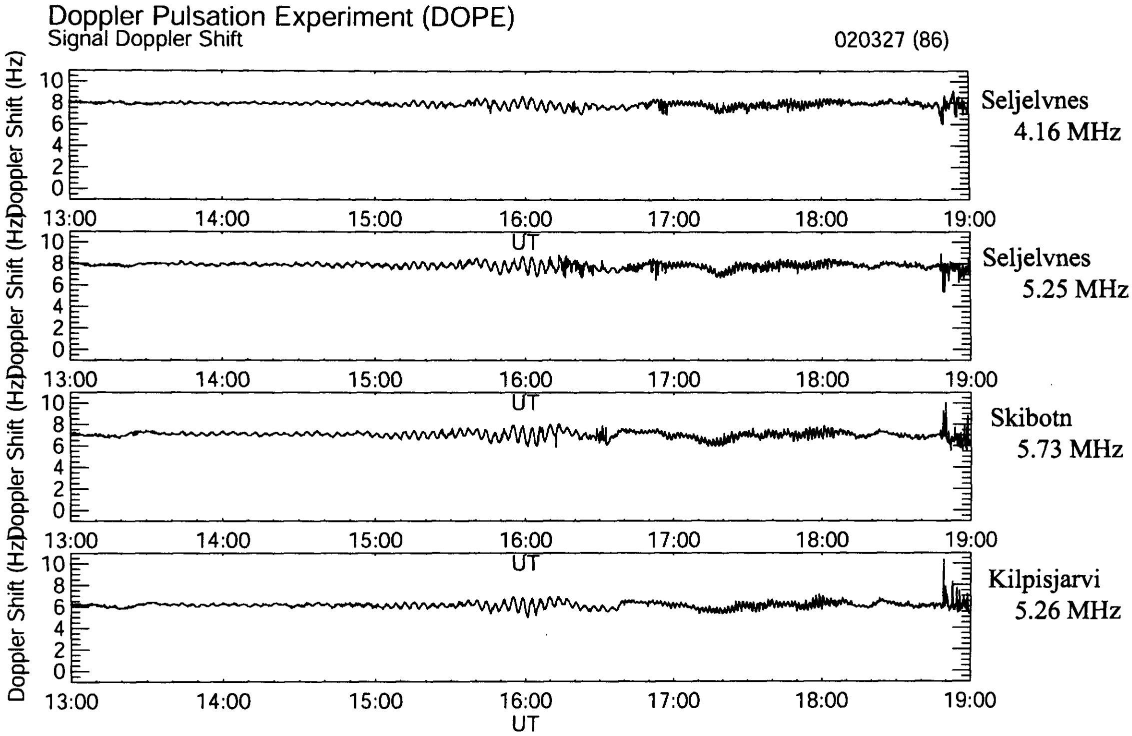

Figure 7.21. Results from the DOPE HF sounder from the 27th March 2002. All four traces indicate the presence of a Pc5 wave followed by a Pc4 wave. The initial Pc5 wave, has a frequency of 4.6 mHz, an azimuthal *m* number of ~ -20 and is observed between ~1430 and 1640 UT. Immediately after this is a much smaller scale Pc4 wave with a frequency of 11.1 mHz, and azimuthal *m* number of ~ -198 which lasts for ~ 1.5 hours.

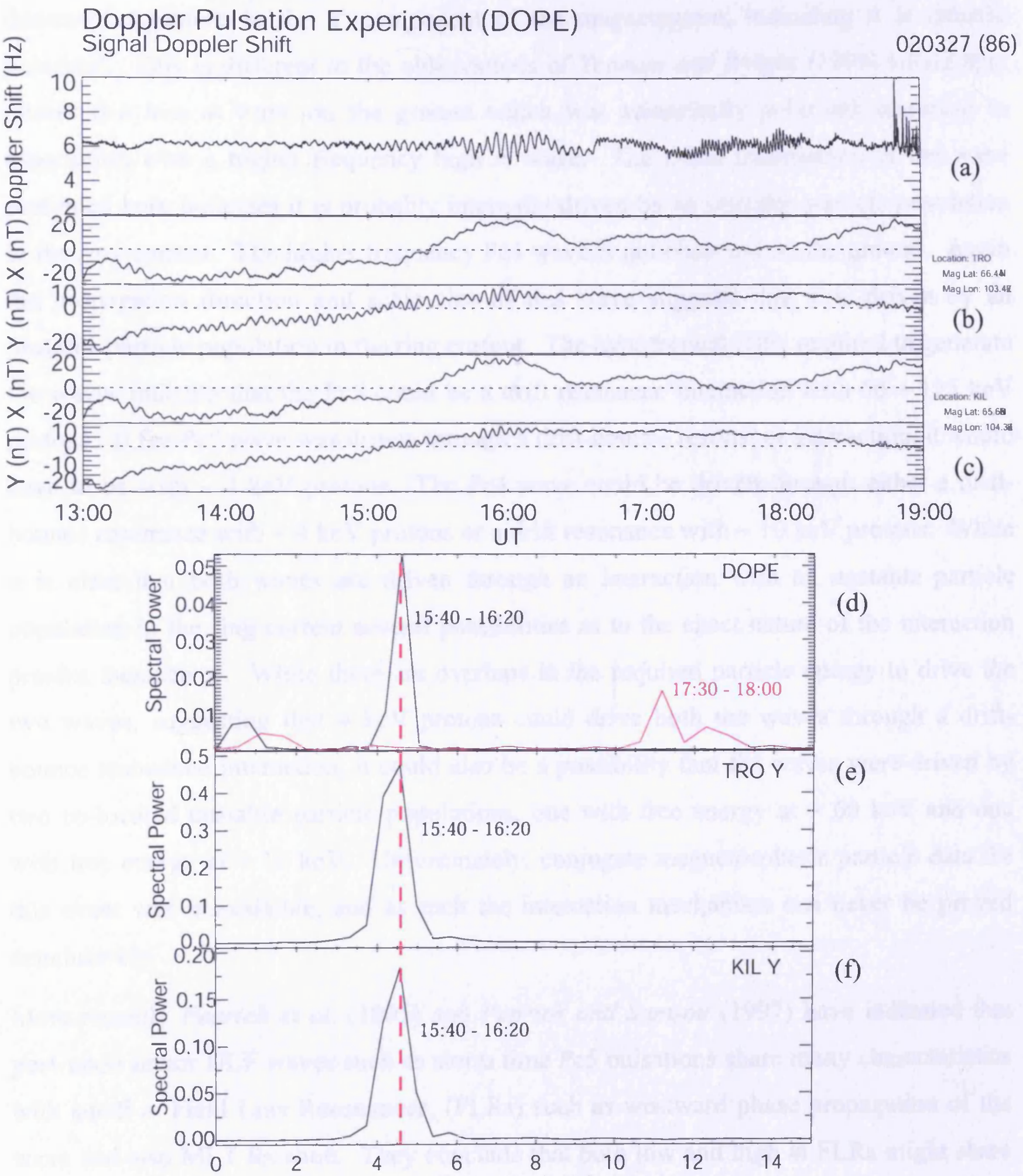

Figure 7.22. The DOPE trace (a) and accompanying magnetograms from (b) TRO and (c) KIL for the wave event on the 27th March 2002. A FFT analysis of the data shown in figuures (d) to (f) indicates the Pc5 wave is observed on the ground, predominantly in the Y component, however the Pc4 event is only observed by the DOPE HF sounder.

dominant signature in the Y component of the magnetogram, indicating it is radially polarised. This is different to the observations of *Yeoman and Wright* (1999) where they observed a low *m* wave on the ground which was azimuthally polarised occurring in association with a higher frequency high *m* wave. The radial polarisation of the wave presented here indicates it is probably internally driven by an unstable particle population in the ring current. The higher frequency Pc4 wave is not observed on the ground. Again the propagation direction and scale size of this wave suggests that it is driven by an unstable particle population in the ring current. The hypothetical IDFs required to generate the waves indicate that the Pc5 could be a drift resonance interaction with 60 – 125 keV protons. If the Pc5 wave was driven through a drift-bounce resonance interaction, it would have to be with ~ 4 keV protons. The Pc4 wave could be driven through either a drift-bounce resonance with ~ 4 keV protons or a drift resonance with ~ 10 keV protons. While it is clear that both waves are driven through an interaction with an unstable particle population in the ring current several possibilities as to the exact nature of the interaction present themselves. While there are overlaps in the required particle energy to drive the two waves, suggesting that 4 keV protons could drive both the waves through a drift-bounce resonance interaction, it could also be a possibility that the waves were driven by two co-located unstable particle populations, one with free energy at ~ 60 keV and one with free energy at ~ 10 keV. Unfortunately, conjugate magnetospheric particle data for this event was unavailable, and as such the interaction mechanism can never be proved conclusively.

More recently *Fenrich et al.* (1995) and *Fenrich and Samson* (1997) have indicated that post-noon sector ULF waves such as storm time Pc5 pulsations share many characteristics with small *m* Field Line Resonances, (FLRs) such as westward phase propagation of the wave and also MLT location. They conclude that both low and high *m* FLRs might share an initial common source mechanism, such as coupling between fast compressional wave modes which travel across the magnetic field from the magnetopause and couple to a standing Alfvén mode. The velocity shear of the low *m* wave is thought to drive the instability which sets up a spectrum of high *m* waves, one of which begins to grow in amplitude. The amplitude of the high *m* wave is then amplified through wave particle interactions. This adds additional complications to previous work discussed here by introducing overlap of generation mechanisms. This has been observed in the post-noon sector previously by *Wright and Yeoman* (1999a) using the DOPE sounder, IMAGE magnetometer and CUTLASS radars. A high m (m~ -38), 10 mHz wave was observed in the ionosphere near noon using the CUTLASS radar and DOPE sounder. Simultaneously, a ~ 4 mHz wave was observed on the ground in the X component (indicating it is azimuthally polarised) of the Tromsø magnetometer. As the instruments moved to a region which maps to the dusk flank of the magnetosphere the higher frequency signature in the ionosphere disappeared and a lower frequency, ~ 4 mHz low m (m~ -4) was observed. The case study presented in this sector highlights the dynamic nature of small scale ULF waves in the magnetosphere and also what a valuable tool the DOPE HF sounder is when observing and documenting these waves. Given the small scale size (m ~ -198) of the Pc4 wave it is unlikely that a spacecraft or radar would have detected it, thus giving an incomplete picture of the nature of the event. This event also highlights how a pulsation can evolve over time. The data suggests that if the interaction mechanism remains the same, the eigenfrequency changes from a Pc5 to a Pc4 wave, making this event not only interesting but most perplexing.

7.2.7. Summary

This chapter has presented some of the most accurate ionospheric measurements to date using the multi-path DOPE HF sounder in northern Norway. The study presented 27 events, predominantly in the post-noon sector. The majority of events were Pc4 waves with azimuthal m numbers ranging from -100 to -200, representing some of the smallest scale waves ever observed in the ionosphere. Four Pc5 waves were observed in the post-noon sector. By accurately obtaining values for the wave azimuthal m number and angular frequency, the resonance equation (equation 7.2) could be solved resulting in hypothetical IDFs required to drive the waves through either a drift or drift-bounce resonance interaction mechanism. These results were then considered alongside the statistical study undertaken in chapter 5 which investigated the statistical likelihood of such driving particle populations occurring in the magnetospheric ring current. There is evidence that the drift-bounce mechanism is dominant in the morning sector, providing an unexpected sink for ring current energy in the region. The case study also presented in section 7.2.6.1 indicated quasi – Pg characteristics. This study has shown that the hypothetical interaction mechanism is statistically more likely to be a drift-bounce resonance interaction mechanism with that of ~ 10 keV protons. This supports mathematical modelling work by *Ozeke and Mann* (2001) and observational work by *Chisham et al.* (1991) and *Wright et al.* (2001) which indicates that morning sector pulsations such as Pgs are second harmonic standing mode structures driven by 10 – 40 keV particles. In the dusk sector there is evidence to suggest that both fundamental and second harmonic waves are observed, driven through drift and drift-bounce resonance interaction mechanisms. However, the particle data would suggest that for a given wave frequency and azimuthal *m* number a driving particle population of < 60 keV is statistically the more likely. This study has presented evidence to suggest that the occurrence of particles of > 60 keV with suitable amounts of free energy to drive the waves is extremely low. This would suggest that some of the Pc5 events observed in the dusk sector were fundamental mode waves while others were second harmonic mode waves. The Pc4 population observed in the dusk sector is similar to that presented by *Engebretson et al.* (1992). However, the data would suggest that the 100 keV driving particle population they cited in their paper as driving the wave is statistically unlikely. The results presented here have also indicated the phenomena of mode coupling where a high *m* Pc5 wave is immediately followed in time by a much smaller scale Pc4 wave. The data further suggests that either the interaction mechanism for the two pulsations remains the same but that the eigenfrequency changes or that two distinct regions of free energy existed in the conjugate IDF. The fact that the Pc4 wave would have unlikely been observed by HF radar and also satellite instruments indicates the importance of the DOPE system.

Chapter 8

Summary, Conclusions and Future Work

8. Introduction

This thesis has discussed the phenomenon of small scale high *m* ULF waves driven through wave-particle interactions between the unstable particle populations in the magnetospheric ring current and standing wave modes on the Earth's magnetic field. The energy from the particle populations is fed into the wave field through the process of inverse Landau damping. This energy is then ultimately dissipated into the collisional medium of the Earth's ionosphere. Given the small scale nature of these waves, observations have proved most difficult. As such it has been unknown whether any particular wave eigenmode and thus generation mechanism is dominant in either the pre or post-noon magnetosphere. In previous work, particular attention has been given to two classes of ULF waves, Giant Pulsations (Pgs) which are observed in the pre-noon sector during geomagnetically quiet times and Storm time Pc5 pulsations which occur in the post-noon sector during geomagnetically active times. Much controversy rages about the eigenmodes and generation mechanisms of these two wave classes with evidence for both odd and even mode standing waves having been presented in the past. This thesis has researched these and other more recently discovered classes of high *m* waves using new and exciting techniques and larger datasets than previously documented.

8.1. Interacting Energetic Particle Populations

The type of resonant interaction mode depends upon the energy of the interacting particle population. Previously, both low (~10 keV) and high (~100 keV) energy particle populations have been cited as providing energy to small scale ULF waves; the particle energy being dependant upon the interaction mechanism and eigenmode structure of the wave. The dynamical nature of the interacting particle populations had never been examined in great detail and as such it was unclear as to the occurrence rate of such populations. Chapter 5 analysed 2.5 years of magnetospheric particle data in the form of Ion Distribution Functions (IDFs). The IDFs were examined to ascertain the statistical likelihood of specific particles containing free energy and also how much free energy the populations contained. A study of this type has never been undertaken before. This has proved a vital result in understanding the generation mechanism of high m ULF waves. The results of this study indicate that lower energy (10 – 45 keV) protons are the dominant non-Maxwellian populations for any interacting wave mode. Not only is the occurrence of these particles dominant, they also routinely contain the largest amount of free energy ($>10^{10}$ J). Bump-on-tail distributions at higher energies (≥100 keV) are rarely observed and also contain greatly reduced amounts of free energy ($<10^9$ J). More IDFs containing free energy were observed on the dawn sector which, in agreement with the work of *Yeoman et al.* (2000), indicates that the dawn sector could be a more fertile region for high m ULF wave generation then previously thought. This work has also indicated possible incompatibilities with work which utilises spacecraft data to identify the wave mode and from that the driving particle population, which is generally inferred to be ~ 100 keV protons. Possible flaws in this method of wave identification using spacecraft data have been outlined, which when combined with the results of this study imply that some wave events may have been misidentified.

8.2. Conjugate Observations of ULF Waves and Driving Magnetospheric Particle Populations

Chapter 6 detailed one of only 3 recorded events which present conjugate ionospheric data of the ULF wave field in addition to magnetospheric data of the driving particle population. The event in question utilised the new artificial backscatter technique, described in chapter 4 to investigate ULF wave processes observed in the morning sector of the magnetosphere. The 15.4 mHz, Pc4 wave had an azimuthal wave number, $m = -45\pm10$, large enough to shield the wave signal completely from ground magnetometers. Conjugate observations from the *Polar* CAMMICE (MICS) instrument indicate the driving non-Maxwellian IDF, with evidence that free energy was available to the wave between 8 and 15 keV. An analysis of the resonance equation supported the conclusion that the wave observed was the result of a drift-bounce (N = 1) resonance interaction between a second harmonic standing wave and the non-Maxwellian particle population. Additional statistical evidence of magnetospheric particle data undertaken using the *Polar* TIMAS instrument suggested that the drift-bounce resonance condition, with particle populations of relatively low energy (~ 10 keV) is the most likely mechanism for the bulk of such high m morning sector waves.

8.3. Confidence Testing of the Wave-Particle Interaction Hypothesis

Although high *m* ULF waves have been cited as being driven by unstable particle populations in the magnetosphere, a statistical cause and effect relationship has never before been determined.

The statistical study undertaken in chapter 5 suggests that the conjugate existence of an IDF containing not only a positive gradient region at the correct particle energy, but also enough free energy to drive the Pg previously observed by *Wright et al.* (2001) is very unlikely to be coincidental given the small probability of such an IDF existing in the magnetospheric particle population. This additional statistical evidence strongly supports the work of *Wright et al.* (2001) that the ~10 keV particle population was indeed the driving source of the Pg via the drift-bounce resonance interaction and is thus strongly supportive of a causal link between unstable IDFs at such energies in the magnetospheric ring current and high *m*, small scale waves in the magnetosphere.

Chapter 7 presented a Monte Carlo analysis of conjugate ionospheric wave events and magnetospheric particle populations. The analysis indicated that the average amount of free energy available from a particle population during times when a high *m* wave is observed in the conjugate ionosphere is statistically significant, with 89.5 % of the distribution located below this value. This implies that the waves occurred during periods when there was a particle distribution present in the magnetosphere at a conjugate location, with an increased amount of free energy available.

These two studies provide the first statistical experimental evidence that high *m* waves are indeed driven by internal unstable plasma populations

8.4. Energy Considerations

This thesis has provided the first observational evidence detailing the amount of energy that is transferred from the unstable magnetospheric particle populations into the high latitude ionosphere by the ULF wave field. Using new analysis techniques which connected the driving particle population to the wave through the amount of energy transferred, chapter 6 investigated a morning sector uncorrelated wave. Such an analysis had never previously been undertaken and provided new evidence to link the driving unstable particle populations to a specific wave event. The calculations were also undertaken for a Giant Pulsation event detailed by *Wright et al.* (2001) for which conjugate wave – particle data was also available. The results indicated that for a wave which displayed no conjugate ground signature, a so called uncorrelated wave (UW) $\sim 10^{10}$ J was transferred from the magnetospheric ring current and dissipated into the ionosphere. In the case of the Pg, $\sim 10^{11}$ J was transferred from the ring current particle population into the ionosphere, an order of magnitude more energy.

Using the results from this new energy calculation technique the properties of Pgs can be explained. The statistical study undertaken in chapter 5 and summarised in section 8.1 indicated than less than 10% of the observed particle populations in the magnetospheric ring current contain this larger amount ($\sim 10^{11}$ J) of free energy and do so only in the pre-noon sector of the magnetosphere. The two examples of Pgs discussed in chapter 6 (Case 2 and an example from *Allan and Poulter,* 1984) both suggest a drift-bounce resonance interaction between a second harmonic standing mode and particles of energy of ~10 keV. For case 2 presented in chapter 6, conjugate particle data were available which did indeed reveal a positive gradient region at ~10 keV. Thus the combination of the increased amount of energy required to drive the Pg, coupled with the statistical particle data suggests that even if the resonance conditions are met, Pgs will be a rare, morning phenomena due to the small statistical probability of a particle population containing enough free energy to drive the wave.

8.5. Ionospheric ULF Wave Observations

Chapter 7 presented some of the most accurate ionospheric measurements to date using the multi-path DOPE HF sounder in northern Norway. The study presented 27 events, predominantly in the post-noon sector. The majority of events were Pc4 waves with azimuthal m numbers ranging from -100 to -200, representing some of the smallest scale waves ever observed in the ionosphere. Four Pc5 waves were observed in the post-noon sector. By accurately obtaining values for the wave azimuthal m number and angular frequency, the resonance equation (equation 8.2) could be solved resulting in hypothetical IDFs need to drive the waves through either a drift or drift-bounce resonance interaction mechanism. These results were then considered alongside the statistical study undertaken in chapter 5. By combining these two statistical studies a more detailed picture of any dominant interaction mechanism was obtained. Evidence from these two studies indicated that the drift-bounce mechanism is dominant in the morning sector, providing an unexpected sink for ring current energy in the region. In the dusk sector there is evidence to suggest that both fundamental and second harmonic waves are observed, driven through drift and drift-bounce resonance interaction mechanisms. However, the particle data would suggest that for a given wave frequency and azimuthal *m* number a driving particle population of < 60 keV is statistically the more likely. This would suggest that some of the Pc5 events observed in the dusk sector were fundamental mode waves while others were second harmonic mode waves. The Pc4 population observed in the dusk sector is similar to that presented by *Engebretson et al.* (1992). However, the data would suggest that the 100 keV driving particle population they cited in their paper as driving the wave is statistically unlikely.

The research undertaken in this thesis has demonstrated the importance of small scale ULF waves in understanding the transport of energy and momentum around the magnetosphere and ionosphere. The results have indicated for the first time, quantitatively, the amount of energy that is transported by these pulsations into the high latitude ionosphere. Statistical studies of the driving particle populations have indicated that the lower energy (10 – 60 keV) protons are responsible for carrying the most amount of free energy. Ionospheric observations have indicated that the occurrence of such pulsations could be more abundant than previously thought. As such this implies that the quantity of energy being transported round the magnetospheric cavity and into the ionosphere via wave-particle interactions has previously been underestimated.

8.6. Future Work

The two case studies presented in chapter 7 have indicated the intriguing nature of these ULF waves and also highlights the dynamical nature of the magnetosphere. One event displayed quasi – Pg characteristics, while the other indicated the phenomena of mode coupling where a high *m* Pc5 wave is immediately followed in time by a much smaller scale Pc4 wave. The data for the latter event suggests that either the interaction mechanism for the two pulsations remains the same even thought the eigenfrequency changes or the two waves are driven by an IDF which contains a double 'bump-on-tail'. Examples of such IDFs exist in the particle statistical database utilised in this thesis, but further investigation is clearly needed.

The fact that the Pc4 wave would have unlikely been observed by HF radar and also satellite instruments illustrates the importance of the DOPE system. As mentioned earlier this also highlights the possibility that small scale ULF waves are a more common occurrence than previously thought, which in turn could imply larger amounts of energy are flowing between the magnetosphere and ionosphere. Further conjugate observations are needed of both the driving particle population and the ionospheric ULF wave using facilities with superior spatial and temporal resolution such as DOPE and also the artificial backscatter technique.

The majority of small scale ULF wave observations have been confined to observations using spacecraft close to geostationary orbit. As this thesis has shown, this is not the ideal tool for investigations of this nature. In order to obtain a more rounded understanding of any processes, other regions of the magnetosphere, both at high and low latitudes must be examined.

The new SPEAR (Space Plasma Exploration by Active Radar, e.g. *Wright et al.,* 2000) facility located on the island of Svalbard (~78° N) offers an excellent tool for examining ULF waves at higher latitudes and also to extend the potential instrument database by utilising the heating capabilities of the new SPEAR system to generate field aligned irregularities. Combining SPEAR observations of ULF waves with conjugate Cluster observations of magnetospheric particle observations could provide a more detailed view of any interaction processes. The higher latitude location of SPEAR in comparison to the EISCAT heater could also allow possible dual experiments to be run using both heater systems. The possibility also exists of inter-hemispheric studies using the 15 radar systems that make up the SuperDARN array. 9 of the radars are located in the northern hemisphere with the remaining 6 located in the southern hemisphere. The TIGER (Tasman International Geospace Environment Radar, *Dyson and Devlin,* 2000) system which is part of the SuperDARN array located on Bruny Island off the coast of Tasmania (43.8° S (geographic), 55.3° S (geomagnetic)) could also contribute to lower latitude studies.

The research undertaken in this thesis also indicated that higher energy particles (≥ 100 keV) contain very little free energy. However, many theoretical models cite these higher energy particles as being responsible for driving the observed pulsations. It is possible that the higher energy particles (~100 keV) are not detected by the *Polar* spacecraft used in this thesis, possibly due to pitch angle effects as discussed in chapter 7. Further investigation is certainly needed utilising multi-satellite particle observations from projects such as Cluster and Double Star. These two experiments not only offer multi-satellite but multi-orbit observations. Double Star will be particularly useful as the two satellites have an equatorial and polar orbit respectively. Future missions will also offer additional orbits for investigation.

References

Allan W, and E. M. Poulter, ULF waves – their relationship to the structure of the Earth's magnetosphere, *Rep. Prog. Phys.*, 55, 533-598, 1992

Allan, W., E. M. Poulter, and E. Nielsen, STARE observations of a Pc5 pulsation with large azimuthal wave number, *J. Geophys. Res.* **87**, 6163, 1982.

Allan, W., E. M. Poulter, and E. Nielsen, Pc5 pulsations associated with ring current proton drifts: STARE radar observations, *Planet. Space Sci.*, **31**, 1279, 1983.

Allan, W., and E. M. Poulter, The spatial structure of different ULF pulsation types: A review of STARE radar results, *Rev. Geophys and Space Phys.*, **22**, 85, 1984.

Anderson, B. J., Statistical studies of Pc 3 – 5 pulsations and their relevance for possible source mechanisms of ULF waves, *Ann. Geophysicae*, **11**, 128, 1993.

Anderson, B. J., M. J. Engebretson, S. P. Rounds, L. J. Zanetti, and T. A. Potemra, A statistical study of Pc 3 – 5 pulsations observed by the AMPTE/CCE magnetic fields experiment. 1. Occurrence distributions, *J. Geophys. Res.*, **95**, 10,495, 1990.

Annexstad, J. O., and C. R. Wilson, Characteristics of Pg micropulsations at conjugate points, *J. Geophys. Res.*, **73**, 1805, 1968.

Arthur, C. W., and R. L. McPherron, The Statistical character of Pc4 magnetic pulsations at synchronous orbit, *J. Geophys. Res.*, **86**, 1325, 1981.

Bond, G. E., T. R. Robinson, P. Eglitis, D. M. Wright, A. J. Stocker, M. T. Rietveld and T. B. Jones, Spatial observations by the CUTLASS coherent scatter radar of ionospheric modification by high power radio waves, *Ann. Geophysicae*, **15**, 1412, 1997.

Buchert, S. C., R. Fujii and K. H. Glassmeier, Ionospheric conductivity modulations in ULF pulsations, *J. Geophys. Res.,* **104**, 10119, 1999.

Brekke, A., Feder, T., and S. Berger, Pc4 giant pulsations recorded at Tromsø, 1929 – 1985. *J. atmos. Terr. Phys.* **49**, 1027.

Cao. M., R. L. McPherron, and C. T. Russell, Statistical study of ULF wave occurrence in the dayside magnetosphere, *J. Geophys. Res.,* **99**, 8731, 1994.

Chapman, P. J., A cost effective frequency synthesizer for Doppler applications, *Radio and Space Plasma Physics Group Tech. Rep. 60*, Leicester University, UK 1995.

Chapman, P. J., HF Doppler receiver, *Radio and Space Plasma Physics Group Tech. Rep. 63*, Leicester University, UK, 1997a

Chapman, P. J., HF Doppler transmitter, *Radio and Space Plasma Physics Group Tech. Rep. 64*, Leicester University, UK, 1997b.

Chapman, S, and V. C. A. Ferraro, A new theory of magnetic storms, *Terrest. Magnetism Atmos. Elec.*, 36, 171, 1931.

Chen, L., and A. Hasegawa, Kinetic theory of geomagnetic pulsations 1. Internal excitations by energetic particles, *J. Geophys. Res.*, **96**, 1503, 1991.

Chen, L., and A. Hasagawa, On magnetospheric hydromagnetic waves excited by energetic ring current particles, *J. Geophys. Res.*, **93**, 8763, 1988.

Cheng , C. Z., Kinetic – Theory of collisionless ballooning modes, Phys. Fluids, **25**, 1020, 1982.

Cheng, C. Z., and Q Qian, Theory of Ballooning – Mirror instabilities for anisotropic pressure plasmas in the magnetosphere, *J. Geophys. Res.*, **99**, 11,193, 1994.

Chisham, G. and D. Orr, Statistical studies of giant pulsations (Pgs): harmonic mode, *Planet. Space Sci.*, **39**, 999, 1991

Chisham, G., D. Orr and T. K. Yeoman, Observations of a giant pulsation (Pg) across an extended array of ground magnetometers and an auroral radar, *Planet. Space Sci.*, **40**, 953, 1992.

Chisham, G., Giant pulsations: An explanation for their rarity and occurrence during geomagnetically quiet times, *J. Geophys. Res.*, **101**, 24,755, 1996.

Clemmow, P. C., and J. P. Dougherty, Electrodynamics of Particles and Plasmas, Addison-Wesley, London 1969.

Cramm, R., K. H. Glassmeier, C. Othmer, K. H. Fornacon, H. U. Auster, W. Baumjohann, and E. Georgescu, A case study of a radially polarised Pc4 event observed by the Equator – S satellite, *Ann. Geophysicae*, **18**, 411, 2000.

Cummings, W. D., R. J. O'Sullivan, and P. J. Coleman Jr., Standing Alfvén waves in the magnetosphere, *J. Geophys. Res.*, **74**, 778, 1969.

De Michelis, P., I. A. Daglis and G. Consolini, Reconstruction of the terrestrial ring current derived from AMPTE/CCE-CHEM, *J. Geophys. Res.*, 102, 14,103, 1997.

Dungey, J. W., Interplanetary magnetic field and the auroral zones, *Phys. Rev. Lett.*, 6, 47, 1961.

Dungey, J. W., Electrodynamics of the outer atmospheres, Rep. 69, *Ions. Res. Lab. Pa. State Univ.*, University Park, 1954.

Dungey, J. W., The Structure of the exosphere or Adventures in velocity space, Geophysics, The Earth's Environment, *C. Dewitt, Ed.*, 537, Gordon and Breach, New York, 1963.

Dungey, J. W., Hydromagnetic Waves, Physics of Geomagnetic Phenomena, *S. Matsushita and W.* H. *Campbell, Eds.*, 913, Academic Press, New York, 1968.

Dyson, P. L., and J. C. Devlin, The Tasman International Geospace Environment Radar, The Physicist (The Australian Institute of Physics), **37**, 48, March 2000.

Eglitis, P., T. R. Robinson, M. T. Rietveld, D. M. Wright and G. E. Bond, The phase speed of artificial irregularities observed by CUTLASS during HF modification of the auroral ionosphere, *J. Geophys. Res.*, **103**, 2253, 1998.

Engebretson, M.J., D. L. Murr, K. N. Erickson, R. J. Strangeway, D. M. Klumpar, S. A. Fuselier, L. J. Zanetti, and T. A. Potemra, The spatial extent of radial magnetic pulsation events observed in the dayside near synchronous orbit, *J. Geophys. Res.*, **97**, 13,741, 1992.

Engebretson, M. J., and L. J. Cahill, Pc5 pulsations observed during the June 1972 geomagnetic storm, , *J. Geophys. Res.*, **86**, 5619, 1981.

Georges, T. M., Ionospheric effects of atmospheric waves, E.*S.S A. Tech. Rep., Inst. Environ. Res. (Boulder, Colo.)* I.E.R. 57-I.T.S.A. 54, October 1967.

Glassmeier, K. H., Magnetometer Array Observations of a Giant Pulsation Event, *J. Geophys. Res.*, **48**, 127, 1980.

Glassmeier, K. H., S. Buchert, U. Motschmann, A. Korth, and A. Pedersen, Concerning the generation of geomagnetic giant pulsations by drift-bounce resonance ring current instabilities, *Ann. Geophysicae*, **17**, 338, 1999.

Glassmeier, K. H., Reply to the comment by I. R. Mann and G. Chisham, *Ann. Geophysicae*, **18**, 167, 2000.

Grocott, A., Radar Observations of Convection in the Nightside High-Latitude Ionosphere., PhD. Thesis, Radio and Space Plasma Physics Group, University of Leicester, UK, 2002.

Grant, I. F., D. R. McDiarmid, and A. G. McNamara, A class of high-*m* pulsations and its auroral radar signature, *J. Geophys. Res.*, **97**, 8439, 1992.

Green, C. A., Observations of Pg pulsations in the northern auroral zones and at lower latitude conjugate points, *Planet. Space Sci.*, **27**, 63, 1979.

Greenwald, R. A., Weiss, W., Nielsen, E., and Thompson, N. R., STARE: A new radar auroral backscatter experiment in northern Scandinavia, *Radio Sci.*, **13**, 1021, 1978.

Greenwald, R. A., K. B. Baker, J. R. Dudeney, M. Pinnock, T. B. Jones, J.-P. Villain, J.-C. Cerisier, C. Senior, C. Hanuise, R. D. Hunsucker, G. Sofko, J. Koehler, E. Nielsen, R. Pellinen, A. D. M. Walker, N. Sato, and H. Yamagishi, DARN/SUPERDARN A global view of the dynamics of high-latitude convection, *Space Sci. Rev.*, **71**, 761, 1995.

Greenwald, R. A., and A. D. M. Walker, Energetics of long period resonant hydromagnetic waves, *Geophys. Res. Lett.*, **7**, 745, 1980.

Hasegawa, A., Drift mirror instability in the magnetosphere, *Phys. Fluids,* **12**, 2642, 1969.

Hasegawa, A., Drift – wave instabilities of a compressional mode in high - β plasma, *Phys. Rev. Lett.,* **27**, 11, 1971.

Hamlin, D. A., R. Karplus, R. C. Vik, and M. Watson, Mirror and azimuthal drift frequencies for geomagnetically trapped particles, *J. Geophys. Res.,* **66**, 1, 1961.

Hillebrand, O., J. Münch, and R. L. McPherron, Ground – Satellite correlative study of a giant pulsation event, *J. Geophys. Res.,* **51**, 129, 1982.

Hughes, W. J., Hydromagnetic waves in the magnetosphere, *Solar Terrestrial Physics* (edited by Carovillano, R. L. and Forbes, J. M.), Reidel, Dordrecht, 1983.

Hughes, W. J. and D. J. Southwood, The screening of micropulsation signals by the atmosphere and ionosphere, *J. Geophys. Res.*, **81**, 3234, 1976.

Hughes, W. J., D. J. Southwood, B. Mauk, R. L. McPherron, J. N. Barfield, Alfvén waves generated by an inverted plasma energy distribution, *Nature*, **275**, 43, 1978

Hughes, W. J., R. L. McPherron, J. N. Barfield and B. H. Mauk, A compressional Pc4 pulsation observed by three satellites in geostationary orbit near local midnight, *Planet. Space Sci.,* **27**, 821, 1979.

Hughes, W. J., R. L. McPherron, and C. T. Russell, Multiple satellite observations of pulsation resonance structures in the magnetosphere, *J. Geophys. Res.*, **82**, 492, 1977.

Hughes, W. J., and R. J. L. Grard, A second harmonic geomagnetic field line resonance at the inner edge of the plasma sheet: GEOS 1, ISEE 1 and ISEE 2 observations, *J. Geophys. Res.*, **89**, 2755, 1986.

Jacobs, J. A., Y. Kato, S. Matsushita and V. A. Troitskaya, Classifications of geomagnetic micropulsations, *J. Geophys. Res.,***69 (A1)**, 180, 1964.

Kelly, M. C., The Earth's Ionosphere: Plasma Physics and Electrodynamics, Academic Press Inc., 1989.

Kivelson, M. G., and C. T. Russell, Introduction to Space Physics, Cambridge University Press, 1995.

Kokubun, S., K. N. Erickson, T. A. Fritz and R. L. Mcpherron, Local time asymmetry of Pc4 – 5 pulsations and associated particle modulations at synchronous orbit, *J. Geophys. Res.*, **94**, 6607, 1989.

Kokubun, S., Statistical characteristics of Pc5 waves at geostationary orbit, *J. Geomag.Geoelectr.,* **37**, 759, 1985.

Kremser, G., A. Korth, J. A. Fejer, B. Wilken, A. V. Gurevish, and E. Amata, Observations of quasi-periodic flux variations of energetic ions and electrons associated with Pc5 geomagnetic pulsations, *J. Geophys. Res.*, **86**, 3345, 1981.

Landau, L. D. and E. M. Lifshitz, Statistical Physics: vol. #5 of Course of Theoretical Physics, Pergamon Press, 1958.

Lessard, M. R., M. K. Hudson, and H. Lühr, A statistical study of Pc 3-Pc 5 magnetic pulsations observed by the AMPTE/Ion Release Module satellite, *J. Geophys. Res.*, **104**, 4523, 1999.

Lester, M., Magnetosphere of the Earth: Substorms, Encyclopaedia of Astronomy and Astrophysics, IOP Publishing and Macmillan Publishers Ltd., 2000.

Lester, M., J. A. Davies, T. K. Yeoman, The ionospheric response during an interval of Pc5 ULF wave activity, *Ann. Geophysicae*, **18**, 257, 2000.

Lühr, H., The IMAGE magnetometer network, *STEP Int. Newslett. 4* , 4, 1994.

Lui, A. T. Y., and D. C. Hamilton, Radial profiles of quiet time magnetospheric parameters, *J. Geophys. Res.*, 97, 19,325, 1992.

Lui, A. T. Y., R, W, McEntire, and S. M. Krimigis, Evolution of the ring current during two geomagnetic storms, *J. Geophys. Res.*, 92, 7459, 1987.

Mann, I. R. and G. Chisham, Comment on "Concerning the generation of geomagnetic giant pulsations by drift-bounce resonance ring current instabilities" by K. H. Glassmeier *et al. Ann. Geophysicae*, **17**, 338, 1999, *Ann. Geophysicae*, **18**, 161, 2000.

McNamara, A. G. , D. R. McDiarmid, G. J. Sofko, J. A. Koeler, P. A. Forsyth, and D. R.Moorcroft, BARS - a dual bistatic auroral radar system for the study of electric fields in the Canadian sector of the auroral zone, *Adv. Space Res.*, **2**, 145, 1983.

Milan, S. E., M. Lester, and J. Moen, A comparison of optical and coherent HF radar backscatter observations of a post-midnight aurora, *Ann. Geophysicae*, 15, 1388, 1997.

Nielsen, E., W. Guttler, E. C. Thomas, C. P. Stewart, T. B. Jones, and A. Hedburg, SABRE - new radar-auroral backscatter experiment, *Nature*, **304**, 712, 1983.

Northrop, T. G., The Adiabatic Motion of Charged Particles Interscience, 109, New York, 1963.

Ozeke, L. G., I. R. Mann, Modeling the properties of high *m* Alfvén waves driven by the drift-bounce resonance mechanism, *J. Geophys. Res.*, **106**, 15583, 2001.

Pokhotelov, O. A., V. A. Pilipenko, Y. M. Nezlina, J. Woch, G. Kremser, A. North and E. Amata, Excitation of high β plasma instabilities at the geostationary orbit – theory and observations, , *Planet. Space Sci.*, **34**, 695, 1986.

Parker, E. N., Interplanetary Dynamical Processes, Wiley-Inter-Science, New York, 1963.

Rietveld, M. T., H. Kohl, H. Kopka and P. Stubbe, Introduction to ionospheric heating at Tromsø – I. Experimental overview, *J. Atmos. Terr. Phys.*, **55**, 577, 1993.

Rishbeth, H., P. J. S. Williams, The EISCAT ionospheric radar: the system and its early results, *Q. J. R. Astron. Soc.*, **26**, 478, 1985.

Robinson, T. R., The heating of the high latitude ionosphere by high power radio waves, *Phys. Rep.*, **179**, 79-209, 1989.

Robinson, T. R., A. J. Stocker, G. E. Bond, P. Eglitis, D. M. Wright and T. B. Jones, O- and X-mode heating effects observed simultaneously with the CUTLASS and EISCAT radars and low power HF diagnostics at Tromsø, *Ann. Geophysicae*, **15**, 134, 1997.

Samson, J. C., J. A. Jacobs, and G. Rostoker, Latitude dependent characteristics of long – period geomagnetic micropulsation, *J. Geophys. Res.*, **76**, 2554, 1971.

Schulz, M., and L. J. Lanzerotti, Particle diffusion in the radiation belts, Springer-Verlag, Berlin, Heidelberg, New York, 1974.

Shelley, E. G., A. G. Ghielmetti, H. Balsiger, R. K. Black, J. A., Bowles, R. P. Bowman, O. Bratschi, J. L. Burch, C. W. Carlson, A. J. Coker, J. F. Drake, J. Fischer, J. Geiss, A. Johnstone, D. L. Kloza, O. W. Lennartsson, A. L. Magoncelli, G. Paschmann, W. K. Peterson, H. Rosenbauer, T. C. Sanders, M. Steinacher, D. M. Walton, B. A. Whalen and D. T. Young, The Toroidal Imaging Mass-Angle Spectrograph (TIMAS) for the *Polar* Mission, *Space Sci. Rev.*, **71**, 497, 1995.

Southwood, D. J., Some features of field line resonances in the magnetosphere, *Planet. Space Sci.,* 22, 483, 1974.

Southwood, D. J., A general approach to low-frequency instability in the ring current plasma, *J. Geophys. Res.*, **81**, 3340, 1976.

Southwood, D. J., J. W. Dungey, and R. J. Etherington, Bounce resonant interactions between pulsations and trapped particles, *Planet. Space Sci.*, **17**, 349, 1969.

Southwood, D., J. and Kivelson, M. G., Charged particle behaviour in low-frequency geomagnetic pulsations; Graphical approach, *J. Geophys. Res.*, 87, 1707, 1982.
Southwood, D. J., 1977

Stewart, B., On the great magnetic disturbance which extended from August 2 to September 7, 1859 as recorded by photography at the Kew Observatory, *Phil. Trans. Roy Soc. Lond.,* 11, 407, 1861.

Takahashi, K., R. W. McEntire, A. T. Y. Lui, and T. A. Potemra, Ion flux oscillations associated with a radially polarised transverse Pc5 magnetic pulsation, *J. Geophys. Res.*, **95**, 3717, 1990.

Takahashi, K, New observations, new theoretical results and controversies regarding Pc3 – 5 waves, *Adv. Space Res.,* **17**, 63, 1996.

Takahashi, K., N. Sato, J. Warnecke, H. Lühr, H. E. Spence, and Y. Tonegawa, On the standing wave mode of giant pulsations, *J. Geophys. Res.*, **97**, 10,717, 1992.

Takahashi, K., P.R. Higbie, and D. N. Baker, Characteristics of compressional Pc5 waves observed at geostationary orbit, *J. Geophys. Res.*, **90**, 1473, 1985.

Takahashi, K., ULF waves: 1997 IAGA division 3 reporter review, *Ann. Geophysicae*, **16**, 787, 1998.

Takahashi, K., J. F. Fennell, E. Amata, and P. R. Higbie, Field-aligned structure of the storm time Pc5 wave of November 14 – 15, 1979, *J. Geophys. Res.*, **92**, 5857, 1987.

Takahashi, K., and B. J. Anderson, Distribution of ULF energy (f < 80 mHz) in the inner magnetosphere: A statistical analysis of AMPTE CCE magnetic field data, *J. Geophys. Res.*, **97**, 19,751, 1992.

Takahashi, K., and R. L. McPherron, Standing hydromagnetic oscillations in the magnetosphere, *Planet. Space Sci.* ,**32**, 1343, 1984.

Thompson, S. M., and M. G. Kivelson, New Evidence for the origin of giant pulsations, *J. Geophys. Res.*,**106**, 21,237, 2001.

Tonegawa, Y., and N. Sato, Conjugate are study of giant geomagnetic pulsations, paper presented at Chapman Conference on Plasma Waves and Instabilities in Magnetospheres and at Comets, AGU, Sendai / Mt. Zao, Japan, Oct. 12 – 16, 1987.

Tsyganenko, N. A., A magnetospheric magnetic field model with a warped tail current sheet, *Planet. Space Sci.*, **37**, 5, 1989.

Walker, A. D. M., R. A. Greenwald, W. F. Stuart, and C. A. Green, STARE auroral radar observations of Pc5 geomagnetic pulsations, *J. Geophys. Res.*, **84**, 3373, 1979.

Wild, J. A., Electrodynamics of the Auroral Ionosphere During Magnetospheric Substorms, PhD. Thesis, Radio and Space Plasma Physics Group, University of Leicester, UK, 2000.

Wilken, B., W. Weiß, D. Hall, M. Grande, F. Sørass and J. F. Fennell, Magnetospheric Ion Composition Spectrometer on board the CRRES spacecraft, *J. Spacecraft and Rockets*, **29**, 1992.

Woch, J., G. Kremser, A. Korth, A comprehensive investigation of compressional ULF waves observed in the ring current, *J. Geophys. Res.*, **95**, 15,113, 1990.

Wright, D. M., T. K. Yeoman, and J. A. Davies, A comparison of EISCAT and HF Doppler observations of a ULF wave, *Ann. Geophysicae*, **16**, 1190, 1998.

Wright, D. M., and T. K. Yeoman, High-latitude HF Doppler observations of ULF waves: 2. Waves with small spatial scale sizes, *Ann. Geophysicae*, **17**, 868, 1999a.

Wright, D. M., and T. K. Yeoman, High resolution bistatic radar observations of ULF waves in artificially generated backscatter, *Geophys. Res. Lett.*, **26**, 2825-2828, 1999b.

Wright, D. M., T. K. Yeoman and P. J. Chapman, High-latitude HF Doppler observations of ULF waves: 1. waves with large spatial scale sizes, *Ann. Geophysicae,* **15**, 1548, 1997.

Wright D. M., T. K. Yeoman, I. J. Rae, J. Storey, A. B. Stockton-Chalk, J. L. Roeder and K. J. Trattner, Ground-based and Polar spacecraft observations of a giant (Pg) pulsation and its associated source mechanism, *J. Geophys. Res.,* **106**, 10,837, 2001.

Wright, D. M., HF Doppler observations of ULF waves: system development and high-latitude results, Ph.D. thesis, Leicester University, UK, August 1996.

Wright, D. M., J. A. Davies, T. R. Robinson, P. J. Chapman, T. K. Yeoman, E. C. Thomas, M. Lester, S. W. H. Cowley, A. J. Stocker, R. B. Horne, F. Honary, Space Plasma Exploration by Active Radar (SPEAR): an overview of a future radar facility, *Ann. Geophysicae*, **18**, 1248, 2000.

Yeoman, T. K. and D. M. Wright, ULF waves with drift resonance and drift-bounce resonance energy sources as observed in artificially-induced HF radar backscatter, *Ann. Geophysicae*, **19**, 159, 2001.

Yeoman, T. K., D. M. Wright, P. J. Chapman and A. B. Stockton-Chalk, High-latitude observations of ULF waves with large azimuthal wavenumbers, *J. Geophys. Res.*, **105**, 5453, 2000.

Yeoman, T. K., Mao Tian, M. Lester and T. B. Jones, A study of Pc5 hydromagnetic waves with equatorward phase propagation, *Planet. Space Sci.,* **40**, 797, 1992.

Yeoman, T. K., M. Lester, D. Orr, and H Lühr, Ionospheric boundary conditions of hydromagnetic waves: the dependence on azimuthal wave number and a case-study, *Planet. Space Sci.,* **38**, 1315, 1990.

Yeoman, Y. K., D. M. Wright, T. R. Robinson, J. A. Davies, and M. T. Reitveld, High spatial and temporal resolution observations of an impulse-driven field line resonance in radar backscatter artificially generated with the Tromsø heater, *Ann. Geophysicae*, **15**, 634, 1997.

Zhu, X., and M. G. Kivelson, Compressional ULF waves in the outer magnetosphere, 1, Statistical study, *J. Geophys. Res.,* **96**, 19,451, 1991.

Appendix

Battenberg Cake

Ingredients:

Butter – 110g (4oz), softened

Caster sugar – 110g (4oz)

Eggs – 2

Ground rice – 50g (2oz)

Self raising flour – 100g (4oz)

Baking powder - ½ tsp

Almond essence – few drops

Red food colouring – few drops

Apricot jam – 3-4 tbsp

Almond paste – 225g (8oz)

Method:

1) Pre-heat oven to 170 °C / 325 °F / Gas 3. Grease and base line an 18 cm (7 inch) shallow square cake tin with buttered greaseproof paper.

2) Place the butter, sugar, eggs, ground rice, flour, baking powder and almond essence in a large bowl and beat well for approximately 2 minutes until smooth.

3) Spoon half the mixture into one half of the prepared tin as neatly as possible. Add a few drops of red food colouring to the remaining mixture to turn it a deep pink colour, then spoon this into the other half of the tin. Try to get the join between the two mixtures as neat as possible. Smooth the surface.

4) Bake for 35-40 minutes or until the cake is well risen, springy to the touch and has shrunk slightly from the sides of the tin. Turn out and leave to cool on a wire rack.

5) Trim the edges of the cake and then cut into 4 equal strips down the length of the colours.

6) Gently heat the apricot jam in a small pan and stick the stripes of cake together, one plain piece next to one coloured one, and then vice versa to make a chequerboard effect.

7) Brush the top of the assembled cake with apricot jam.

8) Roll out the almond paste into a rectangle the length of the cake and sufficiently wide to wrap around the cake.

9) Invert the cake on to the almond paste, then brush the remaining 3 sides with apricot jam. Press the almond paste neatly around the cake, arranging the join in one corner.

10) Score the top of the cake with a criss-cross pattern and crimp the edges with your fingers to decorate.